

ANALYTICAL MODELING AND NUMERICAL SIMULATION OF GATE-ALL- AROUND FIELD EFFECT TRANSISTOR FOR SENSING APPLICATIONS

**Thesis Submitted
in Partial Fulfillment of the Requirements
for the Degree of**

DOCTOR OF PHILOSOPHY

by

**SHIVANI YADAV
(Enrollment No.: 2K21/PHDEC/13)**

**Under the supervision of
DR. SONAM REWARI
Assistant Professor**

ECE Department, DTU, Delhi



**Department of Electronics and Communication
Engineering**

**DELHI TECHNOLOGICAL UNIVERSITY
(Formerly Delhi College of Engineering)
Shahbad Daulatpur, Main Bawana Road, Delhi-110042, India
August, 2024**

**© DELHI TECHNOLOGICAL UNIVERSITY, DELHI,
2024
ALL RIGHTS RESERVED**

ACKNOWLEDGEMENTS

“We are what our thoughts have made us; so take care about what you think. Words are secondary. Thoughts live; they travel far.”

--Swami Vivekananda

Before we get into the thick of things, I would first like to quote a few words of gratitude and appreciation for the people, who have been through all the ups and downs along with me since the very inception of this dissertation. It is because of all of you, that I feel so blessed and fortunate to look back at my beautiful journey so far, and still feel that this is probably not the end but a new beginning, making this an unforgettable and memorable journey for me.

First of all, I thank to **almighty** for his blessings, life, health, and positive energy that helped me move at every stage throughout my life so far. Without the support from God, nothing would have been possible.

I take the opportunity to humbly submit my sincere and heartfelt thanks to my supervisor, **Dr. Sonam Rewari** from the Department of Electronics and Communication Engineering, Delhi Technological University, Delhi, for her invaluable guidance, enthusiastic encouragement, and persistent support. I am truly grateful from the core of my heart for her meticulous approach, wonderful assistance of her perspective, and fruitful discussions on my research topic. Her immense contribution and rare dedication in providing the much-needed guidance, is worth of highest honor. Her careful supervision and personal attention have given me a lot of confidence and enthusiasm, during the different stages of my doctoral investigations. I invariably fall short of words to express my sincere gratitude for her patience and motivation.

I extend my sincere appreciation to the members of my doctoral committee for their insightful comments and thoughtful suggestions that have enhanced the quality of this thesis. I am extremely thankful to **Prof. O. P. Verma**, Head of the Department of Electronics and Communication Engineering, Delhi Technological University, Delhi, and other faculty members for their endless support and cooperation throughout

this dissertation. I am thankful to all staff members of the department of Electronics and Communication Engineering for their kind help and support during the entire period of my research. I am grateful to the management of Delhi Technological University, Delhi, for providing the necessary resources, facilities, and a conducive research environment for my research work.

My appreciation also goes to my colleagues and friends in the Department of Electronics and Communication Engineering, Delhi Technological University, Delhi, for their constant support, encouragement, and assistance especially **Mrs. Aapurva, Mrs. Divya, Dr. Amit, Dr. Palak, Mr. Vijay, Mr. Anil, Ms. Tanvika, Mr. Vishal, Ms. Himanshi, Mr. Arjun, Ms. Yashika, and Mr. Rohit.**

I dedicate this thesis to my parents, husband and son for their endless love, support, encouragement, and blessings throughout my life. My parents, **Mr. K. R. Yadav, Mrs. Reshma Yadav**, my sister, **Mrs. Seema Yadav** and my brother, **Dr. Abhishek Yadav** for their undeterred faith in me since childhood, and being the biggest pillar of strength who supported me all the way till the end. I would like to thank my husband, **Mr. Pallav Yadav** and Father-in-law, **Mr. T.R. Yadav** for their unconditional, continuous motivation, support and guidance right from the very idea of pursuing doctoral research to the end of it.

Exceptional mention for my loving son, **Advik Yadav** to bear with all my absence during your growth years and be very loving and caring kid always. Special mention to my dear mother-in-law **Mrs. Prabha Yadav** and father-in-law **Mr. T. R. Yadav** for their support and giving me time and energy along with huge satisfaction that my home and son is being looked after in a great way. Nothing is comparable to this feeling.

Last but not least, I would like to express my sincere gratitude to everyone who, directly or indirectly, contributed to my journey.

SHIVANI YADAV



DELHI TECHNOLOGICAL UNIVERSITY

Formerly Delhi College of Engineering

Shahbad Daulatpur, Main Bawana Road, Delhi –42

CANDIDATE'S DECLARATION

I **Shivani Yadav** hereby certify that the work which is being presented in the thesis entitled **Analytical Modeling and Numerical Simulation of Gate-All-Around Field Effect Transistor for Sensing Applications** in partial fulfillment of the requirements for the award of the Degree of Doctor in Philosophy, submitted in the **Department of Electronics and Communication Engineering**, Delhi Technological University is an authentic record of my own work carried out during the period from **August 2021** to **August 2024** under the supervision of **Dr. Sonam Rewari**.

The matter presented in the thesis has not been submitted by me for the award of any other degree of this or any other Institute.

Candidate's Signature

This is to certify that the student has incorporated all the corrections suggested by the examiners in the thesis and the statement made by the candidate is correct to the best of our knowledge.

Signature of Supervisor

Signature of External Examinations



DELHI TECHNOLOGICAL UNIVERSITY

Formerly Delhi College of Engineering

Shahbad Daultapur, Main Bawana Road, Delhi –42

CERTIFICATE BY THE SUPERVISOR

Certified that **Shivani Yadav** (Enrollment No.: 2K21/PHDEC/13) has carried out their research work presented in this thesis entitled “**Analytical Modeling and Numerical Simulation of Gate-All-Around Field Effect Transistor for Sensing Applications**”, for the award of **Doctor of Philosophy** from the Department of Electronics and Communication Engineering, Delhi Technological University, under my guidance and supervision. The thesis embodies results of original work, and studies are carried out by the student herself and the contents of the thesis do not form the basis for the award of any other degree to the candidate or to anybody else from this or any other University/Institution.

Dr. Sonam Rewari
Supervisor
Department of ECE
Delhi Technological University,
Delhi –110042, India

Date:

Dedicated to my Parents, Husband, and Son

*For their endless love,
support and encouragement*

ANALYTICAL MODELING AND NUMERICAL SIMULATION OF GATE-ALL-AROUND FIELD EFFECT TRANSISTOR FOR SENSING APPLICATIONS

SHIVANI YADAV

ABSTRACT

Recent decades have seen extensive research and development in advanced sensing techniques for critical applications in diseases detection, drug discovery, pathogen discovery, toxin detection, agriculture, water monitoring and environmental monitoring. Biosensors have emerged as critical tools in modern healthcare, enabling the rapid and precise detection of a wide range of biomolecules. Field Effect Transistor (FET) based biosensors have gained substantial focus because of their ultra-high sensitivity, label-free detection, cost efficiency, and on-chip fabrication.

Gate-All-Around Field Effect Transistors (GAAFETs) are well-known for having excellent electrostatic control because of their surrounding gate structure. This feature minimizes leakage currents and enhances gate control, making GAAFETs particularly suitable for biosensing applications. For developing high-performance FET-based biosensors, designing a high-performance FET is critical. The research presented in this thesis begins with a comprehensive review of the evolution of FETs, tracing the transition from traditional MOSFETs to FinFETs, and ultimately to GAAFETs. In order to maximize sensitivity and reliability in detecting biomolecules, a variety of GAAFET architectures have been thoroughly assessed using analytical modeling and numerical simulations.

One of the key contributions of this research is the development of the Hetero Dielectric Trench Gate Junction Accumulation Mode GAAFET (HDTG-JAM-GAAFET). This biosensor employs a silicon cylindrical Gate-All-Around FET which operates in Junction Accumulation Mode (JAM) and has a hetero dielectric layer comprised of SiO_2 and HfO_2 . The cylindrical gate structure's metal gate is trenched into the Hafnium oxide dielectric layer, which provides the gate with enhanced control over the surface characteristics of the channel. HDTG-JAM-GAAFET biosensor has drain ON-current sensitivity 67.68% greater for gelatin biomolecules, 69.4% higher for positive biomolecules, and 8% higher for negative biomolecules bound in the nanogap cavity than that of a Normal Gate JAM Gate-All-Around FET. This enhanced performance underscores the potential of the HDTG-JAM-GAAFET in sensitive biomolecule detection, crucial for early disease diagnosis.

In addition to the HDTG-JAM-GAAFET, the Trench Gate Engineered Junction Accumulation Mode GAAFET (TGE-JAM-GAA BioFET) is proposed for label-free biomolecule detection. This biosensor exhibits a 236.24 mV drift in threshold voltage for APTES biomolecules, which is 58.75% and 159.18% higher than that of the Triple Metal Normal Gate JAM GAAFET (TMNG-JAM-GAAFET) and the Single Metal Normal Gate JAM GAAFET (SMNG-JAM-GAAFET), respectively. These findings highlight the superior sensitivity and detection capabilities of the TGE-

JAM-GAA BioFET, making it highly suitable for biosensing applications.

The critical need for a highly sensitive, quick, and affordable biosensor to identify the SARS-CoV-2 virus which has sparked a worldwide pandemic is also covered in this thesis. The Dual Metal Dual Layer Gate-All-Around Nanowire FET (DMDL-GAA-NW-FET) biosensor is introduced for the detection of the SARS-CoV-2 virus, specifically targeting the Spike protein and DNA. The device's design, which includes gate work function engineering to segregate the gate into two layers with distinct work functions, significantly improves gate control and enhances the biosensor's ability to detect the virus. The DMDL-GAA-NW-FET biosensor's effectiveness is demonstrated through a detailed analysis of its electrostatic behavior and a comparison with conventional GAAFET biosensors, showing substantial improvements in sensitivity metrics such as threshold voltage drift (ΔV_{th}), I_{ON} current drift (ΔI_{ON}), transconductance (g_m), and the I_{ON}/I_{OFF} ratio.

Another notable innovation in this research is the Dielectric Modulated 4H-SiC Source Triple Metal Gate-All-Around Silicon Carbide FET (DM-TMGAA-SiCFET) biosensor. The primary emphasis of this work lies in the innovative structural design of the GAA Silicon Carbide FET biosensor. Specifically, it involves the integration of a distinct SiC polytype 4H-SiC for the source, and 6H-SiC for channel region, employing a triple material gate, and the incorporation of an Al_2O_3 and HfO_2 stack. The findings highlight that the DM-TMGAA-SiCFET offers substantial improvements in sensitivity compared to silicon-based FET biosensors, with an impressive 140.72% and 36.72% enhancement in threshold voltage sensitivity observed for gelatin and DNA biomolecules, respectively. Furthermore, there is a remarkable 404.4% improvement in I_{ON}/I_{OFF} sensitivity for gelatin biomolecules.

Additionally, the Gate-All-Around Engineered Gallium Nitride FET (GAAE-GANFET) for label-free biosensing for detection of antigen and antibody from the Avian Influenza virus and DNA as the target biomolecules and the GaAs-GAAE-FET biosensor, designed specifically for breast cancer detection, demonstrate exceptional performance. The innovative Gate-All-Around engineering in GANFET integrates various device engineering techniques, such as channel engineering, gate engineering, and oxide engineering, to enhance biosensing performance. The GaAs-GAAE-FET biosensor design provides a 76.58% higher threshold voltage sensitivity for the MDA-MB-231 biomarker contrasting with the Silicon Gate-All-Around FET (Si-GAA-FET) biosensor.

Looking towards the future, FET-based biosensors, particularly those utilizing GAAFET structures, hold immense potential in revolutionizing the field of biosensing. As the demand for rapid, accurate, and cost-effective diagnostic tools continues to grow, the innovations presented in this thesis lay a strong foundation for further advancements in FET-based biosensing technologies and also opens new avenues for detecting a broader range of diseases at earlier stages, ultimately contributing to improved patient outcomes and public health.

LIST OF PUBLICATIONS

Journal Papers

1. **Shivani Yadav** and Sonam Rewari, "Numerical Simulation of Hetero Dielectric Trench Gate JAM Gate-All-Around FET (HDTG-JAM-GAAFET) for Label Free Biosensing Applications," ECS Journal of Solid State Science and Technology, vol. 12, no. 12, p. 127008, 2023, doi: 10.1149/2162-8777/ad161f.
2. **Shivani Yadav** and Sonam Rewari, "Analytical modeling and numerical simulation of graded JAM Split Gate-All-Around (GJAM-SGAA) Bio-FET for label free Avian Influenza antibody and DNA detection," Microelectronics Journal, vol. 142, p. 106011, 2023, doi: 10.1016/j.mejo.2023.106011.
3. **Shivani Yadav** and Sonam Rewari, "Dual metal dual layer GAA NW-FET (DMDL-GAA-NW-FET) biosensor for label free SARS-CoV-2 detection," Microsystem Technologies, 2023, doi: 10.1007/s00542-023-05560-4.
4. **Shivani Yadav**, Amit Das and Sonam Rewari, "Dielectric Modulated GANFET Biosensor for Label-Free Detection of DNA and Avian Influenza Virus: Proposal and Modeling" ECS Journal of Solid State Science and Technology, vol. 13, no. 4, p. 047001, 2024, doi: 10.1149/2162-8777/ad3364.
5. **Shivani Yadav** and Sonam Rewari, "Nanoscale Trench Gate Engineered JAM Gate-All-Around (TGE-JAM-GAA) Label-Free BioFET for Charged/Neutral Biomolecules Detection," IETE Journal of Research, 70(11), 8263–8277, 2024, <https://doi.org/10.1080/03772063.2024.2368636>
6. **Shivani Yadav** and Sonam Rewari, "Dielectric modulated 4 H-SiC source triple metal gate-all-around silicon carbide FET (DM-TMGAA-SiCFET) biosensor for label-free biomolecule detection," Microsystem Technologies (2024). <https://doi.org/10.1007/s00542-024-05796-8>

Conference Papers

1. **Shivani Yadav** and Sonam Rewari, "Dielectric Modulated Gallium-Arsenide Gate-All-Around Engineered Field Effect Transistor (GaAs-GAAE-FET) Biosensor for Breast Cancer Detection," 2024 IEEE International Conference on

Computing, Power and Communication Technologies (IC2PCT), Greater Noida, India, 2024, pp. 1553-1557, doi: 10.1109/IC2PCT60090.2024.10486515.

2. **Shivani Yadav** and Sonam Rewari, “Trench Gate JAM Dielectric Modulated Nanowire FET (TG-JAM-DM-NWFET) Biosensor,” Proc. 2022 IEEE Int. Conf. Electron Devices Soc. Kolkata Chapter, EDKCON 2022, pp. 23–28, 2022, doi: 10.1109/EDKCON56221.2022.10032912.

TABLE OF CONTENTS

ACKNOWLEDGEMENTS	iii
CANDIDATE’S DECLARATION	v
CERTIFICATE BY THE SUPERVISOR	vi
ABSTRACT	viii
LIST OF PUBLICATIONS	x
TABLE OF CONTENTS	xii
LIST OF TABLES	xvii
LIST OF FIGURES	xix
LIST OF ABBREVIATIONS	xxvi
CHAPTER 1: INTRODUCTION	1
1.1 Background and Progress of MOSFET Technology	1
1.2 Introduction to MOSFETs	2
1.3 The Endeavor to create VLSI Circuit Design	2
1.4 Device Scaling (MOSFET)	4
1.5 Effects of scaling	5
1.5.1 Short channel effects	5
1.5.2 Quantum Mechanical Effects	7
1.6 Device Topologies for Reduction of SCE’s	7
1.6.1 DG (Double Gate) FET	8
1.6.2 FINFET	8
1.6.3 Gate-All-Around (GAA) FET	9
1.6.3.1 Rectangular GAAFET	9
1.6.3.2 Triangular GAA FET	9
1.6.3.3 Cylindrical GAA FET	10
1.7 Device Engineering Techniques	10
1.7.1 Gate Material Engineering (GME)	10
1.7.2 Gate Oxide Stack Engineering	11

1.7.3 Channel Engineering	12
1.8 Junctionless Field Effect Transistor	12
1.9 Device Simulation	13
1.10 FET as Biosensor	14
1.10.1 Biosensing Mechanism	15
1.10.2 Evolutionary Progression of BioFETs	16
1.11 Literature Survey	17
1.11.1 Literature Survey on FET Devices	17
1.11.2 Literature Survey on Gate-All-Around FET (GAA-FET)	18
1.11.3 Literature Survey on FET for Biosensing Applications	19
1.12 Thesis Organization	26
CHAPTER 2: NUMERICAL SIMULATION OF HETERO DIELECTRIC TRENCH GATE JAM GATE-ALL-AROUND FET (HDTG-JAM-GAAFET) FOR LABEL-FREE BIOSENSING APPLICATIONS	28
2.1 Introduction	28
2.1.1 Junctionless versus Junction Accumulation Mode FET	30
2.1.2 Hetero Dielectric Structure	30
2.1.3 Trench Gate	31
2.1.4 Gate-All-Around FET	32
2.2 Hetero Dielectric Trench Gate Junction Accumulation Mode Gate-All-Around FET (HDTG-JAM-GAAFET) Biosensor: Device architecture and Simulation Environment	32
2.3 Results and Discussion	36
2.3.1 Electrostatic behaviour of HDTG-JAM-GAAFET biosensor	36
2.3.2 Comparative investigation of electrical performance Properties of HDTG-JAM-GAAFET biosensor	40
2.3.3 Biomolecules' effects on Current sensitivity of Proposed Biosensor	43
2.3.4 Selectivity Analysis and Effect of Cavity Dimensions on Performance of HDTG-JAM-GAAFET Biosensor	46
2.3.5 Limit of Detection (LOD) of proposed biosensor	48
2.4 Summary	49
CHAPTER 3: TRENCH GATE ENGINEERED JAM GATE-ALL-AROUND FET BASED LABEL-FREE BIOSENSOR	50
3.1 Introduction	50
3.1.1 Junction Accumulation Mode FET	52

3.1.2	Gate Material Engineering (GME)	52
3.1.3	Trench Gate Architecture	53
3.2	Trench Gate Engineered JAM Gate-All-Around (TGE-JAM-GAA) Label-Free BioFET: Device Structure and Simulation Framework	53
3.3	TGE-JAM-GAA Biosensor Device Fabrication Illustration	56
3.4	Results and Discussion	57
3.4.1	Impact of Different Biomolecules Species	57
3.4.2	Impact of Biomolecules Charge Concentration	60
3.4.3	Sensitivity Comparison of TGE-JAM-GAA BioFET	63
3.5	Summary	66
CHAPTER 4: ANALYTICAL MODELING AND NUMERICAL SIMULATION OF GRADED JAM SPLIT GATE-ALL-AROUND (GJAM-SGAA) BIO-FET		67
4.1	Introduction	67
4.1.1	JAM FET	69
4.1.2	Graded Doping	69
4.1.3	Split (or Underlap) Gate FET and Open Cavity-Based Biosensors	69
4.1.5	Oxide Stacking	71
4.1.6	Gate Material Engineering	72
4.1.7	Avian Influenza and DNA Detection	72
4.2	GJAM-SGAA Bio-FET Device Structure and Simulation Specification	74
4.3	Analytical Modeling	76
4.3.1	Modeling of Surface Potential	77
4.3.2	Modeling of Threshold Voltage	80
4.3.3	Modeling of Drain Current and Subthreshold Slope	81
4.3.4	Modeling of Transconductance	82
4.3.5	Modeling of Sensitivity	82
4.3.5.1	Drain Current Sensitivity	83
4.3.5.2	Threshold Voltage Sensitivity	83
4.4	Results and Discussion	83
4.5	Summary	90
CHAPTER 5: GAA NW-FET BIOSENSOR FOR LABEL-FREE SARS-COV-2 AND AVIAN INFLUENZA VIRUS DETECTION		94
5.1	Dual Metal Dual Layer GAA NW-FET (DMDL-GAA-NW-FET) Biosensor	

for Label-Free SARS-CoV-2 Detection	95
5.1.1 Introduction	95
5.1.1.1 JAM FET	96
5.1.1.2 Oxide Stacking	96
5.1.1.3 Gate Material Engineering	96
5.1.1.4 SARS-CoV-2 Virus Detection	96
5.1.2 Device Structure and Simulation Specification	98
5.1.3 Device Calibration and Fabrication	100
5.1.4 Results and Discussion	101
5.1.4.1 Sensitivity Comparison of Proposed Biosensor	101
5.1.4.2 Device Electrostatic Analysis	105
5.1.4.3 Sensitivity Analysis of DMDL-GAA-NW-FET Biosensor for SARS-CoV-2 Spike Protein	109
5.1.4.4 Sensitivity Investigation of DNA Charge Density Modulation/Trap Charge Concentration	111
5.1.4.5 Impact of Fill in Factor on Sensitivity	114
5.1.5 Summary	115
5.2 Dielectric Modulated GANFET Biosensor for Label-Free Detection of DNA and Avian Influenza Virus	116
5.2.1 Background and Overview	116
5.2.2 Device and Simulator Specifications	118
5.2.3 Analytical Model	120
5.2.3.1 Surface Potential	121
5.2.3.2 Threshold Voltage	124
5.2.3.3 Subthreshold Slope and Drain Current	124
5.2.4 Results and Discussion	125
5.2.5 Summary	135
CHAPTER 6: HIGH SENSITIVITY BIOSENSORS UTILIZING WIDE BANDGAP SEMICONDUCTORS	138
6.1 4H-SiC source Triple Metal Gate-All-Around Silicon Carbide FET (DM-TMGAA-SiCFET) biosensor	139
6.1.1 Background and Overview	139
6.1.1.1 Silicon Carbide (SiC) Semiconductor	140
6.1.1.2 JAM FET	141

6.1.1.3 Oxide Stacking	141
6.1.1.4 Gate Material Engineering	142
6.1.2 Device Structure, Specification and Fabrication	142
6.1.3 Device Calibration and Fabrication Feasibility	145
6.1.4 Results and discussion	145
6.1.5 Summary	159
6.2 Gallium-arsenide Gate-All-Around engineered Field Effect Transistor (GaAs-GAAE-FET)	160
6.2.1 Background and Overview	160
6.2.2 Device structure	161
6.2.3 Results and Discussion	163
6.2.3.1 Analysis of Electrostatic Characteristics of GaAs-GAAE-FET	163
6.2.3.2 Sensitivity Analysis of Proposed Biosensor	165
6.2.4 Summary	167
CHAPTER 7: CONCLUSION, FUTURE SCOPE AND SOCIAL IMPACT	168
7.1 Summary of the Work Done in the Thesis	168
7.2 Future Scope and Social Impact	170
<i>Bibliography</i>	<i>172</i>
<i>List of Publications Related to the Thesis</i>	<i>202</i>

LIST OF TABLES

Table 1.1 Various Models Available in ATLAS [29]	14
Table 1.2 Comparison of Conventional Chemical Biosensing and Modern FET Biosensing Techniques	14
Table 1.3 Literature Survey on High-Performance Field Effect Transistor and their Application as Sensors	21
Table 1.4 Literature Survey on Sensitivity Improvement and Analytical Modeling of Gate-All-Around FET Sensors	24
Table 2.1 Various Device Dimensions and Characteristics Parameters [63]	34
Table 2.2 Dielectric constant and charge densities of biomolecules used in analysis of HDTG-JAM-GAAFET [63]	35
Table 2.3 Performance Comparison of HDTG-JAM-GAAFET and NG-JAM-GAAFET [63]	45
Table 2.4 Threshold Voltage Sensitivity Comparison of HDTG-JAM-GAAFET to Contemporary Research on Similar Biosensors [63]	45
Table 2.5 I_{ON}/I_{OFF} Ratio Comparison of HDTG-JAM-GAAFET to Contemporary Research on Similar Biosensors [63]	46
Table 3.1 Dielectric constant and type of Biomolecules	55
Table 3.2 Device Design Parameters	55
Table 4.1 Device Design Parameters [32]	75
Table 5.1 Device Parameters	98
Table 5.2 Sensitivity Comparison	104
Table 5.3 Threshold Voltage Sensitivity Comparison of DMDL-GAA-NW-FET to Contemporary Research on Similar Biosensors	105
Table 5.4 Electrical Parameters of DMDL-GAA-NW-FET Biosensor for SARS-COV-2 Spike Protein	111
Table 5.5 Electrical Parameters of DMDL-GAA-NW-FET Biosensor for DNA Biomolecules of SARS-COV-2	114
Table 5.6 Device Structural Parameters	120
Table 5.7 Effect of Channel Length Variation on Various Sensitivity Parameters	132
Table 5.8 Effect of Graded Doping Variation on Various Sensitivity Parameters of GAAE-GANFET Biosensor	132
Table 5.9 Effect of Temperature Variation on Various Sensitivity Parameters	133
Table 5.10 S_{Vth} Comparison of GAAE-GANFET with Several FET Biosensors in the Contemporary Literature for Neutral Biomolecules	135

Table 6.1 Device Design Parameters	144
Table 6.2 Sensitivity Comparison of DM-TMGAA-SiCFET Biosensor with Different Source Materials	156
Table 6.3 Comparison of the DM-TMGAA-SiCFET's Threshold Voltage Sensitivity ($S_{V_{th}}$) for Several Biomolecules	159
Table 6.4 Biosensor Specifications and Parameters	162

LIST OF FIGURES

Fig. 1. 1 (a) Schematic of MOSFET: NMOS (b) Correctional view of MOSFET: PMOS	2
Fig. 1. 2 Evolution of VLSI Technology	4
Fig. 1. 3 Mosfet Scaling: Reduction in Transistor Gate Length Over Several Technological Nodes [3]	5
Fig. 1. 4 DG FET	8
Fig. 1. 5 Structure of FINFET [14]	9
Fig. 1. 6 Rectangular GAA FET Structure [18]	9
Fig. 1. 7 Triangular GAA MOSFET [19]	10
Fig. 1. 8 Structure of Cylindrical GAA MOSFET	10
Fig. 1. 9 Gate Material Engineering (GME) in cylindrical GAAFET [22]	11
Fig. 1.10 MOSFET with Gate Oxide Stacking	12
Fig. 1.11 Operation Mechanism of Junctionless Transistor [27]	13
Fig. 1.12 (a) Basic block diagram of Biosensor [33] (b) Basic block diagram of sensor mechanism in FET Biosensors [34]	16
Fig. 1.13 Evolution of FET Biosensors	16
Fig. 1. 14 Schematic of Nanogap formed in DMFET Biosensor [75]	20
Fig. 2.1 (a) Cross-sectional View of Trench Gate MOSFET [55] (b) Cross-sectional View of Trench Gate TFET Biosensor [56]	32
Fig. 2.2 (a): 3-Dimensional View of HDTG-JAM-GAAFET [63] (b) Calibration of simulation setup with experimental data [63] (c) 2- Dimensional View of HDTG-JAM-GAAFET [63]	34
Fig. 2.3 (a) Surface Potential for the Case of Neutral Biomolecule Analytes [63] (b) Surface Potential for the Case of (+)vely and (-)vely Charged Biomolecules [63] (c) V_{TH} Variation for Various Neutral Biomolecules [63] (d) V_{TH} Variation for DNA Biomolecules [63]	37
Fig. 2.4 Contour Plots of Electron Concentrations of Proposed Device for Neutral Analytes [63] (a) No Biomolecules (K=1) (b) Biotin (c) Ferro-cytochrome c (d) Keratin (e) Gelatin	38
Fig. 2.5 Contour Plots of Electron Concentrations of Proposed Device for Charged Analytes [63] with Constant Dielectric Constant, K=12 and (a) $Q_f = 1 \times 10^{12} \text{cm}^{-2}$ (b) $Q_f = 5 \times 10^{11} \text{cm}^{-2}$ (c) $Q_f = 0$ (d) $Q_f = -5 \times 10^{11} \text{cm}^{-2}$ (e) $Q_f = -1 \times 10^{12} \text{cm}^{-2}$	38
Fig. 2.6 Contour Plots of Electron Velocity in Channel Region of Proposed Device	

for Neutral Analytes [63] (a) No Biomolecules ($K=1$) (b) Biotin (c) Ferrocytochrome C (d) Keratin (e) Gelatin	38
Fig. 2.7 (a) I_D - V_{GS} Characteristics of HDTG-JAM-GAAFET Biosensor for Neutral Biomolecules (b) I_D - V_{GS} Characteristics of HDTG-JAM-GAAFET Biosensor for Charged Biomolecules [63]	39
Fig. 2.8 (a) Transconductance of HDTG-JAM-GAAFET Biosensor for Neutral Biomolecules [63] (b) Transconductance of HDTG-JAM-GAAFET Biosensor for Charged Biomolecules [63]	40
Fig. 2.9 I_{OFF} Current Variation for HDTG-JAM-GAAFET and NG-JAM-GAAFET Biosensor [63]	40
Fig. 2.10 Comparative Study of Switching Ratio (I_{ON}/I_{OFF}) of HDTG-JAM-GAAFET Biosensor and NG-JAM-GAAFET Biosensor [63]	41
Fig. 2.11 Variation of Subthreshold Slope for HDTG-JAM-GAAFET and NG-JAM-GAAFET Biosensor [63]	41
Fig. 2.12 (a) Variation of output conductance (g_d) with drain voltage [63] (b) Variation of Channel Resistance (R_{ch}) for HDTG-JAM-GAAFET biosensor and NG-JAM-GAAFET [63]	42
Fig. 2.13 Variation of Intrinsic Gain ($A_{v_{int}}$) with the gate to source voltage (V_{GS}) for HDTG-JAM-GAAFET and NG-JAM-GAAFET biosensor [63]	43
Fig. 2.14 (a) Sensitivity Comparison of HDTG-JAM-GAAFET and NG-JAM-GAAFET biosensor for different Biomolecule species [63] (b) Sensitivity Comparison of HDTG-JAM-GAAFET and NG-JAM-GAAFET biosensor for charged Biomolecules having $K=12$ [63]	44
Fig. 2.15 Sensitivity Comparison of HDTG-JAM-GAAFET [63] and SE-SB-FET [95] Biosensors	46
Fig. 2.16 Selectivity Comparison of proposed HDTG-JAM-GAAFET and NG-JAM-GAAFET [63]	47
Fig. 2.17 Threshold Voltage (V_{TH}) Sensitivity and I_{ON} Current Sensitivity of HDTG-JAM-GAAFET for Gelatin Biomolecules ($K=12$) at (a) Different Cavity Lengths [63] (b) Different Cavity Thicknesses [63]	47
Fig. 2.18 The relative change in Drain to source Current versus interface charge density for determination of Limit of Detection [53]	48
Fig. 3.1 Junction Accumulation Mode FET [33]	52
Fig. 3.2 The Dual-Material gate FET (DMGFET) structure [28]	53
Fig. 3.3: (a) 3-Dimensional View of TGE-JAM-GAA BioFET (b) 2-D Structure of TGE-JAM-GAA BioFET with its capacitance model	54
Fig. 3.4 Proposed fabrication flowchart for TGE-JAM-GAA BioFET biosensor Device	56
Fig. 3.5 Variation of channel center potential for different biomolecule Species	57

Fig. 3.6 Comparative Study of TGE-JAM-GAA BioFET, TMNG-JAM-GAAFET, and conventional single metal normal gate GAA FET for neutral biomolecules with different K (a) variation in I_{DS} with respect to V_{GS} (b) Deviation in I_{ON} current (c) Transconductance (g_m)	59
Fig. 3.7 Comparative Study of TGE-JAM-GAA BioFET, TMNG-JAM-GAAFET, and SMNG-JAM-GAAFET for neutral biomolecules (a) V_{TH} with respect to K (b) ΔV_{TH} for different biomolecules species	60
Fig. 3.8 Variation of channel center potential for $K=2.1$ and varying charge	61
Fig. 3.9 (a) $I_{DS}-V_{GS}$ characteristics for $K = 2.1$ and varying charge (b) Average drift in drain ON current (ΔI_{ON}) for variation in charge (c) Transconductance (g_m) for varying charge on biomolecule at $K = 2.1$	62
Fig. 3.10 Comparative Study of Variation in V_{TH} for TGE-JAM-GAA BioFET, TMNG-JAM-GAAFET, and conventional normal gate GAA FET for charged biomolecules with $K=2.1$	63
Fig. 3.11 (a) I_{ON} current sensitivity for neutral biomolecules (b) I_{ON} current sensitivity for charged biomolecules	64
Fig. 3.12 (a) I_{ON}/I_{OFF} current sensitivity for neutral biomolecules (b) I_{ON}/I_{OFF} current sensitivity for charged biomolecules	65
Fig. 3.13 (a) V_{TH} sensitivity for neutral biomolecules (b) V_{TH} sensitivity for charged biomolecules	65
Fig. 4.1 Step Graded Doping in the Channel of FET	69
Fig. 4.2 Split Gate FET Structure with Open Cavity for Biomolecules Immobilization	70
Fig. 4.3 Oxide Stack Architecture consisting of Low-K and High-K Oxide in FETs	71
Fig. 4.4 (a) 3-Dimensional View of GJAM-SGAA Bio-FET (b) Calibration of Simulation Setup with Experimental Data [31] (c) 2-Dimensional Structure of GJAM-SGAA Bio-FET	76
Fig. 4.5 Surface Potential of GJAM-SGAA Bio-FET for Charged DNA and Avian Influenza Antibody Analytes	84
Fig. 4.6 Electric Field of GJAM-SGAA Bio-FET for dsDNA and Avian Influenza Antibody (AI-ab) Analytes	84
Fig. 4.7 (a) I_D-V_{GS} Characteristics with Different Biomolecules of GJAM-SGAA Bio-FET (b) Transconductance for Different Biomolecules	85
Fig. 4.8 (a) Drain Current versus Drain Voltage (I_D-V_{DS}) Characteristics with Different Biomolecules of GJAM-SGAA Bio-FET (b) Drain Current Sensitivity for dsDNA and AI-ab Biomolecules	86
Fig. 4.9 Threshold Voltage and Threshold Voltage Sensitivity for DNA and Avian Influenza Analytes	87
Fig. 4.10 Subthreshold Slope and Subthreshold Slope Sensitivity of GJAM-SGAA Bio-FET	87

Fig. 4.11 I_{ON} Current Sensitivity Comparison of GJAM-SGAA Bio-FET and SGAA FET Biosensor	88
Fig. 4.12 Comparative of Switching Ratio (I_{ON}/I_{OFF}) Sensitivity of GJAM-SGAA Bio-FET and SGAA FET Biosensor	89
Fig. 4.13 Threshold Voltage Sensitivity, $S_{V_{th}}$ Comparison of GJAM-SGAA Bio-FET and SGAA FET Biosensor	89
Fig. 4.14 Threshold Voltage Sensitivity, $S_{V_{th}}$ Comparison of GJAM-SGAA Bio-FET with Recent Published FET Biosensors	90
Fig. 5.1 (a) Structure of SARS-CoV-2 [33] (b) Process of SARS-CoV-2 infecting Host Cells [37].	97
Fig. 5.2 (a) 3-Dimensional View of DMDL-GAA-NW-FET (b) Vertical Cross-sectional View of DMDL-GAA-NW-FET (c) 2- Dimensional Structure of DMDL-GAA-NW-FET	99
Fig. 5.3 (a) Calibration of Simulation Setup with Experimental Data [41]	100
Fig. 5.4 Sensitivity Comparison of DMDL-GAA-NW-FET and GAA-NW-FET Biosensor for Dielectric Constant Variation of S-Protein (a) V_{TH} Sensitivity (b) I_{ON} Current Sensitivity	103
Fig. 5.5 Sensitivity Comparison of DMDL-GAA-NW-FET and GAA-NW-FET Biosensor for Charged DNA Biomolecules at $K=2.1$ (a) V_{TH} Sensitivity (b) I_{ON} Current Sensitivity	104
Fig. 5.6 (a) Channel Potential for S-Protein with Dielectric Constant Variations of DMDL-GAA-NW-FET along the Channel Length (b) Channel Potential for $K = 2.1$ and Varying Charge Density of DMDL-GAA-NW-FET Along the Channel Length	106
Fig. 5.7 Energy Band Diagrams of DMDL-GAA-NW-FET Along the Channel Length for (a) S-Protein with Dielectric Constant Variation (b) DNA Biomolecule with Charge Variation	107
Fig. 5.8 Contour Plots of Electron Concentration for (a) Different Biomolecule Dielectric Constants (b) Variation in Charge Concentration of DNA Biomolecule having $K = 2$.	108
Fig. 5.9 (a) I_D - V_G Characteristics at $V_{DS} = 1$ V and for S-Protein with Dielectric Constant Variations (b) I_D - V_D Characteristics at $V_{GS} = 1$ V for S-Protein with Dielectric Constant Variations	109
Fig. 5.10 (a) Transconductance g_m and (b) Output Conductance g_d for S-Protein with Dielectric Constant Variations	110
Fig. 5.11 Sensitivity of S-Protein with Dielectric Constant Variation (a) Drift in Threshold Voltage (ΔV_{TH}), and Drift in Drain ON Current (ΔI_{ON}) with respect to Air ($K=1$) (b) I_{ON}/I_{OFF} Ratio and I_{ON}/I_{OFF} Sensitivity with Change in Dielectric Constant	111
Fig. 5.12 (a) I_D - V_G Characteristics at $V_{DS} = 1$ V and (b) I_D - V_D Characteristics at $V_{GS} = 1$ V for DNA ($K=2.1$) Charged Biomolecules	112

Fig. 5.13 (a) Transconductance, g_m and (b) Output Conductance, g_d for DNA ($K=2.1$) Charged Biomolecules	113
Fig. 5.14 Drift in Threshold Voltage (ΔV_{TH}), and Drift in Drain ON current (ΔI_{ON}) for Charged DNA Biomolecules at Constant $K = 2.1$	113
Fig. 5.15 (a) Drain Current versus Gate to Source Voltage (b) Threshold Voltage Sensitivity (c) I_{ON} Current Sensitivity (d) I_{OFF} Current Sensitivity for Various Fill in Factor of the Biomolecules into the Nanocavity	115
Fig. 5.16 (a) 3-Dimensional View, (b) 2-Dimensional Structure, and (c) Calibration with Experimental Data [97] of GAAE-GANFET Biosensor	118
Fig. 5.17 Flowchart demonstrating the Process of Analytical Modeling	121
Fig. 5.18 Surface Potential of GAAE-GANFET for Different (a) Biomolecules and (b) Cavity Lengths	126
Fig. 5.19 Electric Field Variation along the Channel for AI-ab and DNA Biomolecules	127
Fig. 5.20 Contour Plots of Electron Concentration Variation along the Channel (a) No Biomolecule (b) dsDNA (c) AI-ab (d) Electron Concentration Profile	128
Fig. 5.21 I_D - V_{GS} Characteristics of GAAE-GANFET Biosensor	128
Fig. 5.22 Threshold Voltage (V_{th}) and Threshold Voltage Sensitivity ($S_{V_{th}}$) of GAAE-GANFET Biosensor	129
Fig. 5.23 (a) Drain Current Sensitivity (b) Transconductance Sensitivity for Various Biomolecules	130
Fig. 5.24 (a) Sensitivity of Subthreshold Voltage Swing and Variation in SS (b) I_{ON}/I_{OFF} Ratio and I_{ON}/I_{OFF} Sensitivity for Different Biomolecules	131
Fig. 5.25 Impact of Stacked Gate Oxide on Sensitivity of Drain Current to Various Biomolecules	131
Fig. 5.26 Effect of Neutral Biomolecules (a) Drain Current with respect to Gate to Source Voltage for both Proposed GAAE-GANFET Biosensor and SGAA-Si FET Biosensor (b) Drain Current Sensitivity (c) Threshold Voltage Sensitivity	134
Fig. 5.27 Threshold Voltage Sensitivity ($S_{V_{th}}$) Comparison for Different Charged Biomolecules	134
Fig. 6.1 (a) 3-Dimensional View of DM-TMGAA-SiCFET biosensor (b) 2-Dimensional Structure of DM-TMGAA-SiCFET biosensor	143
Fig. 6.2 (a) Calibration of Simulation Setup with Experimental Data [61] (b) Proposed Fabrication Flowchart of DM-TMGAA-SiCFET Biosensor	146
Fig. 6.3 Surface Potential Along the Channel of DM-TMGAA-SiCFET Biosensor for (a) Various Neutral Biomolecules (b) DNA Biomolecules at $K=8$ and Varying Charge	147
Fig. 6.4 Electric Field of DM-TMGAA-SiCFET Biosensor for (a) Various Neutral	

Biomolecules (b) DNA Biomolecules at $K=8$ and Varying Charge	148
Fig. 6.5 Variation in Electron Concentration in the Silicon Carbide Channel of DM-TMGAA-SiCFET Biosensor	149
Fig. 6.6 (a) I_D - V_{GS} Characteristics with Different Biomolecules of DM-TMGAA-SiCFET Biosensor (b) Transconductance for Different Biomolecules	150
Fig. 6.7 (a) I_D - V_{GS} Characteristics of DM-TMGAA-SiCFET Biosensor for Charged DNA Biomolecules (b) I_D - V_{DS} Characteristics of DM-TMGAA-SiCFET Biosensor for Charged DNA Biomolecules	150
Fig. 6.8 (a) Variation in Output Conductance for Different Neutral Biomolecules (b) Variation in Output Conductance for Charged DNA Biomolecules	151
Fig. 6.9 (a) Drain Current Sensitivity for Different Biomolecules (b) Drain Current Sensitivity for DNA Biomolecules with increased Negative Charge	153
Fig. 6.10 Threshold Voltage and Threshold Voltage Sensitivity for Various (a) Neutral Biomolecules (b) DNA Charged Biomolecules (c) Threshold Voltage Sensitivity with Varying Cavity Thickness	154
Fig. 6.11 I_{ON}/I_{OFF} Ratio and I_{ON}/I_{OFF} Sensitivity of DM-TMGAA-SiCFET Biosensor	155
Fig. 6.12 Subthreshold Slope (SS) and SS Sensitivity of DM-TMGAA-SiCFET Biosensor for Various Biomolecules	155
Fig. 6.13 I_{ON} Current Sensitivity Comparison of DM-TMGAA-SiCFET and SiliconFET Biosensor	157
Fig. 6.14 I_{ON}/I_{OFF} ratio Sensitivity Comparison of DM-TMGAA-SiCFET and SiliconFET Biosensor	158
Fig. 6.15 Threshold Voltage Sensitivity ($S_{V_{th}}$) Comparison of DM-TMGAA-SiCFET and SiliconFET Biosensor for (a) Various Neutral Biomolecules (b) Various Negative Charge on DNA Biomolecules	158
Fig. 6.16 $S_{V_{th}}$ Comparison of DM-TMGAA-SiCFET Biosensor with Recent Published FET Biosensors for Different Charge of the Biomolecules	159
Fig. 6.17 (a) GaAs-GAAE-FET Biosensor: A 3-Dimensional View (b) GaAs-GAAE-FET Biosensor: A 2-Dimensional View	163
Fig. 6.18 Surface Potential Variation of GaAs-GAAE-FET Biosensor	164
Fig. 6.19 I_{DS} - V_{GS} Characteristics of GaAs-GAAE-FET with Different Biomarkers	164
Fig. 6.20 Electron Concentration along the Channel of GaAs-GAAE-FET (a) No Biomolecule (b) MCF-10A (c) MDA-MB-231 (d) Electron Concentration Profile	165
Fig. 6.21 Drain Current Sensitivity (S_{ID}) of GaAs-GAAE-FET with Variation to the Drain Voltage (V_{DS})	165

- Fig. 6.22 Transconductance (g_m) and Transconductance Sensitivity for Various Biomarkers 166
- Fig. 6.23 Threshold Voltage Sensitivity Comparison of GaAs-GAAE-FET and Si-GAA-FET 166

LIST OF ABBREVIATIONS

Al₂O₃	Aluminium Oxide
Aia	Avian Influenza Antigen
AI-ab	Avian Influenza Antibody
AM	Accumulation Mode
APTES	3-Aminopropyltriethoxysilane
ASIC	Application Specific Integrated Circuit
BTBT	Band to Band Tunneling
CAD	Computer Aided Design
CBE	Conduction Band Energy
C_{bio}	Variable Capacitance of Nanogap Cavity containing Biomolecule Species
C_{SiO2}	Capacitance of SiO ₂ Layer
C_{HfO2}	Capacitance of HfO ₂ Layer
CGAA	Cylindrical Gate-All-Around
CLM	Channel Length Modulation
CMOS	Complementary Metal Oxide Semiconductor
CONMOB	Concentration Dependent Mobility Model
CVD	Chemical Vapor Deposition
DG	Double Gate
DIBL	Drain Induced Barrier Lowering
DM	Dielectric Modulated
DMDL-GAA-NW-FET	Dual Metal Dual Layer Gate-All-Around Nanowire Field Effect Transistor
DNA	Deoxyribonucleic Acid
DM-FET	Dielectric Modulated-Field Effect Transistor
DM-TMGAA-SiCFET	Dielectric Modulated Triple Metal Gate-All-Around Silicon Carbide Field Effect Transistor
DRAM	Dynamic Random Access Memory
ds-DNA	Double-stranded DNA
E_F	Fermi Level
EOT	Effective Oxide Thickness
eV	Electron Volt
FET	Field Effect Transistor
FINFET	Fin Field Effect Transistor
FLDMOB	Field Dependent Mobility Model
GAA	Gate-All-Around
GAAE-GANFET	Gate-All-Around Engineered Gallium Nitride Field Effect Transistor
GAA-FET	Gate-All-Around Field Effect Transistor
GaAs	Gallium Arsenide
GaAs-GAAE-FET	Gallium Arsenide Gate-All-Around Engineered Field Effect Transistor
GaN	Gallium Nitride
GD	Graded Doping
GIDL	Gate Induced Drain Leakage

GJAM-SGAA	Graded Channel Junction Accumulation Mode Split Gate-All-Around
GME	Gate Metal Engineered
HCE	Hot Carrier Effects
HDTG-JAM-GAAFET	Hetero Dielectric Trench Gate Junction Accumulation Mode Gate-All Around Field Effect Transistor
HfO₂	Hafnium Oxide
IC	Integrated Circuit
IM	Inversion Mode
I_{OFF}	Off Current
I_{ON}	On Current
JAM	Junction Accumulation Mode
JGAA	Junctionless Gate-All-Around
JL	Junction Less
LDD	Lightly Doped Drain
LOD	Limit of Detection
MOS	Metal Oxide Semiconductor
MOSFET	Metal Oxide Semiconductor Field Effect Transistor
NG-JAM-GAAFET	Normal Gate Junction Accumulation Mode Gate-All-Around Field Effect Transistor
NW	Nano Wire Field Effect Transistor
R_{ch}	Channel Resistance
NWFET	Nano Wire Field Effect Transistor
SARS-CoV-2	Severe Acute Respiratory Syndrome Corona Virus
SCE	Short Channel Effects
SGAA-FET	Split Gate-All-Around Field Effect Transistor
Si	Silicon
SiC	Silicon Carbide
SiO₂	Silicon Dioxide
S_{I_{ON}}	I _{ON} Current Sensitivity
SRH	Shockley-Read-Hall
SS	Subthreshold Slope
ssDNA	Single-stranded DNA
TM	Triple Metal
TCAD	Technology Computer Aided Design
TFET	Tunnel Field Effect Transistor
TGE-JAM-GAA	Trench Gate Engineered JAM Gate-All-Around
TMGAA	Triple Metal Gate-All-Around
VBE	Valence Band Energy
V_{GS}	Gate to Source Voltage
V_{DS}	Drain to Source Voltage
VLSI	Very Large Scale Integration
WF	Work-Function

CHAPTER 1

INTRODUCTION

Over the past two decades, there has been a great deal of interest in exploring the idea of biomolecule sensing using field-effect transistor (FET) devices. This attention is driven by their potential for achieving ultra-high sensitivity sensing, operating without labels, reduced costs, and enabling miniaturization. In order to develop a thorough grasp of Field-Effect Transistors as sensors, we systematically offer an in-depth investigation that covers basic concepts and technical details from the perspectives of design, simulation, modeling, and fabrication. This chapter gives an overview of the research background with an emphasis on clarifying Metal Oxide Semiconductor Field Effect Transistors (MOSFETs) and the demand for novel devices. The chapter lists the various challenges that MOSFET endures within this framework. These challenges include punch-through, channel length modulation, threshold voltage roll-off, drain-induced barrier lowering (DIBL), velocity saturation, and more. All of these challenges greatly disrupt MOSFET's operational efficiency. The chapter also explores a number of device engineering techniques that are intended to improve device performance, such as junctionless MOSFET, dielectric engineering, and multi-gate MOSFETs (such as Double Gate MOSFET, Triple Gate MOSFET, Surrounding Gate MOSFET, Double Surrounding Gate MOSFET). Furthermore, the chapter elaborates on different sensor designs, elucidating how these designs contribute to heightened sensitivity.

1.1 Background and Progress of MOSFET Technology

The FET (Field Effect Transistor) was firstly conceived in 1928 by Lilienfeld [1]. It was later followed by the discovery and demonstration of Integrated Circuit and CMOS which have transfigured the society to a much larger extent. The IC's and the CMOS technology have captured the human life in a way that these technologies manifest our everyday need in domestic purposes ranging from televisions, cell phones, tablets etc. to the various industrial purposes like robotics, automation of the systems, sensors etc. It is eventually impossible to think of life in the contemporary era without IC and CMOS technology. The most integral component of Integrated Circuits and CMOS technology is MOSFET. Due to technological advancements, the number of transistors on a single IC chip doubles every eighteen months, as stated by Gordon Moore [1]. This leads to a rapid reduction in the size of transistors manufactured on ICs.

Advancements like the FinFET, GaAs-FET, and Application Specific Integrated Circuits (ASICs) added new dimensions to the symphony, enabling smaller, faster, and more versatile devices. This symphony of innovation continues to shape our modern world, promising an ever-evolving future where semiconductor technology remains at the forefront of progress, inspiring new melodies of possibility.

1.2 Introduction to MOSFETs

A MOSFET is a device that generally consists of four terminals: source, drain, body, and gate. Nevertheless, the source terminal is commonly linked to the body terminal, so transforming it into a three-terminal device referred to as a FET. A field-effect transistor is a device in which the flow of current between the drain electrode and the source electrode is regulated by an electric field applied to the gate. This electric field is created by a thin layer of metal oxide situated between the semiconductor and metal components of the transistor. There are two types of MOSFETs: NMOS and PMOS. An NMOS device is constructed on a p-doped silicon substrate containing regions of n-type material formed by ion implantation, known as the drain and source as in Fig. 1.1 (a). Conversely, in PMOS devices, this arrangement is reversed, which is apparent in Fig. 1.1 (b).

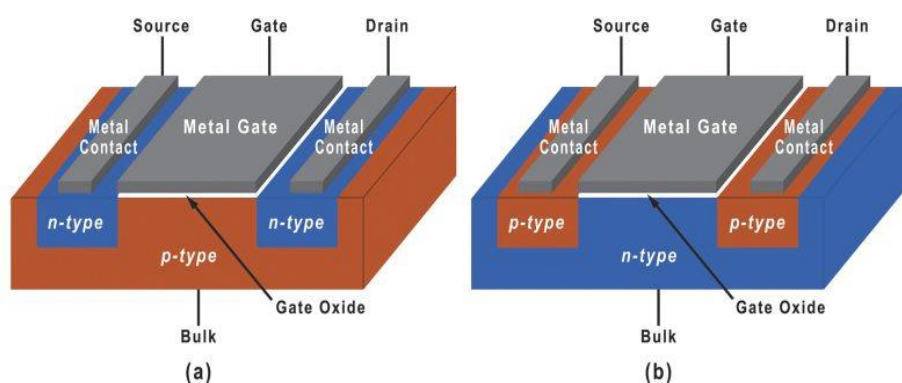


Fig. 1.1 (a) Schematic of MOSFET: NMOS (b) Correctional View of MOSFET: PMOS

1.3 The Endeavor to create VLSI Circuit Design

The driving force behind VLSI circuit design is to achieve higher functionality, faster operating speeds, reduced power consumption, smaller physical size, and lower manufacturing costs. VLSI design engineers employ advanced techniques and methodologies to optimize the performance of integrated circuits. These techniques include layout design, logic synthesis, power analysis, timing optimization, and verification methodologies. The expert CAD tools has notably aided in the development of VLSI design. It made it possible to simulate, construct, and verify complex circuits quickly and effectively. The development of VLSI technology has advanced through different stages, starting from SSI and MSI to LSI, VLSI, and ULSI. This progression has enabled the integration of millions or even billions of components on a single chip. These advancements have been facilitated by significant progress in lithography, materials science, instruments for design, as well as manufacturing techniques.

The introduction of VLSI technology had significant implications in many sectors. For example, in telecommunications, this caused an increase in fast communication systems, breakthrough involving wireless networks, and state-of-the-art signal processing techniques. Consumer electronics also significantly benefited from Very Large-Scale Integration (VLSI) technology, as thousands of applications could be

injected into various devices, which became state of general equipment including multimedia operation, wireless connectivity, and energy-efficient equipment in compact devices. The use of Very Large-Scale Integration technology was evident in the automotive sector, where it was used to improve safety systems, provide autonomous driving experience, and include new in-vehicle infotainment. Medical equipment can be impossible to make without enrolment of VLSI technology, which allows the implementation of modern imaging technology, implanted devices, and diagnostics, again revolutionizing and rendering treatment better.

VLSI design specialists utilize careful layout design methodologies to optimize the physical arrangement of components on a chip, guaranteeing effective signal propagation and minimal interference. Logic synthesis techniques facilitate the automated conversion of high-level circuit descriptions into optimum gate-level representations. Power analysis approaches are utilized to assess and diminish power consumption, a critical aspect for portable devices and energy-efficient systems. To ensure that circuits meet the desired performance requirements considering clock distribution and signal propagation delays is performed through Timing optimization techniques. Verification methodologies are deployed to ensure that the designed circuits operate correctly and are reliable. Efficient VLSI design was made feasible by the introduction of focused CAD instruments. Designing, simulating, and checking the multi-million element count in complex circuits is now much more productive and precise because of these CAD tools.

Electronics, an unprecedented technological achievement, began in 1947 in the Bell Laboratories exploration bases, where the field of electronics was also forever changed. Physicists John Bardeen and Walter Brattain manufactured the first working point-contact transistor. The integrated circuit was first developed at Texas Instruments in 1958. This innovation completely transformed the field of electronic design and laid the foundation for the VLSI revolution.

MOSFET is a critical semiconductor device that has had a profound impact on modern electronics and is a basic device of VLSI technology. The roots of the MOSFET can be traced back to the activities of researchers who were studying semiconductor physics and transistors in the 1920s and 1930s. However, there was limited progress in MOSFET technology until the 1950s and 1960s. Today, MOSFETs have become the fundamental device of modern VLSI chips. The use of MOSFET has made it possible to integrate millions to billions of transistors in a single silicon chip. By the mid-1970s, the benefits of CMOS technology were generally acknowledged, leading to significant advancements.

Major milestones include the invention of the 1 transistor DRAM (dynamic random-access memory) in 1967-68 and the microprocessor in 1971. In the year 1980, with the adoption of VLSI technology, the development of complex systems-on-chip became possible. The emergence of CMOS technology and continuous scaling have enabled the creation of highly efficient and cost-effective electronic devices. The constant transistor miniaturization has significantly improved performance and reduced the cost per function. The creation of smaller, more potent electronic devices that have transformed a number of industry sectors has been fueled by VLSI technology, which

has transformed electronics. The recent advancements in ULSI technology have further pushed the boundaries by the integration of billions of transistors into a chip, making it possible to design memory chips, specialized integrated circuits, and extremely complex and adaptable microprocessors. Figure 1.2 [2] illustrates the sequential development of VLSI technology throughout time. The inset graph highlights the exponential growth in transistor count (blue dots) and the steady reduction in transistor size (yellow dots) over time, driven by Moore's Law. Transistor sizes have shrunk from micrometers in the 1950s to below 10 nm by 2022, while transistor counts have risen from thousands to billions per chip. These advancements, enabled by innovations like FinFETs and Gate-All-Around transistors, have significantly boosted computational power and energy efficiency in modern electronics.

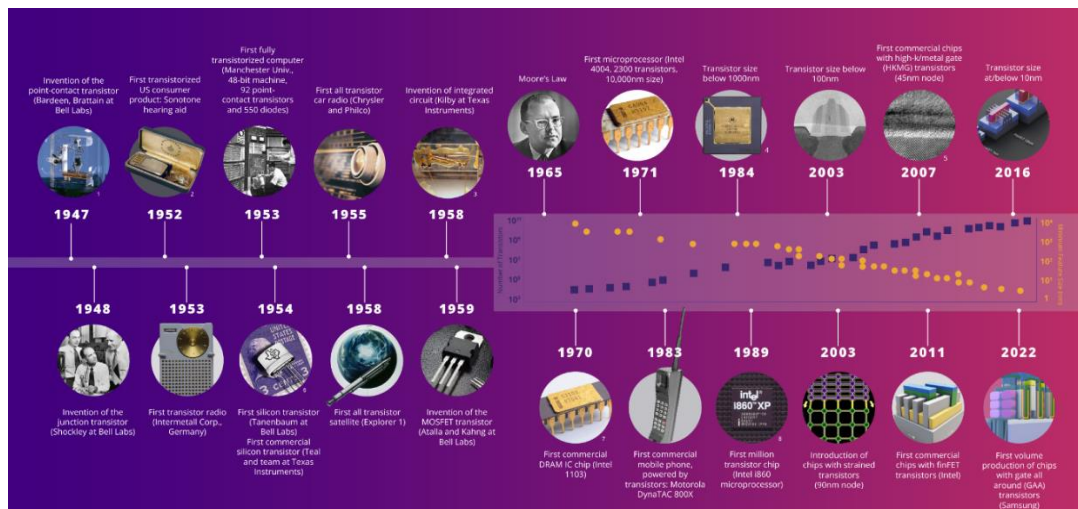


Fig. 1.2 Evolution of VLSI Technology [2]

1.4 Device Scaling (MOSFET)

MOSFET scaling is the ongoing miniaturization of MOSFETs in order to improve their performance and density on integrated circuits. In 1965, Gordon Moore, projected that the transistors count on a semiconductor chip would double about every two years, referred to Moore's Law [3]. This doubling of transistor count has been made feasible by MOSFET scaling, which allows for smaller transistor sizes and the incorporation of a increased transistor count on a chip as shown in Fig. 1.3 [4].

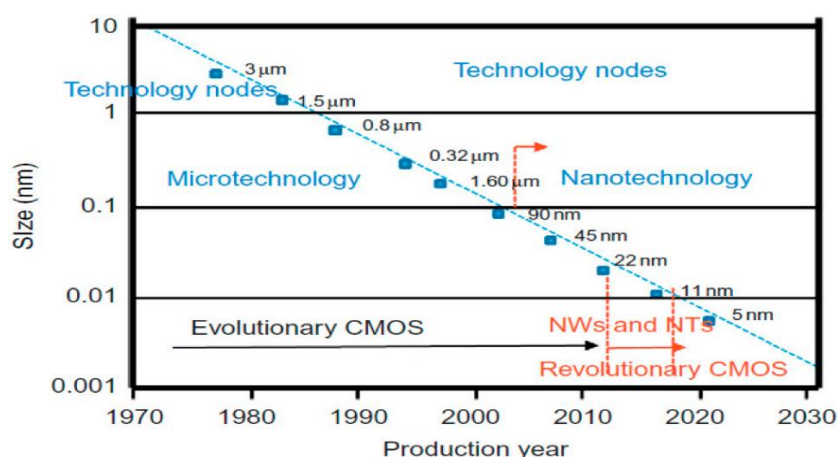


Fig. 1.3 Mosfet Scaling: Reduction in Transistor Gate Length Over Several Technological Nodes [4]

For many years, the semiconductor industry has used Moore's Law as a guiding concept to describe the future of electronic devices. This concept perfectly explains the pattern of transistor density increase and performance improvement. The main reason for scaling MOSFETs is to reduce the size of the transistor. This approach has some advantages, including performance, density, cost, and power consumption. Moreover, a smaller transistor allows for more aggressive packing and can integrate more transistors on a single chip. At the same time, scaling the device has its limitations and issues, such as increased sources of subthreshold leakage and variability of the process. Therefore, to overcome these issues and improve the device, new methods and materials need to be applied by designers. By skillfully balancing scaling and addressing associated issues, semiconductor technology continues to advance, facilitating the development of electrical devices that are more compact, potent, and energy-efficient [5].

Because of the continuous efforts from the semiconductor device engineers, Moore's law has continued to hold remarkably well over the years. However aggressive scaling of MOS device is responsible for improved density, power and speed performance of IC but it encounters with various Short Channel Effects (SCEs). The SCEs dominate with reduced device size and they play a significant role in performance degradation.

Silicon CMOS has evolved throughout the previous few decades as the most efficacious technology in the Micro-Electronics industry. To cater to the requisition of continuous improvement at both device and performance level, device-scaling approach has been persistently adapted over the generations of technology.

1.5 Effects of scaling

1.5.1 Short channel effects

Short channel effects (SCEs) are a significant challenge in contemporary designs of semiconductor devices. The channel length of a transistor, which connects its source and drain, likewise gets shorter as devices get smaller, leading to various physical

effects that can negatively impact device performance. SCE are common in short channel devices (MOSFET and Tunnel FET). Various SCEs are discussed below [6]:

Drain Induced Barrier Lowering (DIBL): One of the most significant effects of SCE is the DIBL effect. DIBL is caused by the drain voltage, which lowers the potential barrier at the source-channel junction, resulting in a reduction in the threshold voltage of the transistor. As the threshold voltage decreases, the transistor may turn on prematurely, leading to increased leakage current, reduced transconductance, and reduced voltage gain [7].

Hot Carrier Effect (HCE): Another important SCE is hot carrier effect (HCE). HCE occurs when carriers, such as electrons or holes, in the channel are accelerated to high energies due to high electric fields or high voltages. These high-energy carriers can cause damage to the gate oxide, resulting in increased leakage current and reduced mobility. HCE can also cause a reduction in the lifetime of the device, leading to reliability issues [8].

Velocity Saturation: Velocity saturation occurs when the carriers in the channel reach a high enough velocity that they begin to interact with the lattice atoms in the material, resulting in a saturation of the carrier velocity. This effect can lead to a reduction in the mobility of the carriers and a decrease in the device's current drive capability. To prevent velocity saturation in FET, various techniques can be employed to minimize the impact of high electric fields and improve carrier mobility [8].

Channel Length Modulation (CLM): CLM (occurs in enhancement type FET) is characterized by the reduction in the effective length of the induced channel for large drain voltage. This occurs due to the overlapping of the induced channel with the depletion region around drain junction, leading to a decrease in the threshold voltage of the device and an increase in the device's leakage current due to reduction in the effective channel length. To mitigate the effect of channel length modulation, one approach is to intentionally adjust the doping profile of the channel region. By keeping the channel doping higher than the drain doping, the impact of CLM can be reduced. This technique is often referred to as channel engineering.

Threshold Voltage Roll-off: As channel length is reduced, the threshold voltage can shift, causing the transistor to turn on at lower gate voltages than expected. This can result in challenges in maintaining precise control over transistor behavior and impacts circuit performance in scaled devices [9].

Punch-Through: In very short channel FET devices, the depletion regions of source and drain regions can overlap, causing punch-through and reducing control over the channel [8]. This phenomenon compromises the control over the channel, effectively turning the transistor into a short circuit and leading to increased leakage currents. This might lead to the breakdown of devices in few cases.

Mobility Degradation: Short-channel effects can lead to mobility degradation, causing carriers to experience lower mobility due to scattering effects. This diminished

carrier mobility in the channel hampers the transistor's ability to conduct current effectively, affecting its overall performance and efficiency [6].

1.5.2 Quantum Mechanical Effects

Quantum mechanical effects become significant when the device dimensions become of the size of atom. Here, the behavior of particles and systems is governed by the principles of quantum mechanics [10].

Tunneling: Tunneling, a remarkable quantum mechanical effect, defies classical phenomenon of charge carrier transportation by allowing electrons to traverse barriers that would normally impede their motion. When faced with an exquisitely thin barrier, the electron's probability wave extends beyond the barrier, defying the odds. In classical terms, lacking sufficient energy to surmount a barrier would prevent electron movement. However, in the quantum mechanical realm, electrons also exhibit wave-like properties. These wave functions do not abruptly terminate at a barrier, but rather diminish rapidly. If the potential barrier thickness is sufficiently thin, the probability function of an electron extends into the adjacent region, penetrating the barrier. Furthermore, the main reason of tunneling phenomenon in FET is high doping due to which potential barrier becomes thin enough for the charge carriers to tunnel through it. As a result, the energy barrier becomes more penetrable, enabling charge carriers to tunnel through it via a quantum mechanical process known as tunneling. Tunneling effect is more profound in TFET or highly doped MOSFET [10].

Ballistic Transport: Ballistic conduction, also known as ballistic transport, refers to the movement of electrons through a material with very little electrical resistance caused by scattering. This phenomenon occurs when the distance an electron can travel freely, known as the mean free path, is significantly longer than the dimensions of the medium it traverses. In a FET, ballistic transport ('ballistic' refers to the motion of charge carriers, such as electrons, through a material with minimal scattering or collisions) represents a deviation from the typical carrier transport mechanism. Normally, as an electron moves from the source to the drain, it undergoes a scattering effect that leads to a decrease in its energy. However, when the device size is significantly reduced, this mechanism undergoes a transformation. The electron now travels directly from the source to the drain, covering a very short distance and experiencing minimal scattering effects. This shift to ballistic transport improves the on-current since there is reduced scattering within the device. Consequently, it is viewed as a desired effect rather than a limiting factor (due to scaling) for FET performance. It mostly occurs in short-channel devices (especially where channel length is below 10 nm) [11].

1.6 Device Topologies for Reduction of SCE's

As the device dimensions approach the nano-scale regime, the short channel effects inhibit optimized device performance. Hence, there is a need of various device technologies so that the SCE's can be mitigated to a larger extent. The non-classical structures have multiple gates which can exert greater command over the channel in contrast to the conventional design. Reduced leakage current, enhanced performance,

and output conductance of the device, even in the nanoscale region, are all benefits of improved gate control. An additional benefit of unconventional design is improved drive current, which is responsible for much faster circuit speed. These benefits are compelled to persist in reducing costs via miniaturization. Below are some device designs that can be used to minimize SCEs:

1.6.1 DG (Double Gate) FET

DG FET has the channel in between two gates. Fig. 1.4 shows the 3-D view of Double Gate (DG) FET [12]. The fundamental concept of a DG FET is to achieve effective regulation of the channel through choosing very small channel widths and appending a gate contact on both the sides of the channel, which helps in suppressing SCEs and results in higher current when contrasted to a single gate FET [13].

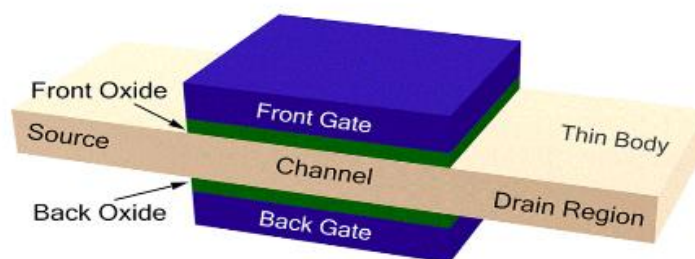


Fig. 1.4 DG FET

DG FET is electrostatically much more powerful in contrast to traditional FET with just one gate, due to the gate shielding of the channel from two sides, thereby concealing field penetration from the gate and thus curbing SCEs. T. Sekigawa and Y. Hayashi published the first article on the DG-MOS transistor in 1984 [14]. The short-channel effect is reduced as a result of the drain electric field's reduced influence on the channel. Two configurations are possible for double gate FET: Asymmetric DG FET and Symmetric DG FET. One gate is coupled to the other by a common gate bias in a symmetric DG MOSFET, and both oxides have the same thickness, while in an asymmetric DG MOSFET, the front and rear gates receive separate biasing and the oxides' thicknesses are also different.

1.6.2 FINFET

The Fin-FET has been introduced by Huang et. al in 1999 [15] to surpass the undesirable types of SCEs seen by deep submicron transistors, such as DIBL and threshold voltage roll-off. Fig. 1.5 illustrates the schematic view of Fin-FET structure. Fin-FET technology involves encasing the gate around a narrow silicon slice, known as a "fin", which is ideally made of intrinsic silicon. The current then travels over the surfaces of the fin, both on the side and the top. This wrap-around nature of the gate increases gate control on the channel, which causes more reduction of SCE's and leakage current.

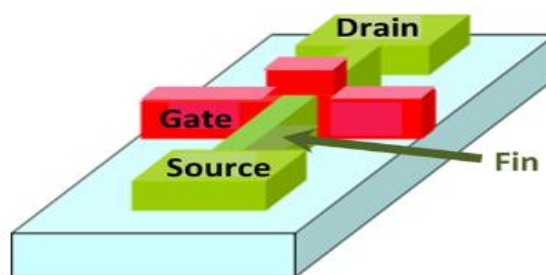


Fig. 1.5 Structure of FINFET [15]

1.6.3 Gate-All-Around (GAA) FET

The gate structure of a GAA FET [16], [17], also known as a Surrounding Gate FET or Wrap Around Gate FET, is wrapped around a silicon beam, which can be square, rectangular, circular, thin or wide, and have different orientations. Studies illustrate that this excess electrostatic confinement allows the Gate-All-Around FET to be scaled to about 50% more as compared to the double gate FET [18]. This characteristic may be utilized to soften the need for the oxide and the silicon layer thickness for a given gate length. Different kinds of gate-all-around structures are characterized by their respective geometries. These include:

1.6.3.1 Rectangular GAAFET

The Rectangular GAA MOSFET features a rectangular substrate material that is fully enclosed by a rectangular-shaped gate. The rectangular GAA construction provides excellent control over the electrostatics of the channel and is more resistant to SCEs compared to DGFET and Fin-FET structures. The device with a rectangular gate offers improved current drivability, enhanced mobility, and an optimal subthreshold swing at a specific crystal orientation [19]. The basic layout of a rectangular GAA FET is shown in Fig. 1.6.

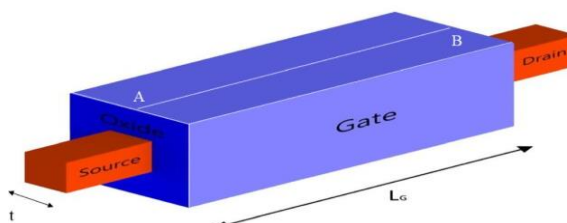


Fig. 1.6 Rectangular GAA FET Structure [19]

1.6.3.2 Triangular GAA FET

Fig. 1.7 (a) displays the three-dimensional and Fig. 1.7 (b) depicts the correctional perspective of the triangular GAA MOSFET. In this configuration, the triangle substrate material is fully enclosed by a triangular-shaped gate. The low field mobility is increased by the local volume inversion in corners and the coupling known as corner effects [20].

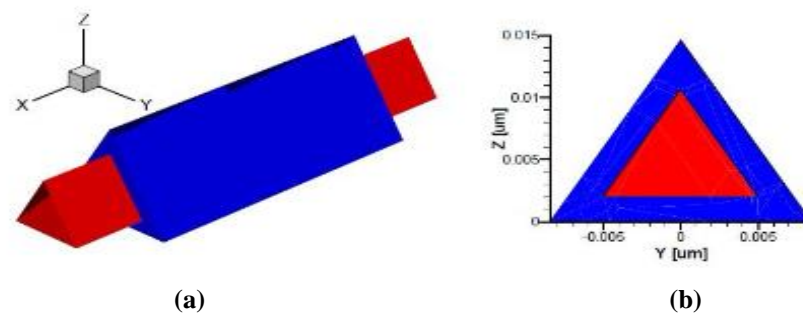


Fig. 1.7 Triangular GAA MOSFET [20]

1.6.3.3 Cylindrical GAA FET

Fig. 1.8 displays a cylindrical GAA FET. It consists of a semiconductor substrate in the shape of a cylinder that is fully enclosed by the gate. This semiconductor cylinder serves as the channel of FET. The CGAA FET [17], [21], [22] is an intriguing design structure for CMOS technology in the future because of its enhanced resistance to SCEs, reduced floating body effects, effective gate controllability, improved transport characteristics, and outstanding compatibility with CMOS.

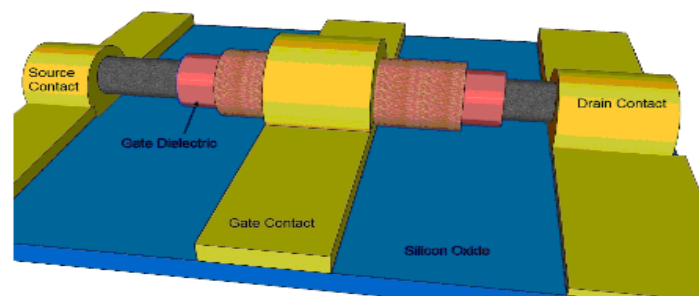


Fig. 1.8 Structure of Cylindrical GAA MOSFET

1.7 Device Engineering Techniques

Guided by all the above mentioned short channel effects and other limitations, various engineering techniques have been applied to the device architecture, some of which are addressed below:

1.7.1 Gate Material Engineering (GME)

A discontinuity in the field along the channel is proposed by engineering in the gate-material with unique work functions, which results in enhanced transport and decreased SCEs. The channel electric field profile is adjusted to amplify the field strength at the source side in order to boost the speed of the carriers, while reducing the field strength at the drain end. Additionally, a metal with a lower work function is placed at the drain end to shield against changes in drain potential thereby curtailing the hot electron effect. Gate Material Engineering (GME) FET, as depicted in Fig. 1.9 [23] can be employed in FET structures, with the aim of improving gate transport efficiency and minimizing SCEs [23], [24].

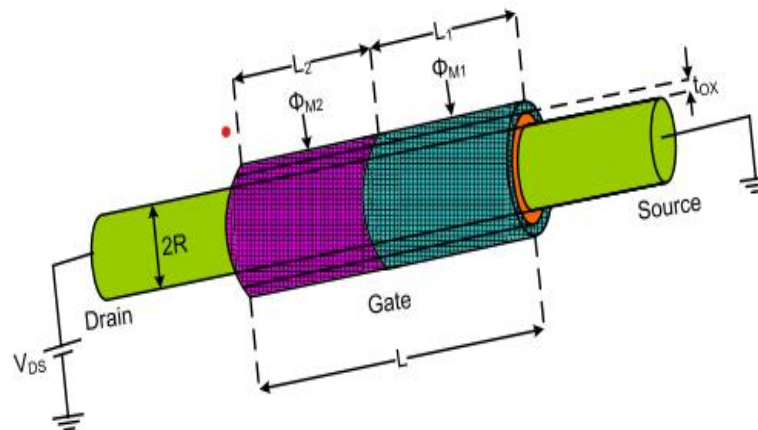


Fig. 1.9 Gate Material Engineering (GME) in Cylindrical GAAFET [23]

1.7.2 Gate Oxide Stack Engineering

Oxide engineering has emerged as a pivotal aspect of modern semiconductor technology, particularly in the realm of FET. High-k dielectric material as the gate oxide material or gate oxide stacking can be employed as the standard oxide engineering strategies which results in the enhanced transistor performance [25]. As the industry aims for more energy-efficient and high-performance FET, oxide engineering evolves as well. Novel materials and innovative design methodologies have been employed to control the properties of oxides and expand the limits of semiconductor technology. This allows the continuous advancement of Moore's Law. High-k dielectrics such as Al_2O_3 and HfO_2 possess a higher permittivity than SiO_2 , allowing for thicker gate oxides without sacrificing capacitance. This simultaneously reduces gate leakage while maintaining the required level of performance. In addition, gate oxide stacking has become increasingly recognized as an advanced method of oxide engineering. As direct deposition of high-k dielectric material is challenging, it is common practice to layer SiO_2 with such material. This enhances the transistor's performance, enabling optimized threshold voltage and improved subthreshold slope. Stacking also contributes to minimizing the short-channel effects, enhancing FET's overall efficiency and speed. In the context of biosensing applications, gate oxide stacking typically leads to a substantial improvement in sensitivity. Fig. 1.10 shows a typical MOSFET with gate oxide stacking. Gate oxide stacking can be further classified into forward and reverse gate oxide stacking.

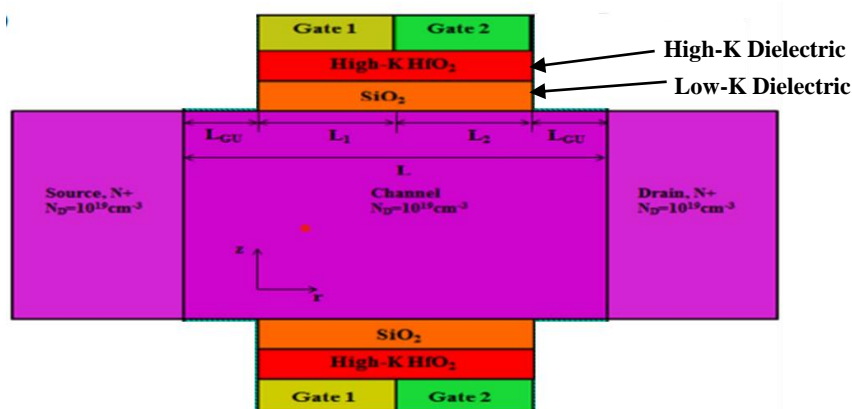


Fig. 1.10 MOSFET with Gate Oxide Stacking

The material with a low dielectric constant is typically positioned close to the channel, and the high dielectric constant material is positioned near the metal gate in the forward gate oxide stacking technique. In the reverse configuration, the material with a high dielectric constant is set up close to the channel, and the material with a low K is situated close to gate. However, the usage, number, and placement of different dielectric materials depend on various factors, such as fabrication complexity, stability of these oxide layers, lattice matching between the channel material and oxide material, and the oxide breakdown voltage limit [25].

1.7.3 Channel Engineering

Intentionally adjusting the doping profile of the channel region is one method that can be utilized to reduce the impact of channel length modulation. It is possible to lessen the influence of CLM by maintaining a channel doping that is equal to or higher than the drain doping. A common name for this method is channel engineering, and it is also sometimes referred to as channel doping gradient [26]. Adjusting the channel doping profile and size can be an effective means of controlling the distribution of the electric field and reducing the likelihood of velocity saturation [27]. In order to lessen the peak electric field intensity and enhance carrier mobility, many techniques are utilized. Some examples of these techniques are graded channel engineering and lightly doped drain (LDD). In order to mitigate the issues that are provided by reducing dimensions, graded doping profiles, also known as dual or triple step-graded profiles, are utilized. These profiles introduce regulated fluctuations in dopant concentration along the transistor channel [26].

1.8 Junctionless Field Effect Transistor

In inversion mode MOSFET, two p-n junctions are connected back to back. Below the 22 nm technology node, the device length is comparable to the length of the depletion region of p-n junctions. Therefore, from a fabrication perspective, controlling these metallurgical p-n channel junctions is quite challenging. Also, short channel effects and hot carriers are undesirably increasing when device design goes below 22 nm technology node. Therefore, to survive prospective designs for ULSIs, there is a growing necessity for substantial adjustments at the device level. The Junctionless

transistor is a new design with exceptional properties that was proposed by Colinge et al. [28]. The source, channel, and drain region are uniformly and strongly doped, without the development of junctions, which eliminates the issue of impurity diffusion. A physicist Julius Edgar Lilienfeld filed the first patent [29] for the Junctionless concept in 1925. The field-effect transistor proposed in this patent comprises a narrow insulator layer that is placed on top of a thin semiconductor film, which in turn is coated onto a metal electrode. The metal electrode functions as the gate of the device. The structure of Colinge [28] et al. is based up on tri-gate design. The structure reduces the effects of various parasitic resistance and capacitances. To improve the gate controllability in Junctionless transistor, cylindrical gate structure has been proposed. The JNT's physics differs significantly from the typical MOSFET's, as depicted in Fig. 1.11.

The strongly doped nanowire experiences a significant reduction in its electric field that is perpendicular to the current flow when it is depleted below the threshold. However, when it is over the threshold, the electric field decreases to zero. Contrary to inversion-mode (IM) or accumulation-mode (AM) devices, where the field strength is maximum when the device is turned on, this is the opposite. From the figure, below threshold voltage, the mobile carriers in channel region are depleted. As a result, there is no pathway for conduction between the source and drain areas. When sufficient amount of gate voltage applied then depletion of carriers removes and carriers start from center of the semiconductor film.

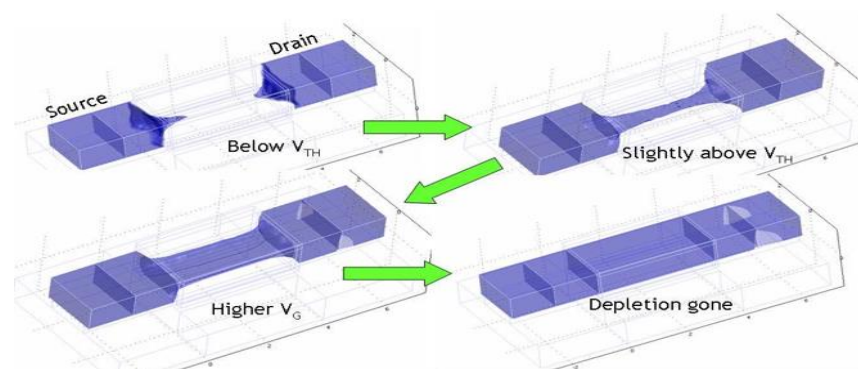


Fig. 1.11 Operation Mechanism of Junctionless Transistor [28]

1.9 Device Simulation

Simulation of the device is an integral part in design of the device. It serves as quick feedback about device design before long and expensive fabrication of discrete device simulators, such as ATLAS [31], TCAD (Technology Computed Aided Design) Non-linear differential equations are solved using iteration techniques like Newton-Raphson method etc. Depending on the number of points a simulation can take several hours. Voltages, terminal currents and charges are calculated based on a set of physical device equations– i.e. continuity and Poisson's equations. Beside a wide variation of materials, such as semiconductor, metal, insulator etc. a device simulator offers to vary a wide variety of parameters to change, such as temperature, pressure and so forth. Also, the variability of models such as carrier statistics, and current continuity seems

endless. In this thesis, ATLAS 3-D device simulator from Silvaco has been used. Table 1.1 demonstrates the various models available in ATLAS to model the various physical phenomena [30].

Table 1.1 Various Models Available in ATLAS [30]

Category	Models
Statistics	Boltzmann, Fermi-Dirac, Incomplete Ionization, Bandgap narrowing
Mobility	Concentration dependent mobility (Standard, Analytic, Arora Model), Carrier-Carrier scattering model, Field dependent mobility model, Surface scattering mobility model, CVT model, Yamaguchi model.
Recombination	Shockley-Read-Hall (SRH) recombination model with fixed lifetime, SRH recombination model with concentration dependent lifetime, Auger recombination model
Impact ionization	Crowell and Sze model, Grant's model, Selberherr model
Tunneling	Fowler-Nordheim tunneling model, Band to Band tunneling model, Direct quantum tunneling model, Hot carrier injection model, Concannon's Injection Model
Energy transport	Energy balance model, Hydrodynamic model.

1.10 FET as Biosensor

In the past 20 years, breakthroughs in semiconductor technology have led to dramatic progress in the broad field of biomolecule sensing. The development of customized treatments suggests better disease categorization and increased diagnostic accuracy with fewer adverse effects. Medical technology facilities must be equipped with biosensors that can detect ultralow concentrations of biomolecules quickly and accurately, in addition to other real-time monitoring features, as part of the advancement to such an advanced health care system [31], [32]. Because of the opportunities for on-chip integration and miniaturization made possible by current semiconductor manufacturing processes and technologies, biosensor devices with an electrical sensing output are attractive candidates [33]. The conventional method of biosensing originated from chemical approaches, which had numerous disadvantages and limited advantages. The advantages and limitations of classic chemical biosensing approaches, in comparison to modern advanced techniques, are presented in Table 1.2.

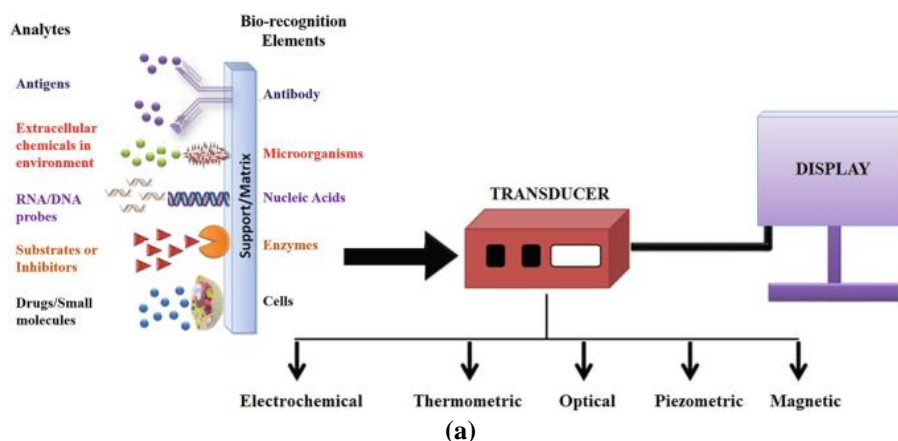
Table 1.2 Comparison of Conventional Chemical Biosensing and Modern FET Biosensing Techniques

Biosensing Technique	Advantages	Limitations
Conventional Chemical Sensing	Offers high sensitivity.	Exhibits slow detection time response.
	Offers high selectivity.	Involves costly equipment and skilled personnel.
		Susceptible to organic contamination.

		Requires complex data analysis and interpretation.
Modern advanced FET Biosensing	Provides rapid detection time.	Prone to noise interference.
	Outputs data in electrical format, facilitating interpretation.	The manufacturing process is complex.
	Demonstrates high sensitivity.	
	Offers reusability and portability.	

1.10.1 Biosensing Mechanism

A biosensor system consists of two main components that work together: the bio-recognition system and the transducer. The bio-recognition system includes a sensing layer where the chemical functionalization of the bio-receptor chemical occurs, typically in a specially designed chemo-receptive cell. The transducer, on the other hand, serves as the means for evaluating the attached target bio-molecules into an equivalent electrical quantity and can be a heterostructure or a field effect transistor (FET) [34]. Fig. 1.12 (a) demonstrates the basic block diagram of biosensor in which the transducer could be of electrochemical, thermometric, optical, piezometric and magnetic. The fundamental block diagram of the sensor mechanism in FET biosensors is depicted in Fig. 1.12(b), where the transducer device is a field effect transistor of several types, including classical FET, double gate FET, FinFET, junctionless FET, and gate-all-around FET [35].



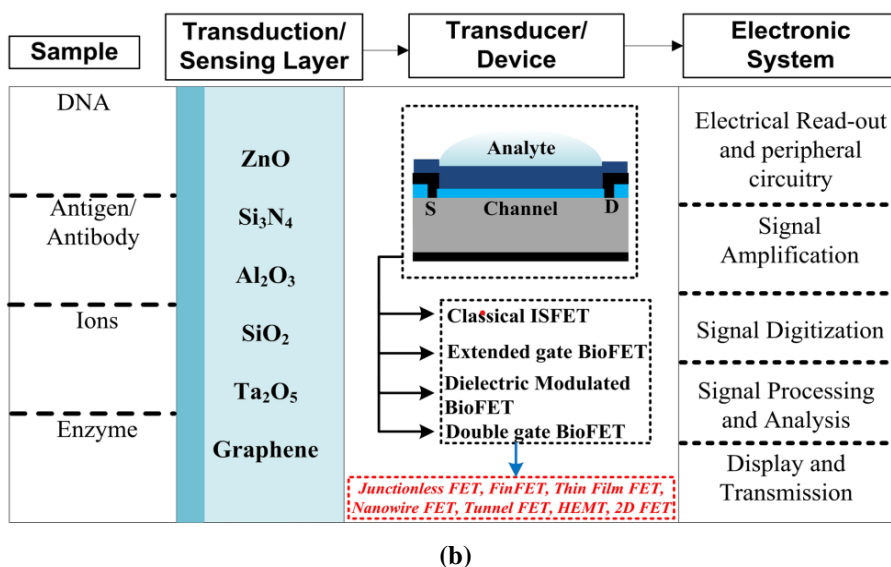


Fig. 1.12 (a) Basic Block Diagram of Biosensor [34] (b) Basic Block Diagram of Sensor Mechanism in FET Biosensors [35]

1.10.2 Evolutionary Progression of BioFETs

The core idea of FET biosensor is the movement of charge in the channel of transistors due to the electrostatic influence of charge on the target biomolecules that are connected to the layer oxide surface. By utilizing suitable compounds as bio-recognition elements, BioFETs have the ability to detect biomarkers of interest, even at extremely low concentrations [36]. Fig. 1.13 illustrates the chronological progression of FET biosensors, highlighting key milestones.

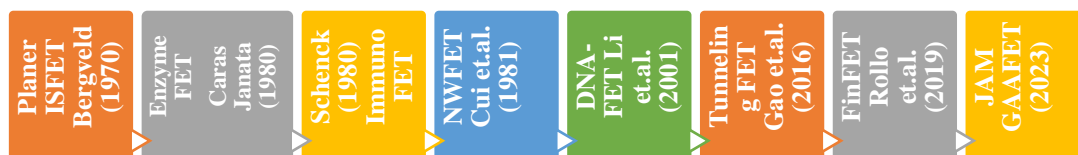


Fig. 1.13 Evolution of FET Biosensors

Bergveld's initial BioFETs are planar ion-sensitive FETs (ISFETs) that functioned as electrochemical sensors for detecting PH or proton concentration [37]. Over time, advancements were made in the design of planar ISFET architectures, allowing for the transition from ion sensing to biomolecule sensing [37]. These improvements enabled the detection of several analytes, including nucleic acids and proteins. FET Biosensors are being used for more complex clinical applications like label-free biomolecule detection and DNA sequencing. However, these applications still face hurdles in both design and implementation. The FET based biosensors are primarily designed for the detection of biomolecules such as DNA without the requirement for labeling. When complementary counterparts are attached to DNA that has been immobilized on a detecting surface such as an oxide layer, consequently, a change in channel surface potential. This change is caused by the negative charge in nucleotides, which enables the detection without the need for labeling. There have been reports of BioFETs with

a planar shape that have a lower detection limit of a micromolar range [38]. Various biomolecules, such as glucose, penicillin, and urea, have been successfully identified using BioFETs [39]–[41]. Modern architecture BioFETs at the device level utilize advanced technologies such as nanowire FET, TFET, Gate-All-Around FET, multi-gate FETs, FinFET, junctionless FETs, and others [42]–[44].

1.11 Literature Survey

1.11.1 Literature Survey on FET Devices

The field-effect transistor (FET) is utilized in different analog applications and comes in numerous variations, including MOSFET, TFET, IIFET, and HEMT. MOSFET is widely used in most analog applications, except for a few cases requiring a low subthreshold swing and ultra-low power consumption. Researchers have investigated different approaches to improve the performance of FETs and customize them to meet specific application needs. Below, we will discuss some notable progress in contemporary literature.

(a) Emerging FETs for improvement in RF and high frequency Applications:

Researchers are exploring different ways to improve transistor performance because of the constant search for better transistor performance in high-frequency applications. Gate length scaling is a highly influential approach that includes systematically decreasing the physical dimensions of the gate region in a FET. This method shows potential for attaining higher cut-off frequencies and enhanced linearity, which are both essential aspects for RF and high-frequency functioning. Biswal et al. [45] thoroughly examined that reducing the gate length of a FET impacts its performance in analog/RF applications. But this improvement is accompanied by difficulties such as increase in gate leakage current and vulnerability to short channel effects.

Various studies highlight the importance of customizing gate architectures to improve high-frequency capabilities. Sarkar et al. [12] presented the impact of gate engineering on a dual-gate MOSFET. Implementing the gate engineering techniques significantly enhances device performance, particularly in terms of high-frequency operation. Several authors have also emphasized the benefits of gate engineering on the analog performance of GAA-FET [46]–[48].

Furthermore, there has been an increase in the investigation of new materials with unique properties, such as Gallium Arsenide (GaAs), Graphene, Molybdenum Disulfide (MoS_2), and Indium Phosphide (InP). These materials demonstrate enhanced electron mobility, resulting in higher intrinsic transit frequencies and improved high-frequency properties of FET [49], [50]. The use of these materials with high electron mobility offers both advantages and difficulties, as their incorporation into current silicon-based technologies requires careful assessment of compatibility and production methods.

In order to improve carrier mobility and device performance at RF frequencies, the usage of strained silicon and silicon-germanium hetero-structures has also been

studied [51], [52]. By systematically applying strain to the crystal structure of silicon, the movement of charge carriers is increased, resulting in quicker charge transport and enhanced performance at high frequencies. Silicon-germanium hetero-structures provide a benefit by utilizing the differences in lattice constants between silicon and germanium to improve the movement of carriers and enhance the performance of transistors in the high-frequency range.

(b) FETs for Low-power applications: Field-effect transistors (FET), such as MOSFETs, and recent FET technologies like FinFET, TFET, and GAA-FET, are very important in different fields for low-power electronic devices [53], [54]. One of the foundational aspects of low power FET applications lies in their ability to achieve reduced power consumption without compromising performance. This is particularly crucial in battery-powered devices, such as smartphones, IoT sensors, and wearable gadgets. The literature underscores the relentless pursuit of smaller feature sizes and improved materials to enhance FET performance in terms of reduced leakage currents, improved switching speed, and lower threshold voltages (essential for low power circuit design). In the realm of low-power digital logic, MOSFET has been extensively researched, and techniques like multi-threshold voltage design, power gating, and clock gating have been deployed to minimize static and dynamic power dissipation [55], [56].

The historical perspective of low-power FET applications can be traced back to the mid-20th century, marked by the emergence of the first practical FET. Early FET, such as the MOSFET, was instrumental in shifting the landscape of electronics away from power-hungry vacuum tube technology. The MOSFET, first conceived in 1960, played a pivotal role in the development of low-power electronic devices. This period of 1960's and 1970's marked the initial applications of MOSFET in calculators, early computers, and digital logic circuits. A new age of low-power electronics started during the 1990s when CMOS technology became widely used. This era saw the proliferation of low-power microcontrollers, memory devices, and systems-on-chip (SoC) that underpin today's mobile phones, tablets, and IoT devices [57]. As the 21st century unfolded, the demand for low-power electronic devices continued to surge, fueled by the proliferation of portable electronics and the global push for energy-efficient technologies. In parallel, the semiconductor industry pushed the boundaries of FET technology with innovations like FinFET, TFET and GAA-FET [58]. These emerging FET architectures promised even better electrostatic control and lower leakage currents, making them highly attractive choices for achieving greater energy efficiency in digital circuits. TFET, for instance, leverages quantum mechanical tunneling effects to achieve extremely low subthreshold slopes, paving the way for further reductions in power consumption [59].

1.11.2 Literature Survey on Gate-All-Around FET (GAA-FET)

The Gate-All-Around Field-Effect Transistor (FET) is a type of FET where the channel is completely surrounded by the gate. This design has been employed in several analog applications in literature [60]–[62]. The ongoing improvements in semiconductor technology have greatly aided the development and use of GAA-FET for radio frequency and analog circuits. The inherent electrostatic control provided by the GAA

architecture enables superior gate control and minimizes parasitic effects, resulting in improved analog performance at high frequencies. Auth and Plummer [16] have shown that Cylindrical Gate-All-Around (CGAA) MOSFET is one of the most promising and attractive structure for future Complementary Metal Oxide Semiconductor (CMOS) technology. Ghosh et al. [63] have further shown that CGAA MOSFET poses better short-channel effects immunity, good gate controllability, suppressed floating-body effects, improved transport property and excellent CMOS compatibility. A lot of work has been carried out by researchers on Gate-All-Around MOSFET, Dual-Metal Nanowire FET (DM-NW-FET) / GAA MOSFET, including the analytical modelling, and effect on gate leakages [64]–[69].

1.11.3 Literature Survey on FET for Biosensing Applications

Over the past decade, there has been a significant effort to create methods and systems for detecting biological compounds that are vital for the environment, human health, and agriculture. An essential criterion for identifying these compounds is a sensing device that is exceptionally discerning, dependable, rapid, sensitive, and portable.

Biosensors can be classified according to their detection method, which can be either labeled or label-free detection [70]. Electrochemical biosensors have gained considerable attention for their capacity to offer real-time electrical detection with minimum power consumption, making them particularly appealing for label-free detection. These biosensors possess high sensitivity, scalability, cost-effectiveness, and lightweight characteristics, which make them appropriate for integration with a measurement system on a chip [71]. CMOS technology is a standout choice for on-chip integration because of its resilience, scalability, and cost-effectiveness. The scaling property of CMOS technology is important because it allows nanostructures to be sized to match biological entities such as nucleic acids and proteins. This enables the integration of electronics, nanotechnology, and biology. CMOS-compatible biosensors have the capability to detect a diverse array of biological molecules, such as proteins, viruses, and nucleic acids, which are bio-chemical species.

Electrochemical Biosensor

An electrochemical biosensor, a type of label-free biosensor, utilizes an electrochemical transducer to convert biotarget-bioreceptor interactions into electrical signals (as depicted in Figure 2.6). These sensors rely on surface interactions for biorecognition, independent of reaction volume, allowing for measurements with small sample volumes [72]. Table 2.1 provides an overview of various electrochemical transducers used in electrochemical sensing, along with their measurement types [73]. The readout circuitry typically includes signal amplifiers (for signal enhancement), signal processors (for analog-to-digital conversion), and display units (for presenting the final output) [74]. Electrochemical biosensors offer numerous advantages for detecting biological substances, including high sensitivity, selectivity, affordability, and portability.

Two widely adopted MOSFET configurations for biosensing applications are the ion-sensitive field effect transistor and the dielectric modulated field effect transistor (the

latter being the most commonly used variant). The general approach to electrically detect biomolecules using MOSFET, drawing from literature sources, is summarized as follows:

i. **Label-Free Detection with a Bioreceptor Layer [73], [75], [79], [80]:**

The upper surface of the MOSFET, typically the gate oxide, is modified and functionalized with a bioreceptor that specifically binds to the target biomolecule (biotarget). A bioreceptor acts as the sensing element in the biosensor which is basically a biological molecule or component that recognizes and binds to a specific biomolecule (target biomolecule), allowing for the detection of the target biomolecule. The interaction between the biotarget and the bioreceptor on the MOSFET results in alterations in the device's electrical characteristics, including electric potential, channel electron concentrations, and conduction current. These changes are analogous to those produced by the application of an external gate voltage. The degree of change in the MOSFET's electrical conductivity after the binding of the biomolecule to the bioreceptor serves as a basis for biomolecule detection. When biomolecules are immobilized inside the cavity, embedded in the gate oxide layer, they alter the equivalent oxide, subsequently affecting the potential distribution across the channel. This modification enhances the selectivity of the biosensor for detecting the presence of biomolecules.

ii. **Label-Free Detection without a Bioreceptor Layer [58], [61], [85]:**

When biomolecules are immobilized inside the cavity, embedded in the gate oxide layer, they alter the equivalent oxide, subsequently affecting the potential distribution across the channel. This modification enhances the sensitivity for detecting the presence or absence of biomolecules (although it may reduce specificity due to the absence of a bioreceptor layer).

Dielectric Modulated FET Biosensor

DM-FET biosensors utilize a nanogap cavity where biomolecules are injected, causing alterations in the gate's effective capacitance. This nano gap is fabricated by etching the gate oxide or sometimes the gate material of FET device [75], as depicted in Fig. 1.14.

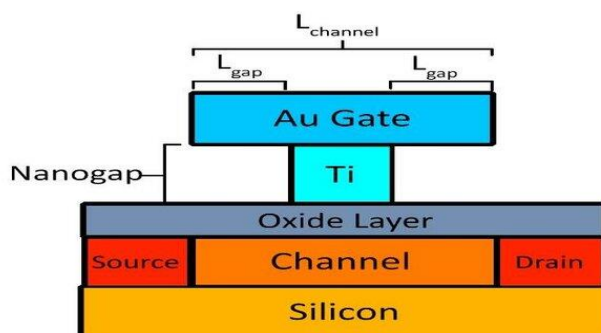


Fig. 1.14 Schematic of Nanogap formed in DMFET Biosensor [76]

The changes in gate capacitance depend on the dielectric constant (K) and charge density (Q_f) of the biomolecules. An important benefit of using DM-FET biosensor is their capacity to detect both charged and neutral biomolecules [76]. These biosensors are extremely important in industries like medical diagnostics, environmental monitoring, and drug research.

The literature review based on significant research on high-performance field effect transistors and their use as sensors is displayed in Table 1.3. On the other hand, Table 1.4 details the significant research on analytical modeling and sensitivity enhancement of Gate-All-Around FET sensors.

Table 1. 3 Literature Survey on High-Performance Field Effect Transistor and their Application as Sensors

Ref. No.	Author Name & Year	Type of FET design and sensor	Summary/Findings
[77]	Colinge et al. (2010)	Junctionless nanowire transistors (JNT)	The junctionless transistor (JLT) is the optimal approach for creating very precise source/drain junctions. Due to its stable doping characteristics, JLT is a promising solution for addressing the issue of costly annealing procedures and thermal budget. Furthermore, different electrostatic traits have been modified by doping the source, channel, and drain using n+ doping.
[78]	Choi et al. (2010)	Junctionless Accumulation Mode FinFET	This research investigates the performance of bulk FinFETs having high-K spacers and doping in junctionless accumulation mode. The study focuses on improvements in SS, DIBL, and I_{ON}/I_{OFF} . The JAM-CSG MOSFET is a variant of the Junctionless MOSFET that has been specifically developed to address the JLT issue. The structure is a homojunction with a single doping type, consisting of an n+-n-n+ configuration.
[79]	S. Rewari et al. (2016)	Nanotube junctionless field effect transistor (NJLFET)	The performance of NJLFET is evaluated by comparing it with that of junctionless gate-all-around FET. The results demonstrate that the junctionless MOSFET in NJLFET exhibits notable enhancements in both digital performance and analog performance.
[80]	Yang et al. (2019)	Si Nanowire Double-Layer Gate FET	The work presents the improved threshold voltage characteristics of the double layer gate configuration in Si Nanowire FET.

[81]	Kumar, Sandeep et al. (2020)	Trench Gate TFET with Dual Channel for biosensor design	The gate in dielectric modulated dual channel trench gate tunnel FET (DM-DCTGTFET) is placed inside a trench vertically to create two channels on both sides of the gate. The simultaneous conduction of two channels increases the current. The sensitivity performance of the DM-DCTGTFET is also enhanced. The simulated results demonstrate that as the cavity width increases, the current sensitivity decreases while the voltage sensitivity exhibits an increase.
[82]	Chen et al. (2021)	Extended Gate Junctionless GAA FET	Explored the potential for deviation and susceptibility in a potentiometric sensor utilizing an extended-gate FET. This investigation compared junctionless and inversion-mode nanowire FETs. Both JL and IM GAA NWFETs were fabricated simultaneously and showed outstanding electrical properties, and a SS of approximately 63 mV/dec and a high switching ratio. Notably, JL GAA NWFETs exhibited superior drift stability compared to their IM counterparts across various operational regions and over prolonged periods.
[83]	A Das al. (2022)	Surrounding Gate MOSFET for Biosensing Applications	Explored multiple challenges that may impede the sensing capabilities of the biosensors based on surrounding FET. <ul style="list-style-type: none"> • Fabrication Challenge • Selectivity • Sensitivity • Short Channel Effects • Reusability • Filling Area
[84]	Kaur, Pawandeep et al. (2022)	Double Gate Junctionless FET	A dielectric-modulated double-gate junctionless metal-oxide-semiconductor field-effect transistor (DM-DGJLT) was investigated for its potential in label-free biomolecule detection. This device boasts an impressive ON/OFF current ratio of 10^{12} , delivering an ON current around 10^{-4} A/ μ m and an OFF current approximately 10^{-16} A/ μ m. For dielectric constants $K=10$ and $K=1$, the threshold voltage variations were measured as $\Delta V_{th}=0.34$ V and $\Delta V_{th}=0.23$ V, respectively. High-k materials are used to insulate the cavities beneath the gate, effectively modulating the dielectric constant.

[85]	Gao et al. (2022)	Poly-L-Lysine-Modified Graphene FET (GFET)	A very sensitive biosensor has been created using PLL modified GFET. SARS-CoV-2 and breast cancer RNA can be identified more quickly, accurately, and adaptively with the use of this biosensor. This biosensor exhibits the capacity to specifically identify and distinguish miRNA and SARS-CoV-2 RNA. It has a dynamic range of five orders and a LOD as low as 1 fM within 20-minute timeframe using just 2 μ L of blood sample. This is a sensitivity enhancement of more than 113% compared to GFET biosensors.
[86]	Shivendra Yadav et al. (2021)	A Dielectric Modulated Biosensor for SARS-CoV-2	The paper presents an innovative biosensor for SARS-CoV-2, specifically targeting the proteins related to spike, envelope, and DNA of virus. The sensor's sensitivity to virus proteins and their charge densities was tested using DC and RF characteristics. Furthermore, a thorough comparison has been conducted between the sensor with and without Hf Gate2, focusing on the DC/RF parameters. The results demonstrate the importance of the suggested improvement. Additionally, the effect of substituting the SiO ₂ with HfO ₂ in relation to DC/RF components has been investigated to analyze the sensing capability.
[87]	Wangkheirakpam et al. (2022)	TFET-based biosensor	A vertical TFET-based dielectric modulated biosensor has been proposed for SARS-CoV-2 detection. Enhanced device drain current is attained by employing the n ⁺ pocket at the source side. The S-protein and DNA, which are separate viral proteins with different electrical properties, combine within the nanogaps. The simulation data clearly demonstrate that the proposed biosensor is highly sensitive.
[88]	Priyadarshani et al. (2022)	Gate-all-around junctionless FET	This paper describes label-free SARS-CoV-2 detection using a gate-all-around junctionless Field effect transistor. The sensitivity analysis examines ΔV_{TH} , ΔI_{ON} , Δg_m , and SS. More variation in the electrical parameters allows sensitive biosensors. GAA-JLFET is chosen here because of its easy fabrication and better sensitivity from gate controllability with additional gates.

Table 1. 4 Literature Survey on Sensitivity Improvement and Analytical Modeling of Gate-All-Around FET Sensors

Ref. No.	Author Name & Year	Analytical Model for FET design and sensor	Findings
[89]	A. Goel et al. (2020)	Junctionless Biotube FET	Under identical bio-molecule settings, Junctionless Biotube FET sensor was developed and compared to Nanowire FET. The Dielectric Modulated Junctionless Biotube FET offers increased drift in drain current, g_m , switching ratio, SS, and V_{th} , hence the sensitivity of the biosensor.
[90]	Banerjee et al. (2022)	Dual-Material Gate Macaroni Channel MOSFET biosensor	This study presents a detailed analysis and simulation of Dual-Material Gate Macaroni-Channel MOSFET. By carefully choosing the outside radius of the device, it is possible to effectively reduce certain significant SCEs parameters like the decrease of V_{th} and the improvement of SS. This leads to enhanced device performance. The comparative threshold voltage shift demonstrates that the proposed biosensor exhibits more sensitivity compared to its DM Full-channel Cylindrical Equivalent with an identical channel thickness.
[91]	Kanungo et al. (2016)	SiGe Source Channel Tunnel FET	Comprehensive device-level simulations analyze the effects of SiGe as a source and n+ pocket-doped channel. The SiGe source in the DMTFET structure optimizes sensitivity current better than the pocket-doped architecture.
[92]	Getnet et al. (2020)	Triple Hybrid Metal GAA Junctionless NWFET	This work shows that hot-carrier and electron dispersion due to a high electric field and saturation velocity can cause short-channel phenomena and quantum mechanical tunneling. Materials with higher work-function and dielectric properties near the drain can mitigate these effects.
[93]	Capua et al. (2022)	Silicon Nanowire FET Sensor Arrays with Enhanced Back-Gate Performance	A CMOS-compatible, label-free C-reactive protein (CRP) sensor has been developed using silicon nanowire arrays based on SOI technology. This double-gate sensor demonstrates excellent stability, minimal hysteresis, and high sensitivity to CRP proteins, particularly when operated in a back-gate configuration, maintaining a linear response range.
[94]	Thomas Holtij et al. (2014)	Junctionless accumulation mode double gate MOSFETs	This paper presents a comprehensive 2-D analytical compact model for junctionless accumulation mode double gate MOSFETs, applicable to both long and short channels.

			The potential distribution in the 2-D model is derived from Poisson's equation and the Schwarz-Christoffel conformal mapping method, rooted in fundamental physical principles. This analytical method allows for simple formulae to be derived for calculating the V_{th} and SS.
[95]	Rewari Sonam et al. (2019)	cylindrical junctionless double surrounding gate (CJLDSG) MOSFET	The performance of a HfO ₂ -based CJLDSG MOSFET has been assessed and compared with HfO ₂ -based CJLSG, SiO ₂ -based CJLDSG, and CJLSG MOSFETs. The HfO ₂ -based CJLDSG MOSFET shows superior analog performance, including higher drain current, transconductance, output conductance, TGF, VEA, MTPG, current gain, and a subthreshold slope near 60 mV/decade, as well as a better I_{on}/I_{off} ratio.
[96]	Kumar et al. (2020)	Dielectric modulated trench double gate junctionless FET (DM-TDGJLFET)	2-D analytical model of the proposed DM-TDGJLFET with two gates positioned vertically in separate trenches has been constructed. The V_{th} , V_{th} sensitivity, drain current, and channel potential of the DM-TDGJLFET are examined. The results generated from the analytical model are also confirmed using the simulated data.
[97]	Rahul Das et al. (2022)	Dielectric Modulated FET Biosensor	Comprehensive data analysis and analytical modeling of a Dielectric Modulated Double Gate Field Effect Transistor (DM-DGFET) for biosensing applications are described. This work discusses novel problems resulting from biomolecule configurations, particularly from a practical standpoint.
[98]	Deepak Kumar et al. (2022)	Triple Metal Stack Engineered Pocket Dielectric Gate All Around (TMSEPDGAA) FET	The implementation of a triple metal gate in TMSEPDGAA FET effectively mitigates the impact ionization effect, resulting in a reduction of SCEs and thus enhancing the current. Dielectric doped pockets reduce off-state tunneling through the channel. Stack engineering, where a high-k oxide is layered on SiO ₂ , increases current due to the fringing field formed at the interface of channel and oxide.
[99]	A. Narang et al. (2017)	Split Gate Junctionless FET	A new analytical model has been developed for a split-gate junctionless (JL) MOSFET which is capable of detecting various analytes like enzymes, cells, proteins, and DNA, using dielectric-modulation techniques.

1.12 Thesis Organization

The thesis entitled, ‘**Analytical Modeling and Numerical Simulation of Gate-All-Around Field Effect Transistor for Sensing Applications**’ comprises seven chapters. The thesis is organized as follows:

Chapter 1: Introduction

This chapter comprehends the framework that develops the aims, motivation, and purpose of the outlined research topic. An overview of nanoscale FETs has been given, along with some scaling challenges and solutions to mitigate these challenges. This chapter also presents the findings from the latest research on semiconductor FETs and their applications in sensing.

Chapter 2: Numerical Simulation of Hetero Dielectric Trench Gate JAM Gate-All-Around FET (HDTG-JAM-GAAFET) for Label-Free Biosensing Applications

This chapter addresses the research gap related to the limited number of low-leakage and high-frequency operation-based sensors. After identifying research gaps and need for novel Gate-All-Around Field Effect Transistor based biosensor we investigated Trench Gate FET for improved performance. The chapter presents the label-free detection of various biomolecules associated with different diseases using the novel Hetero Dielectric Trench Gate Junction Accumulation Mode Gate-All-Around FET (HDTG-JAM-GAAFET). This biosensor employs a cylindrical Gate-All-Around FET with a SiO₂ and HfO₂ hetero dielectric layer, running in Junction Accumulation Mode (JAM). The enhanced gate control over the surface characteristics of the channel and the effects of biomolecules on the sensor’s output properties are thoroughly investigated.

Chapter 3: Trench Gate Engineered JAM Gate-All-Around (TGE-JAM-GAA) Label-Free BioFET

To further improve the device performance, use of triple metal gate engineering in the trench gate FET have been explored to reduce impact ionization and enhance the sensitivity of biosensor device. This chapter aims to investigate a Trench Gate Engineered Junction Accumulation Mode Gate-All-Around FET biosensor and critically analyzes for the label-free identification of biomolecules using extensive numerical device simulations. The investigation explores a simulation-based computational methodology to control and modulate the threshold voltage and current sensitivities using dielectric and charge modulation.

Chapter 4: Analytical Modeling and Numerical Simulation of Graded JAM Split Gate-All-Around (GJAM-SGAA) Bio-FET

Analytical modeling is a powerful tool in the development of FET-based biosensors, enabling a deeper understanding of device physics. This chapter focuses on the analytical modeling of performance parameters of Gate-All-Around FET sensors. It

presents the analytical model of a novel biosensor called Graded JAM Split Gate-All-Around (GJAM-SGAA) Bio-FET for the detection of Avian Influenza antibodies and DNA. The GJAM-SGAA Bio-FET features a silicon Gate-All-Around FET, which operates in the Junction Accumulation Mode (JAM), with a graded doping in the channel. This Bio-FET also features a gate underlap double-sided cavities that overcome nanocavities' fabrication complexity and provide structural stability. The analytical results, in good agreement with simulated results, demonstrate the potential for improving these sensitivities.

Chapter 5: GAA NW-FET Biosensor for Label-Free SARS-CoV-2 and Avian Influenza Virus Detection

Previous chapters have primarily focused on the analysis of biosensors targeting conventional biomolecules. However, there is a growing need to design and study novel biosensors tailored for the detection of specific viruses and diseases. This chapter aims to fill this gap by thoroughly investigating the threshold voltage and current sensitivities, which are vital for the optimal design of Gate-All-Around FET-based sensors. Two innovative biosensors are presented: the "DMDL-GAA-NW-FET" designed for detecting SARS-CoV-2, utilizing a dual metal dual layer nanowire FET structure to improve electrostatic control and overall performance; and the "GAAE-GANFET," which is engineered for the label-free detection of Avian Influenza, featuring advanced gate-all-around technology, a gallium nitride channel, and a dual open cavity configuration.

Chapter 6: High-Sensitivity Biosensors Utilizing Wide Bandgap Semiconductors

To further enhance the performance parameters of Gate-All-Around FET biosensors, the integration of wide bandgap semiconductors offers significant potential. This chapter focuses on advancing the design of novel FET biosensors by leveraging wide bandgap materials to achieve superior sensitivity and performance. Wide bandgap semiconductors such as Silicon Carbide (SiC) and Gallium Arsenide (GaAs) are particularly advantageous due to their inherent properties, including higher breakdown voltage, thermal stability, and increased carrier mobility, making them ideal for applications requiring heightened diagnostic sensitivity. It presents two innovative designs: the Dielectric Modulated 4H-SiC Source Triple Metal Gate-All-Around SiC FET (DM-TMGAA-SiCFET) and the Gallium-Arsenide Gate-All-Around Engineered FET (GaAs-GAAE-FET). The DM-TMGAA-SiCFET features a 6H-SiC channel with dual-sided cavities and a triple metal gate, improving sensitivity for gelatin and DNA biomarkers. While, The GaAs-GAAE-FET, with its gallium arsenide channel and dual nanocavities, significantly boosts sensitivity for breast cancer biomarkers.

Chapter 7: Conclusion, Future Directions, and Social Impact

This chapter provides a concise summary of the key ideas, observations, and results achieved for each objective. It also outlines potential future directions and discusses the broader social implications of the findings in this field.

CHAPTER 2

NUMERICAL SIMULATION OF HETERO DIELECTRIC TRENCH GATE JAM GATE-ALL- AROUND FET (HDTG-JAM-GAAFET) FOR LABEL- FREE BIOSENSING APPLICATIONS

The previous chapter discussed the establishment and evolution of MOSFET over the years, along with what published research led to further investigation of the following structures and principles. This chapter addresses the research gap related to the limited number of low leakage and high-frequency operation-based sensors. After identifying research gaps and the need for a novel Gate-All-Around Field Effect Transistor based biosensor, we investigated Trench Gate FET for improved performance. This chapter presents the label-free detection of various biomolecules associated with different diseases using a novel biosensor design named the Hetero Dielectric Trench Gate Junction Accumulation Mode Gate-All-Around FET (HDTG-JAM-GAAFET). This biosensor employs a cylindrical Gate-All-Around FET that has a SiO₂ and HfO₂ hetero dielectric layer and runs in Junction Accumulation Mode (JAM). The cylindrical gate structure's metal gate is trenched into the Hafnium oxide dielectric layer, which provides the gate with enhanced control over the surface characteristics of the channel. A Trench Gate architecture in a hetero dielectric Gate-All-Around FET is emulated for the biosensing for the first time. The HDTG-JAM-GAAFET has been compared to Normal Gate JAM Gate-All-Around FET (NG-JAM-GAAFET) biosensors immobilizing a variety of neutral biomolecules and biomolecules having a range of positive and negative charges.

Problem statement

Exploring the biosensing performance of a Hetero Dielectric Trench Gate Junction Accumulation Mode Gate-All-Around FET through numerical simulations.

2.1 Introduction

In the current age of pandemics and health crises, efficient biosensors are critical. Rapid and low-cost biosensors having excellent sensitivity are required for advancements in point-of-care diagnostics and future medical technology. Biomolecular species detection has emerged as a crucial area of research for identifying various biological conditions such as Alzheimer's disease, breast cancer, lung cancer, viral infections, as well as contagious diseases like Ebola and Covid-19 [92], [100], [101]. Field effect transistors (FETs) have emerged as highly promising sensing devices, including biosensors, due to their advantages of simple fabrication, affordability, and rapid response. [102]. Label-based biosensing systems are time-consuming, expensive, and labour-intensive. Furthermore, biomolecule labelling may limit the number of active binding sites and impact binding characteristics. Label-free

biosensing devices are designed to detect analytes without the need for labels [103], [104]. Instead, these biosensors rely on the intrinsic physical characteristics of the analytes themselves, such as their molecular weight, electrical impedance, charge, refractive index, or dielectric permittivity, to enable detection [105].

In the Dielectric Modulated FET (DMFET) biosensor, a nanogap cavity structure is implemented within the gate-insulator area [106], [107]. The presence of biomolecules possessing a specific dielectric constant within the nanocavity leads to a modification in the gate dielectric capacitance, resulting in a discernible alteration in the threshold voltage [102], [108]. Also, the variation in the current due to the threshold voltage change confirms the existence of the specific biomolecules [99], [107].

The fabrication of traditional FET biosensors at ultra-small device sizes is currently challenging due to serious issues such as short-channel effects (SCEs) [109], drain-induced barrier lowering (DIBL), hot electron effects, impact ionization effects, sub-threshold swing, and gate tunnelling current [92]. Recent advancements in semiconductor technology have led to significant developments in the field of emerging transistor designs, such as EHBTFETs [110], Line Tunnel FETs with GO-SCOPs [111], and drain-engineered quadruple-gate TFETs [112]. Additionally, novel approaches, including the use of dual MOSCAP-based TFETs [113] and Si/GaAs double gate heterojunction TFETs [114], have shown promising enhancements in performance and suppression of parasitic leakage. Furthermore, the exploration of electrostatically-doped hetero-barrier TFETs [115] has demonstrated remarkable improvements in OFF-state current and ION/IOFF ratio, thereby contributing to the ongoing evolution of next-generation transistor technology. Gate-all-around FETs, also referred to as nanowire FETs, offer an effective solution to combat short channel effects by utilizing a three-dimensional gate structure [83], [116], [117]. These devices encircle the channel entirely, resulting in enhanced electrostatic control and improved gate-to-channel coupling [118].

Altering doping levels in FET-based biosensors significantly impacts parameters like threshold voltage, current, and subthreshold swing [119], directly affecting the device's response to biomolecule variations. Higher source doping increases charge carriers, reducing threshold voltage and boosting on-current, but it also diminishes subthreshold swing sensitivity; meanwhile, channel doping primarily influences threshold voltage and subthreshold swing with a lesser impact on sensitivity, notably concerning these metrics as sensing parameters [120], [121].

When making small-scale devices, the silicon dioxide (SiO_2) gate insulator should be replaced with a high-k dielectric gate oxide material, such as hafnium oxide, while maintaining appropriate oxide thickness (EOT) as a constant [122]. Hetero Dielectric structure in which combinations of low dielectric material together with high dielectric materials are utilised for FETs have been reported in literature to boost ON current [123] and reduce the OFF state leakages [64], [124]. Nanometer sized biomolecules are detectable using Gate-All-Around Field Effect Transistor (GAAFET) based sensors [92], [125], [126]. Gate engineering in GAAFETs refers to the deliberate design and optimization of the gate structure to enhance the device performance and control the flow of charge carriers within the channel [127]–[129]. Joshi et.al proposed

a novel trench-gate tunnel field-effect transistor that demonstrates notable enhancements in both the switching ratio and subthreshold swing [130]. For the label-free detection of biomolecules, Kumar et al. proposed the dielectric modulated trench double gate junctionless FET (DM-TDGJLFET), which has improved threshold voltage sensitivity for both neutral and charged biomolecules [96].

In this study, the electrical characterization of the Dielectric Modulated FET biosensor has been conducted in an air environment. This approach is consistent with previous experimental research in the field, where electrical characterization in an air environment has been achieved through a sequence of de-ionized water washing and dry nitrogen blowing procedures. These steps ensure the removal of any charged particles or contaminants that might influence the measurements, while still preserving the biological functionality of the analytes being studied [107], [131]–[133].

2.1.1 Junctionless versus Junction Accumulation Mode FET

Junctionless Gate-All-Around FET are the most promising contender because of their resistance to short-channel effects (SCEs) and the random dopant profile effect [122], [134]. The Junctionless FET device architecture eliminates the need for metallurgical junctions, thereby eliminating the ultra-steep doping profile required between the source/drain and channel regions, along with the complex thermal budget requirements associated with it [28]. But, Junctionless FETs face challenges including high source-drain resistance, lower mobility, and band-to-band tunnelling [135] in the OFF state [136]. An alternative, Junction Accumulation Mode FET, offers low source/drain resistance due to higher doping in source/drain regions and improved carrier mobility through reduced channel doping [137]–[140]. Junction Accumulation Mode FETs offer significant advantages over conventional MOSFETs and TFETs. They simplify fabrication, excel in gate control, enhance scaling potential, reduce junction-related defects for improved reliability, and promise lower-voltage operation with reduced leakage [141].

2.1.2 Hetero Dielectric Structure

The continuous scaling of MOSFET devices presents numerous crucial issues, such as the occurrence of short channel effects (SCEs) and leakage currents. In addition, it is important to note that the scaling of the device is not restricted to just altering the length and breadth of the channel. It also offers the ability to scale the thickness of the SiO₂ layer, which is beneficial for incorporating the device into low power, high performance CMOS applications. In principle, this is accomplished by lowering down on the gate dielectric's thickness, which increases capacitance of gate and subsequently enhances the ON current. In addition, when the oxide thickness is reduced to less than 2 nm due to downsizing, the tunneling effect causes a significant increase in leakage currents. This results in a decrease in the dependability of the device and an increase in power consumption, which is clearly undesirable. Since its inception, silicon dioxide (SiO₂) has been the favoured material for the gate insulator of silicon-based MOSFETs. Over time, the thickness of the oxide has decreased from 300 nm to 1.2 nm. There are two primary motivations for the persistent effort to decrease the thickness of the oxide layer. Initially, a decrease in oxide thickness results in an

increase in gate capacitance (C_{ox}), which in turn leads to an increase in on-current (I_{ON}). A larger I_{ON} is advantageous for optimizing circuit speed. The second purpose is to regulate the decrease in threshold voltage (ΔV_{th}) (and consequently the amount of leakage) in devices with short channel lengths. When the thickness of SiO_2 films is less than 1.5 nm, the most significant limiting factor is the tunneling leakage current. An additional constraining element is the extended duration of operation under high field conditions, particularly at elevated chip operating temperatures. This leads to the rupture of the less robust atomic bonds at the Si/ SiO_2 interface, resulting in the generation of oxide charge and a shift in threshold voltage (V_{th}). An effective approach to counteract this phenomenon is to employ a dielectric substance with a greater dielectric permittivity than SiO_2 . The achievement of a significant physical thickness at a small Effective Oxide Thickness (EOT) is made possible by these materials, which makes it easier to scale the EOT for upcoming MOS generations. The EOT, or equivalent oxide thickness, is the measure of the thickness of a SiO_2 layer that has the same capacitance as the high-k dielectric layer [142]–[145]. The utilization of high-k dielectrics enhances the gate's capacity to regulate the channel. However, their effectiveness is hindered by the presence of undesirable levels of interface traps, bulk fixed charges, limited interface carrier mobility, and phase stability problems. Given that none of the other dielectric materials naturally produce an oxide layer on silicon, it is difficult to prevent the formation of a thin SiO_2 layer at the interface. Currently, a common configuration for these new dielectrics consists of a small layer of SiO_2 acting as a layer that exists between surfaces, stacked with a thick high-k layer. The gate electrode can be either poly-Si or metal [142].

2.1.3 Trench Gate

A transistor's gate electrode's particular configuration and structure is referred to as trench gate architecture in FET designs. Trenches are made by etching the semiconductor material to produce the gate electrode in this architecture [96]. Gate can also be formed by etching the trenches into the dielectric material [146]. Trench gate design enables enhanced regulation of the conductivity in the channel, resulting in superior performance and scalability in FET devices [147]. This architecture enables a greater number of channels to be packed into each silicon unit, resulting in a decrease in the particular R_{DS} (resistance of the MOSFET per unit area) and an enhancement in the overall device performance [147]. In addition, the trench gate architecture has the ability to decrease the input and Miller capacitances. This reduction results in a lower input gate charge and shorter voltage transients during switching. Consequently, there is a decrease in switching losses in power management applications [147]. However, there are a few challenges with trench gate construction. When the area of the trench wall is significant, it might lead to a large value of capacitors that are integrated into the structure. If the trench bottom overlaps with the epitaxial layer, which is part of the drain terminal, it can result in a substantial gate-to-drain capacitance (C_{GD}) [147]. This can pose a notable drawback, especially in applications that require quick switching. In conclusion, the trench gate architecture is a significant improvement in field-effect transistor (FET) designs, offering better performance and scalability compared to traditional planar gate layouts.

In a trench gate nanowire FET, there is a nanowire as the channel region and a trench gate structure to regulate the current flow. This design offers several advantages, such as improved control over the channel region, reduced leakage current, and increased driving current. The gate electrode of a trench gate nanowire FET is positioned within a trench that encircles the nanowire channel. The trench gate structure offers an expanded gate area, enabling superior regulation of the channel region and minimizing leakage current. Several examples of trench gate MOSFET are present in literature. Fig. 2.1 (a) demonstrates the cross-sectional view of trench gate [148] in a conventional MOSFET and Fig. 2.1 (b) depicts the cross-sectional view of trench gate TFET biosensor [149].

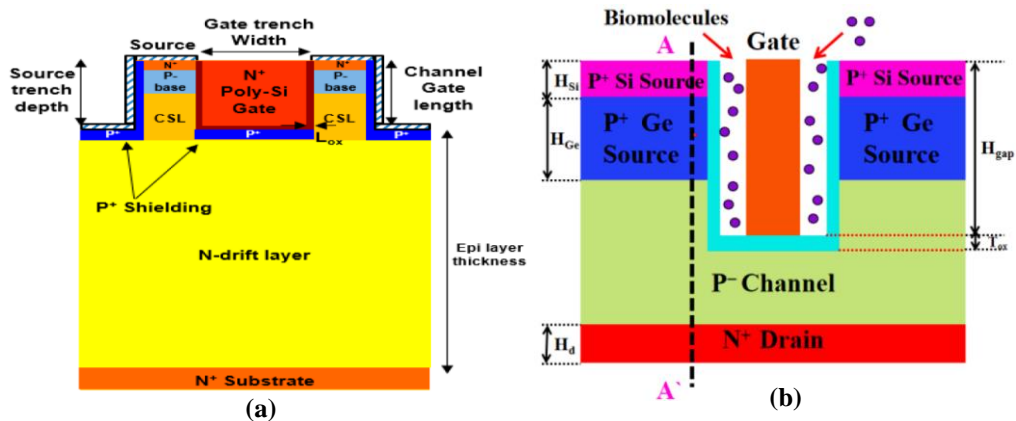


Fig. 2.1 (a) Cross-sectional View of Trench Gate MOSFET [148] (b) Cross-sectional View of Trench Gate TFET Biosensor [149]

2.1.4 Gate-All-Around FET

In GAA MOSFET [16], [17], the gate is wrapped around a silicon channel. The shape of the channel might range from narrow to large, and can be square, rectangular, circular, or have various orientations. Studies [18] illustrates that this excess electrostatic confinement, allows the Gate-All-Around MOSFET to be scaled to about 50% more as compared to the double gate FET which has been experimentally proved by Leobandung et al. [150]. This characteristic may be utilized to soften the need of the oxide and the silicon layer thickness for a given gate length.

2.2 Hetero Dielectric Trench Gate Junction Accumulation Mode Gate-All-Around FET (HDTG-JAM-GAAFET) Biosensor: Device architecture and Simulation Environment

A three-Dimensional view of the proposed HDTG-JAM-GAAFET is shown in Fig. 2.2 (a), depicting the outer part of the gate, HfO₂, and SiO₂ layers, and source and drain extensions. The work function for the gate material employed is 5.1 eV. Fig. 2.2 (c) shows the 2D perspective of the proposed device, clearly depicting the trench structure in the device and etched cavities for biomolecule immobilization. HDTG-JAM-

GAAFET has a combination of SiO_2 and HfO_2 to be used as a hetero-dielectric layer on the silicon semiconductor. Then, a trench-shaped structure is formed to place a part of the gate electrode. This trench is created by etching the HfO_2 dielectric material, and the gate electrode is subsequently placed inside the trench. This results in a gate structure that is also positioned vertically to the semiconductor's surface, enabling enhanced regulation of the channel area. Various device dimensions and other characteristics parameters for the proposed HDTG-JAM-GAAFET and Normal Gate JAM Gate-All-Around FET are mentioned in Table 2.1. The proposed device and the Normal Gate JAM Gate-All-Around FET biosensor structure have identical device specifications, with the exception of the trench section of the Gate. The proposed device is simulated with the Atlas-3D device simulation tool [151]. Several models, including AUGER and SRH for recombination of minority carriers under semiconductors, FLDMOB and CONMOB (concentration-dependent mobility) for mobility, and BGN (band gap narrowing) for carrier statistics to verify the doping versus mobility and high channel doping profile were employed in the simulation process [151].

The simulation setup in this work is calibrated based on experimental data for the Gate-All-Around junctionless FET [152]. Fig. 2.2 (b) illustrates a strong correspondence between the simulated and experimental results [152] for the drain current as a function of gate voltage.

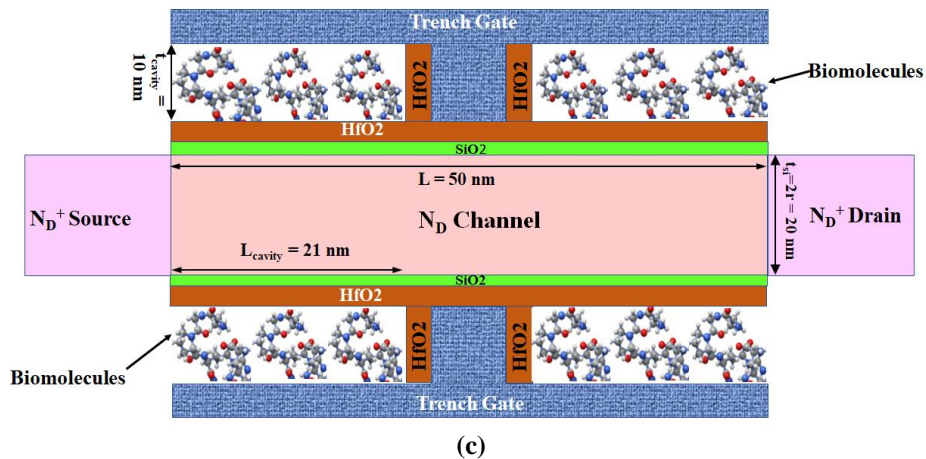
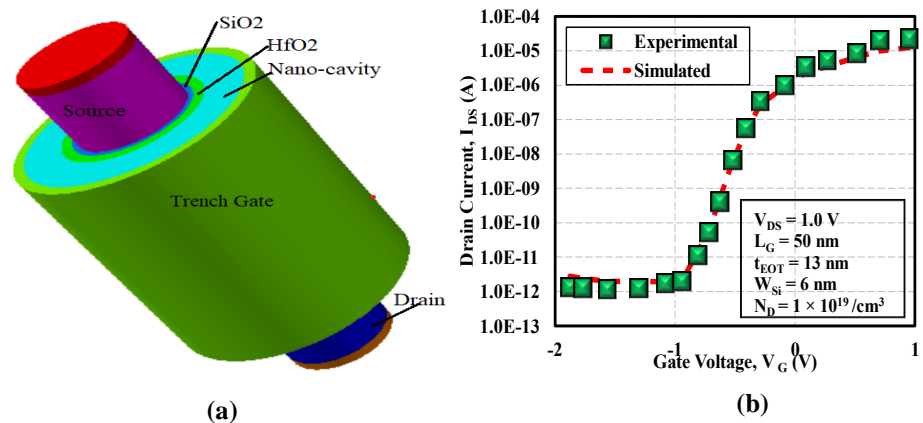


Fig. 2.2 (a): 3-Dimensional View of HDTG-JAM-GAAFET [153] (b) Calibration of simulation setup with experimental data [153] (c) 2- Dimensional View of HDTG-JAM-GAAFET [153]

The process of placing biomolecules within a nanogap is commonly referred to as immobilization. The immobilization process involves techniques to attach the biomolecules to the dielectric layer of the FET, allowing them to recognize and interact with the target analytes. Immobilization techniques can vary and include Covalent Binding, Crosslinking, Entrapment, Adsorption, and Affinity Binding techniques depending on the specific FET biosensor design and the nature of the biomolecules and analytes involved [154]–[156]. These techniques, along with careful design and engineering of the sensor platform, contribute to the successful and accurate placement of biomolecules inside the nanogap of dielectric modulated FET biosensors, enhancing their performance for sensitive and selective detection of target analytes. Neutral biomolecules employed in this work for detection include streptavidin ($K = 2.1$), biotin ($K = 2.63$), ferro-cytochrome c ($K = 4.7$), keratin ($K = 8$), and gelatin ($K = 12$) [96]. The effects of DNA hybridization at various concentrations in the nanocavity are considered to be represented by positive surface charge density from $Q_f = 1 \times 10^{11}$ to 2×10^{12} and negative surface charge density from $Q_f = -1 \times 10^{11}$ to -1×10^{12} [157].

Table 2.1 Various Device Dimensions and Characteristics Parameters [153]

Device Dimensions and other parameters	HDTG-JAM-GAAFET	NG-JAM-GAAFET
Channel Length (nm)	50	50
Thickness of Silicon Film (nm)	20	20
Length of Source/Drain (nm)	15	15
Metal gate work-function (eV)	5.1	5.1
Oxide Thickness	SiO ₂ Layer: 1 nm	SiO ₂ Layer: 1 nm
	HfO ₂ 1 st Layer: 2 nm	
	HfO ₂ 2 nd Layer: 10 nm	HfO ₂ Layer: 2 nm
Doping of Channel Region, N_D (/cm ³)	1×10^{18}	1×10^{18}
Doping of Source and Drain Region N_{D+} (/cm ³)	1×10^{19}	1×10^{19}
Thickness of Cavity (nm)	10	10
Thickness of Trench part of Gate (nm)	10	-
Length of Cavity (nm)	21	21
HfO ₂ and SiO ₂ dielectric constants	25.0 & 3.9	25.0 & 3.9

The proposed fabrication process sequence is outlined in the flowchart displayed in Fig. 2.2 (d). Initial steps in the fabrication [158] of the biosensor include substrate preparation, silicon epitaxial growth, sacrificial layer deposition, gate dielectric deposition [141], [159] using methods like thermal oxidation or chemical vapor

deposition (CVD), gate electrode deposition using methods like PVD or CVD [160] and Gate-All-Around nanowire FET formation [161], [162], which will function as the biosensor's sensing element [160].

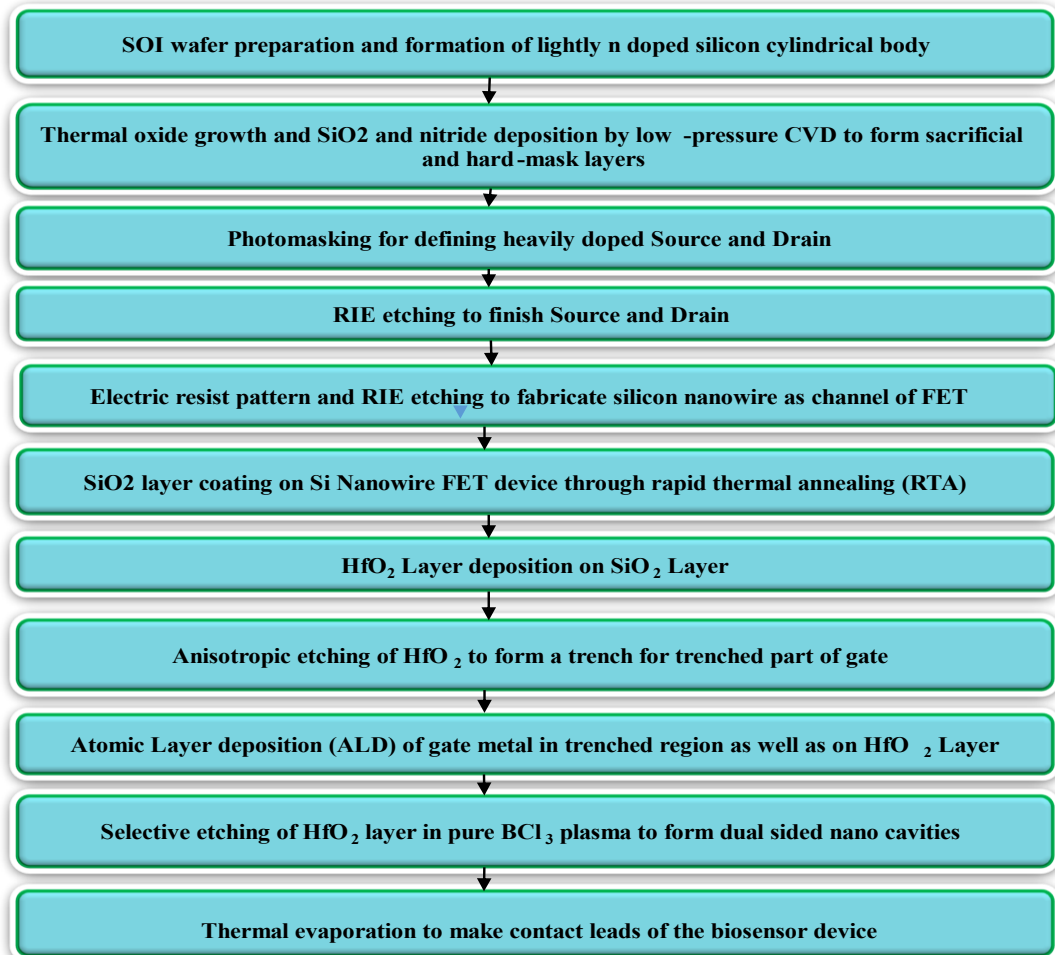


Fig. 2.2 (d) Proposed Fabrication Process Flow of HDTG-JAM-GAAFET Biosensor [153]

Table 2.2 Dielectric constant and charge densities of biomolecules used in analysis of HDTG-JAM-GAAFET [153]

S.No.	Biomolecule	Dielectric Constant	Type of Biomolecule
1	Streptavidin	2.1	Neutral ($Q_f = 0 / \text{cm}^2$)
2	Biotin	2.63	Neutral ($Q_f = 0 / \text{cm}^2$)
3	Ferro-cytochrome c	4.7	Neutral ($Q_f = 0 / \text{cm}^2$)
4	Keratin	8	Neutral ($Q_f = 0 / \text{cm}^2$)
5	Gelatin	12	Neutral ($Q_f = 0 / \text{cm}^2$)
6	DNA	1 – 64	Charged (positive from $Q_f = 1 \times 10^{11}$ to $2 \times 10^{12} / \text{cm}^2$ and

			negative from $Q_f = -1 \times 10^{11}$ to $-1 \times 10^{12} / \text{cm}^2$
--	--	--	--

The biomolecules that the HDTG-JAM-GAAFET biosensor is designed to detect, including both neutral and charged species, are provided in Table 2.2. The dielectric characteristics of biomolecules may be impacted by surrounding factors such as temperature, plasticizer concentration, and moisture content [163]. Moreover, it has been considered that biosensing takes place in a controlled environmental condition.

2.3 Results and Discussion

2.3.1 Electrostatic behaviour of HDTG-JAM-GAAFET biosensor

As illustrated in Fig. 2.3 (a), the surface potential decreases with the immobilization of biomolecules as contrast to the case when no biomolecules are present into the nanocavity. This happens because as the dielectric constant increases, the vertical gate to channel capacitance increases, leading to effective gate capacitance enhancement, boosting gate control, which results in a reduction in surface potential [164], [165].

Fig. 2.3 (b) demonstrates channel potential for various charge concentrations of the biomolecules, which are classified into three categories: uncharged biomolecules (neutral, $K=12$), positively charged biomolecules (1×10^{11} , 5×10^{11} , and $1 \times 10^{12} \text{ cm}^{-2}$), and negatively charged biomolecules (-1×10^{11} , -5×10^{11} , and $-1 \times 10^{12} \text{ cm}^{-2}$). When negatively charged biomolecules are injected into the nanocavity, the minima of surface potential (Ψ_c) lowers, but (+)vely charged biomolecules raise the minima of surface potential (Ψ_c). This is due to the fact that these biomolecules are electrically associated with the rooted silicon and attain a specific energy level known as interface state energy level (E_{IT}), which places itself according to the fermi level (E_F) as follows [132], [166]:

$$E_{IT} > E_F \quad \text{for positively charged biomolecule} \quad (2.1)$$

$$E_{IT} < E_F \quad \text{for negatively charged biomolecule} \quad (2.2)$$

The flat band voltage (V_{FB}) rises with the insertion of (-) vely charged biomolecules and falls with the inclusion of (+) vely charged biomolecules by $\frac{qQ_f}{C_G}$. Where, C_G is Capacitance / unit area of the gate dielectric, and Q_f represents interface charge density for charged biomolecules [167]. When there is a significant change in the flat band voltage, band bending occurs. Consequently, the Gate voltage experiences variations and the Ψ_c undergoes a shift [90]. The threshold voltage is modulated by changes in surface-potential minima. However, the threshold voltage (V_{TH}) for charged biomolecules changes distinctively [168] contrasted to neutral biomolecules as in Fig. 2.3 (c) and 2.3 (d). The calculation of threshold voltage in Fig. 2.3 is based on Linear Extrapolation (LE) method in which the threshold voltage is defined as The gate voltage at which the tangent path, defined at the spot with the maximum slope on the $I_D - V_G$ curve, intersects the voltage axes [169].

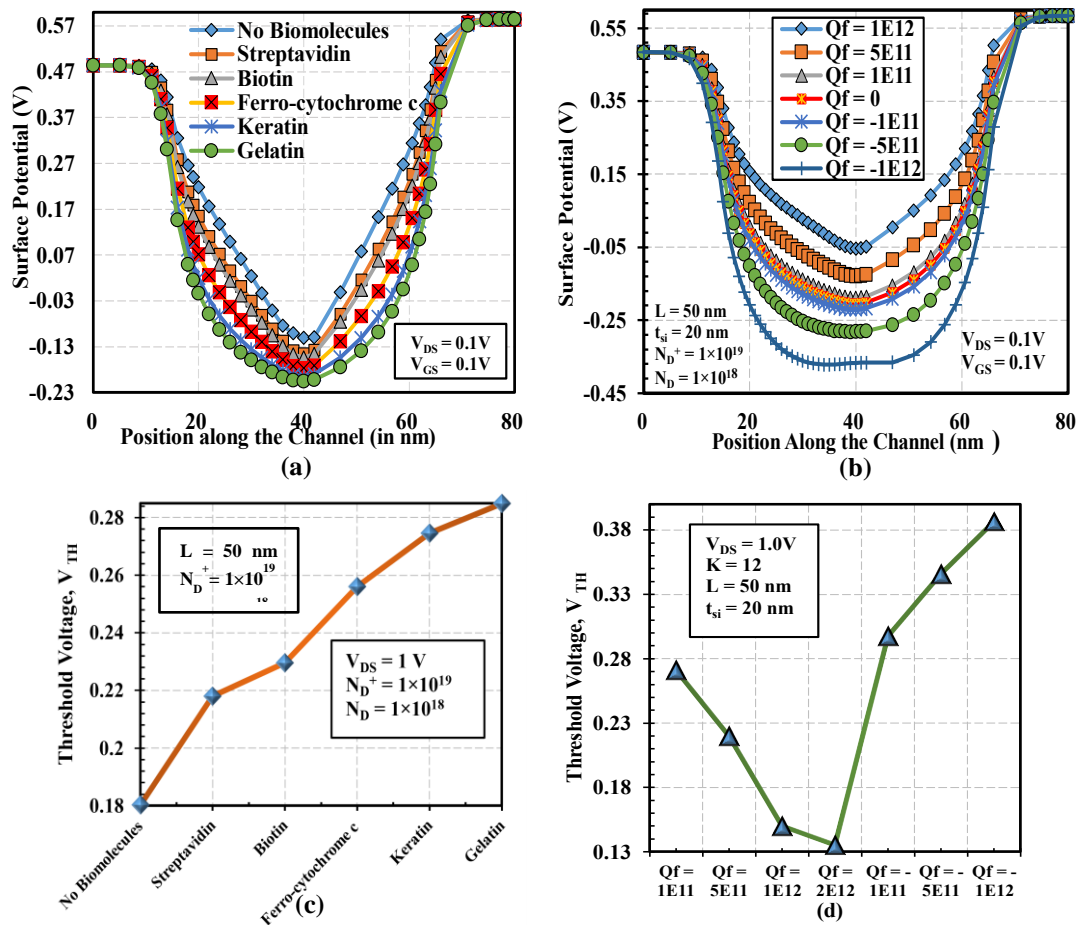


Fig. 2.3 (a) Surface Potential for the Case of Neutral Biomolecule Analytes [153] (b) Surface Potential for the Case of (+)vely and (-)vely Charged Biomolecules [153] (c) V_{TH} Variation for Various Neutral Biomolecules [153] (d) V_{TH} Variation for DNA Biomolecules [153]

In the subthreshold region, the contour plots of the electron concentration for neutral and charged biomolecules are displayed in Fig. 2.4 and Fig. 2.5. According to concentration profile in Fig. 2.4, the electron concentration in channel region decreases as various neutral biomolecules with higher dielectric constants are added. Additionally, the trench part of the gate further reduces the electron concentration in the layer beneath it, forcing an increase in the device's threshold voltage with an increase in K . While for charged biomolecules, as depicted in Fig. 2.5, the electron concentration rises for (+)vely charged biomolecules and falls for (-)vely charged ones, imposing a higher threshold voltage for (-)vely charged biomolecules and a lower threshold voltage for positively charged ones.

Fig. 2.6 depicts the contour plots for electron velocity with varying biomolecules species for $V_{GS} = V_{DS} = 0.1\text{ V}$. The electron velocity reduces as we introduce biomolecules from streptavidin to gelatin, resulting in a reduction in device OFF current which can be clearly inferred from the contours.

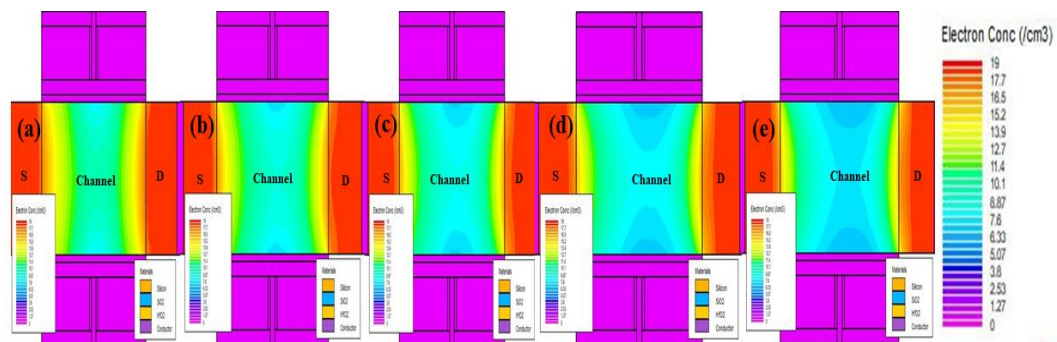


Fig. 2.4 Contour Plots of Electron Concentrations of Proposed Device for Neutral Analytes [153] (a) No Biomolecules ($K=1$) (b) Biotin (c) Ferro-cytochrome c (d) Keratin (e) Gelatin

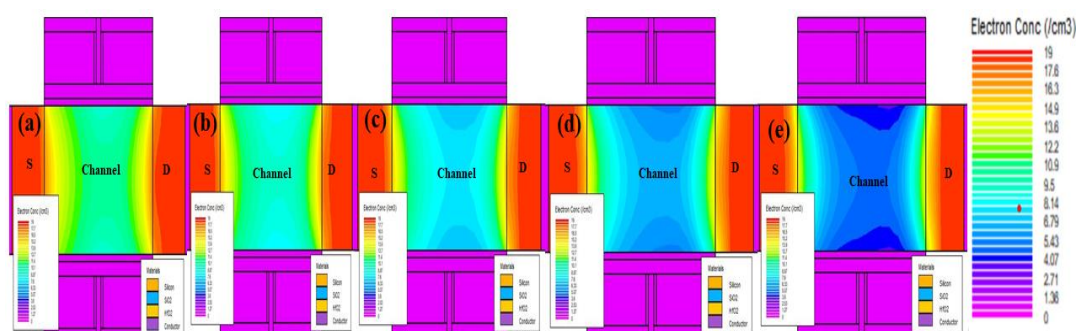


Fig. 2.5 Contour Plots of Electron Concentrations of Proposed Device for Charged Analytes [153] with Constant Dielectric Constant, $K=12$ and (a) $Q_f = 1 \times 10^{12} \text{cm}^{-2}$ (b) $Q_f = 5 \times 10^{11} \text{cm}^{-2}$ (c) $Q_f = 0$ (d) $Q_f = -5 \times 10^{11} \text{cm}^{-2}$ (e) $Q_f = -1 \times 10^{12} \text{cm}^{-2}$

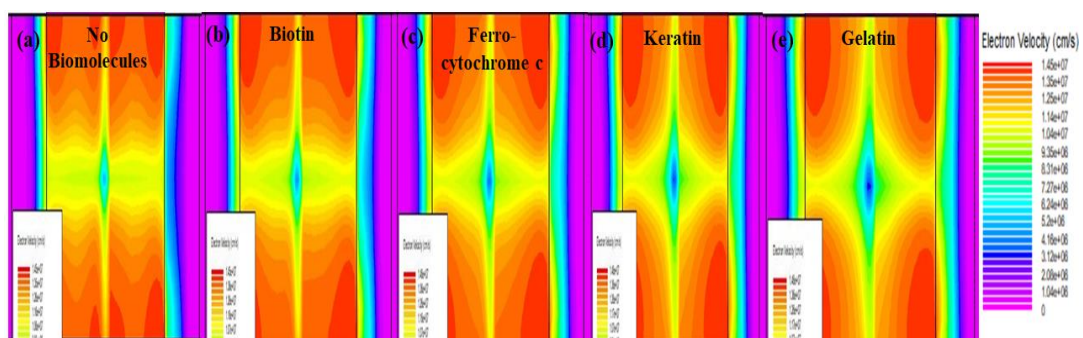


Fig. 2.6 Contour Plots of Electron Velocity in Channel Region of Proposed Device for Neutral Analytes [153] (a) No Biomolecules ($K=1$) (b) Biotin (c) Ferro-cytochrome C (d) Keratin (e) Gelatin

Fig. 2.7 (a) and Fig. 2.7 (b) depicts drain Characteristics of proposed biosensor for neutral and charged biomolecules inserted. As demonstrated in Fig. 2.7 (a), the drain ON current which is measured at $V_{GS} = V_{DS} = 1.0 \text{V}$ [121], significantly increases following the immobilization of several neutral biomolecules, including streptavidin, biotin, ferro-cytochrome c, keratin, and gelatin [96], [157]. This happens because the flat band voltage in nano-cavity is affected by the changing dielectric constant of various biomolecules, which changes the surface potential and, ultimately, the drain current [170]. The I_{ON} of the device is $7.65 \times 10^{-6} \text{A}$ for no biomolecules case, whereas it is $9.13 \times 10^{-6} \text{A}$ when gelatin is present. As a result, the current deviation is 19.3%.

The I_{ON} current varies differently for positive and negative biomolecules in the case of charged biomolecules as shown in Fig. 2.7 (b). As contrast to the condition when the biomolecules have no charge, the I_{ON} current rises for positively charged biomolecules and falls for negatively charged ones. In terms of percentage change, the I_{ON} value for $Q_f = 1 \times 10^{12}$ increased by 104.41%, whereas $Q_f = -1 \times 10^{12}$ have seen an I_{ON} value decline by 86%.

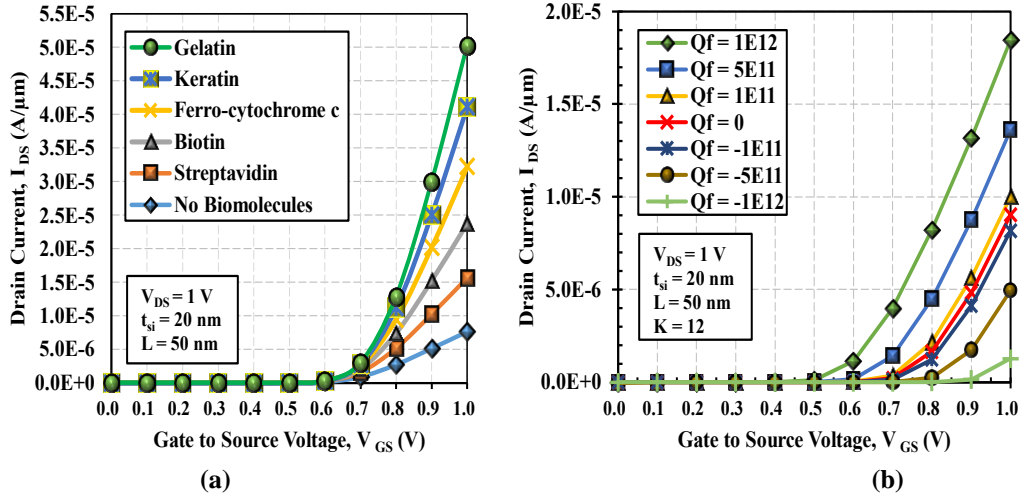


Fig. 2.7 (a) I_D - V_{GS} Characteristics of HDTG-JAM-GAAFET Biosensor for Neutral Biomolecules (b) I_D - V_{GS} Characteristics of HDTG-JAM-GAAFET Biosensor for Charged Biomolecules [153]

Furthermore, we assess the biosensor's sensitivity by evaluating a specific sensing parameter, following the suggestions outlined in prior literature [171]. This method leverages the transconductance fluctuation parameter to show a significant difference for biomolecules with different dielectric constants and different charge concentrations, leading to reduced power dissipation for biosensing applications. Transconductance is a metric that indicates how effectively a device transforms voltage to current. Transconductance (g_m) is calculated numerically using equation (2.1) [157]:

$$g_m = \left. \frac{\partial I_{DS}}{\partial V_{GS}} \right|_{V_{DS}=\text{constant}} \quad (2.3)$$

Where, I_{DS} , V_{GS} and V_{DS} are drain to source current Gate to Source Voltage and Drain to Source Voltage respectively. The peak transconductance value rises as high-dielectric constant biomolecules are immobilized in the nanocavity of the proposed device, as shown in Fig. 2.8 (a), and there is a large drift in g_m as these neutral biomolecules are added. As illustrated in Fig. 2.8 (b), transconductance increases with positive charged biomolecules and decreases with negative charged biomolecules. This is due to a shift in channel potential, which is upward for positive biomolecules and downward for negative ones, as already mentioned in Fig. 2.3 (b).

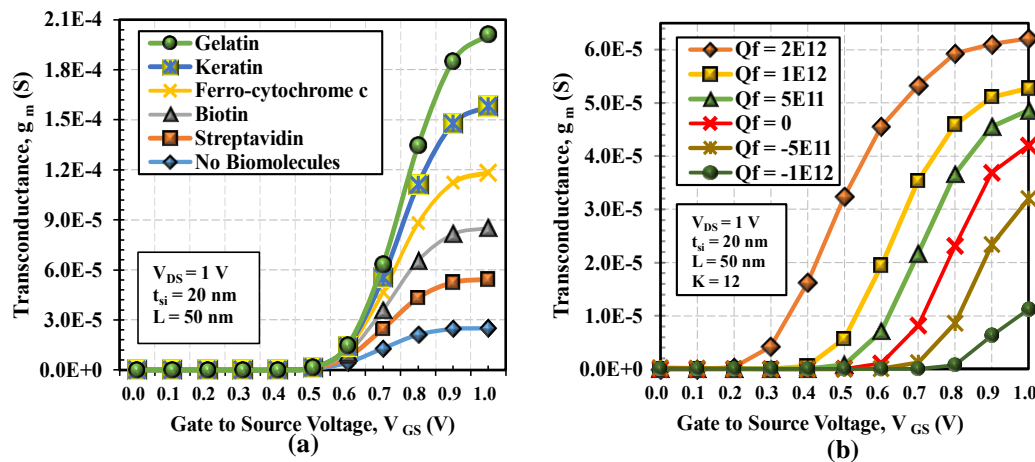


Fig. 2.8 (a) Transconductance of HDTG-JAM-GAAFET Biosensor for Neutral Biomolecules [153] (b) Transconductance of HDTG-JAM-GAAFET Biosensor for Charged Biomolecules [153]

2.3.2 Comparative investigation of electrical performance Properties of HDTG-JAM-GAAFET biosensor

The effect of biomolecules on drain OFF current (I_{OFF}) or leakage current for proposed HDTG-JAM-GAAFET device and Normal Gate-JAM-GAAFET biosensor, is depicted in Fig. 2.9. I_{OFF} is the leakage current when V_{GS} is below the threshold voltage. According to Fig. 2.9, I_{OFF} falls as the dielectric constant rises because the larger the dielectric constant of biomolecules, the better the gate electrostatic controllability due to lower electron tunnelling out of the gate [172]. This is due to the fact that a higher K dielectric oxide inhibits reverse tunnelling current by forming a potential barrier in the channel [172].

Out of the mentioned two devices, the proposed device has reduced I_{OFF} values in both the absence and presence of biomolecules. For instance, the I_{OFF} current for proposed HDTG-JAM-GAAFET biosensor is 6.15×10^{-16} A and 2.06×10^{-17} A, while the I_{OFF} current for NG-JAM-GAAFET biosensor is 2.35×10^{-12} A and 3.33×10^{-16} A for no biomolecule and ferro-cytochrome c, respectively. Thus, the proposed biosensor device promises to have a lower OFF current and reduced short channel effects when compared to the NG- JAM-GAAFET.

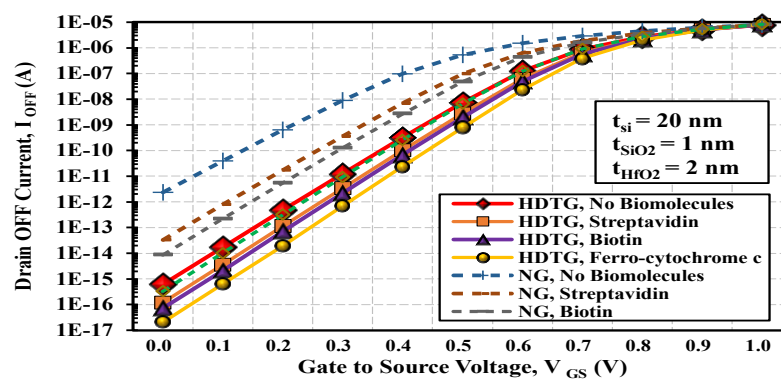


Fig. 2.9 I_{OFF} Current Variation for HDTG-JAM-GAAFET and NG-JAM-GAAFET Biosensor [153]

The speed at which a device can flip between the ON and OFF states is known as the switching ratio (I_{ON}/I_{OFF}) and it is another crucial metric for a device to be employed in digital applications. When expressed mathematically, the switching ratio is [89]:

$$\frac{I_{ON}}{I_{OFF}} = \frac{I_{DS(ON) \text{ at } V_{GS}=1.0V}}{I_{DS(OFF) \text{ at } V_{GS}=0.0V}} \quad (2.4)$$

For faster switching and subsequently higher digital performance, this ratio must be higher. For the two biosensor devices, Fig. 2.10 illustrates the I_{ON}/I_{OFF} ratio for several biomolecules, including ferro-cytochrome c, biotin, and streptavidin. The I_{ON}/I_{OFF} ratio is significantly higher in the HDTG-JAM-GAAFET biosensor compared to the NG-JAM-GAAFET biosensor due to a significant decrease in I_{OFF} and an increase in I_{ON} current with an increase in the dielectric constant (K) value of biomolecules as a result of improved trench gate control over the channel, which increases the potential barrier height and improved channel's conductivity thanks to its hetero dielectric structure.

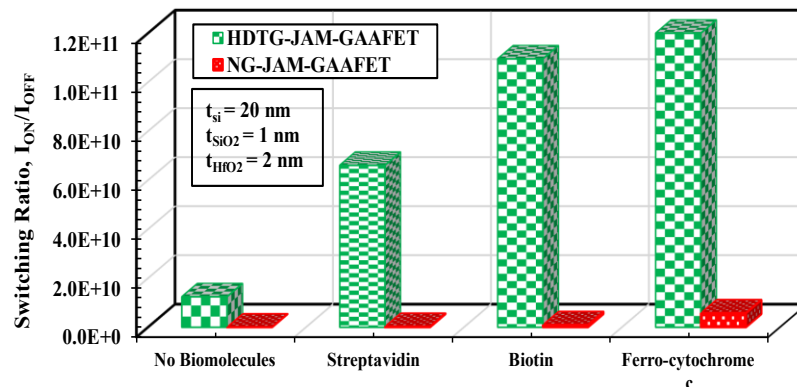


Fig. 2.10 Comparative Study of Switching Ratio (I_{ON}/I_{OFF}) of HDTG-JAM-GAAFET Biosensor and NG-JAM-GAAFET Biosensor [153]

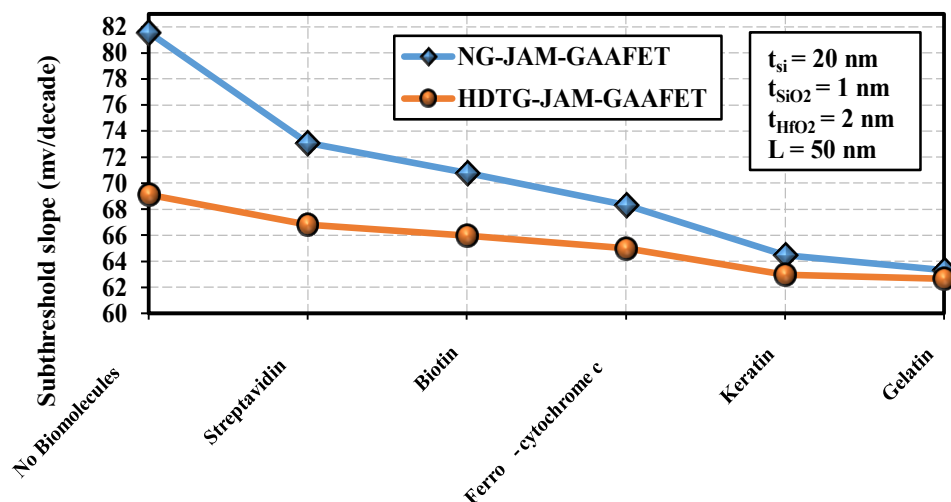


Fig. 2.11 Variation of Subthreshold Slope for HDTG-JAM-GAAFET and NG-JAM-GAAFET Biosensor [153]

Subthreshold slope (SS), which is measured in mV/decade, is used to track the device's turn-on characteristics. Better channel control and, consequently, a higher I_{ON}/I_{OFF} current ratio are achieved with lower SS values [172]. According to Fig. 2.11, biomolecules affect the subthreshold slope in both devices. Subthreshold swing decreases as the dielectric constants of various biomolecules rise because metal work function and the dielectric constant of biomolecules modulate gate control by reducing the threshold voltage roll-off of the channel [146]. The subthreshold slope of the proposed HDTG-JAM-GAAFET biosensor is 69.13 mV/decade, which is 18% less than that of the normal gate JAM-GAAFET biosensor and much closer to the ideal 60 mV/decade for FET devices. We can therefore draw the conclusion that the proposed biosensor has much better turn-on characteristics.

The impact of the neutral analytes streptavidin and gelatin on the output conductance, for both HDTG-JAM-GAAFET and NG-JAM-GAAFET is shown in Fig. 2.12 (a). When V_{GS} is constant at 1.0 V, the output conductance (g_d) analyzes the drain current's first-order derivative with respect to drain to source voltage (V_{DS}). It is evident from Fig. 2.12 (a) that the lower drain-induced barrier lowering (DIBL), short-channel effect, and parasitic resistance under the hetero dielectric trench Gate-All-Around device cause the HDTG-JAM-GAAFET device to exhibit high output conductance (g_d) than the Normal Gate - JAM-GAAFET.

For the HDTG-JAM-GAAFET and NG-JAM-GAAFET biosensors, Fig. 2.12 (b) illustrates the change in the Channel Resistance (R_{ch}) with V_{GS} for the presence and absence of biomolecules scenarios. To ensure higher drain currents and better analog performance, lower R_{ch} is preferred. The R_{ch} is noticeably low for the proposed device, as indicated by the solid lines in Fig. 2.12 (b). With the introduction of gelatin biomolecule into the cavity of either biosensor, the R_{ch} value decreases, ensuring high drain current with the immobilization of biomolecules. However, the proposed device's variation in R_{ch} is greater, contributing to its high I_{ON} sensitivity.

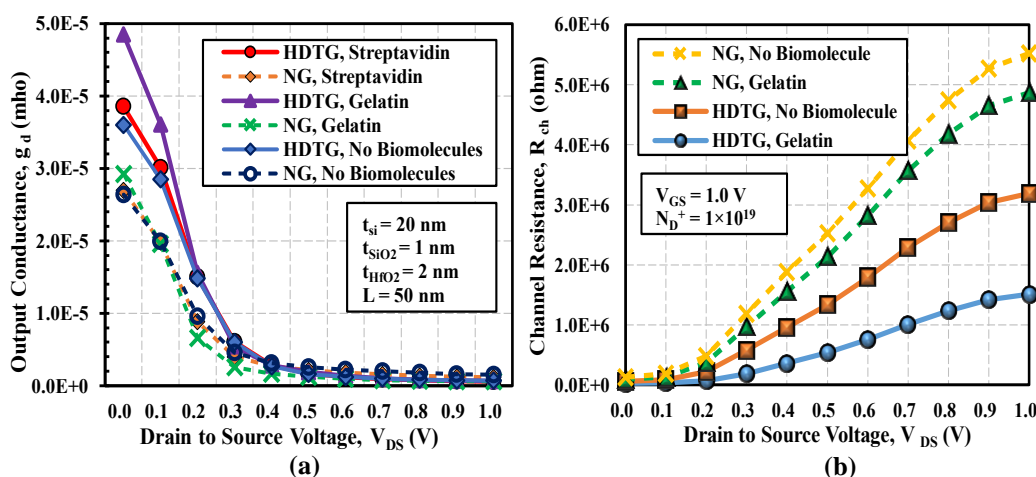


Fig. 2.12 (a) Variation of output conductance (g_d) with drain voltage [153] (b) Variation of Channel Resistance (R_{ch}) for HDTG-JAM-GAAFET biosensor and NG-JAM-GAAFET [153]

The intrinsic dc gain ($A_{V_{int}}$) of a FET is expressed as the ratio of transconductance (g_m) to output conductance (g_d). Mathematically, $A_{V_{int}}$ is expressed as:

$$A_{V_{int}} = \frac{g_m}{g_d} \quad (2.5)$$

It is a crucial operational transconductance amplifier characteristic. Moreover, it provides a bias point to provide a significant gain without endangering the device's linearity [172]. The proposed HDTG-JAM-GAAFET biosensor has a higher intrinsic gain than the conventional gate-JAM-GAAFET biosensor, as can be seen from Fig. 2.13. Hence, even with high gain, the proposed biosensor device assures more linear operation. Additionally, as we introduce biomolecules to the nanocavity, the intrinsic gain continues to rise in comparison to the situation in which there were no biomolecules in the cavity for both the devices. The increase in intrinsic gain is higher in the case of the proposed HDTG-JAM-GAAFET, indicating a higher intrinsic gain sensitivity of the device.

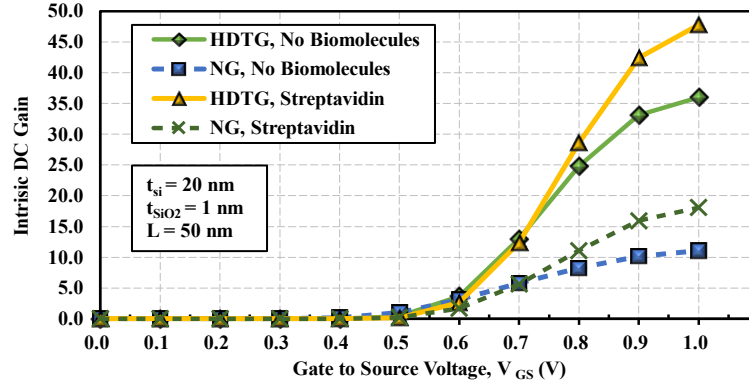


Fig. 2.13 Variation of Intrinsic Gain ($A_{V_{int}}$) with the gate to source voltage (V_{GS}) for HDTG-JAM-GAAFET and NG-JAM-GAAFET biosensor [153]

2.3.3 Biomolecules' effects on Current sensitivity of Proposed Biosensor

Sensitivity is utilized to identify a biomolecule's existence or absence. The biosensor's sensitivity (S) is expressed in general terms as follows [173]:

$$S = \left| \frac{P_{bio} - P_{air}}{P_{air}} \right| \quad (2.6)$$

Where, P_{bio} represents the electrical parameter value when biomolecules are immobilized in the cavity, while P_{air} represents the electrical parameter value when there are no biomolecules in the cavity.

The sensitivity of the device can be assessed by contrasting the current value in the presence of particular biomolecules with the current value when the biomolecules are missing from the cavity. The formulas for I_{ON} current deviation, (ΔI_{ON}) and I_{ON} current sensitivity ($S_{I_{ON}}$) are as follows [174]:

$$\Delta I_{ON} = I_{ON[With\ biomolecules]} - I_{ON[Without\ biomolecules]} \quad (2.7)$$

$$S_{I_{ON}} = \frac{I_{ON[\text{With biomolecules}]} - I_{ON[\text{Without biomolecules}]}}{I_{ON[\text{Without biomolecules}]}} \quad (2.8)$$

Fig. 2.14 (a) illustrates the influence of several biomolecule species with differing dielectric constants on the normalized I_{ON} sensitivity ($S_{I_{ON}}$) for the proposed HDTG-JAM-GAAFET biosensor and NG-JAM-GAAFET biosensor. Fig. 2.14 clearly shows that the proposed HDTG-JAM-GAAFET biosensor, which has greater trench gate structural control over the channel, has higher I_{ON} current sensitivity than the NG-JAM-GAAFET for all the biomolecules taken into account.

Fig. 2.14 (b) shows the % I_{ON} current sensitivity of the both the devices for varying positive and negative charges on the DNA biomolecules. Dielectric constant of DNA lies between 1 to 64. So here a fixed dielectric constant $K = 12$ have been considered for sensitivity calculations. Mathematically, the sensitivity is expressed as [99]:

$$\% SC_{I_{ON}} = \left| \frac{I_{ON(\text{neutral})} - I_{ON(\text{charged})}}{I_{ON(\text{neutral})}} \right| \times 100 \quad (2.9)$$

As depicted by Fig. 2.14 (b), the sensitivity ($SC_{I_{ON}}$) is higher for the proposed device for both positive and negative charge on the DNA biomolecule. This happens because the immobilization of charged biomolecules make distinctive trench gate structure to control the potential barrier more efficiently in the ON-state, increasing the drain current deviation.

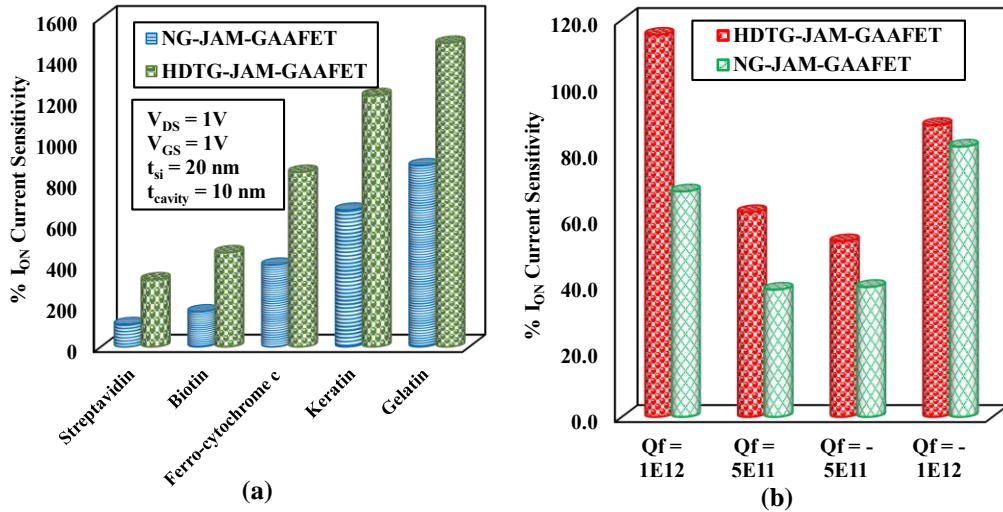


Fig. 2.14 (a) Sensitivity Comparison of HDTG-JAM-GAAFET and NG-JAM-GAAFET biosensor for different Biomolecule species [153] (b) Sensitivity Comparison of HDTG-JAM-GAAFET and NG-JAM-GAAFET biosensor for charged Biomolecules having $K=12$ [153]

In order to compare the performance of the proposed Hetero Dielectric Trench Gate Junction Accumulation Mode Gate-All-Around FET (HDTG-JAM-GAAFET) device with that of the Normal Gate JAM Gate-All-Around FET, Table 2.3 provides a summary of different performance measures and I_{ON} current sensitivity. The comparison of threshold voltage sensitivity of HDTG-JAM-GAAFET biosensor with that of similar existing biosensors for various biomolecules is given in Table 2.4. On

the other hand, Table 2.5 assesses the analog performance of HDTG-JAM-GAAFET and compares it to other structures in terms of I_{ON}/I_{OFF} ratio. The comparison shows that the proposed device outperforms most existing devices in terms of threshold voltage sensitivity and analog performance characteristics. For neutral biomolecules the % I_{ON} sensitivity for $K=12$ (Gelatin) have also been compared with already published work [175] which is 65 while for proposed biosensor its 1478.

Table 2.3 Performance Comparison of HDTG-JAM-GAAFET and NG-JAM-GAAFET [153]

Performance/ Sensitivity Parameters	HDTG-JAM-GAAFET	NG-JAM-GAAFET
Switching Ratio, I_{ON}/I_{OFF} (A)	for $K=1$, 1.24×10^{10} for ferro-cytochrome C, 1.84×10^{11}	for $K=1$, 3.35×10^6 for ferro-cytochrome C, 5.77×10^9
Sub-threshold Slope, SS (mV/decade)	for $K=1$, 69.13 for ferro-cytochrome C, 64.99	for $K=1$, 81.58 for ferro-cytochrome C, 68.31
I_{ON} sensitivity (mA)	for ferro-cytochrome C, 849.79 for Gelatin, 1478.24	for ferro-cytochrome C, 397.47 for Gelatin, 881.60
I_{OFF} current (A/ μm)	for $K=1$, 6.15×10^{-16} for $K=4.7$, 1.90×10^{-17}	for $K=1$, 2.35×10^{-12} for $K=4.7$, 3.33×10^{-16}
Output Conductance, g_d (mho)	for $K=1$, 3.60×10^{-05} for Gelatin, 4.85×10^{-05}	for $K=1$, 2.64×10^{-05} for Gelatin, 2.92×10^{-05}
Channel Resistance, R_{ch} (ohm)	for $K=1$, 3.42×10^4 for Gelatin, 2.06×10^4	for $K=1$, 3.79×10^4 for Gelatin, 3.42×10^4
Intrinsic Gain ($A_{V_{int}}$)	for $K=1$, 36 for Streptavidin, 47.8	for $K=1$, 11.1 for Streptavidin, 18.1

Table 2.4 Threshold Voltage Sensitivity Comparison of HDTG-JAM-GAAFET to Contemporary Research on Similar Biosensors [153]

Structural Parameters	[25]	[170]	[176]	[177]	Our Work
Cavity length (nm)	20	25	25	25	21
Q_{bio} (C cm^{-2})	-4×10^{12}	-2×10^{12}	-2×10^{12}	-1×10^{12}	-1×10^{12}
(K_{BIO})	10	5	-	-	12
$S_{V_{TH}}$ in terms of ΔV_{TH} (mV)	192	110	160	201	206.3

Table 2.5 I_{ON}/I_{OFF} Ratio Comparison of HDTG-JAM-GAAFET to Contemporary Research on Similar Biosensors [153]

Structural Parameters	[160]	[178]	[179]	[180]	[181]	Our Work
Channel Length (nm)	60	60	30	75	60	50
Cavity length (nm)	29	13	-	20	25	21
Cavity thickness (nm)	6	5.5	9	5	6	10
(K_{BIO})	8	2	2	4	5	4.7
I_{ON}/I_{OFF}	1.25×10^{10}	2×10^6	1×10^8	2×10^9	3×10^8	1.84×10^{11}

The comparison of I_{ON} current sensitivity between the proposed HDTG-JAM-GAAFET and the SE-SB-FET [182] is depicted in Fig. 2.15. The figure clearly illustrates that the HDTG-JAM-GAAFET exhibits superior sensitivity both for neutral and charged biomolecules. This enhanced sensitivity has been attributed to the distinctive structural design of the HDTG-JAM-GAAFET, which features a Junction Accumulation Mode silicon cylindrical Gate-All-Around FET with a hetero dielectric layer consisting of SiO_2 and HfO_2 . Additionally, a trench gate is incorporated into the Hafnium oxide dielectric layer, allowing for precise control of the channel.

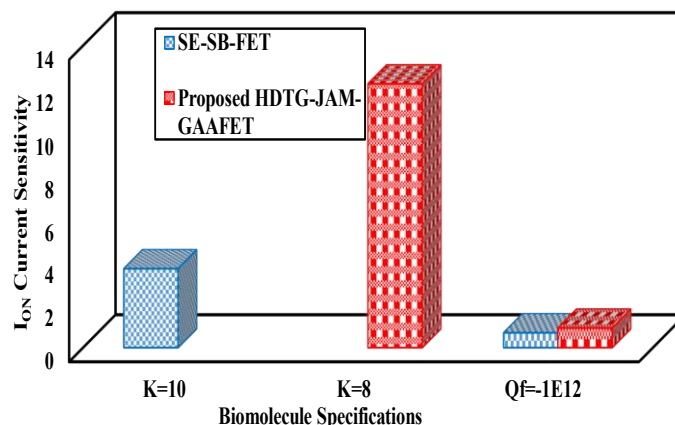


Fig. 2.15 Sensitivity Comparison of HDTG-JAM-GAAFET [153] and SE-SB-FET [182] Biosensors

2.3.4 Selectivity Analysis and Effect of Cavity Dimensions on Performance of HDTG-JAM-GAAFET Biosensor

Selectivity in the biosensors refers to the ability of a biosensor to specifically detect a target biomolecule in a complex sample, while minimizing interference from other substances that might be present in the sample. In the field of biosensors, selectivity is critical because biological samples, like blood, urine, or environmental samples, often contain a wide range of compounds and biomolecules that could potentially interfere with the accurate detection of the target biomolecules. The selectivity is crucial for the

accuracy and reliability of biosensor measurements in various applications. Mathematically, selectivity is determined by calculating the relative ratio of drain current for two distinct biomolecules, each having different dielectric constants, as expressed in equation (9) [183], [184].

$$\% \text{Selectivity, } \% \Delta S = \frac{I_{ON(K=4.7,8,10)} - I_{ON(K=2.1)}}{I_{ON(K=2.1)}} \times 100 \quad (2.10)$$

In this work, ΔS represents the selectivity value of ferro-cytochrome c ($K = 4.7$), keratin ($K = 8$), and gelatin ($K = 12$) to streptavidin ($K = 2.1$). Fig. 2.16 shows the percentage selectivity comparison of proposed HDTG-JAM-GAAFET and NG-JAM-GAAFET, in which it is evident that the selectivity of HDTG-JAM-GAAFET is notably higher than that of the conventional NG-JAM-GAAFET.

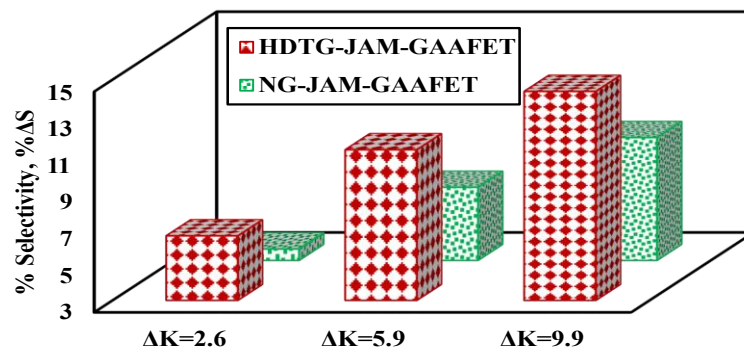


Fig. 2.16 Selectivity Comparison of proposed HDTG-JAM-GAAFET and NG-JAM-GAAFET [153]

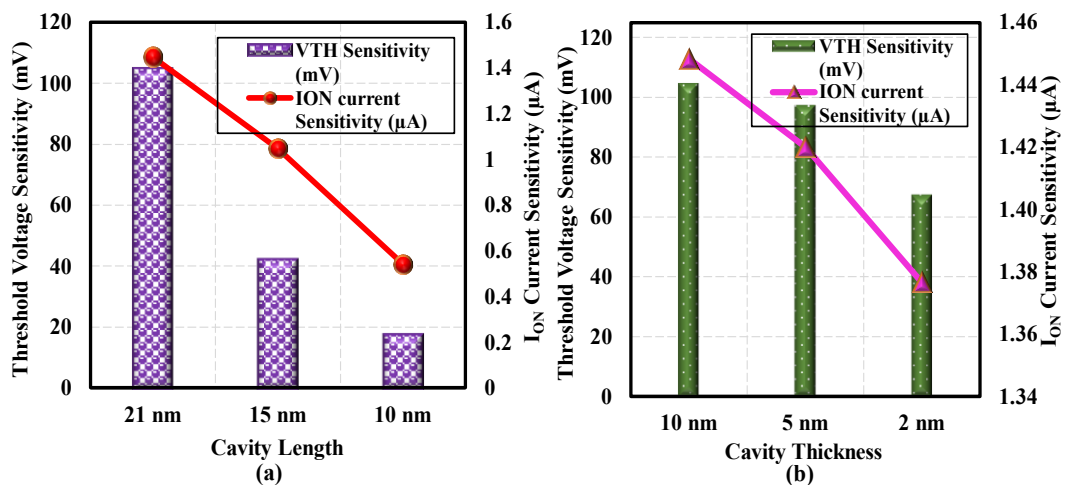


Fig. 2.17 Threshold Voltage (V_{TH}) Sensitivity and I_{ON} Current Sensitivity of HDTG-JAM-GAAFET for Gelatin Biomolecules ($K=12$) at (a) Different Cavity Lengths [153] (b) Different Cavity Thicknesses [153]

The effect of variations in the cavity's dimensions on the biosensor's sensitivity performance is examined in Fig. 2.17. The analysis specifically involves the use of

gelatin biomolecules with a dielectric constant (K) of 12 to assess variations in both cavity length and thickness. In Fig. 2.17 (a), the plot displays the relationship between threshold voltage sensitivity (on the primary axis) and I_{ON} current sensitivity (on the secondary axis) for three distinct cavity lengths. While, Fig. 2.17 (b) illustrates the changes in V_{TH} and I_{ON} current sensitivities in response to varying cavity thickness. It is evident from Fig. 2.17 that the biosensor's sensitivity performance diminishes as the cavity length and thickness decrease. This decline is primarily due to the fact that a larger cavity allows for a greater volume and, consequently, a higher concentration of biomolecules inside the cavity, leading to more significant changes in oxide capacitance and the potential barrier in the source-channel [120], [185]. However, it's worth noting that the impact on threshold voltage sensitivity is more noticeable when the cavity length is varied as opposed to the cavity thickness variations.

2.3.5 Limit of Detection (LOD) of proposed biosensor

Limit of detection (LOD) is a crucial performance attribute in biosensing method validation. Along with sensitivity, a biosensor's LOD should also receive sufficient attention because it can be utilised to assess a device's capacity to identify the analyte with the lowest charge concentration [186]. For the computation of LOD, the proposed biosensor is introduced with a number of positive interface charge densities Q_F , such as 1×10^{10} , 1×10^{11} , 5×10^{11} , 1×10^{12} , and 5×10^{12} in the nanocavity region to represent charged biomolecules at constant dielectric, $K = 3.7$. The following equation is used to determine the LOD for concentration [187].

$$Y_{LOD} = m \cdot \log_{10} X_{LOD} + c \quad (2.11)$$

$$Y_{LOD} = 3\sigma \quad (2.12)$$

The calibration curve's slope, y-intercept, and standard deviation are each represented by m , c , and σ respectively. Fig. 2.18 illustrates the determination of the LOD of proposed device at $V_{DS}=1$ V and $V_{GS}=1$ V. LOD of the proposed device is 3.58×10^{10} cm^{-2} which is 2.21 times less than the LOD of normal GAA-DM-NWFET biosensor.

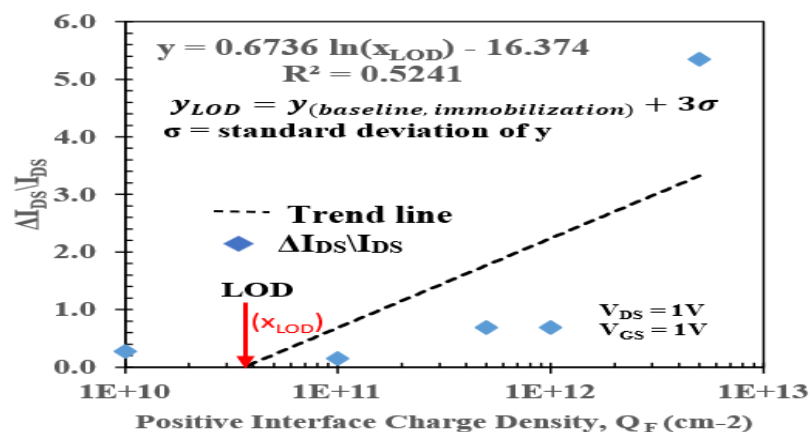


Fig. 2.18 The relative change in Drain to source Current versus interface charge density for determination of Limit of Detection [146]

2.4 Summary

This chapter presents the HDTG-JAM-GAAFET, a hetero dielectric trench gate-all-around FET in Junction Accumulation Mode, which was proposed for the detection of biomolecules associated with different diseases. Under identical biomolecule circumstances, the HDTG-JAM-GAAFET and Normal Gate-JAM-GAAFET biosensors have been contrasted and compared. For instance, HDTG-JAM-GAAFET biosensor has drain ON-current sensitivity ($S_{I_{ON}}$) which is 67.68% greater for gelatin biomolecules, 69.4% higher for positive biomolecules, and 8% higher for negative biomolecules bound in the nanogap cavity than that of a Normal Gate JAM Gate-All-Around FET. Also, according to comparisons, it has been conclusively proven that HDTG-JAM-GAAFETs exhibit superior device performance characteristics in terms of lower leakage current (I_{OFF}), higher switching ratio (I_{ON}/I_{OFF}), lower subthreshold slope (SS), higher output conductance, and lower channel resistance. It has been reported that HDTG-JAM-GAAFET is more sensitive than Normal Gate-JAM-GAAFET for a variety of neutral biomolecules, including streptavidin, biotin, ferrocytochrome c, keratin, gelatin, and positive and negative charges on the DNA biomolecule with fixed $K = 12$. The electron concentrations and velocities depicted in contour plots have been analyzed in various situations involving both neutral and charged biomolecules. Therefore, superior bio sensing is observed in HDTG-JAM-GAAFET biosensors due to the trench gate architecture in the HDTG-JAM-GAAFET biosensor, which provides enhanced regulation of the channel area. In summary, it can be deduced that the proposed biosensor device has the potential to detect different biomarkers of diseases quickly and at an early stage.

CHAPTER 3

TRENCH GATE ENGINEERED JAM GATE-ALL-AROUND FET BASED LABEL-FREE BIOSENSOR

To further improve the device performance, use of triple metal gate engineering in the trench gate FET have been explored to reduce impact ionization and enhance the sensitivity of biosensor device. This chapter aims to investigate a Trench Gate Engineered Junction Accumulation Mode Gate-All-Around FET biosensor and critically analyzes for the label-free identification of biomolecules using extensive numerical device simulations. The investigation explores a simulation-based computational methodology to control and modulate the threshold voltage and current sensitivities using dielectric and charge modulation.

Problem Statement

Design, Analysis, and Implementation of a novel Gate-All-Around Field Effect Transistor for sensing application, which utilizes the Trench Gate in the Gate-All-Around structure. This work will explore the gate metal engineering as well as gate oxide stack engineering in trench gate architecture to enhance the performance of device.

3.1 Introduction

Biosensing is basically the sensing of target molecules using principles similar to those utilised by live systems like the immune system. A molecular recognition element known as receptor and a biophysical transducer are the two core components of a biosensor. The transducer takes the bio-recognition data and changes it into a quantifiable quantity, such as an electrochemical, optical or electrical signal.

Detection specificity and sensitivity are two crucial characteristics to consider while performing biosensing. Various designs have been developed in the literature to improve detection sensitivity. Biosensors based on semiconductors are one of the most rapidly evolving sensor technologies.

Label-based biosensing technologies are labour-intensive, costly, and time-consuming. Biomolecule labelling also has the characteristic to block active binding sites and change binding properties. Label-free biosensing technologies do not use labels in order to permit measurements [103]. They use the analytes' inherent physical properties, such as molecular weight, size, electrical impedance, charge, refractive index, or dielectric permittivity for sensing purpose [105]. Biosensors have a wide range of applications in the food business, medical treatment, forensic science, environmental science, and agriculture [188]–[190].

In order to monitor and examine diverse biohazards, Biosensors are proven to be a significant asset. These biosensors are extremely useful in the biomedical area, especially as they can assist in the early identification of a number of diseases, including breast cancer, ovarian cancer, lung cancer, Alzheimer's disease, and a few viral diseases [191] [192] [193] [194] [195]. The most recent covid-19 outbreak has shattered societies and sparked panic around the world [196]. Many biosensors have been developed recently for the purpose of detecting SARS-CoV-2 from clinical samples by analyzing its spike, envelope, and DNA proteins [197] [101] [87]. Research is still being done on the development of increasingly sophisticated, extremely sensitive, and real-time biosensors.

Biosensors based on FETs have captured the attention of researchers for the detection of biomolecules due to their numerous benefits, including high sensitivity, label-free detection, power efficiency, scaling, and CMOS compatibility [198]-[43]. Recent research has focused a lot on biosensors based on nanowire FETs because of their scalability and high packing density [199]. Junctionless device designs, such as Nanowire-FETs, Nanotube-FETs and Fin-FETs, have evolved in recent times to manage good electrostatic gate control and enhance short channel effects [200], [89]. The junctionless transistor (JLT) device was conceived by Colinge et al. [28] and later manufactured. Traditionally, it has no junctions and no doping gradient. JLT transistors have the benefits of an enhanced and simpler fabrication technique and less susceptibility to short-channel effects (SCEs). Additionally, the usage of Junctionless Transistors as biosensors and the tremendous progress made in the fabrication sector allows for the mass production of these biosensors at a low cost. Modern junctionless device designs, like Nanowire-FETs, Nanosheet-FETs, and Fin-FETs, have improved short-channel effects and electrostatic gate control [89], [200]. In comparison to the NS FET and FinFET, the Nanowire FET provides superior sub-threshold properties like lower I_{OFF} , an optimal subthreshold slope (SS), and a significantly superior I_{ON}/I_{OFF} ratio for gate length scaled below 16 nm. Also, Nanowire FETs can be stacked, providing a higher density of transistors on the same die area than FinFETs placed side by side [201], [202].

However, the junctionless FET devices have a number of shortcomings, including deteriorated mobilities caused by high doping concentrations and the need for a larger gate work function for fully depleted channel region in order to ensure the device turns off [203].

A key factor in improving the performance of FET devices is gate design. Dual Metal Gate (DMG), which uses a higher work function metal near the source and a lower work function metal near the drain, improves carrier transport efficiency and immunity to SCEs due to the velocity enhancement [204]. In order to further improve performance in terms of the electric field, surface potential, drain current, transconductance, and output conductance, the triple metal gate devices have been developed in the literature, exhibiting superior band-to-band tunneling [205]. Furthermore, trench gate FETs, in which the device's Gate is positioned in a prefabricated trench, demonstrate both great current sensitivity and exceptional voltage sensitivity [81], [96].

A nanogap cavity structure is created in the gate-insulator area in the Dielectric Modulated FET (DMFET) type of biosensor [106], [107]. Wet etching and simple thin-film deposition techniques are used to create the nanogap cavity [131]. DMFET biosensors work on the fundamental principle that band modulation results from changes in the effective coupling between the Gate and the channel, which are caused by variations in the immobilized biomolecules' dielectric constants and charge concentration within the nanogap cavity [182].

3.1.1 Junction Accumulation Mode FET

The Junction Accumulation Mode (JAM) FET is a modified type of Junctionless FET that can be employed to mitigate the drawbacks of junctionless FET. As shown in Fig. 3.1, there is no junction in JAM Gate-All-Around field effect transistors either, although the channel's doping level is a little bit lower than that of the source/drain region. The basic operation regime in JAM Gate-All-Around FET is accumulation ($V_{GS} > V_{FB}$), and the $V_{FB} - V_{TH}$ difference can be regulated by doping level modulation in the channel [206]. A Junction Accumulation Mode Gate-All-Around FET is a type of transistor that doesn't have a traditional p-n junction, which is a region where two types of doped semiconductor materials meet. Instead, it has a structure where the same type of doping is used in the source, channel, and drain with the exception of slightly higher doping in source and drain regions than in the channel region. It also simplifies the fabrication process since it doesn't require different doping types. Furthermore, this type of transistor has improved analog and RF performance compared to traditional junctionless FETs, making it a promising option for various electronic applications. In summary, the Junction Accumulation Mode Gate-All-Around FET is a type of transistor that offers better performance and scalability than traditional transistors, thanks to its cylindrical gate design and lack of p-n junctions.

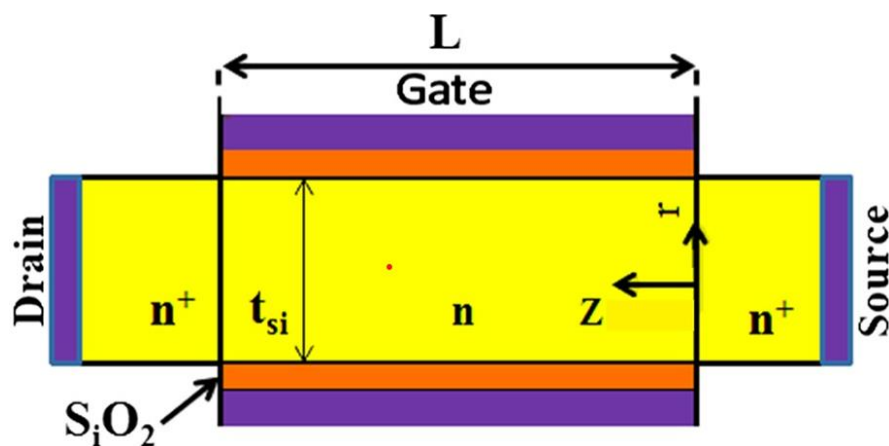


Fig. 3.1 Junction Accumulation Mode FET [207]

3.1.2 Gate Material Engineering (GME)

Engineering in the Gate-material with distinctive work functions, proposes a discontinuity in the field along the channel, leading to transport enhancement and suppressed SCEs. The channel electric field profile is tuned so as to have enhanced field at source side to increase carrier velocity and smaller values at drain end and a

lower work function metal at the drain end screens the drain potential variations. The work function Φ_{M2} at the drain side should be less than Φ_{M1} at the source side. The control gate is screened from drain potential variations by screen gate and hence reduces Channel Length Modulation (CLM) and drain conductance. It also leads to a reduction in the electric field near the drain thereby curtailing the hot electron effect. The increase in carrier transport efficiency further enhances the drain current and hence, the Transconductance. To enhance the gate transport efficiency and to reduce the SCE's, Gate Material Engineering (GME) MOSFET as shown in Fig. 3.2 was proposed by Long et al. and P. Ghosh et. al [25-26] in 1997.

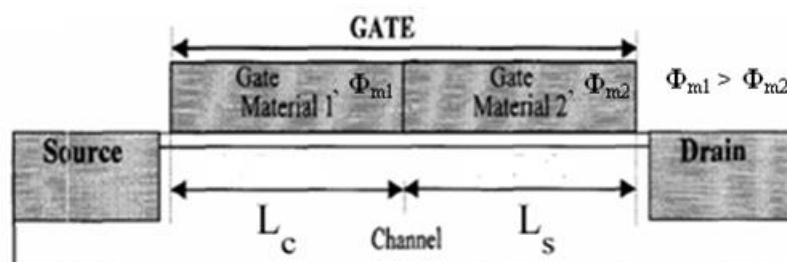


Fig. 3.2 The Dual-Material gate FET (DMGFET) structure [28]

3.1.3 Trench Gate Architecture

A transistor's gate electrode's particular configuration and structure is referred to as trench gate architecture in FET designs. Trenches are made by etching the semiconductor material to produce the gate electrode in this architecture [96]. Gate can also be formed by etching the trenches into the dielectric material [146]. Trench gate design enables enhanced regulation of the conductivity in the channel, resulting in superior performance and scalability in FET devices [147]. The structure and detailed description of trench gate has been already explained in chapter 2.

3.2 Trench Gate Engineered JAM Gate-All-Around (TGE-JAM-GAA) Label-Free BioFET: Device Structure and Simulation Framework

Fig. 3.3 (a) presents a three-dimensional representation of the TGE-JAM-GAA BioFET. The Gate of this biosensor structure is designed with triple metals. Gate Metal-1 is trenched into two HfO_2 dielectric layers of 7 nm thickness each. This trenched part of the Gate is of 2 nm length and 9 nm thickness with a metal work function of 5.0 eV. By using metal with a reduced work function, the trench gate layer creates an extra electrostatic control [86]. The other two layers of Gate, Gate Metal-2 and Gate Metal-3, are made of two metals having work functions, 5.5 eV and 4.8 eV, respectively. The Two-Dimensional perspective of the TGE-JAM-GAA BioFET biosensor, along with its analogous capacitance model, is shown in Fig. 3.3 (b). Dielectric modulation uses the impact of a variation in dielectric constant in a specific region of the gate dielectric on the drain current and the other accompanying parameters. This specific region, which is created through the etching process, is referred to as the nano-cavity region. Biomolecules have been inserted uniformly in this nano-cavity region, as depicted in the 2D structure. The

capacitances of the TGE-JAM-GAA BioFET are represented in the capacitance analogous circuit in Fig. 3.3 (b) by C_{bio} for the variable capacitance of nanogap cavity containing biomolecule species, C_{SiO_2} for the capacitance of SiO_2 layer, and C_{HfO_2} for the capacitance of HfO_2 layer.

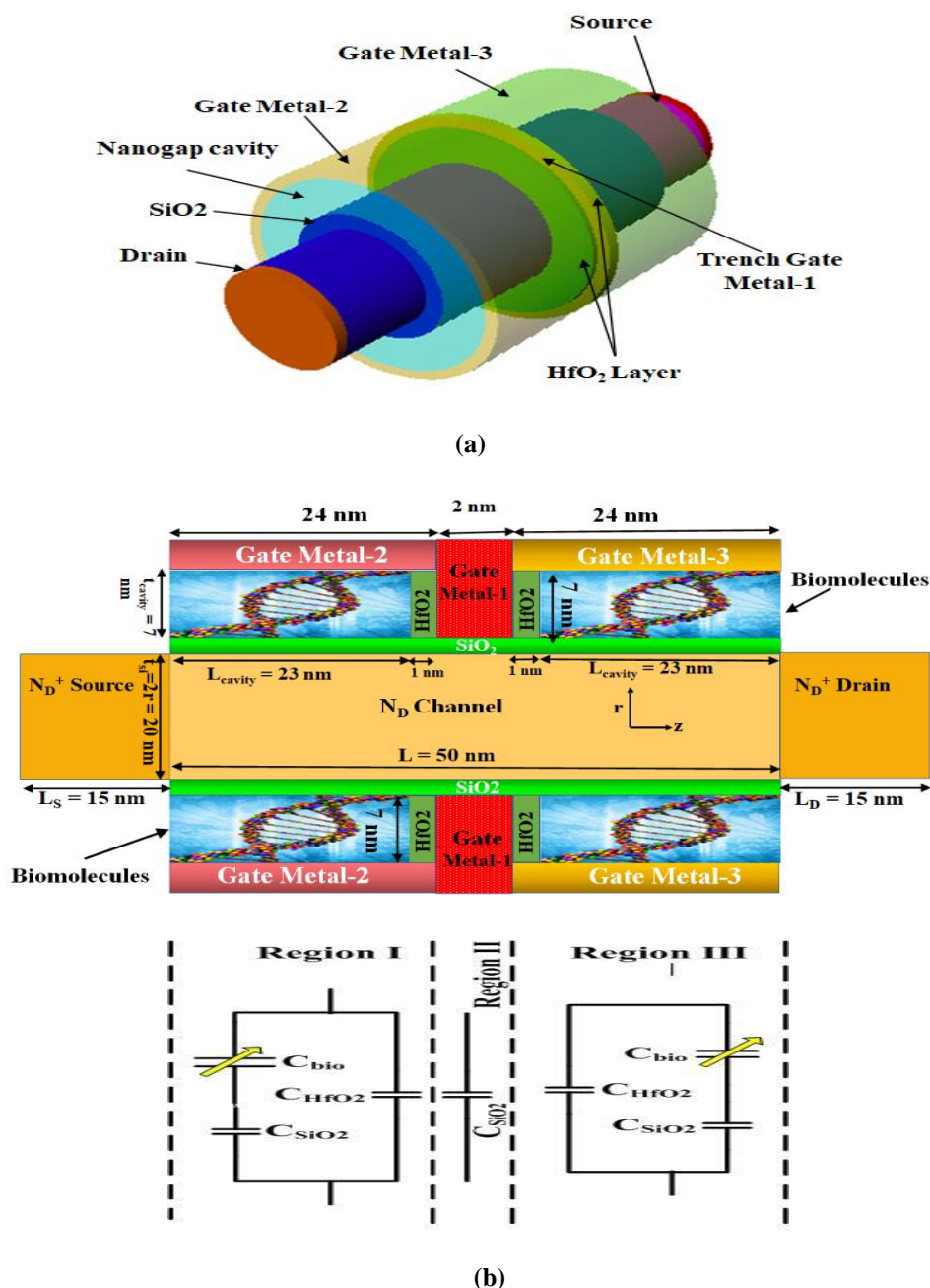


Fig. 3.3: (a) 3-Dimensional View of TGE-JAM-GAA BioFET (b) 2-D Structure of TGE-JAM-GAA BioFET with its capacitance model

The SILVACO Atlas-3D device simulation tool [151] has been used to carry out the simulations. Carrier recombination and carrier mobility generation models are among the models used in the simulations. The CONMOB (concentration-dependent mobility) model, as well as BGN (band gap narrowing) model, have been used to

verify the doping versus mobility and high channel doping profile. The recombination of minority carriers under semiconductors was also accounted for using Boltzmann transport equations and Shockley–Read–Hall (SRH) [151]. The Fermi-Dirac model is employed in devices with high doping concentrations. Quantum effects have not been considered in simulations as the channel thickness taken is not less than 7 nm [208]. The potential biomolecules (neutral and charged) [157] which can be detected by the TGE-JAM-GAA BioFET biosensor are listed in Table 3.1. Table 3.2 illustrates the device parameters for the proposed TGE-JAM-GAA BioFET, TMNG-JAM-GAAFET, and SMNG-JAM-GAAFET biosensors.

Table 3.1 Dielectric Constant and Type of Biomolecules

Biomolecule	Dielectric Constant	Type of Biomolecule
Streptavidin	2.1	Neutral
Biotin	2.63	Neutral
APTES	3.57	Neutral
DNA	1 – 64	Charged

Table 3.2 Device Design Parameters

Physical Device Parameters	TGE-JAM-GAA BioFET	TMNG-JAM-GAAFET	SMNG-JAM-GAAFET
Channel Length (nm)	50	50	50
the thickness of silicon film (nm)	20	20	20
Length of source/drain (nm)	15	15	15
Metal gate work function (eV) (M_1, M_2, M_3)	5.5, 5.0, 4.8	5.5, 5.0, 4.8	5.5
Oxide Thickness, SiO ₂ & HfO ₂ (nm)	3.0 & 7.0	3.0 & 7.0	3.0 & 7.0
Doping of Channel Region, N_D (/cm ³)	1×10^{18}	1×10^{18}	1×10^{18}
Doping of Source and Drain Region, N_D^+ (/ cm ³)	1×10^{19}	1×10^{19}	1×10^{19}
Thickness of Cavity (nm)	7	7	7
Trench Gate Thickness (nm)	9	-	-
Length of Cavity (nm)	23	23	23
HfO ₂ and SiO ₂ dielectric constants	25.0 & 3.9	25.0 & 3.9	25.0 & 3.9

3.3 TGE-JAM-GAA Biosensor Device Fabrication Illustration

For the fabrication of Gate-All-Around nanowire FET sensors, two techniques are used, bottom-up and top-down [209]. Contrary to bottom-up techniques, top-down techniques based on microfabrication on silicon-on-insulator (SOI) or single-crystalline Silicon (SCS) wafers are capable of producing nanowires that are compatible with conventional CMOS technology [210]. The fabrication is often carried out using a combination of the standard semiconductor fabrication methods, which include photolithography, silicon dry etching, anisotropic wet etching, and thermal oxidation. The first stage begins with a layer of Silicon. After that, a photomask pattern is used to designate the source and drain with doping of $10^{19}/\text{cm}^3$. Reactive ion etching (RIE) is then used in the third phase to complete the source and drain electrodes, which are of nm in size. In step 4, using an electric resist pattern and RIE etching, we create Si nanowires with a diameter of 20 nanometres. As illustrated in the flowchart in Fig. 3.4, the ensuing process includes the deposition of a dielectric stack (SiO_2 and HfO_2), the formation of triple metal surrounding Gate, and the etching of the nano-cavity region. The dielectric stack was successively removed by wet etching to be able to reveal the Gate-All-Around channel to complete the cylindrical surrounding gate structure in the proposed device.

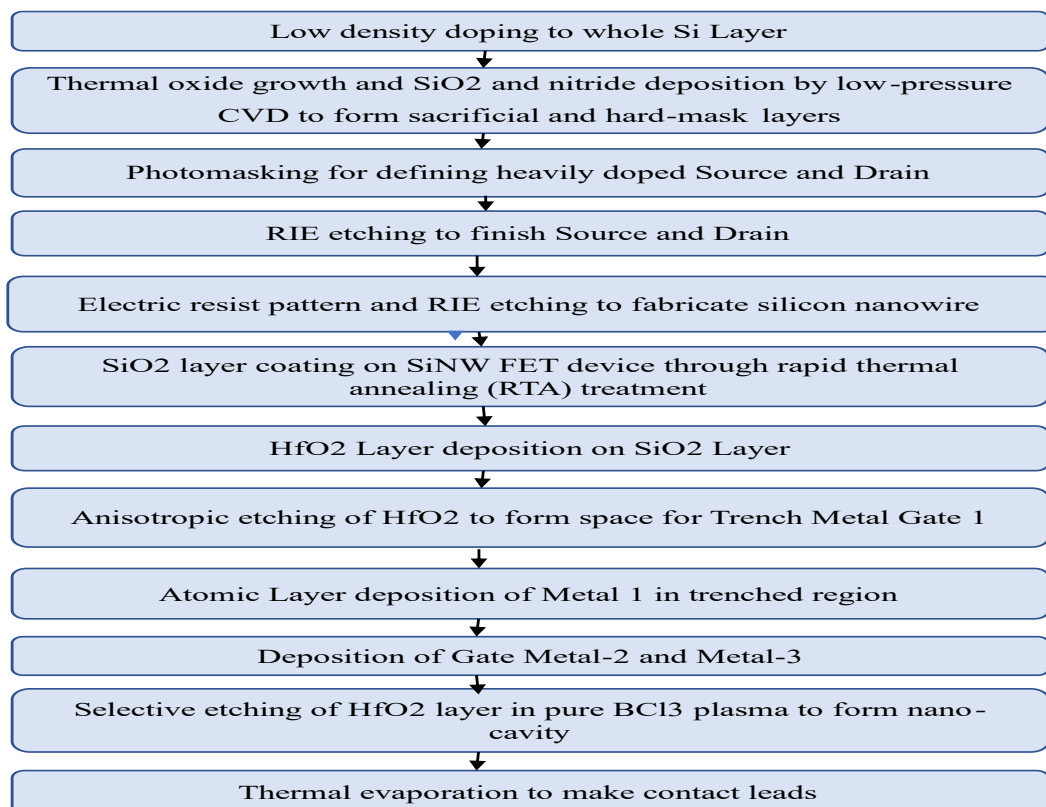


Fig. 3.4 Proposed fabrication flowchart for TGE-JAM-GAA BioFET biosensor Device

3.4 Results and Discussion

In this work, specific biomolecules are immobilized in the nanogap cavity of the proposed TGE-JAM-GAA BioFET biosensor device. The change in channel conductance brought on by biomolecule conjugation can be quantified and utilized as a sensing parameter. The magnitude of such a shift in channel conductance results from variations in the dielectric constant and charge density of the biomolecule sample.

3.4.1 Impact of Different Biomolecules Species

The channel center potential along the channel has been investigated in order to conceptualize the nature of the biosensor in terms of electrostatic potential. The channel potential variation caused by different neutral biomolecules having various dielectric constant (K) values is depicted in Fig. 3.5. The nanogap cavity filled with air represents the biosensor having no biomolecules in the cavity region. When the nanogap is filled with air ($K = 1$), the channel center potential minimum (Ψ_c) is at its maximum value because the source-channel barrier height is at its lowest value among all other situations where $K > 1$. This indicates that the nanogap cavity, without any biomolecule ($K = 1$), will reflect the lowest threshold voltage. The source-channel barrier height increases in tandem with the steady increase in the K -value in the nanogap, boosting the threshold voltage. This change in threshold voltage can be used as a metric to identify the type of biomolecules. Furthermore, as the dielectric constant value of biomolecules rises, the effective oxide thickness (EOT) falls, increasing the gate control over the channel and resulting in weaker Short Channel Effects. Thus, the other metrics like OFF current and I_{ON}/I_{OFF} ratio can be utilized as sensitivity metrics for the biosensor [99], [182].

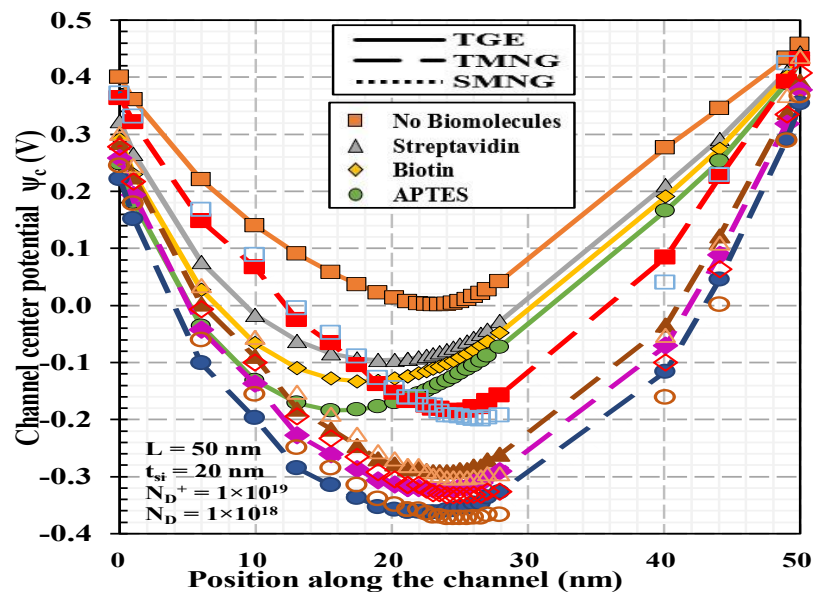


Fig. 3.5 Variation of channel center potential for different biomolecule Species

The decrement in center potential minimum (Ψ_c) from no biomolecules to streptavidin, Biotin, and APTES is apparent from Fig. 3.5 for all three biosensors, although it is most pronounced in the case of the TGE-JAM-GAA BioFET biosensor. Furthermore, compared to the SMNG-JAM-GAAFET biosensor having conventional single metal gate, the Ψ_c shift is greater for Triple Metal Gate GAAFET biosensor. This negative shift in channel center potential minimum (Ψ_c) with increasing K value in the nano-cavity enhances the control of the Gate over the channel [96]. More of a decrease in Ψ_c is relative to a rise in K will give more control to Gate over the channel. Therefore, it is possible to draw the conclusion that the proposed Triple Metal Trench Gate has greater control over the channel than Triple Metal Normal Gate and Single Metal Normal Gate.

Fig. 3.6 (a) shows the effect of different biomolecule species on the drain-to-source current (I_{DS}) with respect to the gate to source voltage (V_{GS}). The drain ON current for TGE-JAM-GAA BioFET, TMNG-JAM-GAAFET, and SMNG-JAM-GAAFET biosensors are $3.57 \mu A$, $1.32 \mu A$, and $0.512 \mu A$, respectively, for APTES biomolecule immobilized in the nanogap cavity region. Hence proposed biosensor has 170.45% and 597.2% higher drain ON current for the case of APTES biomolecule than that of TMNG-JAM-GAAFET and SMNG-JAM-GAAFET. It has been found that when the value of the dielectric constant increases, the I_{ON} drain current for all three biosensor devices decreases, although the influence of the dielectric constant is stronger for the proposed TGE-JAM-GAA BioFET, as evident in Fig. 3.6 (b) depicting drift in I_{ON} current with change in biomolecule species. I_{ON} current drift, ΔI_{ON} is calculated as equation (1) [174].

$$\Delta I_{ON} = I_{ON[With\ biomolecules]} - I_{ON[Without\ biomolecule]} \quad (3.1)$$

Fig. 3.6 (c) represents the effect of Streptavidin, Biotin, and APTES biomolecules on the transconductance (g_m) for TGE, TMNG, and SMNG JAM-GAAFET biosensors. Transconductance (g_m) is the first-order derivative of I_{DS} current with respect to gate to source voltage (V_{GS}).

It is observable from Fig. 3.6 (c) that TGE-JAM-GAA BioFET has higher transconductance than the other two biosensor devices. Also, there is a significant drift in g_m for various biomolecules inserted in the nano-cavity for all three biosensor devices. However, the drift in g_m is the highest for the proposed device for all three considered biomolecules (Streptavidin, Biotin, and APTES). This is because the TGE-JAM-GAA BioFET's unique trench Gate and its different work functions boost the electrostatic coupling and improve the carrier mobility, which contributes to the improved performance of the proposed device [211].

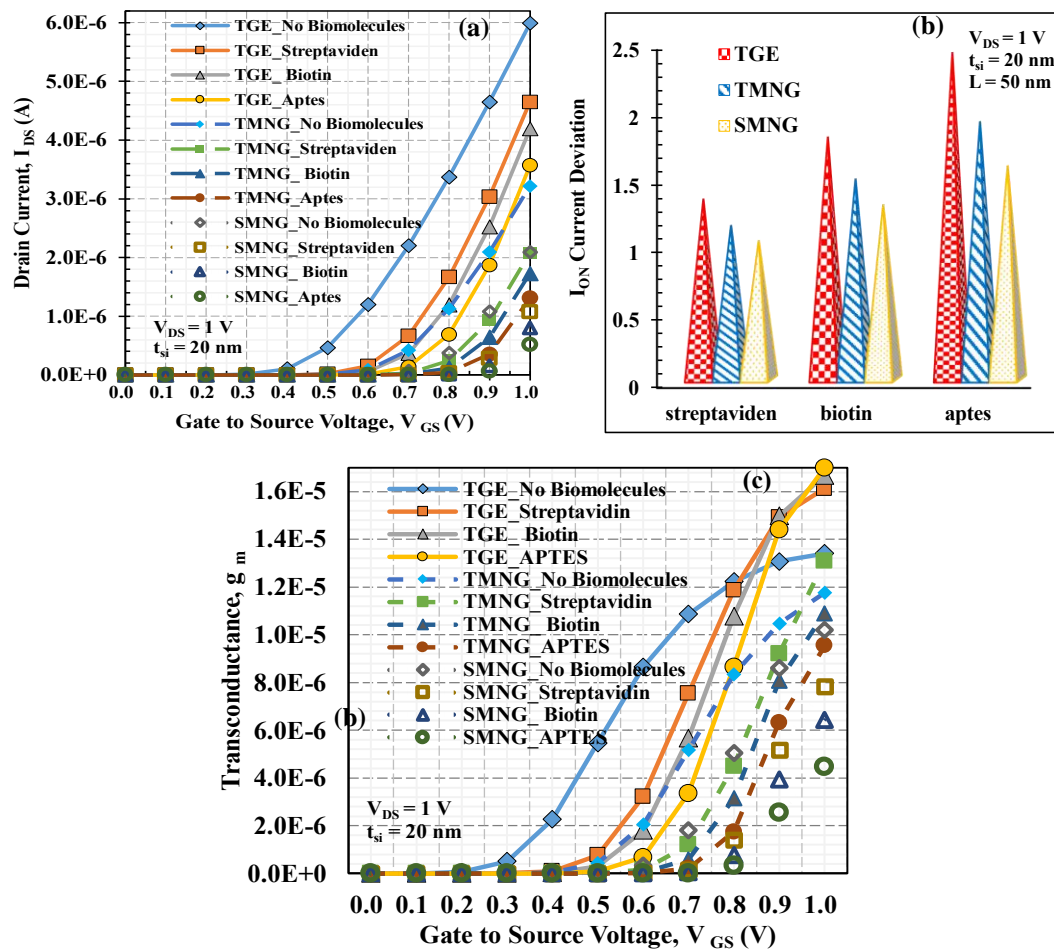


Fig. 3.6 Comparative Study of TGE-JAM-GAA BioFET, TMNG-JAM-GAAFET, and Conventional Single Metal Normal Gate GAA FET for Neutral Biomolecules with Different K
 (a) Variation in I_{DS} with respect to V_{GS} (b) Deviation in I_{ON} Current (c) Transconductance (g_m)

Fig. 3.7 (a) illustrates the impact of neutral biomolecules for TGE-JAM-GAA BioFET, TMNG-JAM-GAAFET, and conventional normal gate GAA FET on threshold voltage, V_{TH} . The threshold voltage is determined by the constant current method [169]. In all three cases, the threshold voltage increases with the increase in the dielectric constant of biomolecules inserted because the V_{TH} roll-off is minimized by Gate dielectric materials [212]. The drift in threshold voltage ΔV_{TH} , defined as the difference between the threshold voltages at $K = 2.1, 2.63, 3.57$, and $K = 1$, is used as a metric to compute the sensitivity of the biosensors.

As depicted in Fig. 3.7 (b), ΔV_{TH} is the highest for TGE-JAM-GAA BioFET than that of the TMNG-JAM-GAAFET and conventional normal gate GAA FET-based biosensors. For APTES, the V_{TH} shift for TMTG, TMNG, and SMNG biosensor devices are 236.24 mV, 148.81 mV, and 91.15 mV, respectively. Therefore, the proposed TGE-JAM-GAA BioFET biosensor has 58.75% and 159.18% higher V_{TH} shift than that of the TMNG-JAM-GAAFET and SMNG-JAM-GAAFET, respectively. The larger shift in V_{TH} occurs from the triple Metal trench gate's superior gate control over the channel compared to the other two devices, which is caused by

the higher drift in flat band voltage (V_{fb}), which causes more drift in channel center potential. The proposed device has a higher V_{TH} shift than the reported split Gate DM-JL-MOSFET which has a V_{TH} shift of 160 mV even for the high value of $K=10$ [99].

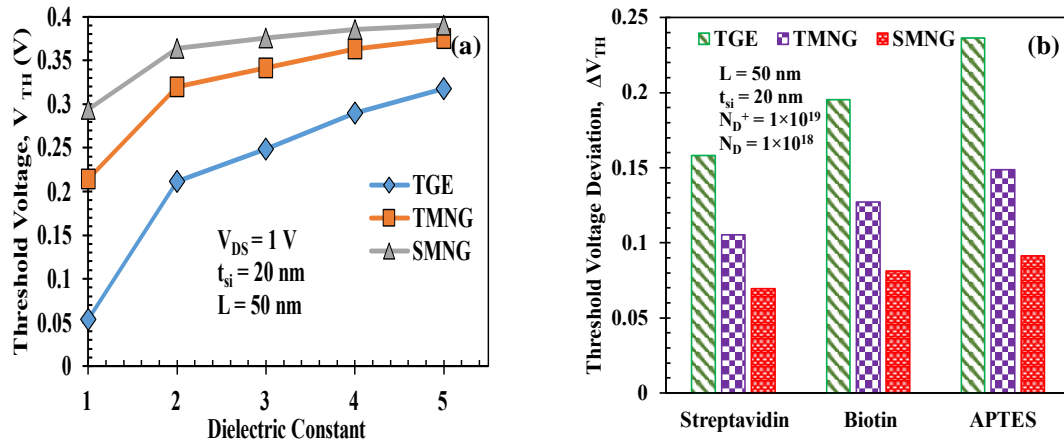


Fig. 3.7 Comparative Study of TGE-JAM-GAA BioFET, TMNG-JAM-GAAFET, and SMNG-JAM-GAAFET for Neutral Biomolecules (a) V_{TH} with respect to K (b) ΔV_{TH} for Different Biomolecules Species

3.4.2 Impact of Biomolecules Charge Concentration

Fig. 3.8 shows the variation of channel center potential for immobilization of various positively and negatively charged ($N_f = -1 \times 10^{11}$ and 1×10^{11}) biomolecules at a fixed $K = 2.1$ in the nano-cavity region. In contrast to neutral biomolecules, the center potential of all three biosensor devices decreases for negatively charged biomolecules and increases for positively charged biomolecules. This is explained by the fact that positive charges reduce flat band voltage (V_{fb}), but negative charges raise V_{fb} [96]. Due to the largest variation in V_{fb} caused by the Trench structure of the Gate compared to that of the other two devices, the proposed TGE-JAM-GAA BioFET biosensor has the highest increment (decrement) of center potential for positively (negatively) charged biomolecules.

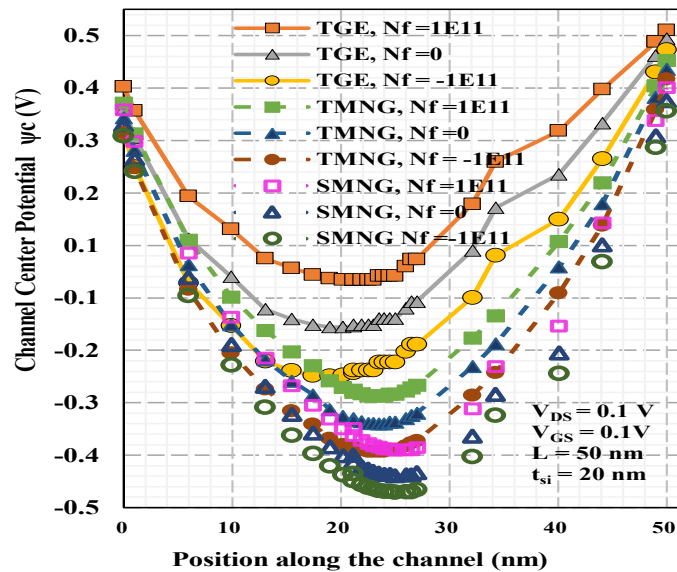


Fig. 3.8 Variation of Channel Center Potential for $K=2.1$ and Varying Charge

The change of I_{DS} with V_{GS} for the above-mentioned three devices for the case of different charged biomolecules are shown in Fig. 3.9 (a). It can be observed that drain ON current rises for the positive charge and decreases for the negative charge on the biomolecules with respect to the case when there is no charge ($K = 2.1$, $N_f = 0$) on the biomolecule. The reason behind this change is that increase in negative charge causes the minimum center potential to drop, which lowers the drain current I_D . In contrast, a rise in positive charges raises the minimum center potential, which raises the drain current I_D .

The drift in I_{DS} with V_{GS} for the TGE-JAM-GAA BioFET, TMNG-JAM-GAAFET, and conventional biosensors at various biomolecule concentrations is shown in Fig. 3.9 (b). The concentrations of biomolecules in the nano-cavity may be altered, making it possible to detect DNA biomolecules. The Fig. 3.9 (b) indicates that TGE-JAM-GAA BioFET exhibits a larger shift in the drain current for detecting different biomolecules than the other two devices. The TGE-JAM-GAA BioFET structure, which has a triple metal trench gate, is responsible for the greater variation in drain current due to better control of the triple metal trench gate structure over the channel both for neutral as well as charged biomolecules. For each of the three biosensors, Fig. 3.9 (c) displays the transconductance (g_m) vs. V_{GS} for various biomolecule concentrations. It follows logically that transconductance (g_m), a measure of electrical conductivity, rises when positive-charged biomolecules are inserted and fall when negative-charged biomolecules are introduced. This is because of a shift in channel potential, which is upward for positive biomolecules and downward for negative biomolecules, as discussed in Fig. 3.8.

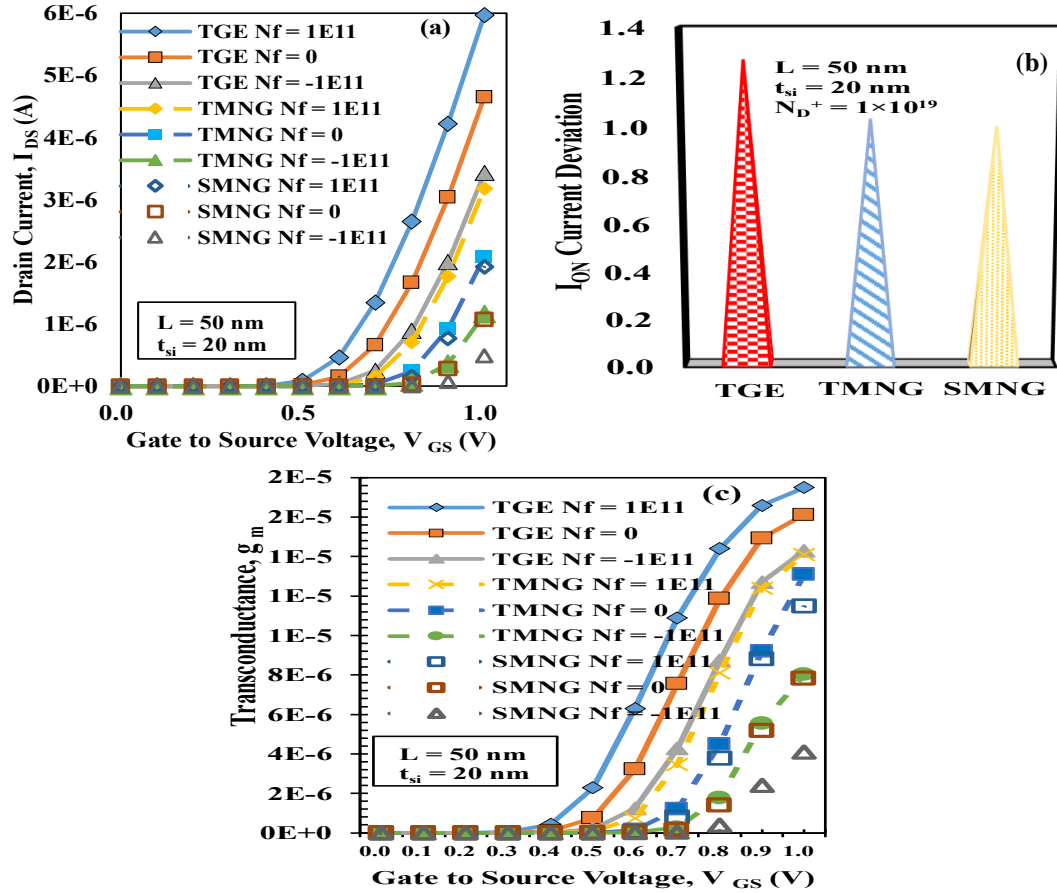


Fig. 3.9 (a) I_{DS} - V_{GS} Characteristics for $K = 2.1$ and Varying Charge (b) Average Drift in Drain ON current (ΔI_{ON}) for Variation in Charge (c) Transconductance (g_m) for Varying Charge on Biomolecule at $K = 2.1$

Fig. 3.10 illustrates the effect of charged analytes on the biosensor devices' threshold voltage (V_{TH}). Positively charged biomolecules cause a drop in V_{TH} , whereas negatively charged biomolecules cause a rise in V_{TH} . The channel center potential minimum (Ψ_c) value rises with increasing biomolecule positive charge, resulting in a drop in source channel barrier height and the corresponding drop in V_{TH} . Also, as the charge becomes increasingly negative, the source-channel barrier height rises, raising the threshold voltage [90]. This shift in threshold voltage serves as a metric for identifying the nature of charged biomolecules. The threshold voltage drift (ΔV_{TH}) is calculated as the difference between the threshold voltages when charged biomolecules are present in the nano-cavity and when no charge is taken into account for the biomolecule. The drift in threshold voltage (ΔV_{TH}) of the proposed TGE-JAM-GAA BioFET device is 53 mV for $N_f = 1 \times 10^{11}$ and 49.14 mV for $N_f = -1 \times 10^{11}$, which are 18.34% and 38.06% higher than the ΔV_{TH} of TMNG-JAM-GAAFET biosensor respectively. This leads us to the conclusion that the proposed device is more suitable for negatively charged biomolecules in terms of ΔV_{TH} than the TMNG-JAM-GAAFET biosensor.

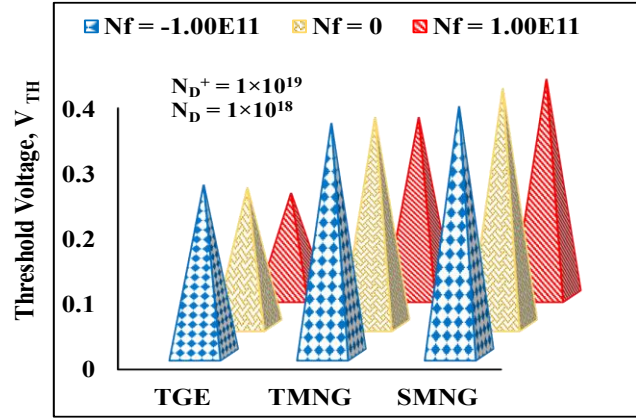


Fig. 3.10 Comparative Study of Variation in V_{TH} for TGE-JAM-GAA BioFET, TMNG-JAM-GAAFET, and Conventional Normal Gate GAA FET for Charged Biomolecules with $K=2.1$

3.4.3 Sensitivity Comparison of TGE-JAM-GAA BioFET

As illustrated in Fig. 3.11, several sensitivities, including current sensitivity, I_{ON}/I_{OFF} sensitivity, and threshold voltage sensitivity, have been computed for all three biosensor devices for sensitivity performance comparison.

The I_{ON} current sensitivity for neutral biomolecules, $SN_{I_{ON}}$, is calculated as the ratio of drain ON current at $K = 2.1, 2.63, 3.57$ to drain ON current at $K=1$ as given by equation (3.2) [213]:

$$SN_{I_{ON}} = \frac{I_{ON} [With\ biomolecules]}{I_{ON} [air]} \quad (3.2)$$

Fig. 3.11 (a) demonstrates that for all the neutral biomolecules taken into consideration in this work, the I_{ON} sensitivity is maximum for TGE-JAM-GAA BioFET. For positive and negative charged biomolecules at constant dielectric constant $K = 2.1$, the I_{ON} current sensitivity is calculated as drift in drain ON current from the case when no charge is there on the biomolecules. As depicted in Fig. 3.11 (b), for both $N_f = 1 \times 10^{11}$ and $N_f = -1 \times 10^{11}$, the current sensitivity is higher for the proposed TGE-JAM-GAA BioFET.

The reason behind higher I_{ON} current sensitivity is the higher deviation in I_{ON} current value for both the change in neutral biomolecules and charged biomolecules. Device switching speed is governed by the I_{ON}/I_{OFF} ratio. Therefore, it is a crucial factor to consider while assessing a device's performance. Mathematically, I_{ON}/I_{OFF} ratio is represented in equation (3.3) [89]:

$$\frac{I_{ON}}{I_{OFF}} = \frac{I_{DS(ON)at\ VGS=1.0V}}{I_{DS(OFF)\ at\ VGS=0.0V}} \quad (3.3)$$

The calculation of I_{ON}/I_{OFF} sensitivity and Threshold voltage sensitivity for two different cases, i.e., neutral and charged biomolecules, following two mathematical formulae have been employed [99]:

$$SN_{V_{TH}} = \left| \frac{V_{TH}(air, K=1) - V_{TH}(bio, K>1)}{V_{TH}(K=1)} \right| \quad (3.4)$$

$$SN_{I_{ON}/I_{OFF}} = \left| \frac{I_{ON}/I_{OFF}(K=1) - I_{ON}/I_{OFF}(K>1)}{I_{ON}/I_{OFF}(K=1)} \right| \quad (3.5)$$

$$SC_{I_{ON}/I_{OFF}} = \left| \frac{I_{ON}/I_{OFF}(neutral) - I_{ON}/I_{OFF}(charged)}{I_{ON}/I_{OFF}(neutral)} \right| \quad (3.6)$$

$$SC_{V_{TH}} = \left| \frac{V_{TH}(neutral) - V_{TH}(charged)}{V_{TH}(neutral)} \right| \quad (3.7)$$

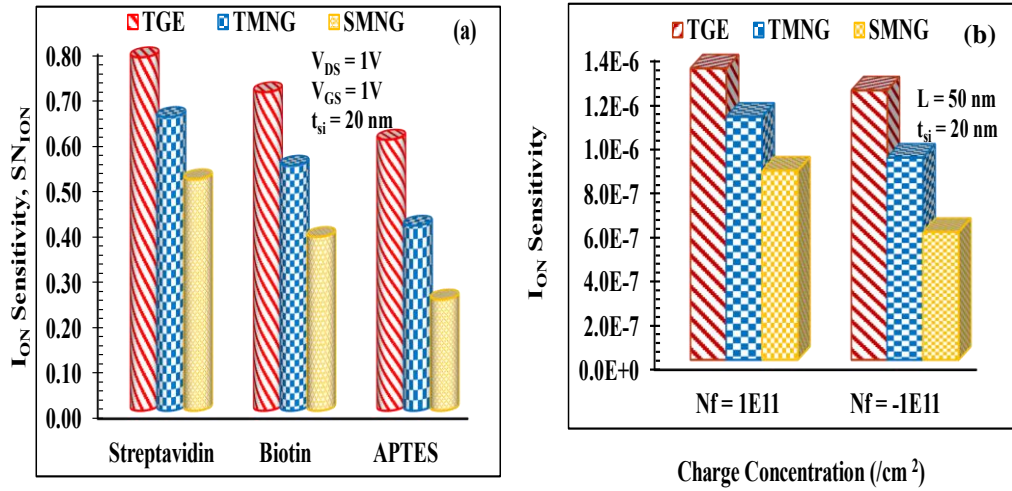


Fig. 3.11 (a) I_{ON} Current Sensitivity for Neutral Biomolecules (b) I_{ON} Current Sensitivity for Charged Biomolecules

Fig. 3.12 (a) shows the comparative analysis of I_{ON}/I_{OFF} sensitivity for different neutral biomolecules, streptavidin, biotin, and APTES. Higher drift in drain ON current and drain OFF current due to better control of triple metal trench gate for TGE-JAM-GAA BioFET than that of the TMNG-JAM-GAAFET and conventional normal gate GAA FET governs the better I_{ON}/I_{OFF} sensitivity for the TGE-JAM-GAA BioFET device for neutral biomolecules. The I_{ON}/I_{OFF} sensitivity for charged biomolecules is shown in Fig. 3.12 (b), and it is apparent that the I_{ON}/I_{OFF} sensitivity for negatively charged biomolecules is higher for all three biosensors than the I_{ON}/I_{OFF} sensitivity for positively charged biomolecules. The I_{ON}/I_{OFF} sensitivity of the proposed device, however, is greater than that of the other two devices for both positively and negatively charged biomolecules.

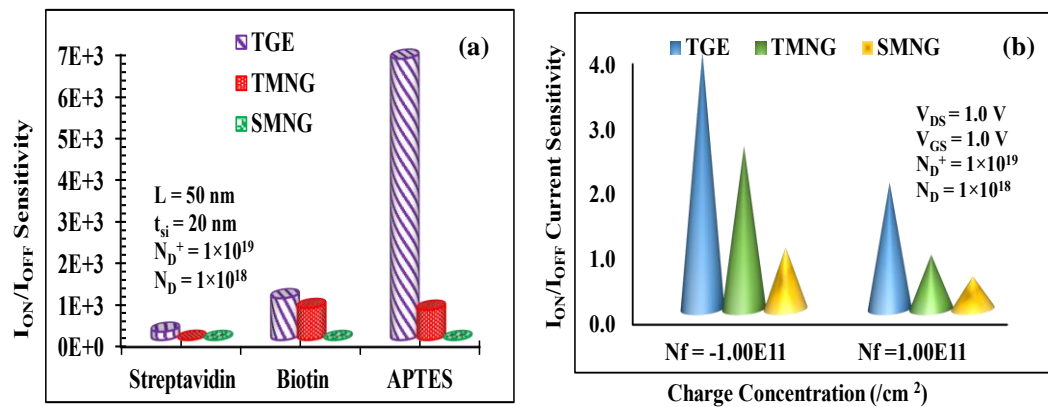


Fig. 3.12 (a) I_{ON}/I_{OFF} Current Sensitivity for Neutral Biomolecules (b) I_{ON}/I_{OFF} Current Sensitivity for Charged Biomolecules

Fig. 3.13 (a) depicts the variance in V_{TH} sensitivity ($SN_{V_{TH}}$) with distinct neutral biomolecules. It has been found that the increase in $V_{TH}(\text{bio})$ with reference to air, causes the $SN_{V_{TH}}$ to rise with K . For the proposed TGE-JAM-GAA BioFET biosensor, Streptavidin, Biotin, and APTES have $SN_{V_{TH}}$ values of 2.96, 3.65, and 4.42, respectively. These values are higher by 501%, 514.5%, and 536.1%, respectively, than those for TMNG-JAM-GAAFET and by 1154.8%, 1223.9%, and 1327.83%, respectively than those for SMNG-JAM-GAAFET. Also, for $K=3.57$, the proposed device's V_{TH} sensitivity is 15.24 times greater than that of the previously reported split Gate Junctionless FET [99].

The threshold voltage sensitivity ($SC_{V_{TH}}$) with the inclusion of charged biomolecules at $K=2.1$ is modeled in Equation 3.7. The proposed TGE-JAM-GAA BioFET biosensor has higher V_{TH} sensitivity for positively and negatively charged biomolecules both as compared to TMNG and SMNG biosensor devices, which is evident in Fig. 3.13 (b). Also, TGE-JAM-GAA BioFET reflects almost the same V_{TH} sensitivity ($SC_{V_{TH}}$) for positive and negative charged biomolecules. $SC_{V_{TH}}$ is 0.25 for Positive charge value $1 \times 10^{11} \text{ cm}^{-2}$ and 0.23 for negative charge value $-1 \times 10^{11} \text{ cm}^{-2}$.

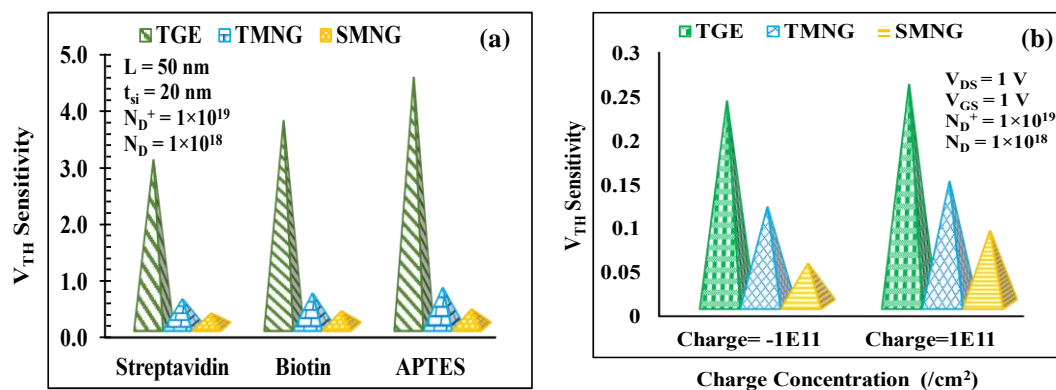


Fig. 3.13 (a) V_{TH} Sensitivity for Neutral Biomolecules (b) V_{TH} Sensitivity for Charged Biomolecules

3.5 Summary

In this work, Trench Gate Engineered JAM Gate-All-Around (TGE-JAM-GAA) BioFET architecture for label-free biosensing applications has been thoroughly examined. The findings of this work showed that the TGE-JAM-GAA BioFET incorporates the enhanced electrostatic integrity of the trench gate, along with the efficient transport efficiency and improvement in hot carrier effects owing to the triple metal gate. These characteristics offer better immunity from short-channel effects in Junction Accumulation Mode design, which significantly enhances sensing performance. The comparative performance analysis in terms of channel center potential, electron concentration, drain current characteristics, and various sensitivities exhibit that the TGE-JAM-GAA BioFET significantly outperforms the TMNG-JAM-GAAFET and SMNG-JAM-GAAFET. For neutral APTES biomolecules, the TGE-JAM-GAA BioFET demonstrates 46.45% and 143.58% greater I_{ON} current sensitivity and six times and 14 times higher V_{TH} sensitivity than that of the TMNG-JAM-GAAFET and SMNG-JAM-GAAFET. The I_{ON}/I_{OFF} sensitivity of the proposed device for the case of neutral APTES biomolecules is 6×10^3 which is 9.32 times higher than that of the TMNG-JAM-GAAFET and 9.46×10^3 times higher than that of SMNG-JAM-GAAFET. The proposed biosensor's efficacy has also been examined for positive and negative charged biomolecules. It has been reported that for charged biomolecules, the TGE-JAM-GAA BioFET biosensor has superior biosensing performance characteristics in terms of V_{TH} , I_{ON} , and I_{ON}/I_{OFF} sensitivities, along with the larger drift in transconductance. Following a thorough investigation, it has been determined that the proposed TGE-JAM-GAA BioFET biosensor device exhibits a considerable improvement in biosensing characteristics and is a suitable contender for biosensing applications.

CHAPTER 4

ANALYTICAL MODELING AND NUMERICAL SIMULATION OF GRADED JAM SPLIT GATE-ALL-AROUND (GJAM-SGAA) BIO-FET

This chapter presents the analytical model of a novel biosensor called Graded JAM Split Gate-All-Around (GJAM-SGAA) Bio-FET for the detection of Avian Influenza antibodies and DNA. The GJAM-SGAA Bio-FET utilizes a silicon Gate-All-Around FET, which operates in the Junction Accumulation Mode (JAM), with a graded doping in the channel. This Bio-FET also features a gate underlap double-sided cavity that enables the detection of biomolecules without the use of labels. Gate underlap cavities overcome the fabrication complexity of nanocavities and provide structural stability. A comparative analysis between the GJAM-SGAA Bio-FET and non-graded JAM Split Gate-All-Around FET (SGAA-FET) demonstrates that the proposed BioFET has 5.72 times higher I_{ON} current sensitivity, 5.3 times increase in threshold voltage sensitivity ($S_{V_{th}}$), and 2.13×10^2 times improvement in switching ratio sensitivity for avian influenza biomolecule. The $S_{V_{th}}$ of the proposed biosensor is compared with the existing biosensors, and it was found that a triple-metal engineered gate and graded doped channel substantially boost the sensitivity of the proposed biosensor.

Problem Statement

Analytical modeling of a Gate-All-Around Field Effect transistor-based sensor that utilizes JAM-graded doping in the channel and a split Gate-All-Around structure for the detection of biomolecules, specifically for avian influenza antibody and DNA, while investigating the influence of triple metal gate, oxide stacking, and other factors on threshold voltage and current sensitivities.

4.1 Introduction

For a disease to be identified and eventually receive the proper treatment, an effective disease diagnosis is necessary. Many diseases are currently diagnosed using a variety of symptoms, which might lead to a delayed diagnosis or be misleading because of their ambiguous relationship to the clinical state and subjective character. The infection produced by various strains of influenza is referred to as avian influenza. This is a virus known to infect birds and sometimes trigger epidemics of viral sickness in humans. There have been various outbreaks of avian influenza, including an H5N1 strain outbreak in Hong Kong in 1997 and a H7N9 pandemic in Eastern and Southern China in 2013. Despite the fact that avian influenza viruses mostly infect birds, in humans too, a significant number of confirmed cases necessitate hospitalization and often intensive care unit (ICU) care [214].

Detection of deoxyribonucleic acid (DNA) gives new impetus to fundamental research in essential areas that directly impact human health. Currently, DNA molecular analysis can directly diagnose more than 400 diseases, and this number is continually

increasing, making DNA detection more and more crucial [215], [216]. Single-stranded DNA (ssDNA) is a linear structure with only one DNA strand, whereas double-stranded DNA (dsDNA) is a helical form with two DNA strands connected by hydrogen bonds.

Gate-All-Around Field Effect Transistors (GAAFETs) have gained prominence due to their increased gate control capabilities over the channel. This enhanced control results in improved resistance against short-channel effects (SCEs), effective field confinement, and increased packing density [83], [217]. GAA-based FETs are acknowledged as the ultimate entity for down scaling devices shorter than 50 nm [218], since they enable higher packing density, steeper sub-threshold slope, and excellent current driving capabilities. Biosensors based on nanogap etched field-effect transistors (FETs) [131], [219], [220] and tunnel FET [221]–[225] are becoming more popular for label-free detection of neutral/charged biomolecules. These Nanogaps are incorporated in the oxide layers where the biomolecules are trapped [131]. As a result, depending on the dielectric constant and charge behaviour of the biomolecules, the threshold voltage (V_{th}) and on current (I_{ON}) of the device vary dramatically, making detection of specific types of biomolecules conceivable [220]. The hovering of the gate in the nanogap causes the device structure to be unstable. Lee et al. introduced an innovative solution in the form of an underlapped FET biosensor to address the challenge of structural instability [226]. Additionally, the underlapped design enhances the likelihood of biomolecules binding and sensitivity of the biosensor [226], [227]. In contrast to nanogap FETs, in an underlap gate FET, a significant portion of the gate metal and oxide are etched to provide the sensing area. As a result, the hovering gate electrode problem is resolved. A thin gate oxide is retained in the nanogap or underlap region of both structures to act as a binding site [226].

Gate Metal work function Engineering (GME) is an effective technique to improve the performance parameters of GAAFET. Y. Pratap et al. and A. Das et al. presented GME architectures made up of three metal-gate materials [228], [229]. The gate situated closer to the source side has a higher work function material, while the gate material positioned near the drain side possesses the lowest work function. The work function of the central gate falls between the work functions of the two outer gates. This combination improves transport efficiency and decreases the electric field at the drain side, which improves hot-carrier effects dramatically [228], [230]. Recently, A. Das et al. [231] introduced a new type of triple metal surrounding gate FET biosensor, which incorporates a channel with a step graded doping profile. This design enhancement has led to a significant improvement in the transistor's sensitivity.

This work makes use of a Gate-All-Around FET that operates in the Junction Accumulation Mode (JAM). JAM FETs have no junctions, despite the channel's doping level being slightly lower than that of the source/drain area. In this work, the advantages of GAA JAMFET are used to create an extremely sensitive biosensor by employing graded doping in channel region, gate metal work function engineering and double-sided open cavities.

4.1.1 JAM FET

The concept of Junction Accumulation Mode (JAM) Field Effect Transistor (FET) has been previously discussed in earlier chapters.

4.1.2 Graded Doping

Despite uniform doping, the gradual variation in the doping concentration of the channel region of the field effect transistor is known as the graded channel. This gradual variation in doping concentration provides a non-uniform electric field, resulting in a decrease in the peak electric fields and hence lowers the hot carrier injections and other reliability issues. The graded doping profile enhances the carrier mobility in the channel, resulting in higher I_{ON} currents and better switching characteristics [232], [233]. As transistors continue to shrink, these strategies offer innovative solutions to combat short-channel effects and performance limitations.

Grading can be provided in steps of two or more. In this work, a step graded doping profile has been considered for the channel. The channel has been divided into three equal parts with doping of $N_{Doping1}$ (part of the channel near the source), $N_{Doping2}$ (in the middle part of the channel), and $N_{Doping3}$ (part of the channel near the drain) as depicted in Fig. 4.1. Lateral step-graded doping in the channel enhances the sensitivity by creating a doping gradient that improves charge carrier mobility. This gradient facilitates faster charge transport and increases the effective carrier concentration, resulting in enhanced current and voltage modulation [234]. Consequently, sensitivity increases due to the step-graded doping profile if used in FET based biosensors.

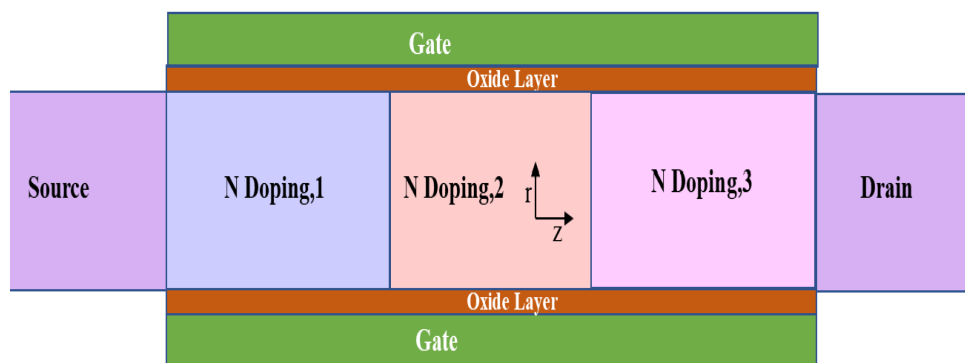


Fig. 4.1 Step Graded Doping in the Channel of FET

4.1.3 Split (or Underlap) Gate FET and Open Cavity-Based Biosensors

In the context of dielectric modulated FET biosensors, a nanogap is created by selectively removing the oxide layer through etching [131], [219], [220]. The DMFET biosensors are becoming increasingly popular for the label-free detection of both neutral and charged biomolecules. The nanogaps, which are included in the oxide layers, confine biomolecules and, based on their dielectric constant and charge behavior, result in substantial changes in the threshold voltage and ON current of the device [220]. This modification allows for the identification of particular

biomolecules. The main concern with nanogaps is the lack of structural stability due to the gate floating within the nanogap, which might result in possible reliability problems.

Lee et al. [226] proposed underlapped FET biosensors to solve the structural instability observed in split gate FETs. This novel design entails selectively removing a substantial percentage of the gate metal and oxide to form a specific area for sensing. This design successfully addresses the problem of the hovering gate electrode, resulting in a more stable and sensitive platform for detecting biomolecules. This design is referred to as a split gate FET design, as the gate has been divided into sections to form a cavity.

The underlap design has numerous benefits:

1. Improved Structural Stability:

Reliability is increased by strengthening the device's structural integrity through the elimination of the hovering gate.

2. Enhanced Biomolecule Binding and Sensitivity:

A thin gate oxide that serves as a binding site for biomolecules is retained in the sensing region of both nanogap and underlap gate FETs [226]. The design with an underlap gate enhances the probability of biomolecules binding to the sensing region, enhancing the biosensor sensitivity [16].

Thus, the development of underlap cavity-based biosensors marks a significant improvement over traditional nanogap FETs by addressing structural instability and enhancing biomolecule binding and sensitivity. These advancements contribute to more reliable and effective biosensors for label-free detection of biomolecules. Fig. 4.2 depicts the underlap FET structure with two open cavities for biomolecule immobilization.

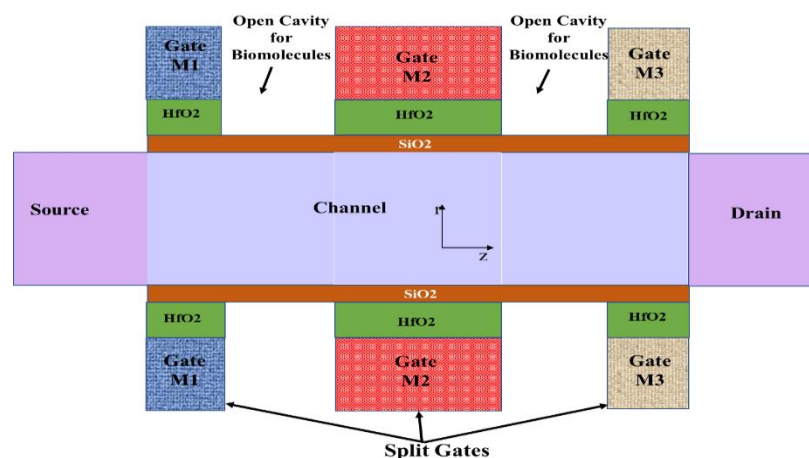


Fig. 4.2 Split Gate FET Structure with Open Cavity for Biomolecules Immobilization

4.1.5 Oxide Stacking

Rigorous and continual scaling of the MOSFET devices paves the path for many critical challenges, which include the short channel effects (SCEs). The scaling is not limited to the length and width of the channel only but extends its advantages to scaling the thickness of the SiO_2 layer for implementation of the device in low power, high-performance CMOS applications also. Curtailing the thickness of the dielectric layer boosts the gate capacitance and further the drive current, elevating the performance of the device. Also, with further miniaturization of oxide thickness below 2 nm, owing to the tunneling effect, the leakage currents rise drastically, thus leading to an inferior reliability of the device and higher power consumption.

With time, the oxide thickness has decreased. On-current (I_{ON}) rises with a thinner oxide, as a result of greater gate capacitance (C_{ox}). To optimize the circuit speed, high value of I_{ON} is required. In short channel length devices, controlling threshold voltage roll-off and therefore subthreshold leakage is the second reason for lower oxide thickness.

But the oxide thickness less than 1.5 nm causes the tunnelling leakage which limits the further minimization of the oxide thickness. Also, at high chip temperatures, the prolonged operation under high electric fields limits the oxide thickness minimization. At these temperatures, the weaker atomic bonds associated with Si/ SiO_2 interface can break, leading to the creation of oxide charges and shifts in the threshold voltage.

To overcome the limitations of thin oxide layers is to use the dielectric materials which has a higher dielectric permittivity. These materials enable the attainment of a large physical thickness while maintaining a small Effective Oxide Thickness (EOT), while is crucial in nanoscale devices. The EOT is the measure of the thickness of a SiO_2 layer that has the same capacitance as the high-k dielectric layer [122], [235], [236].

High-k dielectrics improve gate control over the channel, but interface traps, bulk fixed charges, and low interface carrier mobility concerns limit their use. Since none of the alternative dielectric materials generate a native oxide on silicon, a thin SiO_2 interfacial layer is inevitable. As illustrated in Fig. 4.3, the innovative dielectric stacks consist of a thin low K oxide (SiO_2 , Al_2O_3) layer and a thick high-k layer (HfO_2).

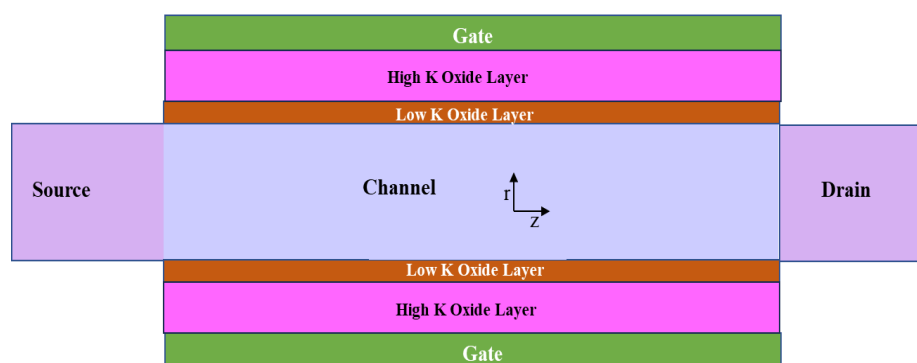


Fig. 4.3 Oxide Stack Architecture consisting of Low-K and High-K Oxide in FETs

The implementation of an extremely thin low K dielectric layer enhances both quality as well as consistency of the interface. The inclusion of a low-k layer in the stack architecture greatly reduces the fringing electric field, hence lowering the DIBL effect. This reduction in fringing electric field is achieved by reducing the thickness of the high-k layer while maintaining the same Equivalent Oxide Thickness (EOT). The high fringing fields are concentrated electrically into the low-k dielectric layer as a result of the continuity of displacement. This has the potential to alter the impact of the fringing field on the properties of the device. MOSFETs are particularly prone to hot carrier effects, which are mainly caused by the high electric field at the drain side.

4.1.6 Gate Material Engineering

The previous chapters have previously covered the topic of gate material engineering, which involves the usage of gate metals with varying workfunctions. This chapter presents a design proposal that utilizes gate material engineering with three distinct work function gates in a split gate structure. The three gates are independent and not connected to each other.

4.1.7 Avian Influenza and DNA Detection

Avian influenza, or bird flu, is a virus that has affected bird populations for over a century. The virus is categorized by two proteins on its surface: hemagglutinin (H) and neuraminidase (N). There have been various outbreaks of avian influenza, including an H5N1 strain outbreak in Hong Kong in 1997 and a H7N9 pandemic in Eastern and Southern China in 2013. Despite the fact that avian influenza viruses mostly infect birds, in humans too, a significant number of confirmed cases necessitate hospitalization and often intensive care unit (ICU) care [214]. This strain has spread to various parts of the world, causing major outbreaks in poultry and leading to millions of birds being culled to control the disease. Human infections with H5N1 are rare but often fatal, highlighting the need for quick and effective detection.

Most current detection methods for avian influenza, such as viral culture and PCR, are highly accurate but can take a while and require specialized labs. Semiconductor technology in FET biosensors rapidly and sensitively detects viral biomolecules. Some key advantages of this FET biosensor are as follows; Their results are quick which helps in fast outbreak control. Because of their portability, they can be employed in remote areas or in on-site settings causing delays related to sample transport to be minimized. This makes the devices easy to operate and can be used by anyone with minimal training. In addition, because FET biosensors are inexpensive, they are appropriate for frequent testing and can help both prevent economic losses in the poultry industry and protect public health.

Detection of deoxyribonucleic acid (DNA) gives new impetus to fundamental research in essential areas that directly impact human health. Currently, DNA molecular analysis can directly diagnose more than 400 diseases, and this number is continually increasing, making DNA detection more and more crucial [215], [216]. Single-stranded DNA (ssDNA) is a linear structure with only one DNA strand, whereas

double-stranded DNA (dsDNA) is a helical form with two DNA strands connected by hydrogen bonds.

There is a great need of rapid detection of DNA biomolecules in various domains such as health care, biotechnology, agriculture, environmental monitoring and forensic science. The ability to identify DNA sequences quickly and with accuracy holds enormous potential for improved outcomes, better research, and ensuring security and sustainability.

Medical Diagnostics

Rapid screening of diseases - with the help of rapid DNA detection - is the hallmark of this technology that allows for immediate identification of diseases, including genetic issues, cancers, and viruses. By detecting such diseases at an early stage, healthcare providers can promptly initiate therapies, thereby greatly improving the likelihood of recovery. In addition, the identification of specific genetic markers facilitates the development of individualized treatment strategies.

Infectious Disease Control

Rapid identification of pathogenic DNA is crucial in the context of infectious diseases. Rapid detection of bacteria, viruses, and other pathogens enables prompt actions in reaction to outbreaks, aiding in the containment of diseases. It is crucial for effectively handling novel diseases and avoiding global outbreaks and pandemics.

Biotechnology and Research

DNA detection speed is an extremely important factor in the fields of biotechnology and research. The investigation of genetic sequences, the roles of genes, and the development of projects involving genetic engineering are all sped up as a result of this, which is crucial for the advancement and innovation of scientific research.

Agriculture

Rapid DNA detection is essential for enhancing crop quality and controlling pests in the field of agriculture. Researchers can enhance crop types by promptly finding advantageous genetic features, resulting in increased yields, enhanced disease resistance, and superior nutritional profiles.

Environmental Monitoring

Quick DNA detection is a huge boon to environmental monitoring. To preserve ecosystems and comprehend ecological dynamics, this technology is crucial for assessing and monitoring biodiversity through identifying species in environmental samples. On top of that, protecting and cleaning up polluted areas can be made easier when DNA from particular microbes can be detected.

Forensic Science

Forensic science relies heavily on quick DNA detection to analyze evidence from crime scenes. The prompt identification of individuals using biological samples expedites criminal investigations and enhances the precision of forensic findings, contributing to the more effective and dependable resolution of crimes.

4.2 GJAM-SGAA Bio-FET Device Structure and Simulation Specification

A depiction of the Graded JAM Split Gate-All-Around (GJAM-SGAA) Bio-FET in a three-dimensional format is illustrated in Fig. 4.4 (a). The structure has cylindrical Gate-All-Around FET with Gate Metal Engineering consisting three independent gates, Gate M_1 , Gate M_2 and Gate M_3 with different work functions. Gate work function engineering provides the inherent ability to reduce different SCEs while improving threshold voltage and drain current characteristics [230]. Fig. 4.4 (c) depicts the GJAM-SGAA Bio-FET from a two-dimensional aspect. The channel in the GJAM-SGAA Bio-FET design is divided into three distinct regions, namely R-1, R-2, and R-3. These regions are assigned with different doping concentrations designated as N_{D1} , N_{D2} , and N_{D3} respectively. The doping concentrations in R-1, R-2, and R-3 are arranged in a graded manner, with N_{D1} being the highest and N_{D3} being the lowest. This graded doping profile in the channel enhances carrier depletion within the channel, thereby contributing to the reduction in OFF current and improvement in sensor performance [120], [233]. In order to create two nano-cavities known as open cavities or gate underlap regions for analyte binding, the device's cylindrical gate is split at the source side and drain side as shown in Fig. 4.4 (c). To increase the physical thickness of the gate oxide, a high-K (HfO_2) oxide has been placed on top of silicon dioxide (SiO_2). Several work focusing on stack gate MOSFETs have been introduced in literature with the aim of improving performance and sensitivity [237]–[239]. The analytes have been bound to the open-cavity of device on the incredibly thin SiO_2 layer in the cavity area. With the exception of the same work function gate (no GME) and one split gate open cavity, SGAA-FET biosensor has been modeled and simulated with the same dimension as the proposed BioFET.

While performing research involving devices like transistors or sensors, it is important to validate the theoretical and simulated results by comparing them with experimental data. The correctness and reliability of the simulations and models being employed are ensured through this validation process. Fig. 4.4 (b) illustrates the calibration of the simulations for the proposed device with respect to the experimental data [152]. The drain current versus gate voltage characteristics shows excellent agreement in this graph for both simulated and experimental data. Table 1. presents the characteristics of two biosensors: the GJAM-SGAA Bio-FET and the SGAA-FET. It provides information on the device parameters of both biosensors, such as the dimensions, type of material used, gate oxide thickness, length and thickness of cavity etc.

Table 4.1 Device Design Parameters [141]

Physical Device Parameter	GJAM-SGAA Bio-FET	SGAA-FET Biosensor
Channel Length, L_{Channel} (nm)	100	100
Thickness of silicon film, t_{si} (nm)	20	20
Length of source/drain, L_S/L_D (nm)	15	15
Metal gate work-function (eV)	5.1, 5.0, 4.7	5.3
Oxide Thickness, SiO ₂ & HfO ₂ , (nm)	$t_1=1.0$ & $t_2=3.0$	$t_1=1.0$ & $t_2=3.0$
Doping of Channel Region, N_{D1} , N_{D2} , N_{D3} (/cm ³)	5×10^{18} , 1×10^{18} , 1×10^{17}	1×10^{18}
Doping of Source and Drain Region, N_D (/cm ³)	1×10^{19}	1×10^{19}
Thickness of Cavity, t_c (nm)	10	10
Gate Thickness, t_g (nm)	7	7
Gate Length, L_{G1} , L_{G2} , L_{G3} (nm)	$L_{G1}=20$, $L_{G2}=30$, $L_{G3}=20$	$L_{G1}=35$, $L_{G2}=35$
Length of Cavity, L_{Cavity} (nm)	$L_{\text{Cavity}}=L_{\text{Cavity}1}+L_{\text{Cavity}2}=15+15=30$	30
HfO ₂ and SiO ₂ dielectric constants	22.0 & 3.9	22.0 & 3.9

The proposed device underwent simulation using the Silvaco Atlas-3D tool for device simulation [151]. Different models such as AUGER and SRH were utilized to represent the recombination of minority carriers in semiconductors. The modeling of recombination through the Shockley-Read-Hall (SRH) mechanism is described in the following equation [240], [241]:

$$R_{SRH} = \frac{pn - n_i^2}{\tau_p^0 \left[n + n_i \exp\left(\frac{ETRAP}{kT_L}\right) \right] + \tau_n^0 \left[p + n_i \exp\left(\frac{-ETRAP}{kT_L}\right) \right]} \quad (4.1)$$

ETRAP stands for the difference between the energy level of the trap and the intrinsic Fermi level. T_L refers to the temperature measured in kelvin, and τ_n^0 and τ_p^0 correspond to the lifetimes of electrons and holes, respectively. The expression for the Boltzmann transport statistics equation is as follows:

$$f(\varepsilon) = \frac{1}{1 + \exp\left(\frac{\varepsilon - E_F}{kT_L}\right)} \quad (4.2)$$

Here, $f(\varepsilon)$ represents the likelihood of an accessible electron state with energy ε being occupied by an electron. E_F denotes the fermi energy level, and k stands for Boltzmann's constant.

FLDMOB and CONMOB models were used to represent mobility that is dependent on concentration, while BGN was used to represent carrier statistics, all aimed at validating the high channel doping profile against doping versus mobility [151]. Quantum effects have not been taken into account in this work, as they become significant only when the channel's thickness and length are less than 10 nm [92], [160], [242]–[247].

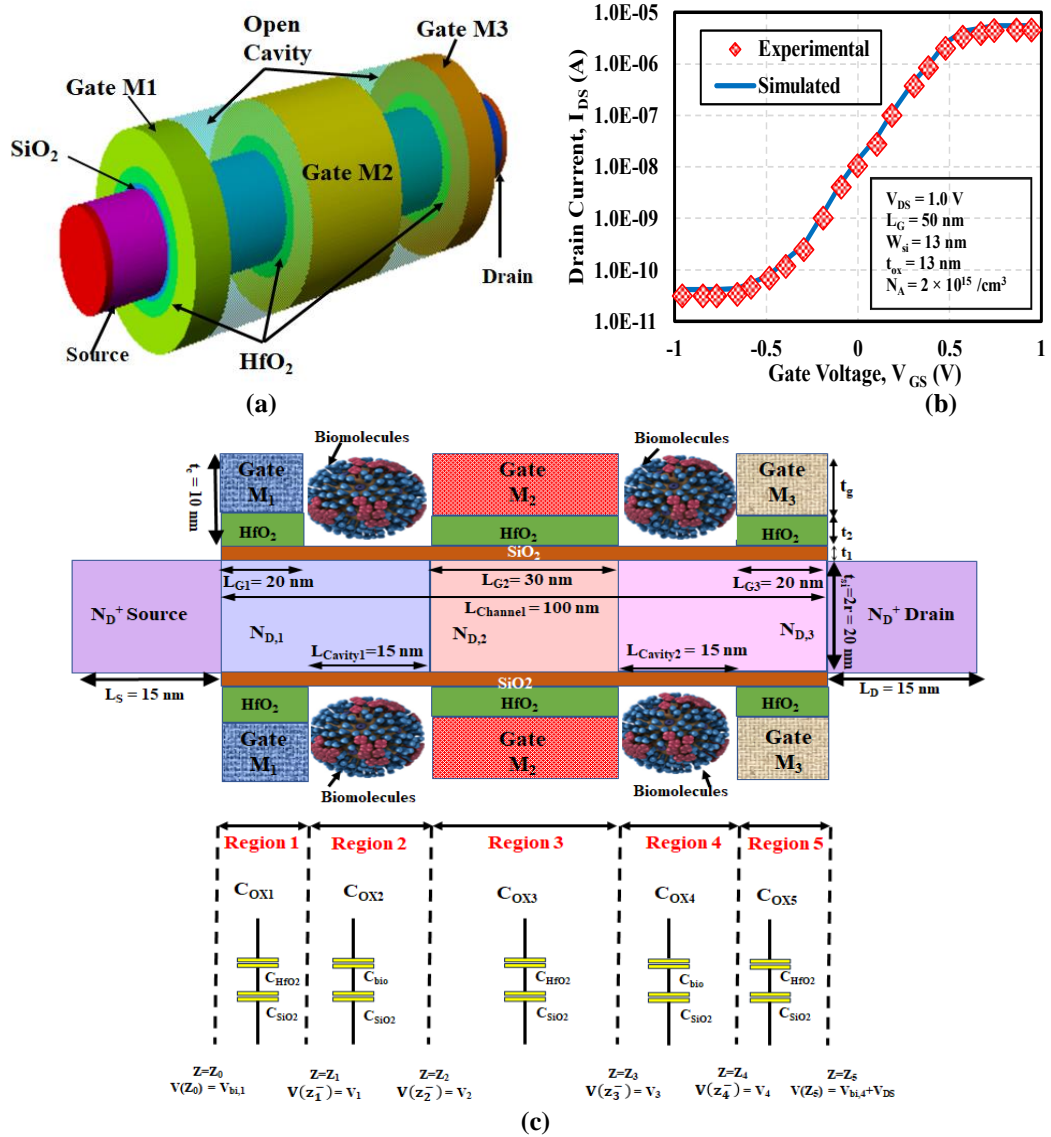


Fig. 4.4 (a) 3-Dimensional View of GJAM-SGAA Bio-FET (b) Calibration of Simulation Setup with Experimental Data [152] (c) 2-Dimensional Structure of GJAM-SGAA Bio-FET

4.3 Analytical Modeling

To comprehensively analyze the electrical properties of the proposed device, it becomes imperative to solve the two-dimensional Poisson's equation. The analytical framework used to determine the channel potential, threshold voltage, and subthreshold slope relies on the center-channel potential approach.

4.3.1 Modeling of Surface Potential

To derive the surface potential, the Poisson's equation describing the potential distribution in each respective region of the channel (Region 1 to 5) is as follows:

$$\frac{1}{r} \frac{\partial}{\partial r} \left[r \frac{\partial}{\partial r} \{ \psi(r, z) \} \right] + \frac{\partial^2}{\partial z^2} \psi(r, z) = - \frac{qN_{Ch,i}}{\epsilon_{Si}} \quad (4.3)$$

$\psi(r, z)$ stands for the channel potential within region i , $N_{Ch,i}$ indicates the doping concentration specific to channel region i , and ϵ_{Si} corresponds to the dielectric permittivity of silicon.

Let the diameter of channel is '2d' so the radius $r=d$. The center channel potential can be represented as $\psi_C(z)$ or $\psi(0, z)$. The potential at the surface interface ($r = d$) is denoted by $\psi_1(z)$ or $\psi(d, z)$.

The general solution of potential can be expressed in accordance with a parabolic profile,

$$\psi(r, z) = P_0(z) + P_1(z)r + P_2(z)r^2 \quad (4.4)$$

where, P_0 , P_1 and P_2 are arbitrary constants. To solve the above Poisson's equation, different boundary conditions used are [25], [248]:-

- i. At $z = z_0$, potential at the source-channel boundary can be expressed as,

$$\psi(r, z_0) = V_{bi,1} = \frac{k_B T}{q} \left\{ \ln \left(\frac{N_S N_{D1}}{n_i^2} \right) \right\} \quad (4.5)$$

where, N_S and n_i represents the source doping and intrinsic charge carrier concentration of silicon. N_{D1} is the doping concentration of region R1.

- ii. At $z = z_5$, potential at the drain-channel boundary can be expressed as,

$$\psi(r, z_5) = V_{bi,4} + V_{DS} = \frac{k_B T}{q} \left\{ \ln \left(\frac{N_{D3} N_{Drain}}{n_i^2} \right) \right\} + V_{DS} \quad (4.6)$$

Where, $V_{bi,4}$ is the built-in potential, V_{DS} is drain to source voltage, N_{D3} is channel concentration in R-3 and N_{Drain} is drain region doping.

- iii. Potential at z_i is given by,

$$\psi(r, z_1^-) = V_1 \quad (4.7a)$$

$$\psi(r, z_2^-) = V_2 \quad (4.7b)$$

$$\psi(r, z_3^-) = V_3 \quad (4.7c)$$

$$\psi(r, z_4^-) = V_4 \quad (4.7d)$$

- iv. Electric field is continuous at intersection of two regions, $z = z_1/z_2/z_3/z_4$,

$$\left. \frac{\partial \{ \psi(r, z) \}}{\partial z} \right|_{z=z_1^-} = \left. \frac{\partial \{ \psi(r, z) \}}{\partial z} \right|_{z=z_1^+} \quad (4.8a)$$

$$\left. \frac{\partial \{ \psi(r, z) \}}{\partial z} \right|_{z=z_2^-} = \left. \frac{\partial \{ \psi(r, z) \}}{\partial z} \right|_{z=z_2^+} \quad (4.8b)$$

$$\left. \frac{\partial \{ \psi(r, z) \}}{\partial z} \right|_{z=z_3^-} = \left. \frac{\partial \{ \psi(r, z) \}}{\partial z} \right|_{z=z_3^+} \quad (4.8c)$$

$$\left. \frac{\partial\{\psi(r,z)\}}{\partial z} \right|_{z=z_4^-} = \left. \frac{\partial\{\psi(r,z)\}}{\partial z} \right|_{z=z_4^+} \quad (4.8d)$$

v. Electric field at the center of the channel is zero,

$$\left. \frac{\partial\psi(r,z)}{\partial r} \right|_{r=0} = 0 \quad (4.9)$$

vi. Potential at z_1 and z_4 is continuous,

$$\psi(r, z_1^-) = \psi(r, z_1^+) \quad (4.10a)$$

$$\psi(r, z_4^+) = \psi(r, z_4^-) \quad (4.10b)$$

vii. Potential at z_2 and z_3 is discontinuous due to step-doping profile,

$$\psi(r, z_2^+) = V_2 + V_{bi,2} \quad (4.11a)$$

$$\psi(r, z_3^+) = V_3 + V_{bi,3} \quad (4.11b)$$

viii. Electric field is continuous at Si-SiO₂ interface,

$$\varepsilon_{Si} \left. \frac{\partial\{\psi(r,z)\}}{\partial r} \right|_{r=d} = C_{ox} [V_{GS} - V_{fbi} - \psi(r, z)] \Big|_{r=d} \quad (4.12a)$$

$$\left. \frac{\partial\{\psi(r,z)\}}{\partial r} \right|_{r=d} = \frac{C_{ox}}{\varepsilon_{Si}} [V_{GS}^* - \psi_I(z)] \quad (4.12b)$$

V_{fbi} refers to the flat band voltage associated with region R_i . Using the above boundary conditions, the potential $\psi(r, z)$ can be written in terms of $\psi_I(z)$.

$$\psi(r, z) = \frac{1}{2\varepsilon_{ch}} [\psi_I(z) \{C_{ox}d + 2\varepsilon_{ch}\} - (V_{GS} - V_{fbi})C_{ox}d] + \frac{C_{ox,i}}{2\varepsilon_{Si}} [V_{GS} - V_{fbi} - \psi_I(z)] r^2 \quad (4.13)$$

For $r = 0$ in equation (4.11), $\psi(0, z) = \psi_C(z)$ and relationship between $\psi_C(z)$ and $\psi_I(z)$ can be expressed as:

$$\psi_I(z) = \frac{[C_{ox,i}d(V_{GS} - V_{fbi}) + 2\psi_C(z)\varepsilon_{Si}]}{2\varepsilon_{Si} + C_{ox,i}d} \quad (4.14)$$

Now, a differential equation can be formed in terms of center channel potential by putting equation (4.13) and (4.14) in equation (4.3).

$$\mu^2 \frac{\partial^2 \psi_C(z)}{\partial z^2} + \theta = \psi_C(z) \quad (4.15a)$$

$$\theta = (V_{GS} - V_{fbi}) + \frac{qN_{Ch,i}}{2C_{ox,i}} + \frac{qN_{Ch,i}d^2}{4\varepsilon_{Si}} \quad (4.15b)$$

$$\mu = \sqrt{\frac{d\varepsilon_{Si}}{2C_{ox,i}}} \quad (4.15c)$$

Generalized solution of equation (4.15 a) can be written as,

$$\psi_C(z) = pe^{\frac{z}{\mu}} + qe^{-\frac{z}{\mu}} + \theta \quad (4.16)$$

where, μ and θ are material dependent parameters. While p and q are arbitrary constants. The effective capacitance in each region (Region 1 /Region 3/Region 5) is the series combination of two capacitances, C_{SiO_2} and C_{HfO_2} ignoring the dielectric leakage current and absorption [249]. In the proposed GJAM-SGAA Bio-FET device structure, there is no gate over nanocavities. Such structure is known as Underlap gate FET structure where the gate electrode does not fully cover the channel region, leaving a gap or "underlap". When a voltage is applied to the gate electrode, it creates an

electric field in the semiconductor channel underneath the gate. However, due to the underlap design, some electric field lines extend beyond the gate's physical boundaries. Capacitance associated with these fringing field lines is referred to as fringing field capacitance (C_{fr}). It represents the ability of these field lines to store electrical charge and affect the potential energy in the channel region. Fringing capacitance (C_{fr}) takes on a pivotal role in the GJAM-SGAA Bio-FET. This Bio-FET design includes two underlap regions, specifically Region 2 and Region 4, in which the influence of fringing capacitance will be substantial. In the underlap regions, capacitance (C_{fr}) is modeled by considering the approximate effect of biomolecules occupying the cavity under the fringing fields [250]–[252].

So, $\psi_C(z)$ can be expressed in five regions (Region 1/ Region 2/ Region 3/ Region 4 /Region 5) separately:

Region 1: $z_0 \leq z \leq z_1$

$$\psi_{C1}(z) = p_1 e^{\frac{z}{\mu_1}} + q_1 e^{\frac{-z}{\mu_1}} + \theta_1 \quad (4.17a)$$

$$p_1 = \frac{1}{e^{-\frac{(z_0-z_1)}{\mu_1}} - e^{\frac{(z_0-z_1)}{\mu_1}}} \left[V_1 e^{\frac{-z_0}{\mu_1}} - V_{bi,1} e^{\frac{-z_1}{\mu_1}} - \theta_1 \left(e^{\frac{-z_0}{\mu_1}} - e^{\frac{-z_1}{\mu_1}} \right) \right] \quad (4.17b)$$

$$q_1 = \frac{1}{e^{-\frac{(z_1-z_0)}{\mu_1}} - e^{\frac{(z_1-z_0)}{\mu_1}}} \left[V_1 e^{\frac{z_0}{\mu_1}} - V_{bi,1} e^{\frac{z_1}{\mu_1}} - \theta_1 \left(e^{\frac{z_0}{\mu_1}} - e^{\frac{z_1}{\mu_1}} \right) \right] \quad (4.17c)$$

$$C_{ox,1} = \frac{\epsilon_{SiO_2}}{d \ln\left(1 + \frac{t_{eff}}{d}\right)}, t_{eff} = t_2 \left(\frac{\epsilon_{SiO_2}}{\epsilon_{HfO_2}} \right) + t_1 \quad (4.17d)$$

Region 2: $z_1 \leq z \leq z_2$

$$\psi_{C2}(z) = p_2 e^{\frac{z}{\mu_2}} + q_2 e^{\frac{-z}{\mu_2}} + \theta_2 \quad (4.18a)$$

$$p_2 = \frac{1}{e^{-\frac{(z_1-z_2)}{\mu_2}} - e^{\frac{(z_1-z_2)}{\mu_2}}} \left[V_2 e^{\frac{-z_1}{\mu_2}} - V_1 e^{\frac{-z_2}{\mu_2}} - \theta_2 \left(e^{\frac{-z_1}{\mu_2}} - e^{\frac{-z_2}{\mu_2}} \right) \right] \quad (4.18b)$$

$$q_2 = \frac{1}{e^{-\frac{(z_2-z_1)}{\mu_2}} - e^{\frac{(z_2-z_1)}{\mu_2}}} \left[V_2 e^{\frac{z_1}{\mu_2}} - V_1 e^{\frac{z_2}{\mu_2}} - \theta_2 \left(e^{\frac{z_1}{\mu_2}} - e^{\frac{z_2}{\mu_2}} \right) \right] \quad (4.18c)$$

$$\frac{1}{C_{ox,2}} = \frac{1}{C_{SiO_2}} + \frac{1}{C_{fr}}, C_{SiO_2} = \frac{\epsilon_{SiO_2}}{d \ln\left(1 + \frac{t_{t1}}{d}\right)}, \quad (4.18d)$$

$$C_{fr} = C_{bio} = \frac{2\epsilon_{bio}}{n\pi L_C} \sinh\left(\cosh^{-1}\left(\frac{(t_2+t_1)+t_g}{t_2+t_1}\right)\right) \quad (4.18e)$$

Region 3: $z_2 \leq z \leq z_3$

$$\psi_{C3}(z) = p_3 e^{\frac{z}{\mu_3}} + q_3 e^{\frac{-z}{\mu_3}} + \theta_3 \quad (4.19a)$$

$$p_3 = \frac{1}{e^{-\frac{(z_2-z_3)}{\mu_3}} - e^{\frac{(z_2-z_3)}{\mu_3}}} \left[V_3 e^{\frac{-z_2}{\mu_3}} - (V_2 + V_{bi,2}) e^{\frac{-z_3}{\mu_3}} - \theta_3 \left(e^{\frac{-z_2}{\mu_3}} - e^{\frac{-z_3}{\mu_3}} \right) \right] \quad (4.19b)$$

$$q_3 = \frac{1}{e^{-\frac{(z_3-z_2)}{\mu_3}} - e^{\frac{(z_3-z_2)}{\mu_3}}} \left[V_3 e^{\frac{z_2}{\mu_3}} - (V_2 + V_{bi,2}) e^{\frac{z_3}{\mu_3}} - \theta_3 \left(e^{\frac{z_2}{\mu_3}} - e^{\frac{z_3}{\mu_3}} \right) \right] \quad (4.19c)$$

$$C_{ox,3} = C_{ox,1} \quad (4.19d)$$

Region 4: $z_1 \leq z \leq z_2$

$$\psi_{C4}(z) = p_4 e^{\frac{z}{\mu_4}} + q_4 e^{\frac{-z}{\mu_4}} + \theta_4 \quad (4.20a)$$

$$p_4 = \frac{1}{e^{-\frac{(z_3-z_4)}{\mu_4}} - e^{-\frac{(z_3-z_4)}{\mu_4}}} \left[V_4 e^{\frac{-z_3}{\mu_4}} - (V_3 + V_{bi,3}) e^{\frac{-z_4}{\mu_4}} - \theta_4 \left(e^{\frac{-z_3}{\mu_4}} - e^{\frac{-z_4}{\mu_4}} \right) \right] \quad (4.20b)$$

$$q_4 = \frac{1}{e^{-\frac{(z_4-z_3)}{\mu_4}} - e^{-\frac{(z_4-z_3)}{\mu_4}}} \left[V_4 e^{\frac{z_3}{\mu_4}} - (V_3 + V_{bi,3}) e^{\frac{z_4}{\mu_4}} - \theta_4 \left(e^{\frac{z_3}{\mu_4}} - e^{\frac{z_4}{\mu_4}} \right) \right] \quad (4.20c)$$

$$C_{ox,4} = C_{ox,2} \quad (4.20d)$$

Region 5: $z_4 \leq z \leq z_5$

$$\psi_{C5}(z) = p_5 e^{\frac{z}{\mu_5}} + q_5 e^{\frac{-z}{\mu_5}} + \theta_5 \quad (4.21a)$$

$$p_5 = \frac{1}{e^{-\frac{(z_4-z_5)}{\mu_5}} - e^{-\frac{(z_4-z_5)}{\mu_5}}} \left[(V_{bi,4} + V_{DS}) e^{\frac{-z_4}{\mu_5}} - V_4 e^{\frac{-z_5}{\mu_5}} - \theta_5 \left(e^{\frac{-z_4}{\mu_5}} - e^{\frac{-z_5}{\mu_5}} \right) \right] \quad (4.21b)$$

$$q_5 = \frac{1}{e^{-\frac{(z_3-z_2)}{\mu_5}} - e^{-\frac{(z_3-z_2)}{\mu_5}}} \left[(V_{bi,4} + V_{DS}) e^{\frac{z_4}{\mu_5}} - V_4 e^{\frac{z_5}{\mu_5}} - \theta_5 \left(e^{\frac{z_4}{\mu_5}} - e^{\frac{z_5}{\mu_5}} \right) \right] \quad (4.21c)$$

$$C_{ox,5} = C_{ox,1} \quad (4.21d)$$

Values of μ_1 - μ_5 and θ_1 - θ_5 are mentioned in Appendix-A. Values of unknown constants V_1 , V_2 , V_3 and V_4 can be find using the boundary conditions mentioned in equation (4.3)-(4.10).

$$V_1 = \frac{c_6 c_2 - c_3 c_5}{c_2 c_4 - c_1 c_5} \quad (4.22a)$$

$$V_2 = \frac{c_6 c_1 - c_3 c_4}{c_1 c_5 - c_2 c_6} \quad (4.22b)$$

$$V_3 = d_1 + d_2 + d_3 \quad (4.22c)$$

$$V_4 = d_4 V_2 + d_5 V_3 + d_6 \quad (4.22d)$$

Values of c_1 - c_6 and d_1 - d_6 are given in Appendix-C. Each region's electric field can be expressed as,

$$E_{Z_i} = -\frac{1}{\mu_i} \left(p_i e^{\frac{z}{\mu_i}} - q_i e^{\frac{-z}{\mu_i}} \right) \quad (4.23)$$

4.3.2 Modeling of Threshold Voltage

For junctionless device, The threshold voltage is the gate voltage at which the minimum central potential $\psi_{C_{min}}$ equals to the Fermi potential when the flat band voltage is measured with respect to the intrinsic Fermi level [208], [253].

$$\psi_{C_{min}} \left(z, \frac{t_{si}}{2} \right) = V_b \quad (4.24a)$$

Where, V_b is the quasi-Fermi potential. The lowest potential point is consistently identified within region-2, which is associated with the negative charges introduced by biomolecules in the oxide layer [25].

$$\psi_{C_{min}}\left(z, \frac{t_{si}}{2}\right) = \psi_{C_2}(z = z_{Minima})\Big|_{V_{GS}=V_{th}} = V_b \quad (4.24b)$$

By setting the derivative of the channel-center potential expression in region-2 equal to zero, the exact position of this minimum potential point within the channel can be established.

$$\frac{d\psi_{C_2}(z)}{dz}\Big|_{z=z_{Minima}} = 0 \quad (4.24c)$$

$$z_{Minima} = \mu_1 \ln\left(\sqrt{\frac{q_2}{p_2}}\right) \quad (4.24d)$$

The expression for the minimum channel-center potential can be easily found by putting the value of z_{Minima} into equation (4.18 a). Then solving equation (4.24b), the threshold voltage is expressed as

$$V_{th} = \frac{-W_b + \sqrt{W_b^2 - 4W_aW_c}}{2W_a} \quad (4.25)$$

Appendix-B contains the values of W_a , W_b and W_c .

4.3.3 Modeling of Drain Current and Subthreshold Slope

In linear region, the drain current (I_{DS}) is determined separately in the five different regions, as outlined in references [99] and [254].

$$I_{DS(Lin,I)} = \frac{2\pi C_{ox1} d\mu_n}{L_{G1}} \left[(V_{GS} - V_t)(V_1 - V_{bi,1}) - \frac{(V_1 - V_{bi,1})^2}{2} \right] \quad (4.26)$$

$$I_{DS(Lin,II)} = \frac{2\pi C_{ox2} d\mu_n}{L_{Cavity1}} \left[(V_{GS} - V_t)(V_2 - V_1) - \frac{(V_2 - V_1)^2}{2} \right] \quad (4.27)$$

$$I_{DS(Lin,III)} = \frac{2\pi C_{ox3} d\mu_n}{L_{G2}} \left[(V_{GS} - V_t)(V_3 - V_x) - \frac{(V_3 - V_x)^2}{2} \right] \quad (4.28)$$

$$I_{DS(Lin,IV)} = \frac{2\pi C_{ox4} d\mu_n}{L_{Cavity2}} \left[(V_{GS} - V_t)(V_4 - V_y) - \frac{(V_4 - V_y)^2}{2} \right] \quad (4.29)$$

$$I_{DS(Lin,V)} = \frac{2\pi C_{ox5} d\mu_n}{L_{G3}} \left[(V_{GS} - V_t)(V_5 - V_4) - \frac{(V_5 - V_4)^2}{2} \right] \quad (4.30)$$

V_x and V_y can be calculated using appropriate boundary conditions and expressed as,

$$V_x = V_{bi,2} + \psi_2(r, z_2) \quad (4.31a)$$

$$V_y = V_{bi,3} + \psi_3(r, z_3) \quad (4.31b)$$

To calculate the drain current in the saturation region, V_{DS} is replaced with $V_{DS,Sat}$ [99], [248],

$$V_{DS,Sat} = \frac{(V_{GS} - V_{th})}{1 + \frac{\mu_{efld}(V_{GS} - V_{th})}{(L_{G1} + L_{Cavity1} + L_{G2} + L_{Cavity2} + L_{G3})v_{Sat}}} \quad (4.32)$$

$$\mu_{efld} = \frac{\mu_n}{\{1 - \zeta(V_{GS} - V_{th})\} \left\{ 1 + \Omega \frac{V_{DS}\mu_n}{(L_{G1} + L_{Cavity1} + L_{G2} + L_{Cavity2} + L_{G3})v_{Sat}} \right\}} \quad (4.33)$$

$$\Omega = \left[\frac{V_{DS}\mu_n}{(L_{G1} + L_{Cavity1} + L_{G2} + L_{Cavity2} + L_{G3})v_{Sat}} \right] \left[1.5 + \left\{ \frac{V_{DS}\mu_n}{(L_{G1} + L_{Cavity1} + L_{G2} + L_{Cavity2} + L_{G3})v_{Sat}} \right\}^{-1} \right]^{-1} \quad (4.34)$$

where V_{Sat} is the electron saturation velocity ($v_{Sat} = 1 \times 10^7$ cm/s), and μ_{efld} is the maximal low-field mobility of electrons. The symbol μ_n denotes the electron mobility, while η is a fitting constant with a precise 0.43 value.

SS, the subthreshold slope is calculated using minimum center-channel potential and can be expressed as,

$$SS = V_T \log(10) \left[\left(\frac{\partial \Psi(d,z)}{\partial V_{GS}} \right)^{-1} \right] \Big|_{z=z_{min}} \quad (4.35)$$

4.3.4 Modeling of Transconductance

Transconductance (g_m) is the change in the output current (I_{DS}) with respect to a change in the input voltage (V_{GS}) while keeping the drain to source voltage (V_{DS}) constant. Mathematically, it is expressed as:

$$g_m = \frac{dI_{DS}}{dV_{GS}} \Big|_{V_{DS} = constant} \quad (4.36)$$

According to equation (4.36), the transconductance in five different regions can be determined differentiating equations (4.26), (4.27), (4.28), (4.29) and (4.30).

$$g_{m1} = \frac{2\pi C_{ox1} d \mu_n}{L_{G1}} (V_1 - V_{bi,1}) \quad (4.37)$$

$$g_{m2} = \frac{2\pi C_{ox2} d \mu_n}{L_{Cavity1}} (V_2 - V_1) \quad (4.38)$$

$$g_{m3} = \frac{2\pi C_{ox3} d \mu_n}{L_{G2}} (V_3 - V_x) \quad (4.39)$$

$$g_{m4} = \frac{2\pi C_{ox4} d \mu_n}{L_{Cavity2}} (V_4 - V_y) \quad (4.40)$$

$$g_{m5} = \frac{2\pi C_{ox5} d \mu_n}{L_{G3}} (V_5 - V_4) \quad (4.41)$$

4.3.5 Modeling of Sensitivity

The sensitivity of a biosensor is indeed commonly calculated by measuring the relative change in the value of a sensing metric. This sensing metric could be any quantifiable electrical parameter that indicates the presence of the biomolecules, including the threshold voltage, current, subthreshold slope or other electrical parameters. Mathematically, sensitivity (S) can be defined as:

$$S_M = |M_{No\ Biomolecule} - M_{With\ Biomolecules}| \quad (4.42)$$

Where, $M_{No\ Biomolecule}$ is biosensor's output signal (e.g., voltage, current, SS) before exposure to the bio-analytes (biomolecules) and $M_{Biomolecules}$ is biosensor's output signal after immobilization of the biomolecules.

4.3.5.1 Drain Current Sensitivity

According to equation (4.42) drain current sensitivity (S_{ID}) can be modeled as:

$$S_{ID} = |I_{D\ No\ Biomolecule} - I_{D\ With\ Biomolecules}| \quad (4.43)$$

4.3.5.2 Threshold Voltage Sensitivity

Threshold voltage sensitivity ($S_{V_{th}}$) is the difference in V_{th} without biomolecule and with biomolecules calculated according to equation (4.42):

$$S_{V_{th}} = |V_{th\ No\ biomolecules} - V_{th\ With\ biomolecules}| \quad (4.44)$$

4.4 Results and Discussion

DNA and avian influenza antibody (AI-ab) are the target charged analytes used in the investigation. Dielectric and charge modulation detection principles are employed for charged analytes detection. The base layer for detection of AI-ab, consisting of SBP and AIa, was grouped together and simulated with an dielectric constant $K = 2$ and a surface charge density $Q_f = 2 \times 10^{11} \text{ C/cm}^2$ [255]. AI-ab binding to the base layer has been simulated using $K = 3$ and $Q_f = -6 \times 10^{11} \text{ C/cm}^2$ [255]. $K = 2$ and $Q_f = 1 \times 10^{11} \text{ C/cm}^2$ have been used to imitate the base layer for detecting DNA, or ssDNA while $K = 8$ and $Q_f = 5 \times 10^{11} \text{ C/cm}^2$ have been used to model the binding of dsDNA to its base layer [256], [257].

Fig. 4.5 illustrates the change in surface potential across the channel in two scenarios: first, when the cavity is devoid of biomolecules ($K=1$, $Q_f=0$), indicating the absence of bound analytes in the open cavity region; and second, when DNA and Avian Influenza antibody (AI-ab) are introduced into the open cavity area. From no biomolecules to AI-ab biomolecules, the surface potential decreases. The surface potential profile differs for each section of the channel. The surface potential of AI-ab biomolecules is the lowest of the analysed charged DNA and AI-ab biomolecules. As a result, we obtain maximum surface potential variation and thus maximum sensitivity for AI-ab analytes immobilized in the proposed biosensor's underlap region. This is due to AI-ab biomolecules having the highest negative charge density of all the biomolecules analyzed. The reason for this is that the rise in flat band voltage from

qQ_f/C_{eff} reduces the central potential. This also represents higher depletion in the channel area, which results in enhanced gate control [99].

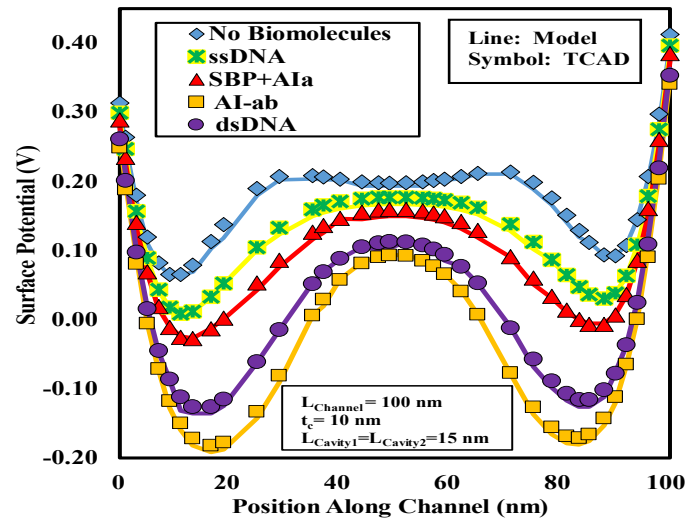


Fig. 4.5 Surface Potential of GJAM-SGAA Bio-FET for Charged DNA and Avian Influenza Antibody Analytes

Fig. 4.6 displays the change in electric field of the GJAM-SGAA Bio-FET for dsDNA and AI-ab biomolecules. The changes in the electric field in the channel under the gate regions and the gate underlap region (open cavity) indicate the presence of the biomolecules. Because of the significant impact resulting from the strong negative charge of AI-ab, the alteration in the electric field holds greater significance for AI-ab compared to dsDNA. Fig. 4.6 also demonstrates that the immobilization of the biomolecules in the cavity has no impact on the electric field at the junction of the channel-drain and source-channel. This avoids velocity saturation of the GJAM-SGAA Bio-FET device caused by analyte binding in the open cavity.

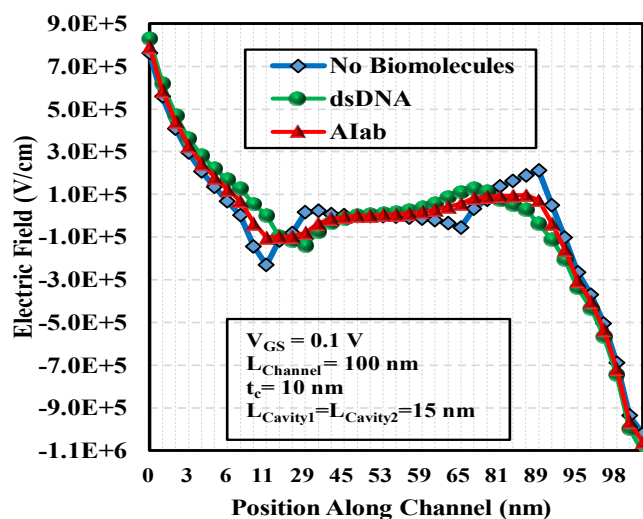


Fig. 4.6 Electric Field of GJAM-SGAA Bio-FET for dsDNA and Avian Influenza Antibody (AI-ab) Analytes

The drain current characteristics for the scenario where charged analytes are immobilised in the open cavity region are shown in Fig. 4.7 (a). This graph displays the drain current in both normal and logarithmic scales. The value of OFF current decreases for all the charged biomolecules as indicated at logarithmic scale of Fig. 4.7 (a) because all the DNA and AI-ab biomolecules are negatively charged and the OFF current decreases for negatively charged analytes [96]. In the GJAM-SGAA Bio-FET, a significant reduction in OFF current is observed for ssDNA, SBP+AI-ab, dsDNA, and AI-ab. For instance, the OFF current for AI-ab is reduced from 3.18×10^{-14} A/ μm (for $K = 1$) to 1.65×10^{-17} A/ μm (for AI-ab). The reason for the reduction in OFF current is attributed to the gate's complete control over the channel, which results in a substantial carrier depletion within the channel. The channel's graded doping in the GJAM-SGAA Bio-FET design also plays a significant role in enhancing carrier depletion, further reducing the OFF current. The drain ON current decreases for DNA and AI-ab biomolecules and it is minimum for AI-ab biomolecules. This is related to the fact that when negative biomolecules are immobilised, the drain current reduces due to a downward change in the surface potential profile [89].

Fig. 4.7 (b) represents the effect of ssDNA, AI-ab, dsDNA, and SBP + AIa biomolecules on the transconductance (g_m) for proposed biosensor device. The first derivative of I_{DS} current with respect to V_{GS} is transconductance (g_m). There is a large drift in g_m for various charged biomolecules inserted in the open cavity (gate underlap region) as clearly depicted in Fig. 4.7 (b). As the drain current decreases from the case with no biomolecules to the AIab biomolecules case as depicted in Fig. 4.7 (a), the maximum g_m value (at $V_{GS}=1.0$ V) also diminishes. However, it's worth noting that the most significant decline in the peak g_m occurs for the AIab biomolecules, as evident from Fig. 4.7 (b).

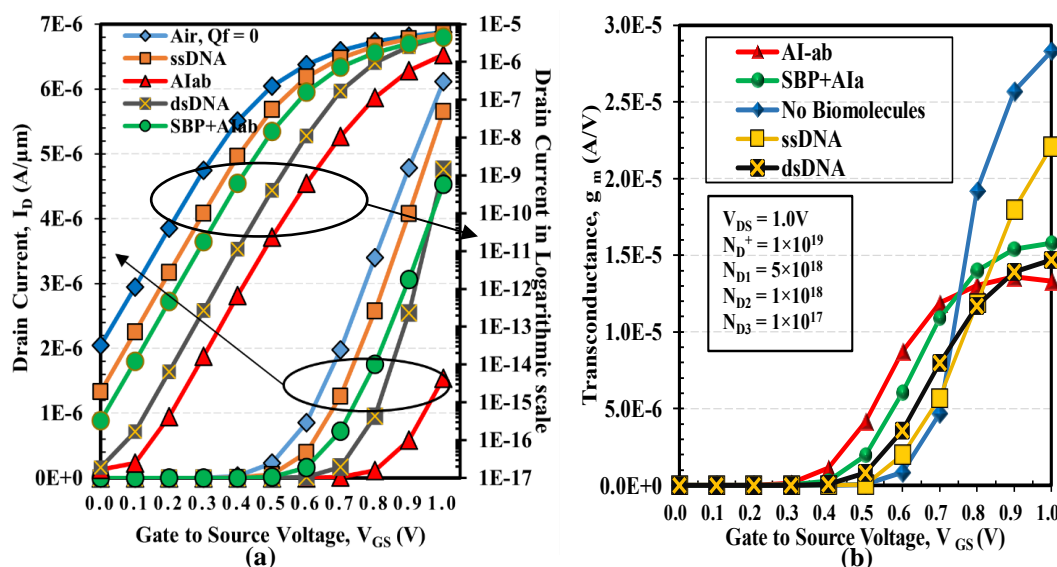


Fig. 4.7 (a) I_D - V_{GS} Characteristics with Different Biomolecules of GJAM-SGAA Bio-FET (b) Transconductance for Different Biomolecules

Fig. 4.8 (a) displays the FET's output characteristics (drain current with respect to drain voltage) for the cases where different biomolecules have been introduced into the open

cavity region as well as for the case where there are no biomolecules present. The derived analytical model and TCAD simulation show good agreement for the drain current characteristics. When no biomolecules are present, the drain current is at its highest, and it lowers for ssDNA, SBP+AIa, dsDNA, and AI-ab, respectively. The increasing negative charge on the biomolecules is the factor that causes this reduction in drain current. Fig. 4.8 (b) depicts the drain current sensitivity of the GJAM-SGAA Bio-FET for dsDNA and AI-ab bio-analytes.

The drain current sensitivity calculated according to equation (4.43), clearly shows that for all values of drain voltage, the drain current sensitivity is higher for avian influenza antibody than for dsDNA biomolecules as shown in Fig. 4.8 (b) indicating that biomolecules with higher negative charge has higher sensitivity because of the highest relative difference in drain current at every gate-to-source voltage (V_{GS}) value when compared to other biomolecules. At $V_{GS} = V_{DS} = 1.0$ V, AI-ab biomolecules exhibit the highest level of drain current sensitivity, 4512.78 nA.

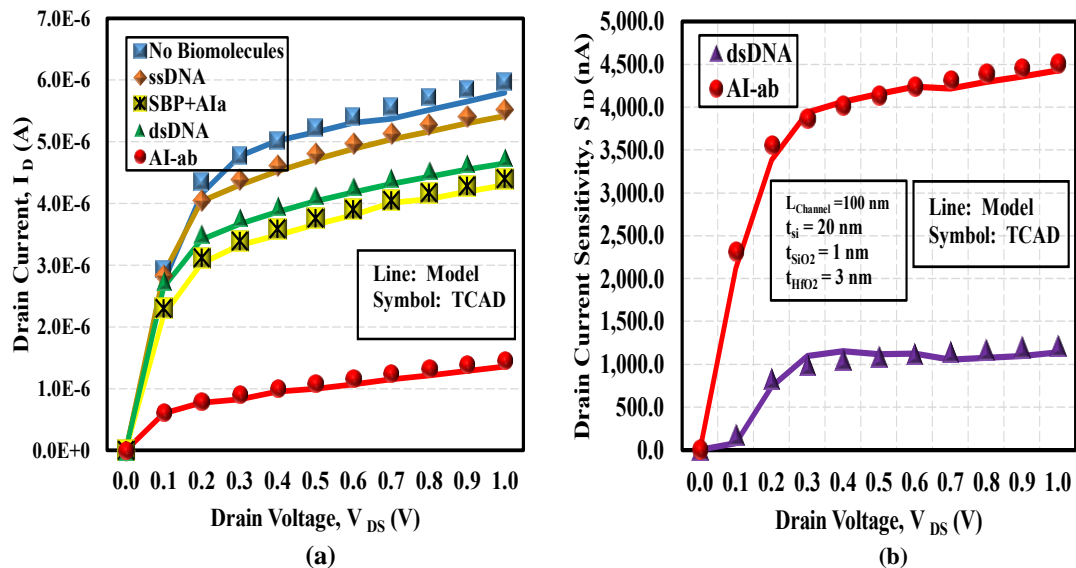


Fig. 4.8 (a) Drain Current versus Drain Voltage (I_D - V_{DS}) Characteristics with Different Biomolecules of GJAM-SGAA Bio-FET (b) Drain Current Sensitivity for dsDNA and AI-ab Biomolecules

The variation in the threshold voltage is an important factor in the case of biosensors because it assists in assessing the device's sensitivity. As shown in Fig. 4.9, rising biomolecule permittivity and increasing negative charge concentration on biomolecules related to different DNA and avian influenza analytes increases the threshold voltage, and as shown on the secondary axis of Fig. 4.9, AI-ab has maximum V_{th} drift. This is due to the fact that as the channel surface potential decreases from no biomolecule to ssDNA, SBP+AIa, dsDNA, and AI-ab as shown in Fig. 4.5, increasing the gate voltage is necessary to fully deplete the channel, hence elevating the threshold voltage.

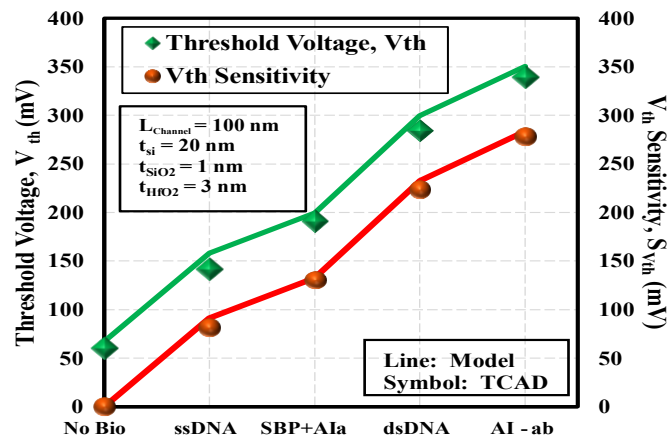


Fig. 4.9 Threshold Voltage and Threshold Voltage Sensitivity for DNA and Avian Influenza Analytes

The FET biosensor is also evaluated using the subthreshold slope (SS) and transconductance (g_m) for the sequential range of operation. The effectiveness of a transistor's response to changes in gate potential is determined by the SS value, which is a measurement of transistor reliability. The SS is estimated to have a minimum value of around 60 mV/decade at room temperature for FETs [89]. For a given variation in gate voltage, a lower value of the SS correlates to a greater change in drain current. So, for a biosensor, a smaller subthreshold slope is desirable because it allows for more accurate and sensitive detection of changes in the biomolecule's properties. As shown in Fig. 4.10, the subthreshold slope for the GJAM-SGAA Bio-FET is 64.13 mV/decade, and it further decreases as more negatively charged and dielectrically more stable biomolecules are immobilized because of an increase in gate oxide capacitance. Secondary axis on Fig. 4.10 depicts the SS sensitivity according to equation (4.42). Out of all the examined biomolecules in this work, the SS sensitivity for dsDNA is the highest at 3.4 mV/decade.

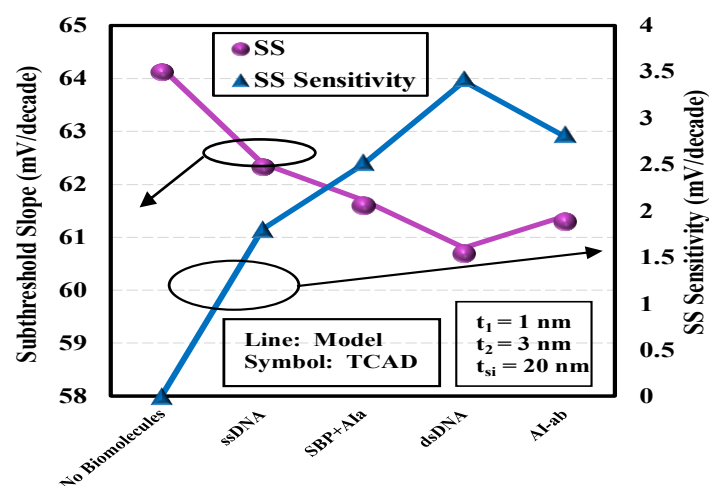


Fig. 4.10 Subthreshold Slope and Subthreshold Slope Sensitivity of GJAM-SGAA Bio-FET

To investigate the sensing capability of the devices, various sensitivity variables such as ON current sensitivity, switching ratio sensitivity, and threshold voltage sensitivity have been calculated. All of these sensitivity parameters of the proposed GJAM-SGAA

Bio-FET have been compared to those of a SGAA FET biosensor. Fig. 4.11 depicts the I_{ON} current sensitivities for the proposed GJAM-SGAA Bio-FET and SGAA FET biosensor for the case of DNA and Avian Influenza bio-analytes. For increased sensitivity of biosensors, the I_{ON} current variation should be high. The I_{ON} current sensitivity, $S_{I_{ON}}$ of the GJAM-SGAA Bio-FET is substantially greater than the $S_{I_{ON}}$ of SGAA FET biosensor due to the significant property of graded junctionless channel with gate metal work function engineering of the three split gates supporting higher drive current. Additionally, dual sided cavities improve the biosensors' current sensitivity.

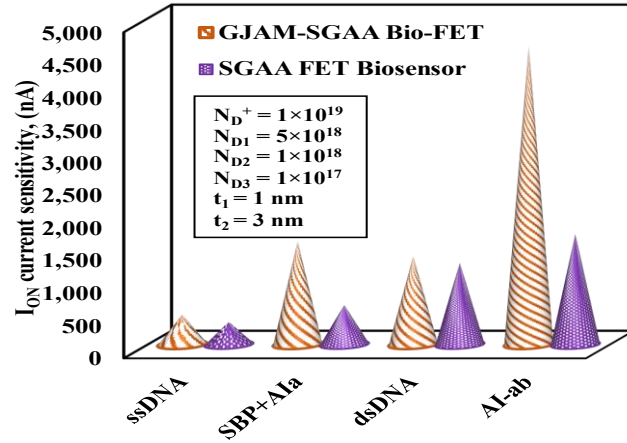


Fig. 4.11 I_{ON} Current Sensitivity Comparison of GJAM-SGAA Bio-FET and SGAA FET Biosensor

The I_{ON}/I_{OFF} ratio sensitivity for various biomolecules ssDNA, SBP+AIa, dsDNA, and AI-ab is shown in Fig. 4.12. Mathematically, I_{ON}/I_{OFF} ratio is represented as:

$$\frac{I_{ON}}{I_{OFF}} = \frac{I_{DS(ON)} \text{ at } V_{GS}=1.0V}{I_{DS(OFF)} \text{ at } V_{GS}=0.0V} \quad (4.37)$$

As illustrated in Fig. 4.12, the I_{ON}/I_{OFF} sensitivity of GJAM-SGAA BioFET is more than the SGAA FET's I_{ON}/I_{OFF} sensitivity due to the proposed device's graded JAM channel, Gate work function engineering, and double-sided open cavity. As we change the biomolecules in the cavity region from ssDNA to AI-ab, the above-mentioned unique properties of the proposed device are accountable for the device's high ON current and low OFF current. The I_{ON}/I_{OFF} ratio sensitivity for SGAA FET Biosensor ranges from 1.41 to 6.02, whereas for GJAM-SGAA Bio-FET ranges from 15.3 to 1.28×10^3 for various biomolecules.

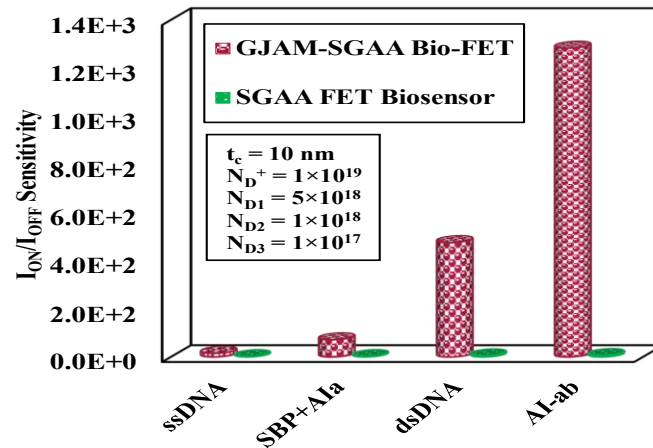


Fig. 4.12 Comparative of Switching Ratio (I_{ON}/I_{OFF}) Sensitivity of GJAM-SGAA Bio-FET and SGAA FET Biosensor

Proposed GJAM-SGAA Bio-FET and JAM Split Gate-All-Around FET (SGAA-FET) biosensor both experience a change in threshold voltage in the presence of biomolecules. This in turn can be utilised as a sensitivity parameter to identify target DNA and Avian Influenza biomolecules. Fig. 4.13 displays the threshold voltage sensitivity comparison for DNA and Avian Influenza antibody analytes. The immobilization of the target biomolecules in the gate underlap cavities of biosensors makes it difficult for a conducting layer to form at the interface between the oxide and the channel. This makes it necessary to apply a higher gate voltage to initiate conduction in the device. The threshold voltage of the device increases when ssDNA hybridizes to form dsDNA or when AI-ab is bound to SBP+AIa, as depicted in Fig. 4.9. The increase in V_{th} sensitivity is more prominent when AI-ab binds due to its higher charge compared to DNA. The sensitivity of the threshold voltage ($S_{V_{th}}$) will be higher when there is higher variation in the value of threshold voltage for DNA and AI-ab analytes, as per equation (4.44). The GJAM-SGAA Bio-FET demonstrates a higher $S_{V_{th}}$ compared to the SGAA FET Biosensor, particularly when AI-ab is bound due to its higher charge content. The proposed device's graded channel and cylindrical gate, along with metal work function engineering, contribute to its higher $S_{V_{th}}$, as illustrated in Fig. 4.13.

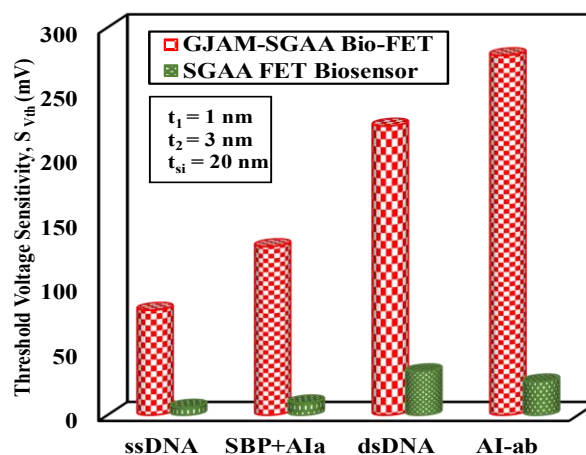


Fig. 4.13 Threshold Voltage Sensitivity, $S_{V_{th}}$ Comparison of GJAM-SGAA Bio-FET and SGAA FET Biosensor

A comparative sensitivity performance study was conducted to assess the proposed GJAM-SGAA Bio-FET against other FET biosensors with similar structural and material specifications, including GaN-GME-DE-SNW-FET [258], GC-GAA-NWFET [259], DETMS/DPDN FET [260], DM DPDG-TFET [261] and rBioFET [262] biosensor. The results displayed in Fig. 4.14 clearly indicate that the proposed GJAM-SGAA Bio-FET exhibits higher $S_{V_{th}}$ values. This indicates that the proposed device possesses superior sensing capabilities for the target analytes when compared to the other biosensors in the study.

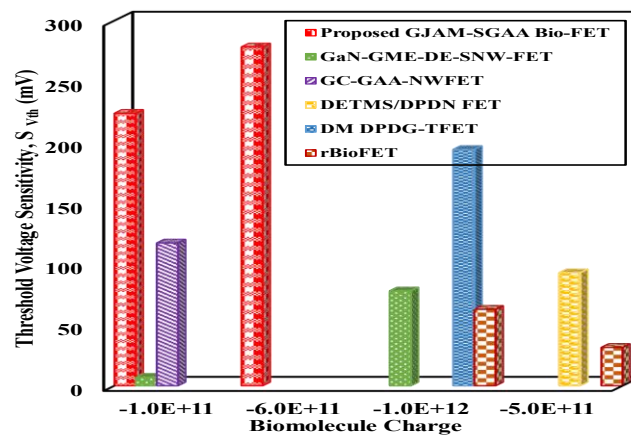


Fig. 4.14 Threshold Voltage Sensitivity, $S_{V_{th}}$ Comparison of GJAM-SGAA Bio-FET with Recent Published FET Biosensors

4.5 Summary

In this chapter, an analytical model of Graded JAM Split Gate-All-Around (GJAM-SGAA) Bio-FET has been devised for efficient detection of DNA and the avian influenza virus. A thorough set of numerical device simulations have been used to validate the analytical model. The manuscript shows that the two open cavities and graded Junction Accumulation Mode Gate-All-Around FET construction have a strong influence on the proposed biosensor's sensing performance in terms of current sensitivity and threshold voltage sensitivity. Greater gate control over the channel and enhanced device performance are made possible by the combination of graded channel and gate triple metal work function engineering. The relevance of the proposed structural modification in the GAA-NWFET is shown by a comparison of the sensitivity analysis of the proposed GJAM-SGAA Bio-FET with Junction Accumulation Mode Split Gate-All-Around FET (SGAA-FET) biosensor. Surface potential, electric field, drain ON current, drain OFF current, I_{ON}/I_{OFF} ratio, g_m , subthreshold slope and threshold voltage have all been used to assess the proposed device's sensitivity to the avian influenza virus and DNA analytes. The proposed BioFET has 430.32% higher threshold voltage sensitivity for the case of avian influenza antibody (AI-ab) biomolecule immobilization in the cavity region, while for dsDNA biomolecules it has 402.22% increase in threshold voltage sensitivity. The attributes of high sensitivity and structural stability of open cavity make GJAM-SGAA Bio-FET a promising candidate for applications like DNA and Avian Influenza detection. Thus, the GJAM-SGAA Bio-FET offers a sensitive and reliable approach for disease diagnosis.

Appendix-A

$$\mu_1 = \sqrt{\frac{d\epsilon_{Si}}{2C_{ox,1}}} , \theta_1 = (V_{GS} - V_{fb,1}) + \frac{qN_{D,1}}{2C_{ox,1}} + \frac{qN_{D,1}d^2}{4\epsilon_{Si}} , V_{fb,1} = \phi_{M_1} - \phi_{Ch,1} ,$$

$$\phi_{Ch,1} = \chi + \frac{E_g}{2} - V_T \ln \frac{N_{D,1}}{n_i}$$

$$\theta_2 = (V_{GS} - V_{fb,2}) + \frac{qN_{D,1}}{2C_{ox,1}} + \frac{qN_{D,1}d^2}{4\epsilon_{Si}} , \mu_2 = \sqrt{\frac{d\epsilon_{Si}}{2C_{ox,2}}}$$

$$V_{fb,2} = V_{fb,1} - \frac{qQ_f}{C_{ox,2}} ,$$

$$\mu_3 = \sqrt{\frac{d\epsilon_{Si}}{2C_{ox,3}}} , \theta_3 = (V_{GS} - V_{fb,3}) + \frac{qN_{D,2}}{2C_{ox,3}} + \frac{qN_{D,2}d^2}{4\epsilon_{Si}} ,$$

$$V_{fb,3} = \phi_{M_2} - \phi_{Ch,3} , \phi_{Ch,3} = \chi + \frac{E_g}{2} - V_T \ln \frac{N_{D,2}}{n_i}$$

$$\mu_4 = \sqrt{\frac{d\epsilon_{Si}}{2C_{ox,4}}} , \theta_4 = (V_{GS} - V_{fb,4}) + \frac{qN_{D,3}}{2\epsilon_{Si}} + \frac{qN_{D,3}d^2}{4\epsilon_{Si}}$$

$$\mu_5 = \sqrt{\frac{d\epsilon_{Si}}{2C_{ox,5}}} , \theta_5 = (V_{GS} - V_{fb,5}) + \frac{qN_{D,3}}{2\epsilon_{Si}} + \frac{qN_{D,3}d^2}{4\epsilon_{Si}}$$

$$V_{fb,5} = \phi_{M_3} - \phi_{Ch,5} , \phi_{Ch,5} = \chi + \frac{E_g}{2} - V_T \ln \frac{N_{D,3}}{n_i}$$

$$V_{fb,4} = V_{fb,5} - \frac{qQ_f}{C_{ox,4}}$$

After equation 4.12b, following equation shows the deduction the equation 4.15a.

Differentiating equation 4.4

$$\frac{\partial \psi(r,z)}{\partial r} = P_1(z) + 2P_2(z)r \quad (4.12c)$$

Putting equation 4.9 in equation 4.12(c)

$$P_1(z) = 0 \quad (4.12d)$$

at r=d, from equation 4.12 (c)

$$\left. \frac{\partial \{\psi(r,z)\}}{\partial r} \right|_{r=d} = 2dP_2(z)$$

$$P_2(z) = \frac{1}{2d} \left[\left. \frac{\partial \{\psi(r,z)\}}{\partial r} \right|_{r=d} \right]$$

Putting value from 4.12b

$$P_2(z) = \frac{1}{2d} \frac{C_{ox}}{\epsilon_{Ch}} [V_{GS} - V_{fb} - \psi_I(z)] \quad (4.12e)$$

Putting the value of $P_1(z)$ and $P_2(z)$ into equation 4.4, and using at r=d,

$$\psi(r,z) = \psi_I(z) , \psi_I(z) = P_0(z) + \frac{C_{ox}d}{2\epsilon_{Si}} [V_{GS} - V_{fb} - \psi_I(z)]$$

$$P_0(z) = \psi_I(z) \left[1 + \left(\frac{C_{ox}d}{2\epsilon_{Ch}} \right) \right] - \frac{C_{ox}d}{2\epsilon_{Ch}} (V_{GS} - V_{fb}) \quad (4.12f)$$

Substituting values of $P_0(z)$, $P_1(z)$ and $P_2(z)$ in equation 4.4 we get equation 4.13

$$\psi(r,z) = \frac{1}{2\epsilon_{Ch}} [\psi_I(z) \{C_{ox}d + 2\epsilon_{Ch}\} - (V_{GS} - V_{fb})C_{ox}d] + \frac{C_{ox,i}}{2\epsilon_{Ch}} [V_{GS} - V_{fb} - \psi_I(z)]r^2 \quad (4.13)$$

Use equation 4.13 into equation 4.3

$$\frac{\partial \psi(r,z)}{\partial r} = \frac{2rC_{ox}}{2\epsilon_{Ch}} [V_{GS} - V_{fb} - \psi_I(z)] \quad (4.13a)$$

$$\frac{\partial^2 \psi(z)}{\partial z^2} = \frac{2\epsilon_{Ch}}{2\epsilon_{Ch} + C_{ox}d} \frac{\partial^2 \psi_C(z)}{\partial z^2} \quad (4.13b)$$

Using equation 4.13a and 4.13b in equation 4.3 and simplifying the equation we get

$$\frac{d \varepsilon_{Si}}{2C_{ox}} \frac{\partial^2 \psi_C(z)}{\partial z^2} + \frac{d(2\varepsilon_{Ch} + C_{ox}d)}{4C_{ox}\varepsilon_{Ch}} qN_{Ch} + (V_{GS} - V_{fb}) = \psi_C(z) \quad (4.13c)$$

Equation 4.13 c can be written in simplified form as equation 4.15a

$$\mu^2 \frac{\partial^2 \psi_C(z)}{\partial z^2} + \theta = \psi_C(z) \quad (4.15a)$$

Now comparing equation 4.13c and 4.15a the expressions for μ and θ would be

$$\theta = (V_{GS} - V_{fb,i}) + \frac{qN_{Ch,i}}{2C_{ox,i}} + \frac{qN_{Ch,i}d^2}{4\varepsilon_{Si}} \quad (4.15b)$$

Appendix-B

$$O_1 = \frac{1}{e^{-\frac{(z_1-z_2)}{\mu_2}} - e^{\frac{(z_1-z_2)}{\mu_2}}} \left[\frac{c_1 c_{61} e^{-\frac{z_1}{\mu_2}}}{c_1 c_5 - c_2 c_4} - \frac{c_2 c_{61} e^{-\frac{z_2}{\mu_2}}}{c_2 c_4 - c_1 c_5} + \frac{c_5 c_{31} e^{-\frac{z_2}{\mu_2}}}{c_2 c_4 - c_1 c_5} - \frac{c_4 c_{31} e^{-\frac{z_1}{\mu_2}}}{c_1 c_5 - c_2 c_4} \right]$$

$$O_2 = \frac{1}{e^{-\frac{(z_1-z_2)}{\mu_2}} - e^{\frac{(z_1-z_2)}{\mu_2}}} \left[\frac{(c_1 c_{62} - c_4 c_{32}) e^{-\frac{z_1}{\mu_2}}}{c_1 c_5 - c_2 c_4} - \frac{(c_2 c_{62} - c_5 c_{32}) e^{-\frac{z_2}{\mu_2}}}{c_2 c_4 - c_1 c_5} + n_2 (e^{-\frac{z_1}{\mu_2}} - e^{-\frac{z_2}{\mu_2}}) \right],$$

$$O_3 = \frac{1}{e^{-\frac{(z_2-z_1)}{\mu_2}} - e^{\frac{(z_2-z_1)}{\mu_2}}} \left[\frac{(c_1 c_{61} - c_5 c_{31}) e^{\frac{z_1}{\mu_2}}}{c_1 c_5 - c_2 c_4} - \frac{(c_2 c_{61} - c_5 c_{31}) e^{\frac{z_2}{\mu_2}}}{c_2 c_4 - c_1 c_5} \right]$$

$$O_4 = \frac{1}{e^{-\frac{(z_2-z_1)}{\mu_2}} - e^{\frac{(z_2-z_1)}{\mu_2}}} \left[\frac{(c_1 c_{62} - c_4 c_{32}) e^{\frac{z_1}{\mu_2}}}{c_1 c_5 - c_2 c_4} - \frac{(c_2 c_{62} - c_5 c_{32}) e^{\frac{z_2}{\mu_2}}}{c_2 c_4 - c_1 c_5} + n_2 (e^{\frac{z_1}{\mu_2}} - e^{\frac{z_2}{\mu_2}}) \right]$$

$$W_a = O_1 O_3, W_b = O_1 O_4 + O_3 O_4, W_c = -\left(\frac{2\phi_F + n_2}{2}\right)^2$$

$$c_{31} = a_7 e^{\frac{z_1}{\mu_1}} - a_{10} e^{-\frac{z_1}{\mu_2}} - n_2 - a_2 e^{\frac{z_1}{\mu_1}} - a_4 e^{-\frac{z_1}{\mu_1}} + n_1$$

$$c_{32} = a_7 e^{\frac{z_1}{\mu_1}} - a_{10} e^{-\frac{z_1}{\mu_2}} - n_2 - a_{21} e^{\frac{z_1}{\mu_1}} - a_4 e^{-\frac{z_1}{\mu_1}} + n_1$$

$$C_{61} = \frac{a_{22} e^{\frac{z_1}{\mu_1}}}{\mu_1} - \frac{a_{42} e^{-\frac{z_1}{\mu_1}}}{\mu_1}, C_{62} = \frac{a_{21} e^{\frac{z_1}{\mu_1}}}{\mu_1} + \frac{a_{41} e^{-\frac{z_1}{\mu_1}}}{\mu_1} + \frac{a_7 e^{\frac{z_1}{\mu_2}}}{\mu_2} - \frac{a_{10} e^{-\frac{z_1}{\mu_2}}}{\mu_2}$$

$$a_{21} = \frac{-V_{bi} e^{-\frac{z_1}{\mu_1}}}{e^{-\frac{(z_0-z_1)}{\mu_1}} - e^{\frac{(z_0-z_1)}{\mu_1}}} + n_1 a_{22}, a_{22} = \frac{e^{-\frac{z_1}{\mu_1}} - e^{-\frac{z_0}{\mu_1}}}{e^{-\frac{(z_0-z_1)}{\mu_1}} - e^{\frac{(z_0-z_1)}{\mu_1}}}, a_{42} = \frac{e^{\frac{z_0}{\mu_1}} - e^{\frac{z_1}{\mu_1}}}{e^{\frac{(z_1-z_0)}{\mu_1}} - e^{-\frac{(z_1-z_0)}{\mu_1}}},$$

$$a_{41} = \frac{-V_{bi} e^{\frac{z_1}{\mu_1}}}{e^{-\frac{(z_1-z_0)}{\mu_1}} - e^{\frac{(z_1-z_0)}{\mu_1}}} + n_1 a_{42}$$

Appendix-C

$$a_1 = \frac{e^{-\frac{z_0}{\mu_1}}}{e^{-\frac{(z_0-z_1)}{\mu_1}} - e^{\frac{(z_0-z_1)}{\mu_1}}}, a_2 = \frac{-1}{e^{-\frac{(z_0-z_1)}{\mu_1}} - e^{\frac{(z_0-z_1)}{\mu_1}}} \left[V_{bi,1} e^{-\frac{z_1}{\mu_1}} + \theta_1 \left(e^{-\frac{z_0}{\mu_1}} - e^{-\frac{z_1}{\mu_1}} \right) \right],$$

$$a_3 = \frac{e^{\frac{z_0}{\mu_1}}}{e^{-\frac{(z_1-z_0)}{\mu_1}} - e^{\frac{(z_1-z_0)}{\mu_1}}}, a_4 = \frac{-1}{e^{-\frac{(z_1-z_0)}{\mu_1}} - e^{\frac{(z_1-z_0)}{\mu_1}}} \left[V_{bi,1} e^{\frac{z_1}{\mu_1}} + \theta_1 \left(e^{\frac{z_0}{\mu_1}} - e^{\frac{z_1}{\mu_1}} \right) \right], a_5 =$$

$$\begin{aligned}
& \frac{-e^{\frac{-z_2}{\mu_2}}}{e^{\frac{(z_1-z_2)}{\mu_2}} - e^{\frac{(z_1-z_2)}{\mu_2}}} , a_6 = \frac{e^{\frac{-z_1}{\mu_2}}}{e^{\frac{(z_1-z_2)}{\mu_2}} - e^{\frac{(z_1-z_2)}{\mu_2}}} , a_7 = \frac{-1}{e^{\frac{(z_1-z_2)}{\mu_2}} - e^{\frac{(z_1-z_2)}{\mu_2}}} \left[\theta_2 \left(e^{\frac{-z_1}{\mu_2}} - e^{\frac{-z_2}{\mu_2}} \right) \right] , a_8 = \frac{e^{\frac{-z_2}{\mu_2}}}{e^{\frac{(z_2-z_1)}{\mu_2}} - e^{\frac{(z_2-z_1)}{\mu_2}}} , a_9 = \frac{e^{\frac{z_1}{\mu_2}}}{e^{\frac{(z_2-z_1)}{\mu_2}} - e^{\frac{(z_2-z_1)}{\mu_2}}} \\
& a_{10} = \frac{-1}{e^{\frac{(z_2-z_1)}{\mu_2}} - e^{\frac{(z_2-z_1)}{\mu_2}}} \left[\theta_2 \left(e^{\frac{z_1}{\mu_2}} - e^{\frac{z_2}{\mu_2}} \right) \right] , c_1 = a_1 e^{\mu_1} + a_3 e^{\mu_1} - a_5 e^{\frac{z_1}{\mu_2}} - a_8 e^{\frac{z_1}{\mu_2}} \\
& a_{12} = \frac{e^{\frac{-z_2}{\mu_3}}}{e^{\frac{(z_2-z_3)}{\mu_3}} - e^{\frac{(z_2-z_3)}{\mu_3}}} , c_4 = \frac{a_1}{\mu_1} e^{\mu_1} - \frac{a_3}{\mu_1} e^{\mu_1} + \frac{a_7}{\mu_2} e^{\mu_2} + \frac{a_8}{\mu_2} e^{\mu_2} , \\
& c_6 = \frac{-a_2}{\mu_1} e^{\mu_1} + \frac{a_4}{\mu_1} e^{\mu_1} + \frac{a_7}{\mu_2} e^{\mu_2} - \frac{a_{10}}{\mu_2} e^{\mu_2} \\
& \quad - (V_{bi,2}) e^{\mu_3} - \theta_3 \left(e^{\frac{-z_2}{\mu_3}} - e^{\frac{-z_3}{\mu_3}} \right) \\
& a_{13} = \frac{-e^{\frac{z_3}{\mu_3}}}{e^{\frac{(z_2-z_3)}{\mu_3}} - e^{\frac{(z_2-z_3)}{\mu_3}}} , a_{14} = \frac{-e^{\frac{z_3}{\mu_3}}}{e^{\frac{(z_3-z_2)}{\mu_3}} - e^{\frac{(z_3-z_2)}{\mu_3}}} \\
& a_{15} = \frac{e^{\frac{z_2}{\mu_3}}}{e^{\frac{(z_3-z_2)}{\mu_3}} - e^{\frac{(z_3-z_2)}{\mu_3}}} , a_{16} = \frac{e^{\frac{z_4}{\mu_4}}}{e^{\frac{(z_3-z_4)}{\mu_4}} - e^{\frac{(z_3-z_4)}{\mu_4}}} , q_3 = \frac{-(V_{bi,2}) e^{\mu_3} - \theta_3 \left(e^{\frac{z_2}{\mu_3}} - e^{\frac{z_3}{\mu_3}} \right)}{e^{\frac{(z_3-z_2)}{\mu_3}} - e^{\frac{(z_3-z_2)}{\mu_3}}} , \\
& a_{17} = \frac{-e^{\frac{-z_4}{\mu_4}}}{e^{\frac{(z_3-z_4)}{\mu_4}} - e^{\frac{(z_3-z_4)}{\mu_4}}} , a_{19} = \frac{-(V_{bi,3}) e^{\mu_4} - \theta_4 \left(e^{\frac{-z_3}{\mu_4}} - e^{\frac{-z_4}{\mu_4}} \right)}{e^{\frac{(z_3-z_4)}{\mu_4}} - e^{\frac{(z_3-z_4)}{\mu_4}}} , a_{20} = \frac{e^{\frac{z_4}{\mu_4}}}{e^{\frac{(z_4-z_3)}{\mu_4}} - e^{\frac{(z_4-z_3)}{\mu_4}}} \\
& a_{21} = \frac{e^{\frac{z_3}{\mu_4}}}{e^{\frac{(z_4-z_3)}{\mu_4}} - e^{\frac{(z_4-z_3)}{\mu_4}}} , a_{22} = \frac{-(V_{bi,3}) e^{\mu_4} - \theta_4 \left(e^{\frac{z_3}{\mu_4}} - e^{\frac{z_4}{\mu_4}} \right)}{e^{\frac{(z_4-z_3)}{\mu_4}} - e^{\frac{(z_4-z_3)}{\mu_4}}} \\
& d_1 = \frac{1}{a_{12} e^{\mu_2} + a_{15} e^{\mu_2}} \left[\left(\frac{c_6 c_2 - c_3 c_5}{c_2 c_4 - c_3 c_5} \right) \left(a_5 e^{\frac{z_2}{\mu_2}} + a_8 e^{\frac{-z_2}{\mu_2}} \right) \right] \\
& d_2 = \frac{1}{a_{12} e^{\mu_2} + a_{15} e^{\mu_2}} \left[\left(\frac{c_6 c_1 - c_3 c_4}{c_1 c_5 - c_2 c_4} \right) \left(a_6 e^{\frac{z_2}{\mu_2}} + a_9 e^{\frac{-z_2}{\mu_2}} - a_{11} e^{\frac{z_2}{\mu_2}} - a_{14} e^{\frac{-z_2}{\mu_2}} \right) \right] \\
& c_2 = -a_6 e^{\mu_2} - a_9 e^{\mu_2} , \\
& d_3 = \frac{1}{a_{12} e^{\mu_2} + a_{15} e^{\mu_2}} \left[e^{\frac{z_2}{\mu_2}} (a_7 - a_{13}) + e^{\frac{-z_2}{\mu_2}} (a_{10} - a_{16}) + \theta_2 - \theta_3 \right] \\
& c_5 = \frac{-a_6}{\mu_2} e^{\frac{z_1}{\mu_2}} + \frac{a_9}{\mu_2} e^{\frac{-z_1}{\mu_2}} , d_4 = \frac{1}{\frac{a_{12} e^{\frac{z_3}{\mu_4}}}{\mu_4} + \frac{a_{21} e^{\frac{-z_3}{\mu_4}}}{\mu_4}} \left[\left(\frac{a_{11}}{\mu_3} e^{\frac{z_3}{\mu_3}} + \frac{a_{14}}{\mu_3} e^{\frac{-z_3}{\mu_3}} \right) \right] \\
& c_3 = a_7 e^{\mu_1} - a_4 e^{\mu_1} + a_{10} e^{\mu_2} + \theta_2 - a_8 e^{\mu_1} - \theta_1 \\
& d_5 = \frac{1}{\frac{a_{18} e^{\frac{z_3}{\mu_4}}}{\mu_4} - \frac{a_{21} e^{\frac{-z_3}{\mu_4}}}{\mu_4}} \left[\frac{a_{12}}{\mu_3} e^{\frac{z_3}{\mu_3}} - \frac{a_{15}}{\mu_3} e^{\frac{-z_3}{\mu_3}} - \frac{a_{17}}{\mu_4} e^{\frac{z_3}{\mu_4}} - \frac{a_{20}}{\mu_4} e^{\frac{-z_3}{\mu_4}} \right] , \\
& a_{18} = \frac{e^{\frac{-z_3}{\mu_4}}}{e^{\frac{(z_3-z_4)}{\mu_4}} - e^{\frac{(z_3-z_4)}{\mu_4}}} , d_6 = \frac{1}{\frac{a_{18} e^{\frac{z_3}{\mu_4}}}{\mu_4} - \frac{a_{21} e^{\frac{-z_3}{\mu_4}}}{\mu_4}} \left[\frac{a_{22}}{\mu_4} e^{\frac{-z_3}{\mu_4}} + \frac{a_{13}}{\mu_3} e^{\frac{z_3}{\mu_3}} - \frac{a_{19}}{\mu_4} e^{\frac{z_3}{\mu_4}} - \frac{a_{16}}{\mu_3} e^{\frac{-z_3}{\mu_3}} \right] \\
& a_{11} = \frac{-e^{\frac{-z_3}{\mu_3}}}{e^{\frac{(z_2-z_3)}{\mu_3}} - e^{\frac{(z_2-z_3)}{\mu_3}}}
\end{aligned}$$

CHAPTER 5

GAA NW-FET BIOSENSOR FOR LABEL-FREE SARS-COV-2 AND AVIAN INFLUENZA VIRUS DETECTION

Previous chapters have primarily focused on the analysis of biosensors targeting conventional biomolecules. However, there is a growing need to design and study novel biosensors tailored for the detection of specific viruses and diseases. This chapter aims to fill this gap by thoroughly investigating the threshold voltage and current sensitivities, which are vital for the optimal design of Gate-All-Around FET-based sensors.

This chapter is divided into two main sections, each detailing a unique biosensor architecture, their underlying principles, and performance evaluations. Section 5.1 introduces the DMDL-GAA-NW-FET biosensor, tailored for SARS-CoV-2 detection. This section comprehensively describes its dual metal dual layer gate-all-around nanowire FET structure. This section analyzes the device's electrostatic behavior, including channel potential, energy band variation, and electron concentration. Performance metrics like threshold voltage drift (ΔV_{th}), I_{ON} current drift (ΔI_{ON}), transconductance (g_m), I_{ON}/I_{OFF} ratio, and conductance (g_d) are evaluated upon virus immobilization in the nanocavity. A comparative analysis highlights the enhanced sensitivity and specificity of the DMDL-GAA-NW-FET biosensor over conventional GAA-NW-FET biosensors.

Section 5.2 delves into the GAAE-GANFET biosensor, designed for label-free biosensing applications emphasizing Avian Influenza virus detection. This part elaborates on the advanced gate-all-around engineering in GANFET, incorporating channel engineering, gate work function engineering, and oxide engineering techniques. It describes using a gallium nitride channel. The section also highlights the dual open cavity structure, emphasizing its structural stability and fabrication simplicity. An evaluation of the biosensor's viability as a label-free biosensor is included, supported by analytical modeling and TCAD simulation results, which show excellent agreement. Sensitivity analysis is also presented, which considers factors like cavity length, doping concentration, gate metal work function, and temperature variation.

Problem Statement

Current biosensors for detecting viral pathogens, such as SARS-CoV-2 and Avian Influenza, often fall short in terms of sensitivity, specificity, and ease of use, which are crucial for effective disease control. This chapter presents two cutting-edge biosensor designs: the DMDL-GAA-NW-FET, aimed at enhancing electrostatic properties and performance for detecting SARS-CoV-2, and the GAAE-GANFET, which incorporates advanced engineering for label-free detection of the Avian Influenza virus. The objective is to create biosensors that are not only highly sensitive

and specific but also simple to fabricate, thereby overcoming the limitations of conventional biosensing methods.

5.1 Dual Metal Dual Layer GAA NW-FET (DMDL-GAA-NW-FET) Biosensor for Label-Free SARS-CoV-2 Detection

5.1.1 Introduction

The severe acute respiratory syndrome corona virus (SARS-CoV-2) that led in coronavirus disease 2019 (covid-19) outbreak was proclaimed a pandemic by the World Health Organization on March 11, 2020 [263]. This ongoing COVID-19 pandemic, with its rapidly changing variants, is looming as the biggest threat to world health in a century [264].

FET based biosensors are among the most recent developments in rapid diagnostic techniques and have a number of benefits including compact size, real-time detection, high sensitivity, and ability for integrated multiplexing [265], [266], [267], [197], [101]. GAA Nanowire FETs in which the Gate material encircles the whole channel, are best suited for biosensing applications due to their maximum gate controllability, compatibility with current semiconductor industry trends, intrinsic simplicity of fabrication, and greater sensitivity [83][146]. Biomolecules are immobilized in the carved nanocavities created by etching off the dielectric material below the gate in a Dielectric Modulated-FET (DM-FET) biosensor [132], [131]. The immobilized biomolecules in the cavity region cause the gate capacitance to change in DM-FET biosensors, which in turn causes changes in electrical characteristics like the threshold voltage and current [132],[131],[268]. It is worth noticing that the device characteristics such as threshold voltage and current are significantly influenced by doping [269] and hence, sensitivity also gets affected.

Labels are not used in label-free biosensing technology for measurements. For sensing purposes, they employ the analytes' innate physical characteristics, such as molecular weight, size, electrical impedance, charge, refractive index, or dielectric permittivity [103].

This work presents the label free detection method of the Covid-19 with the help of S-protein and C-DNA immobilization of SARS-CoV-2 in the nanocavity region of DMDL-GAA-NW-FET. In this work, the Junction Accumulation Mode (JAM) nanowire FET device has mainly been implemented using the dual-metal (DM) and cylindrical Gate-All-Around (GAA) schemes because it has been already illustrated [270], [271] that the dual metal gate provides better drive current, transconductance, and reduced SCEs and is thus suitable for augmented analog performance, while the cylindrical GAA helps to increase the gate control over the channel. As the channel length is reduced, several effects start to occur in FETs, such as impact ionization, drain-induced barrier lowering (DIBL), carrier velocity saturation, gate oxide leakage, hot carrier effects, increased subthreshold swing, and increased leakage current [272]. These effects are known as short channel effects. Dual Metal Gate (DMG) is a technique that involves using two different metal gates with different work functions so that $\phi_{m1} > \phi_{m2}$. When the electrons travels from source to drain region its velocity

is reduced for DMG structure as $\phi_{m1} > \phi_{m2}$ in comparison to single metal gate (SMG) structure [273]. The dual metal gates also allow for better electrostatic control over the channel, as the combination of different work functions helps in optimizing the threshold voltage (V_{th}) of the device.

5.1.1.1 JAM FET

The concept of Junction Accumulation Mode (JAM) Field Effect Transistor (FET) has been previously discussed in earlier chapters.

5.1.1.2 Oxide Stacking

To overcome the limitations of thin oxide layers, use of the dielectric materials which has a higher dielectric permittivity can be opted. These materials enable the attainment of a large physical thickness while maintaining a small Effective Oxide Thickness (EOT). The EOT is the measure of the thickness of a SiO_2 layer that has the same capacitance as the high-k dielectric layer [122], [235], [236]. High-k dielectrics improve gate control over the channel, but interface traps, bulk fixed charges, and low interface carrier mobility concerns limit their use. Since none of the alternative dielectric materials generate a native oxide on silicon, a thin SiO_2 interfacial layer is inevitable.

5.1.1.3 Gate Material Engineering

The previous chapters have covered the topic of gate material engineering, which involves the usage of gate metals with varying work functions. This chapter presents a design proposal that utilizes gate material engineering with two distinct work function gates.

5.1.1.4 SARS-CoV-2 Virus Detection

The World Health Organization declared the outbreak of coronavirus disease 2019 (COVID-19), caused by the severe acute respiratory syndrome coronavirus 2 (SARS-CoV-2), a pandemic on March 11, 2020 [263]. This ongoing pandemic, exacerbated by rapidly mutating variants, stands as the most significant global health threat in a century [264].

The most common approach for diagnosis of this disease at the moment is real-time reverse transcription–polymerase chain reaction (RT-PCR), which uses an inner nasal swab material to identify the genes for E-protein, N- protein, open frame reading b1 (OFRb1), and OFRb2. Placing the viral RNA in the test kit is the first step in the detection process. After that, primer is applied to the viral Ribonucleic acid (RNA) to create a copy of it. Further, this virus's RNA is transformed into complementary deoxyribonucleic acid (C-DNA) by the reverse transcriptase process, and different copies are created utilizing the DNA polymerization procedure [274],[275]. Although the RT-PCR detection method is sensitive and has excellent specificity for COVID-19 detection, this approach requires expensive reagents, sophisticated equipment, trained staff and has a lengthy processing time of almost 4 hours [276].

Understanding the structural intricacies of the SARS-CoV-2 virus [277] is pivotal not only in deciphering its behavioural patterns but also as a cornerstone for the development of vaccines [278], antiviral drugs [279], [280], and diagnostic tools [281]. While traditional vaccination strategies have been invaluable in curbing the virus's spread, novel approaches rooted in mechanical principles and natural frequencies show promise as innovative alternatives. Dastjerdi et al. have probed the mechanical characteristics of SARS-CoV-2 using a viscoelastic spherical model, suggesting that targeted application of specific natural frequencies, delivered through mechanical loads and vibrations, could hold the potential for virus destruction [282]. Warsame et al. further supports this, highlighting that the natural frequencies of 88.52–125.13 MHz computed through modal analysis can denature SARS-CoV-2 when subjected to external frequencies, potentially utilizing ultrasound or electromagnetic waves [283]. These findings align with the work of Wierzbicki et al., which identifies distinct resonant frequencies specific to the SARS-CoV-2 virus and introduces ultrasound-induced vibrations as a groundbreaking alternative to conventional vaccination strategies, particularly in addressing emerging viral strains [284].

Spike (S), Membrane (M), Nucleocapsid (N), and Envelope (E) proteins are the four different kinds of proteins present in SARS-CoV-2. Fig. 5.1 (a) [100] shows the same. Spike protein (S-protein) is on the viral envelope, and its S1 subunit is the virus' outermost part [285],[286],[287]. Human ACE2 serves as a host for spike (S) proteins, which initiate an infection. Following this, SARS-CoV-2 enters the host cell and generate greater number of viruses that are later spread the infection to new cells as shown in Fig. 5.1 (b) [288].

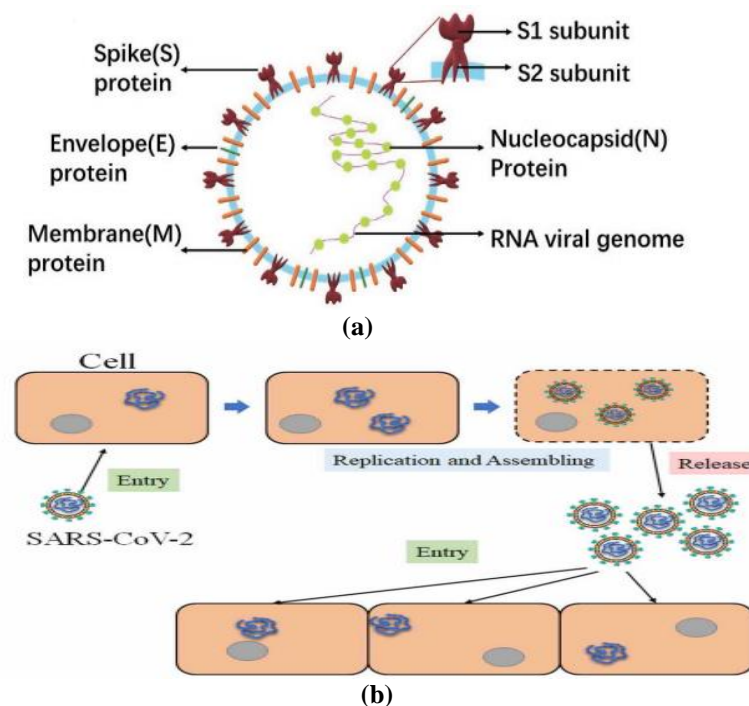


Fig. 5.1 (a) Structure of SARS-CoV-2 [100] (b) Process of SARS-CoV-2 infecting Host Cells [288].

5.1.2 Device Structure and Simulation Specification

The proposed device in its three-dimensional view is shown in Fig. 5.2 (a). While the Fig. 5.2 (b) depicts the proposed biosensor structure in vertical cross-sectional aspect. The DMDL-GAA-NW-FET biosensor's two-dimensional view and its capacitance model is depicted in Fig. 5.2 (c). The internal device construction can be explained with the help of the Fig. 5.2 (c). Deposition of high-K dielectric materials directly on silicon substrates would reduce performance, predominantly because of the fringing field that permeates the channel from the source and drain terminals, weakening the gate control [289]. Therefore, in this work, gate oxide stack engineering (SiO₂+High K material HfO₂) has been used to reduce the fringing Filed and to improve device performance [290]. The device is having Dual metal Dual Layer structure in which the two layers of Gate are made of different metals having different work functions. Gate Layer 1 is formed by depositing gate metal of work function 5 eV in a trench that is created by etching the HfO₂ dielectric layer, which is 7 nm thick. After that, GATE Layer 2 is created by selectively depositing a metal with a 5.5 eV work-function on top of the HfO₂ layer. Further, plasma dry etching process can be used to realize the nanocavity region in the biosensor device for immobilization of biomolecules. In the nanocavity, as shown by the 2D structure in Fig. 5.2 (c), biomolecules have been introduced evenly, by varying the dielectric permittivity. In the capacitance analogous circuit, the lumped capacitances of the DMDL-GAA-NW-FET biosensor are represented by C_{bio} for the variable capacitance of nanogap cavity having biomolecule species, C_{SiO_2} for the capacitance of SiO₂ layer, and C_{HfO_2} for the capacitance of HfO₂ layer. The capacitance of the nanocavity will vary depending on the physical parameters of the virus, modifying the biosensor characteristics and thus sensing the virus according to the capacitance model of the device. Table 5.1 illustrates various device parameters for both proposed DMDL-GAA-NW-FET and conventional GAA-NW-FET.

Table 5.1 Device Parameters

Physical Device Parameter	DMDL-GAA-NW-FET	Conventional GAA-NW-FET
Channel Length (nm)	50	50
Thickness of siliconfilm (nm)	20	20
Length of source/drain (nm)	15	15
Oxide Thickness, SiO ₂ & HfO ₂ (nm)	3.0 & 7.0	3.0 & 7.0
Doping of Channel Region, N_D (/cm ³)	1×10^{18}	1×10^{18}
Doping of Source and Drain Region, N_D^+ (/cm ³)	1×10^{19}	1×10^{19}
Thickness of Cavity (nm)	7	7
Gate Layer-1 Thickness (nm)	9	-
Gate Layer-2 Thickness (nm)	2	2
Length of Cavity (nm)	23	23
HfO ₂ and SiO ₂ dielectric constants	25.0 & 3.9	25.0 & 3.9

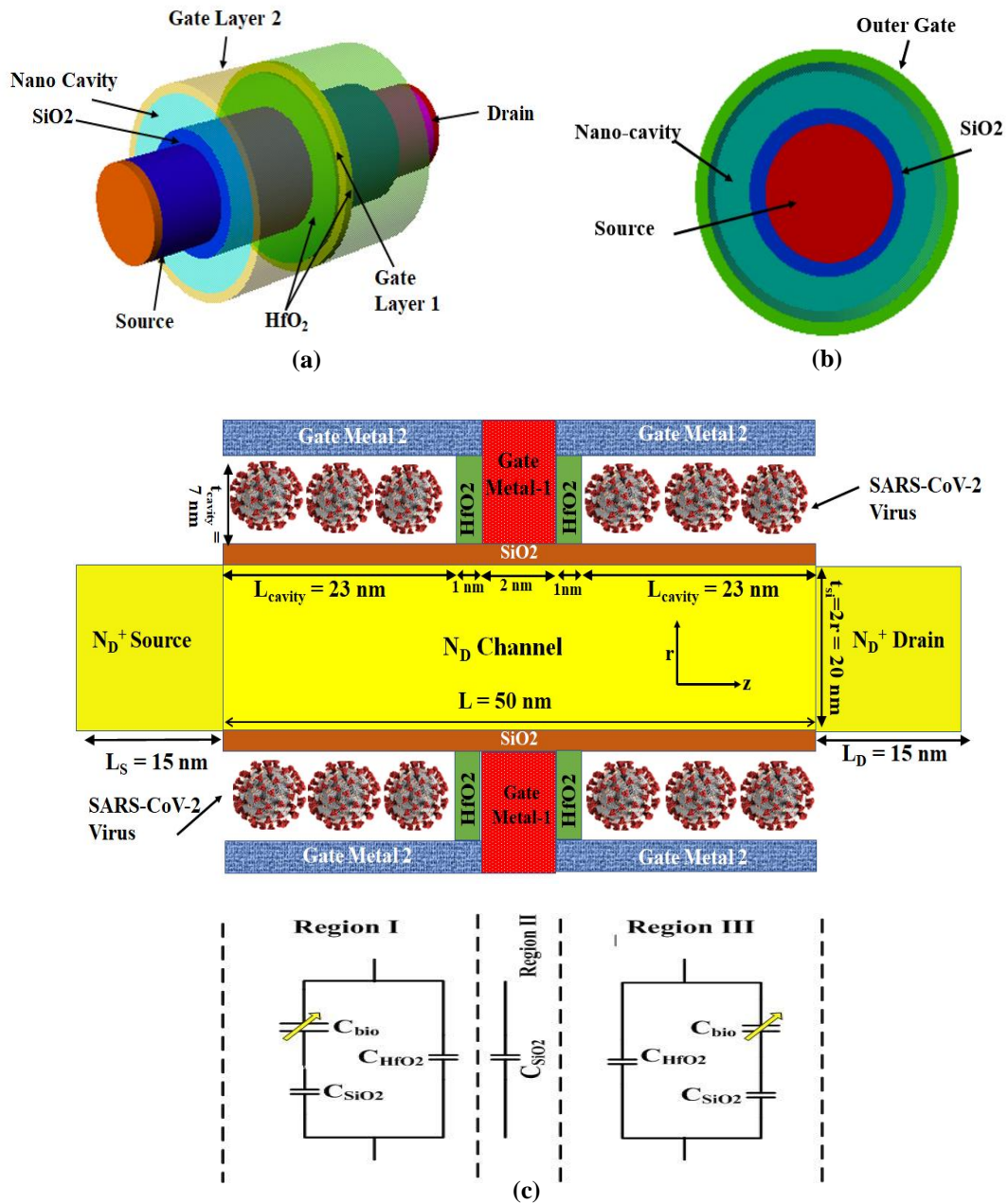


Fig. 5.2 (a) 3-Dimensional View of DMDL-GAA-NW-FET (b) Vertical Cross-sectional View of DMDL-GAA-NW-FET (c) 2- Dimensional Structure of DMDL-GAA-NW-FET

The simulation results were evaluated using the Atlas-3D device simulation tool. The simulations include models for carrier recombination and carrier mobility generation. CONMOB model has been employed for doping versus mobility validation and BGN model has been used for high channel doping. The CONMOB model is used to calculate the effective mobility of carriers in the channel region of the GAA FET. This model takes into account the effect of impurities, interface roughness, and scattering mechanisms on carrier mobility. The mobility values calculated using the CONMOB model can be used to determine the device performance parameters such as drain

current, transconductance, and subthreshold swing [291]. On the other hand, the BGN model is used to model the narrowing of the bandgap in the channel region of the GAA FET due to the presence of an electric field. This model takes into account the quantum confinement effect and the variation of the effective mass of carriers in the channel region. The BGN model is important for accurately predicting the device performance in the sub-threshold regime [291].

5.1.3 Device Calibration and Fabrication

In order to validate the reliability of the simulation models, the simulation data have been calibrated with experimental data from a pre-fabricated JAM nanowire FET [206]. The simulation and experimental results are fairly well matched for the transfer characteristics (I_{DS} versus V_{GS} curve), as shown in Fig. 5.3.

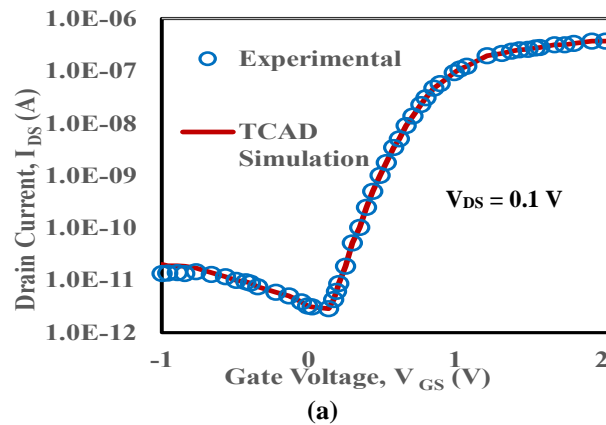
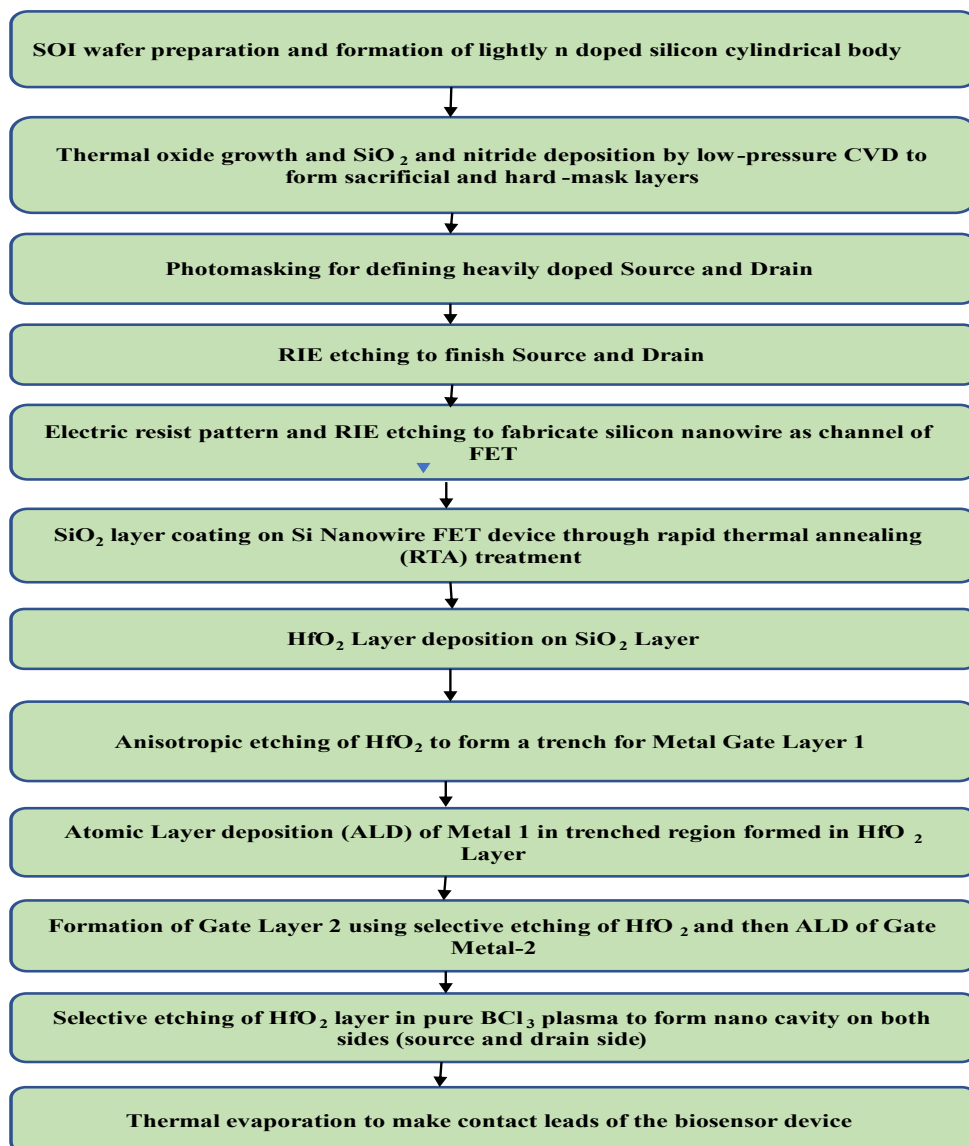


Fig. 5.3 (a) Calibration of Simulation Setup with Experimental Data [206]

The fabrication of the biosensor begins with some fundamental fabrication steps [158] such as substrate preparation, silicon epitaxial growth, sacrificial layer deposition, Gate Dielectric Deposition using techniques such as thermal oxidation or chemical vapor deposition (CVD), Gate Electrode Deposition using techniques such as PVD or CVD [229], and Nanowire Formation [161], [162], which will serve as the sensing element of the biosensor. The proposed detailed fabrication steps of Dual Metal Dual Layer Gate-All-Around Nanowire Field Effect Transistor (DMDL-GAA-NW-FET) Biosensor are mentioned in a flowchart in Fig. 5.3 (b).



(b)

Fig. 5.3 (b) Proposed Fabrication Flowchart of DMDL-GAA-NW-FET Biosensor

5.1.4 Results and Discussion

The SARS-CoV-2 virus's spike (S) protein protrusions have a dielectric constant that ranges from 2 to 4 [292], [293]. Furthermore, the DNA of the virus contains positive and negative charge densities, which make it possible to identify viruses based on charge density modulation. DNA has a constant dielectric constant between 1 and 64. Therefore, S-protein and C-DNA are represented in this work by $K = 2.1$ and $K = 4$.

5.1.4.1 Sensitivity Comparison of Proposed Biosensor

The conventional GAA-NW-FET biosensor has been designed and simulated for the same dimensions as the proposed biosensor for the detection of the SARS-CoV-2 virus in order to compare the proposed DMDL-GAA-NW-FET biosensor's performance to that of the reported conventional GAA biosensor [88]. For sensitivity performance

comparison the V_{TH} sensitivity and I_{ON} current sensitivity has been taken as a measure for S-Protein and DNA based charged biomolecule detection of SARS-CoV-2 virus.

For Label Free SARS-CoV-2 Detection using DMDL-GAA-NW-FET, the gate dielectric constant of the FET is altered depending upon the type of S-protein immobilized. Furthermore, the device's threshold voltage, on-state current, and off-state current are all calculated as per the S-Protein and its sensitivity. A biosensor's sensitivity can be determined using one of three methods: drift in an electrical parameter, fractional change in an electrical parameter, or the ratio of an electrical parameter with a biomolecule present to an electrical parameter without a biomolecule.

Threshold Voltage sensitivity ($S_{V_{t_{Nbio}}}$) is defined as the fractional change in threshold voltage (V_{TH}) with and without S-Protein immobilized into the nanocavity. It can be formulated as [96]:

$$S_{V_{t_{Nbio}}} = \frac{V_{TH[with\ S-protein, K=2.1/4]} - V_{TH[without\ S-protein]}}{V_{TH[without\ S-protein]}} \quad (5.1)$$

The impact of S-protein on the V_{TH} sensitivity of the DMDL-GAA-NW-FET and GAA-NW-FET is shown in Fig. 5.4 (a), revealing that the proposed device is more sensitive to S-Protein than the GAA-NW-FET in terms of threshold voltage sensitivity. The $S_{V_{t_{Nbio}}}$ is 7.08 times higher than $S_{V_{t_{Nbio}}}$ of the conventional GAA-NW-FET biosensor for S-protein with $K=4$.

The ratio of drain current (I_{ON}) method has been used to calculate the sensitivity of both the devices in terms of I_{ON} current sensitivity ($S_{I_{Nbio}}$) for S-Protein. The I_{ON} current is defined as the value of drain current at $V_{GS} = V_{DS} = 1V$. The following mathematical equations have been used to determine the I_{ON} current sensitivity [96]:

$$S_{I_{Nbio}} = \frac{I_{ON[with\ S-protein, K=2.1/4]}}{I_{ON[Withwithout\ S-protein]}} \quad (5.2)$$

I_{ON} sensitivity is plotted for DMDL-GAA-NW-FET and GAA-NW-FET for S-Protein having $K=2.1$ and 4 in Fig. 5.4 (b). The I_{ON} sensitivity for DMDL-GAA-NW-FET is 2.38 times higher than that of the conventional GAA-NW-FET biosensor for S-protein with dielectric constant $K=4$.

The density of the charges carried by the biomolecules affects a biosensor's sensitivity. For negatively charged biomolecules, the channel center potential of the DMDL-GAA-NW-FET decreases because the flat band voltage (V_{FB}) rises due to the negative charge density. In turn, this causes the threshold voltage for negatively charged biomolecules to rise, and vice versa. This change in threshold voltage is utilized to calculate the sensitivity of biosensor. Equation (5.3) has been used to determine the threshold voltage sensitivity of charged DNA biomolecules for negative and positive charge associated with the biomolecule.

$$S_{V_{t_{Cbio}}} = \frac{V_{TH[Neutral]} - V_{TH[Charge]}}{V_{TH[Neutral]}} \quad (5.3)$$

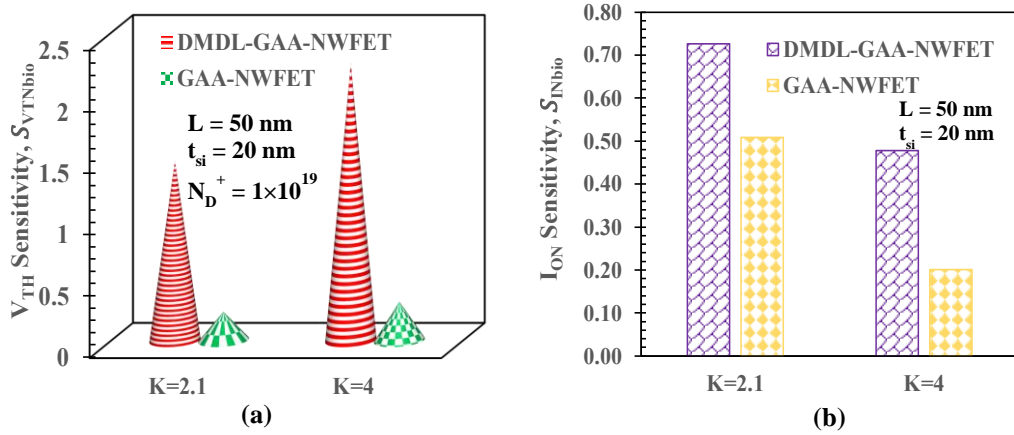


Fig. 5.4 Sensitivity Comparison of DMDL-GAA-NW-FET and GAA-NW-FET Biosensor for Dielectric Constant Variation of S-Protein (a) V_{TH} Sensitivity (b) I_{ON} Current Sensitivity

The drain current is decreased for negatively charged biomolecules, whereas it is increased for positive charge density. The reason for this is that the positively charged biomolecules produce a shift in channel potential upward, whereas negatively charged biomolecules cause a shift in channel potential downward [89]. This shift in the drain current magnitude directly affects the sensitivity of the DMDL-GAA-NW-FET biosensor. Equation (5.4) has been utilised as the I_{ON} current sensitivity in terms of shift in drain current caused by the insertion of positive and negative charge DNA biomolecules into the nanocavity [157]:

$$S_{I_{cbio}} = I_{ON[Charge]} - I_{ON[Neutral]} \quad (5.4)$$

As demonstrated in Fig. 5.5 (a) and Fig. 5.5 (b), the DMDL-GAA-NW-FET biosensor outperforms the GAA-NW-FET biosensor for the DNA charged biomolecules detection.

For DNA charged biomolecules, the average V_{TH} sensitivity of DMDL-GAA-NW-FET is 0.19 which is 3.2 times higher than the V_{TH} sensitivity of the conventional GAA-NW-FET biosensor. However, the I_{ON} sensitivity is only 1.68 times greater than that of the conventional GAA-NW-FET biosensor. The aforementioned discussion leads to the conclusion that the proposed device is more sensitive to S-protein for changing dielectric constants than DNA charged biomolecules. Also, the V_{TH} Sensitivity is dominant over I_{ON} sensitivity.

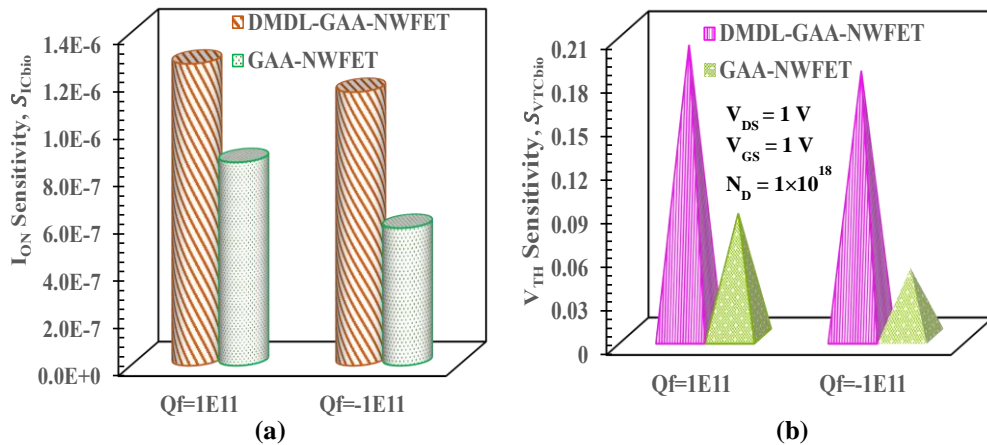


Fig. 5.5 Sensitivity Comparison of DMDL-GAA-NW-FET and GAA-NW-FET Biosensor for Charged DNA Biomolecules at $K=2.1$ (a) V_{TH} Sensitivity (b) I_{ON} Current Sensitivity

Table 5.2 compares the DMDL-GAA-NW-FET biosensor's sensitivities to those of the conventional GAA-NW-FET biosensor for both the S-protein and DNA biomolecules. A common sensitivity parameter is required in order to compare the sensitivity of proposed DMDL-GAA-NW-FET biosensor with that of similar existing biosensors in the recent literature. An effective sensitivity metric known as relative drift in threshold voltage (ΔV_{TH}) aids in determining which biosensor device structure has the highest sensitivity. Table 5.3 compares the threshold voltage sensitivity (in terms of ΔV_{TH}) of the DMDL-GAA-NW-FET biosensor with that of similar existing biosensors for various biomolecules.

Table 5.2 Sensitivity Comparison

Sensitivity Parameter	DMDL-GAA-NW-FET	Conventional GAA-NW-FET	% Improvement
I_{ON} sensitivity for S-protein	0.73 for $K=2.1$, 0.48 for $K=4$	0.51 for $K=2.1$, 0.20 for $K=4$	43% for $K=2.1$, 140% for $K=4$
V_{TH} sensitivity for S-protein	1.46 for $K=2.1$, 2.25 for $K=4$	0.23 for $K=2.1$, 0.32 for $K=4$	534.7% for $K=2.1$, 603% for $K=4$
I_{ON} sensitivity for DNA biomolecules (in μA)	1.27 for $Q_f = 1E11$, 1.15 for $Q_f = -1E11$	0.86 for $Q_f = 1E11$, 0.58, for $Q_f = -1E11$	47.7% for $Q_f = 1E11$, 98.3% for $Q_f = -1E11$
V_{TH} sensitivity for DNA biomolecules	0.20 for $Q_f = 1E11$, 0.18 for $Q_f = -1E11$	0.08 for $Q_f = 1E11$, 0.05 for $Q_f = -1E11$	150% for $Q_f = 1E11$, 260%, for $Q_f = -1E11$

Table 5.3 Threshold Voltage Sensitivity Comparison of DMDL-GAA-NW-FET to Contemporary Research on Similar Biosensors

Structural Parameters	Ref. [238]	Ref. [258]	Ref. [294]	Ref. [92]	Ref. [231]	Ref. [227]	Ref. [295]	Our Work
Cavity length (nm)	25	15	20	10	29	20	8	23
Cavity thickness	9	4	9	1	6	10	2	7
Channel length	100	50	40	20	60	40	20	50
(K_{BIO})	5	8	12	2.1	2.63	5	5	4
S_{VTH} in terms of ΔV_{TH} (mV)	130	105	161	17	182	137	87	226

5.1.4.2 Device Electrostatic Analysis

Electrostatics Analysis is crucial to thoroughly characterize and comprehend the electrical behavior of the FET biosensor with varying dielectric constant and charge of the biomolecule to ensure proper functioning of the biosensor. Understanding the electrostatic interactions between the biomolecules and the FET surface provides insights into the sensitivity of the biosensor device and its ability to accurately detect the biomolecules. Also, electrostatic analysis can be used to optimize the design and operation of the device such as the choice of materials, the size and shape of the sensing area (nano cavity), and the operating conditions. Fig. 5.6 (a) depicts the variation of the DMDL-GAA-NW-FET biosensor's center potential along the channel as the dielectric constant for S-Protein is varied. When a bias voltage is provided to the gate electrode, the electrostatic potential at the center of the nanowire channel region is referred to as the channel center potential. The behavior of the charge carriers in the channel is influenced by the channel center potential, which makes it a crucial parameter in biosensing. When the nanogap cavity is devoid of biomolecules, the potential in the channel at source and drain sides are 0.48 V, 0.58 V, and the channel potential minimum (Ψ_c) is 0.03 V. When the S-protein analytes having dielectric constants $K = 2.1$ and $K = 4$, are immobilized in the nanocavity, the channel center potential reaches a minimum of -0.06 V and -0.16 V respectively, indicating that the channel potential minimum (Ψ_c) is at its maximum value for the case when nanogap cavity has no biomolecules ($K = 1$). A rise in the dielectric constant in the cavity region, which increases the vertical electric field and leads to an increase in gate capacitance, is the cause of this drop in Ψ_c [296].

The threshold voltage, subthreshold slope, and other electrical properties of the transistor are all impacted by the decrease in the channel center potential minimum that occurs with an increase in the K value of the biomolecules. The channel center potential minimum reduces when the dielectric constant of biomolecules rises, which also raises the gate capacitance. This decreased potential minimum increases the voltage difference between the gate and the channel, which leads to an increase in the threshold

voltage. Therefore, the nanogap cavity without biomolecules will reflect the smallest threshold voltage (V_{TH}) and as we increase the K value, the V_{TH} rises as well.

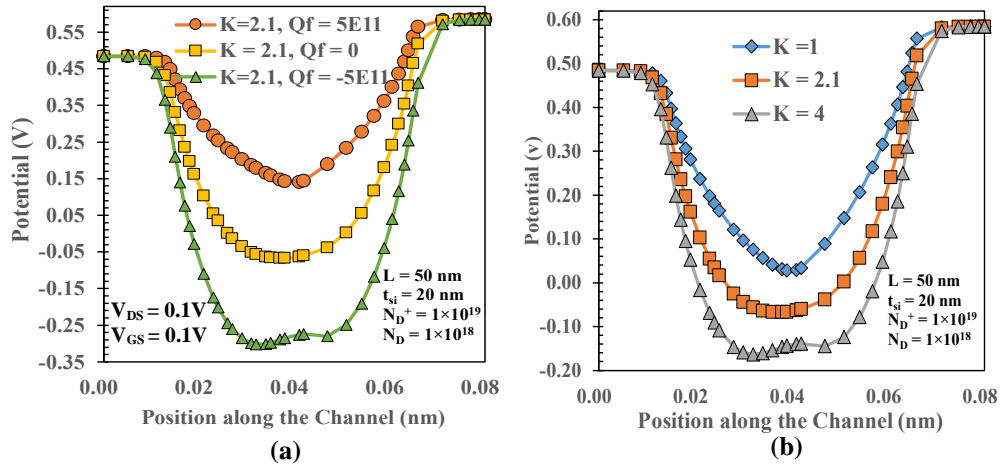


Fig. 5.6 (a) Channel Potential for S-Protein with Dielectric Constant Variations of DMDL-GAA-NW-FET along the Channel Length (b) Channel Potential for $K = 2.1$ and Varying Charge Density of DMDL-GAA-NW-FET Along the Channel Length

Fig. 5.6 (b) depicts the center potential for positive and negative charge on DNA biomolecules along the channel's position. The center potential is found to be around -0.067 V for $Q_f = 0$ Coulomb/cm² and -0.301 V for $Q_f = -5 \times 10^{11}$ coulomb/cm² indicating that the channel potential reduces for negative charge analytes. This decrease in center potential is the result of an increase in flat band voltage. This also suggests higher depletion in the channel area, which leads to greater gate control. Also, negatively charged analytes produce an electric field that repels the channel's majority carriers (electrons), pushing them out of the sensing region. As a result, the channel's majority carrier concentration declines, which lowers the channel potential. The center potential for positive charged DNA biomolecule ($Q_f = 5 \times 10^{11}$ coulomb/cm²) is 0.143 V, showing that the central potential increases for positive charge biomolecules. This is because the charges in the cavity and channel have a stronger attraction. The greater central potential of positive charged DNA biomolecules signifies that the charges in the channel are not depleted, implying that the gate control is weakening. This lowers the threshold voltage even more.

When the dielectric constant value of the biosensor changes, it can affect the electric field distribution in the device. A higher dielectric constant will result in a stronger electric field, while a lower dielectric constant will result in a weaker electric field. This change in the electric field can in turn affect the energy levels of the conduction and valence bands. Overall, changing the dielectric constant value of the biomolecule in a DMDL-GAA-NW-FET biosensor impacts the energy levels of both the conduction and valence bands, affecting the charge carrier behaviour and ultimately the electrical performance of the biosensor. The specific changes in conduction and valence band energies would depend on the biomolecule properties, biosensor device design, and operating conditions of the biosensor. The energy band profiles have been used to examine the impact of channel center potential variation on the carrier transport mechanism. Fig. 5.7 (a) depicts the energy band diagram for both conduction band

energy (CBE) and valence band energy (VBE) of DMDL-GAA-NW-FET biosensor with Spike protein analytes having various dielectric constants in the nanogap cavity. It is evident from Fig. 5.7 (a) that the energy band barrier at the channel-drain interface is greatly impacted by changes in the dielectric constant of biomolecules in the nanogap, which causes a significant variation in device conduction. S-Protein analytes into the cavity change the channel's gate capacitance and lateral electric field, which marginally boosts the band energies (CBE and VBE).

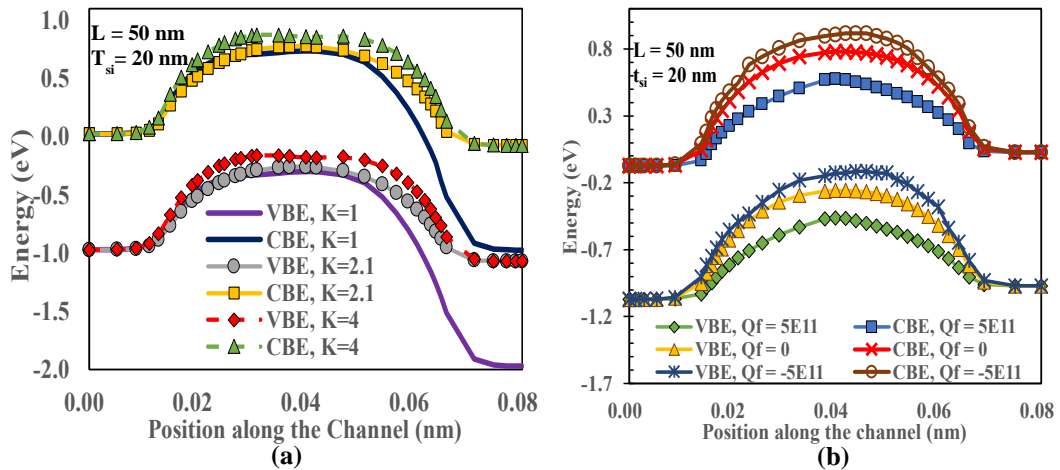


Fig. 5.7 Energy Band Diagrams of DMDL-GAA-NW-FET Along the Channel Length for (a) S-Protein with Dielectric Constant Variation (b) DNA Biomolecule with Charge Variation

In contrast to the energy band profile with no charge for a constant dielectric constant $K = 2.1$, Fig. 5.7 (b) illustrates the shift in the energy band profile for charged DNA biomolecules. The CBE and VBE levels are observed to shift downward for positively charged ($Q_f = 5 \times 10^{11}$ coulomb/cm²) biomolecules and slightly upward for negatively charged ($Q_f = -5 \times 10^{11}$ coulomb/cm²) biomolecules relative to the level of CBE and VBE for neutral biomolecules ($Q_f = 0$) when these biomolecules are inserted into the nanogap cavity. The potential barrier for the thermionic emission of electrons from the source to channel decreases for positively charged DNA biomolecules and increases for negatively charged DNA biomolecules as a result of this shift in band energy [296]. Changing the charge concentration value of the DNA biomolecules alter the position of the Fermi level and, subsequently, the energy required to excite an electron from the valence band to the conduction band. This change in energy can be detected by FET biosensor and used to determine the presence of the DNA biomolecules.

In Fig. 5.8 (a), the contours of the electron concentration are shown before ($K = 1$) and after ($K = 2.1$ and $K = 4$) conjugation of the biomolecules. While Fig. 5.8 (b) depicts the electron concentration contours for positive charge concentration ($Q_f = 5 \times 10^{11}$ coulomb/cm²), no charge ($Q_f = 0$), and negative charge concentration ($Q_f = -5 \times 10^{11}$ coulomb/cm²) on DNA biomolecule species having dielectric constant $K = 2.1$. These electron concentration contours have been plotted at $V_{DS} = V_{GS} = 0.1V$. On the right-hand side of the contour plots in Fig. 5.8 (a) and Fig. 5.8 (b), the level of electron concentration is depicted using a color scale.

In a FET biosensor, the concentration of electrons in the channel region is influenced by the dielectric constant and charge of the surrounding medium. The contour plot displays the electron concentration as a function of the dielectric constant, charge and the position along the channel region. Dielectric constant is a measure of a material's ability to store electrical energy in an electric field. It affects the capacitance of the FET biosensor, which in turn influences the electron concentration at the surface of the transistor. As depicted in Fig. 5.8 (a), the electron concentration in the centre of channel becomes lower (as indicated by the colour scale) with the immobilisation of S-Protein ($K = 2.1$ and $K=4$) in the nanocavity, indicating a decrease in the electron concentration. A decrease in electron concentration shifts the threshold voltage, requiring a higher gate voltage to turn on the transistor. The decrease in electron concentration also leads to a fall in current value in the subthreshold region as we increase the value of the dielectric constant.

Charged biomolecules, such as DNA, introduce additional charges at the surface of the FET biosensor, altering the electric field and potential distribution in the channel region. This result in changes in the electron concentration which is reflected in the contour plot in Fig. 5.8 (b). According to Fig. 5.8 (b), the electron concentration rises when positively charged DNA biomolecules are inserted into the nanocavity region, while it falls when negatively charged biomolecules are inserted, indicating an increase in the current value for positively charged biomolecules and a decrease in the current value for negatively charged biomolecules in subthreshold regime. The threshold voltage is inversely proportional to the electron concentration. As the electron concentration decreases, the threshold voltage tends to increase, and vice versa.

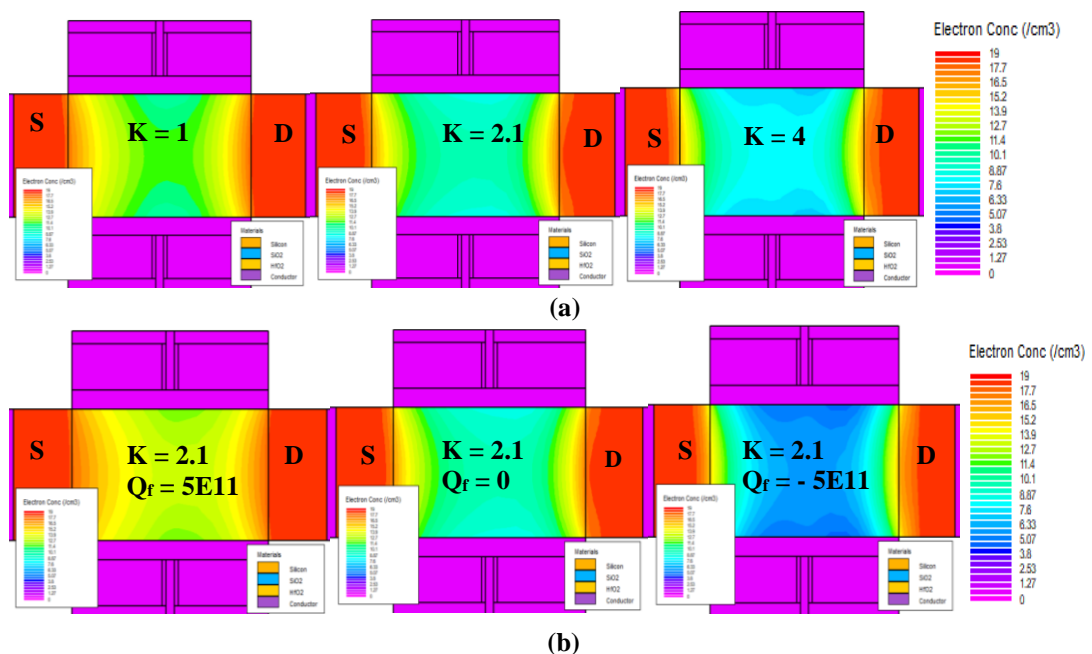


Fig. 5.8 Contour Plots of Electron Concentration for (a) Different Biomolecule Dielectric Constants (b) Variation in Charge Concentration of DNA Biomolecule having $K = 2$.

5.1.4.3 Sensitivity Analysis of DMDL-GAA-NW-FET Biosensor for SARS-CoV-2 Spike Protein

Fig. 5.9 (a) examines I_D - V_G characteristics (drain current versus gate voltage) of the DMDL-GAA-NW-FET biosensor for dielectric constants, $K = 2.1$ and $K = 4$ of S-Protein, assuming that they are neutrally charged. The subthreshold current dramatically decreases from 4.62×10^{-13} A/ μm to 2.78×10^{-16} A/ μm after immobilization of the biomolecules such as air whose $K = 1$ to $K = 4$ for the instance of S-Protein. This decrease in drain subthreshold current is caused by the efficient control of Dual Metal Dual Layer Gate over the channel and the decreased concentration of charge carriers within the channel area when the S-Protein biomolecules having high dielectric constants are immobilized into nanocavity region. This reduction in subthreshold current is accompanied by a drift in the ON current (ΔI_{ON}) as well which is clearly depicted in Fig. 5.9 (b) showing the drain current versus drain Voltage curve for $V_{GS} = 1$ V. As we immobilize the biomolecules with increased dielectric constant, they effectively screen the gate electric field, lowering the effective gate voltage that reaches the channel. This reduces the electrostatic potential at the channel surface, therefore decreases the drain current.

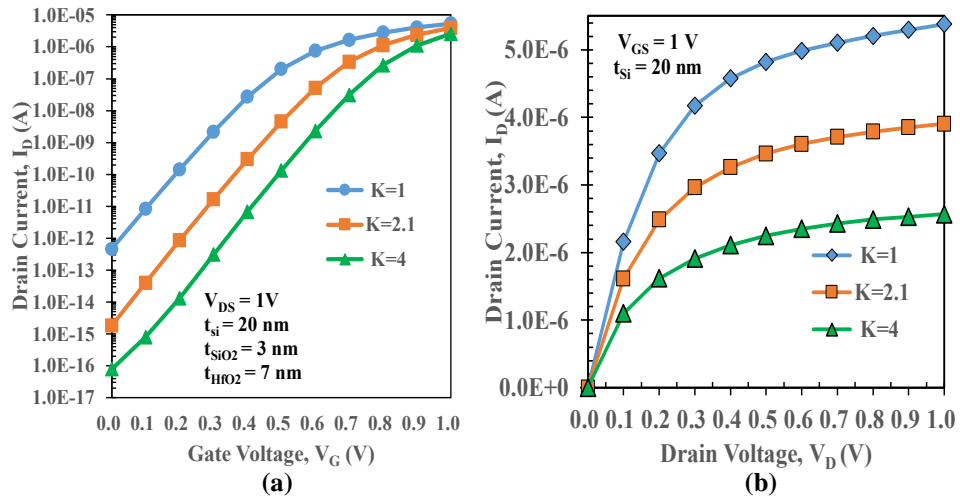


Fig. 5.9 (a) I_D - V_G Characteristics at $V_{DS} = 1$ V and for S-Protein with Dielectric Constant Variations (b) I_D - V_D Characteristics at $V_{GS} = 1$ V for S-Protein with Dielectric Constant Variations

Transconductance (g_m) is demonstrated with a change in gate voltage, V_G in Fig. 5.10 (a) for the proposed design. Transconductance is defined as the ratio of the change in drain current to the change in gate voltage across a pre-set, arbitrarily short interval on the I_{DS} vs V_{GS} curve. Mathematically, g_m is given by equation (5.5)

$$g_m = \left. \frac{\partial I_{DS}}{\partial V_{GS}} \right|_{V_{DS}=\text{constant}} \quad (5.5)$$

A high transconductance value indicates that a slight change in V_G results in a substantial change in I_D . The unique Dual Metal Dual Layer Gate of the DMDL-GAA-NW-FET increases electrostatic coupling and enhances carrier mobility, all of which improve the performance of the proposed device and increases its transconductance. As

S-Protein biomolecules are incorporated into the nano cavity, there is a substantial drift in g_m , as illustrated in this Fig. 5.10 (a). The highest value of the drift in transconductance is 7.05×10^{-6} A/V which is at $V_{GS} = 0.6$ V. This variation in g_m is caused by the variation in drain on current on immobilization of S-protein at different dielectric constants.

The impact of S-Protein immobilization on the output conductance (g_d) of the DMDL-GAA-NW-FET biosensor is shown in Fig. 5.10 (b). At constant $V_{GS} = 1.0$ V, the output conductance (g_d) is evaluated by the first order derivative of the drain current with respect to the drain voltage (V_D). According to Fig. 5.10 (b), output conductance decreases as S-protein of SARS-CoV-2 virus is injected into the nanocavity compared to the case in which no biomolecule is present. The reason for this drop in output conductance is a decrease in drain current caused by a rise in the dielectric constant of the biomolecules in the nanocavity region.

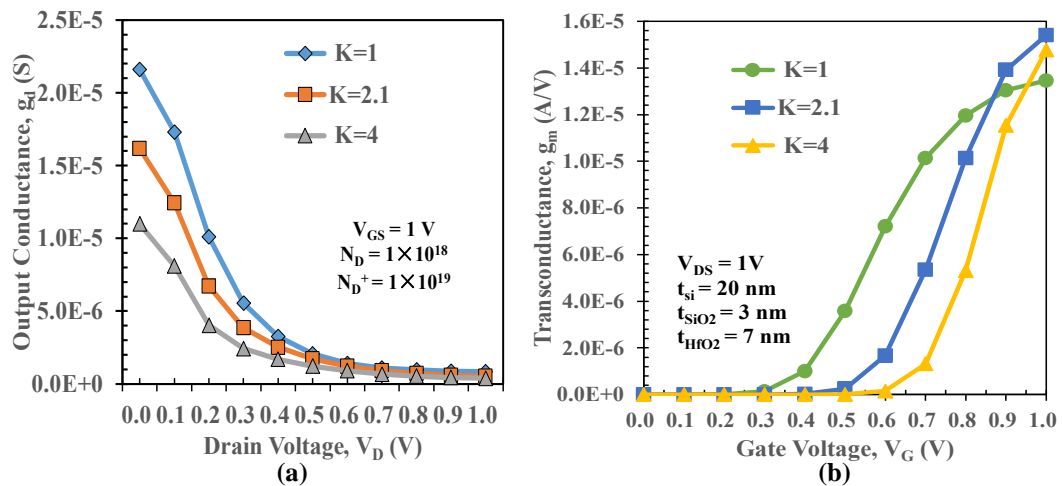


Fig. 5.10 (a) Transconductance g_m and (b) Output Conductance g_d for S-Protein with Dielectric Constant Variations

Fig. 5.11 (a) shows the drift in the threshold voltage (ΔV_{TH}) and drift in I_{ON} drain current (ΔI_{ON}), which are utilized as sensitivity measures of the DMDL-GAA-NW-FET biosensor. The threshold voltage of the proposed biosensor increases with an increase in the dielectric constant of biomolecule in the nano-cavity which can be explained by the fact that the channel centre potential is maximum when there are no biomolecules inside the nanocavity region as shown in Fig. 5.6 (a), and that as soon as biomolecules are inserted, the centre potential decreases with an increase in the K value of the biomolecules and subsequently the threshold voltage. Fig. 5.11 (b) shows the variation in I_{ON}/I_{OFF} ratio for different dielectric constants (K values) of S-Protein considered in this work. It is evident from this figure that when the value of the dielectric constant rises, the I_{ON}/I_{OFF} ratio also rises because of the decreased subthreshold current (I_{OFF}) caused by improved DMDL GATE control over the channel, which raises the potential barrier height. Secondary axis of Fig. 5.11 (b) shows the I_{ON}/I_{OFF} sensitivity for varying K values of S-Protein. The ratio of I_{ON}/I_{OFF} current at various S-protein dielectric constants and the I_{ON}/I_{OFF} current at $K=1$ have been used to compute the I_{ON}/I_{OFF} sensitivity illustrated in Fig. 5.11 (b). The value of I_{ON}/I_{OFF} sensitivity for $K = 4$ of S-Protein is 795.63.

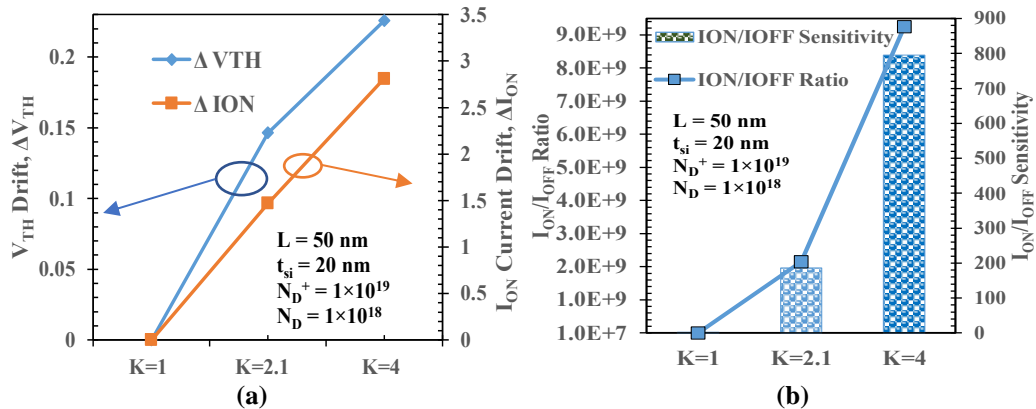


Fig. 5.11 Sensitivity of S-Protein with Dielectric Constant Variation (a) Drift in Threshold Voltage (ΔV_{TH}), and Drift in Drain ON Current (ΔI_{ON}) with respect to Air (K=1) (b) I_{ON}/I_{OFF} Ratio and I_{ON}/I_{OFF} Sensitivity with Change in Dielectric Constant

Table 5.4 summarizes the various device electrical parameters on the immobilization of S-protein with changing dielectric constants within the nanocavity region.

Table 5.4 Electrical Parameters of DMDL-GAA-NW-FET Biosensor for SARS-COV-2 Spike Protein

Device Electrical Parameter	K Value	Parameter Value	Sensitivity of the parameter
Subthreshold current, I_{OFF} (μA)	K = 1 K = 2.1 K = 4	$4.62E-13$ $1.81E-15$ $7.79E-17$	2.5×10^2 for K = 2.1 5.93×10^3 for K = 4
Drain I_{ON} Current (μA)	K = 1 K = 2.1 K = 4	$5.38E-06$ $3.91E-06$ $2.57E-06$	72.6% for K = 2.1 47.8% for K = 4
Threshold Voltage Drift (ΔV_T) (mV)	K = 2.1 K = 4	146.4 225.7	146.1% for K = 2.1 225.3% for K = 4
I_{ON}/I_{OFF} current ratio	K = 1 K = 2.1 K = 4	$1.16E+07$ $2.16E+09$ $9.26E+09$	1.9×10^2 for K = 2.1 7.96×10^2 for K = 4

5.1.4.4 Sensitivity Investigation of DNA Charge Density Modulation/Trap Charge Concentration

The reverse transcriptase process transforms the virus's RNA into DNA, enabling the detection of the virus through its DNA. A biosensor's sensitivity can be changed based on the density of the charges carried by the DNA biomolecules. This section examines the reactions of the proposed biosensor to charged DNA immobilized in the nanocavity regions. The positive and negative charges taken into account for the investigation are -1×10^{11} , -5×10^{11} , 1×10^{11} , and 5×10^{11} cm^{-2} and the DNA biomolecule's fixed dielectric constant is 2.1. Consideration of fixed oxide interface trapped charges ($Q_f = \pm 1 \times 10^{11}$ and $\pm 5 \times 10^{11}$) in the oxide-Air interface can be used to illustrate the effects of the presence of a charged biomolecule in the nanogap cavity. The flat band voltage (V_{FB})

risers due to the negative trap charge (and vice versa) which results in a decrease in the channel centre potential of the DMDL-GAA-NW-FET biosensor. The concept is similar to a well-known approach used to model the interface trapped charges present in the oxide-semiconductor interface in MOSFETs [25], [268].

Fig. 5.12 (a) depicts the change in I_D with respect to V_G for different negative and positive charge densities of C-DNA. These $I_D - V_G$ characteristics are displayed on the assumption that DNA biomolecules with $K = 2.1$ completely occupy the nanocavities. The drain current is shown to be falling as the negative charged density increases, whereas it is found to be rising when the positive charge density increases. The reason for this is that positively charged biomolecules produce a shift in channel potential upward, whereas negatively charged biomolecules cause a shift in channel potential downward. And this shift in the drain current magnitude directly affects the sensitivity of the DMDL-GAA-NW-FET biosensor.

The drain current against drain voltage ($I_D - V_D$ curve) for the proposed biosensor is shown in Fig. 5.12 (b) with the variation in charge of DNA biomolecules. The Fig. 5.12 (b) clearly shows that the drain current continued to rise as the charges on biomolecules shifted from negative to positive. For biomolecules with positive charges, the positive charge draws electrons to the surface and reduces the space charge region. This leads to more carriers entering the channel, which lowers resistance and boosts drain current. Also, negative charges on biomolecules deflect electrons away from the surface, broadening the space charge region of the channel and lowering drain current.

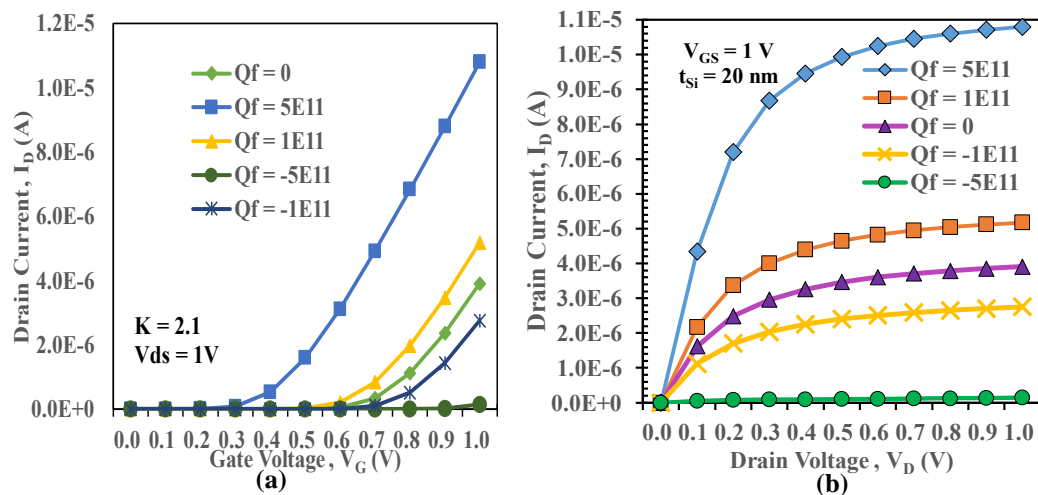


Fig. 5.12 (a) $I_D - V_G$ Characteristics at $V_{DS} = 1V$ and (b) $I_D - V_D$ Characteristics at $V_{GS} = 1V$ for DNA ($K=2.1$) Charged Biomolecules

The transconductance (g_m) curves of the proposed biosensor with biomolecule's positive and negative charge density variations are demonstrated in Fig. 5.13 (a). With rising positive charge density, peak transconductance's V_{GS} value falls. While, when negative charge density increases, the V_{GS} value of the peak transconductance increases. This is the cause of a decrease in the threshold voltage for positively charged biomolecules and an increase in the V_{TH} for negatively charged biomolecules.

The variation in output conductance (g_d) with variation in charge on the DNA biomolecule of the SARS-COV-2 virus is shown in Fig. 5.13 (b). The increase in positive charge increases the output conductance, while increasing the negative charge decreases the g_d value.

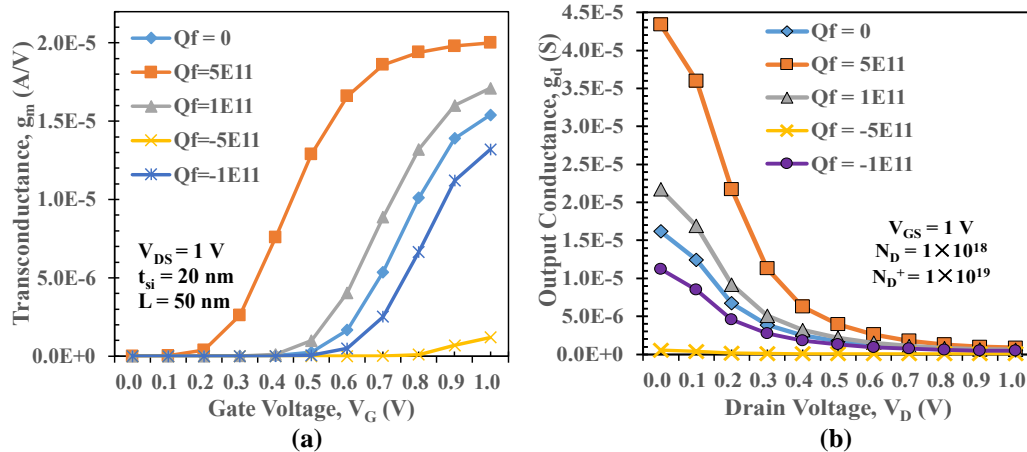


Fig. 5.13 (a) Transconductance, g_m and (b) Output Conductance, g_d for DNA (K=2.1) Charged Biomolecules

The impact of positive and negative charges on the DNA biomolecule with a fixed dielectric constant of 2.1 is summarised in Fig. 5.14. With the immobilization of positive and negative DNA biomolecules into the nanocavity, the variation in drain current and transconductance (which in turn alters the threshold voltage) as shown in Fig. 5.12 and Fig. 5.13 can be translated into drift in I_{ON} drain current (ΔI_{ON}) and drift in threshold voltage (ΔV_{TH}). ΔV_{TH} and ΔI_{ON} are calculated as the difference of V_{TH} and I_{ON} at $Q_f = 0$ and V_{TH} and I_{ON} at $Q_f = 1 \times 10^{11} \text{ cm}^{-2}$, $-5 \times 10^{11} \text{ cm}^{-2}$, $1 \times 10^{11} \text{ cm}^{-2}$, and $5 \times 10^{11} \text{ cm}^{-2}$. It is clear from Fig. 14 that proposed biosensor device exhibits a significant drift in the drain current and threshold voltage with the change in charged biomolecules which directly affects the sensitivity of the biosensor. Furthermore, as shown in Fig. 5.14, the DMDL-GAA-NW-FET biosensor exhibits larger V_{TH} and I_{ON} drift for positively charged DNA biomolecules than for negatively charged DNA biomolecules.

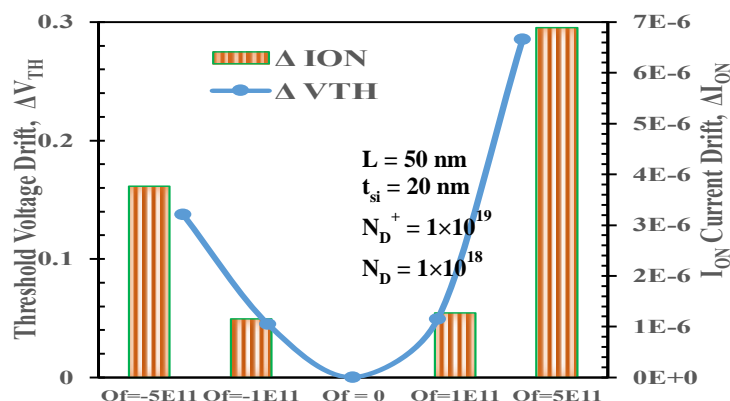


Fig. 5.14 Drift in Threshold Voltage (ΔV_{TH}), and Drift in Drain ON current (ΔI_{ON}) for Charged DNA Biomolecules at Constant K = 2.1

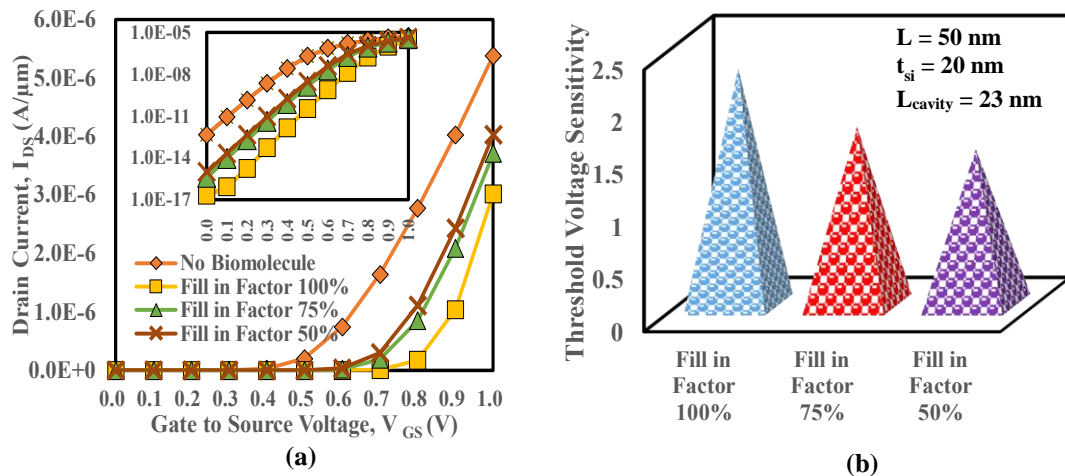
The several electrical parameters that are sensitive to the immobilization of the SARS-CoV-2 virus' DNA biomolecules in the nanocavity region are listed in Table 5.5.

Table 5.5 Electrical Parameters of DMDL-GAA-NW-FET Biosensor for DNA Biomolecules of SARS-COV-2

Device Electrical Parameter	Charge Value	Parameter Value	Sensitivity of the parameter
Subthreshold current, I_{OFF} (μA)	$Q_f = 0$ $Q_f = 5 \times 10^{11}$ $Q_f = -5 \times 10^{11}$	1.81E-15 1.18E-11 7.77E-16	6.5×10^3 for $Q_f = 5 \times 10^{11}$ 0.42 for $Q_f = -5 \times 10^{11}$
Drain I_{ON} Current (μA)	$Q_f = 0$ $Q_f = 5 \times 10^{11}$ $Q_f = -5 \times 10^{11}$	3.91E-06 1.08E-05 1.39E-07	2.7×10^2 % for $Q_f = 5 \times 10^{11}$ 3.56% for $Q_f = -5 \times 10^{11}$
Threshold Voltage Drift (ΔV_T) (mV)	$Q_f = 5 \times 10^{11}$ $Q_f = -5 \times 10^{11}$	285.5 137.5	50.54% for $Q_f = 5 \times 10^{11}$ 56.81% for $Q_f = -5 \times 10^{11}$

5.1.4.5 Impact of Fill in Factor on Sensitivity

Biomolecules congregate in the nanogap at random, and fully filled nanogaps are rarely observed. Biomolecules that are partially filled have different surface profiles within the nanogaps and give varied capacitances as a result. Fig. 5.15 (a) illustrates three distinct scenarios for drain current to biomolecule fill in area in the nanocavity for biomolecule dielectric constant $K = 4$. The drain ON current and OFF current increases with decreasing fill in factor of the biomolecules as depicted in Fig. 5.15 (a). The OFF current is shown as inset in Fig. 5.15 (a). The threshold voltage sensitivity calculated using equation (1), decreases with decreasing fill in factor as shown in Fig. 5.15 (b). Similarly, the I_{ON} and I_{OFF} current sensitivities decreases with decreasing fill in factor but this decrement is more prominent for the case of I_{OFF} current sensitivity as shown in Fig. 5.15 (c) and Fig. 5.15 (d). Therefore, when the fill-in factor is high, the device is more sensitive to biomolecules for all the sensitivity parameters.



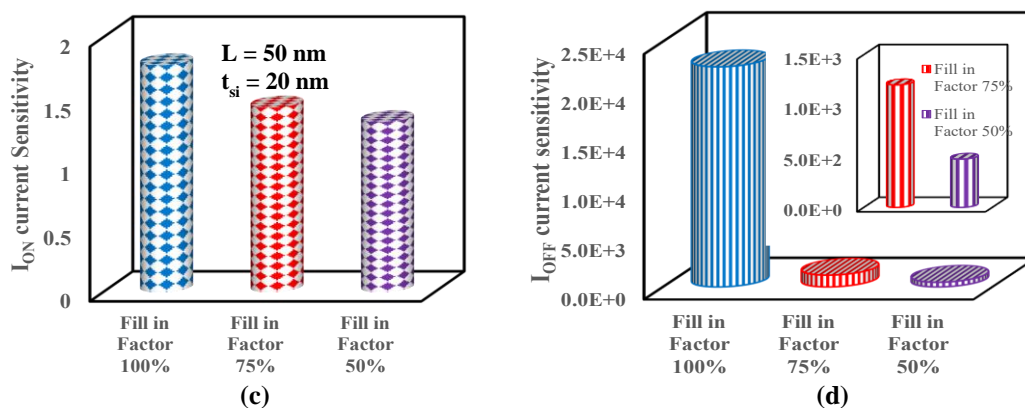


Fig. 5.15 (a) Drain Current versus Gate to Source Voltage (b) Threshold Voltage Sensitivity (c) I_{ON} Current Sensitivity (d) I_{OFF} Current Sensitivity for Various Fill in Factor of the Biomolecules into the Nanocavity

5.1.5 Summary

In an effort to combat COVID-19, we successfully designed a biosensor that uses Dual Metal Dual Layer Gate-All-Around Nanowire FET for detection of SARS-CoV-2 Spike protein and DNA. This work demonstrates that the Dual Metal and Dual Layered Gate-All-Around structure has a persuasive effect on the sensing ability of the proposed biosensor. The combination of layered structure and dual metal work function engineering allows greater Gate control over the channel and improved analog performance. Comparative sensitivity analysis of the proposed DMDL-GAA-NW-FET biosensor device with normal Gate-All-Around NWFET device demonstrates the significance of the proposed Gate structural alteration in GAA-NW-FET. The proposed device's sensitivity to S-protein and DNA biomolecules of the SARS-CoV-2 virus has been evaluated in terms of drain ON current, subthreshold current, I_{ON}/I_{OFF} ratio, g_m , and g_d . The greater variation in these electrical parameters enables the development of biosensor that is incredibly sensitive. The DMDL-GAA-NW-FET achieves a V_{TH} shift of 225.74 mV as compare to GAA-NW-FET biosensor which produces a V_{TH} shift of 93.56 mV while varying the dielectric constant (K) from 1 to 4. The simulation findings show that DMDL-GAA-NW-FET is 7 times more sensitive to threshold voltage and 2.4 times more sensitive to I_{ON} current than GAA-NW-FET when it comes to immobilizing biomolecules with $K=4$ inside the cavity. Furthermore, the proposed sensor's sensitivity for variation in DNA charge density has been investigated and concluded that as the charge on biomolecules changes from negative to positive, sensitivity increases. Therefore, the proposed DMDL-GAA-NW-FET biosensor is more applicable for the detection of the SARS-CoV-2 virus. The proposed biosensor design is responding better in term of sensitivity for different neutral and charged biomolecules so it can also be used for detecting other biological diseases like breast cancer, Alzheimer, Ebola and various other viral infections.

5.2 Dielectric Modulated GANFET Biosensor for Label-Free Detection of DNA and Avian Influenza Virus

5.2.1 Background and Overview

Due to the widespread influence of biomolecules on numerous areas of pharmaceutical science during the past few decades, their acknowledgment has become increasingly crucial. For many biomedical applications, including the detection of cellular programming, the quantification and study of biological mechanisms is of the utmost importance [297], [298]. Advancements in biosensor technology have paved the way for precise and rapid detection of a wide range of biological molecules. These sensors leverage the interaction between specific biomolecules and transducing elements to convert molecular recognition events into measurable signals. Among these, Field-Effect Transistor (FET) based biosensors have emerged as a prominent class. These sensors offer exquisite sensitivity and real-time monitoring capabilities, making them pivotal tools in various applications ranging from healthcare diagnostics to environmental monitoring.

FET-based biosensors exhibit a remarkable capacity for detecting biomolecules at the nanoscale. These sensors have the ability to carry out label-free detection while maintaining the device's intrinsic properties [104], [299]. The gate-all-around field effect transistor (GAA-FET) has garnered the greatest research attention as a result of recent advancements in device architecture, mostly because of its stronger electrostatic channel control [119], [202], [300], [301]. Among the variants of the Gate-All-Around MOSFET, one that holds substantial promise within the biomedical field is distinguished by its seamless integration with established CMOS technologies. This remarkable compatibility significantly enhances its relevance and potential impact [302].

To enhance the current level and bolster other performance parameters, various innovative device engineering techniques are being applied to FET device structures [62], [78], [95], [303]–[305]. In order to address the challenges associated with short-channel effects (SCEs), merely scaling down gate lengths is insufficient. Consequently, alternative materials to silicon have been investigated to enhance nanowire based FET devices [306], [307]. In recent research, various FET biosensors utilizing base material other than silicon have been explored for enhanced sensing performance [308]–[310]. Trench gate structure provides excellent improvement in biosensing [146], [153], [159], [311]. The biosensor designs introduced recently, including GC-CPTFET [312] and Lg-TGNFET [313], are aligned in their objective to progress label-free biomolecule detection. Each design incorporates distinct features, such as a graphene channel and tri-layer graphene nanoribbon, contributing collaboratively to the ongoing development of biosensing technologies.

Gallium Nitride (GaN), with its notably wider bandgap (3.4 eV), emerges as a compelling substitute. This material not only enhances thermal stability but also mitigates gate-induced drain leakage (GIDL) and band-to-band tunneling (BTBT) due to its significantly higher bandgap compared to silicon. In GaN's wurtzite structure, the

lattice parameters are approximately $a = 3.189 \text{ \AA}$ and $c = 5.185 \text{ \AA}$, outlining the unit cell's dimensions crucial for understanding GaN's properties in semiconductor applications. These parameters impact GaN's bandgap energy, crystal growth quality, device fabrication, and strain effects. GaN also boasts a remarkable breakdown field (3.3 MV/cm), representing a tenfold increase over that of silicon, underscoring its suitability for high-voltage applications [61]. Gallium Nitride FETs present a range of advantages over their silicon counterparts, including the reduction of source/drain leakage, facilitation of larger drive currents, and simplification of device cooling requirements [314]–[316]. The amalgamation of a GAA FET device architecture with GaN as the channel material leads to diminished off-state leakage, favourable linearity, and a decrease in subthreshold slope. These attributes collectively position the device as an apt choice for digital electronics and biomedical applications [317], [318].

The presence of a hovering gate within the nanogap gives rise to structural instability in the device. In response to this challenge, K.W. Lee et al. introduced an innovative solution through the concept of an overlapped FET biosensor [226]. This overlap structure not only effectively mitigated the problem of structural instability but also demonstrated enhancements in the biosensor's binding probability and sensitivity [226], [227]. In contrast to conventional nano-FET, the overlap gate-FET configuration involves substantial etching of the gate metal and oxide, creating the sensing area. This strategic alteration eliminates the predicament of the hovering gate electrode. The incorporation of a cavity within the gate oxide serves as a binding site to immobilize biomolecules [226].

Utilizing graded channel in FET can boost operational voltage range by improving performance metrics like breakdown voltage [319] and noise performance [320]. Channel grading enhances device performance properties and offers great sensitivity [248], [321]. Numerous works in the literature have showcased the advantages of GaN as the channel material and the graded channel architecture [23], [24].

This work proposes a Gate-All-Around engineered gallium nitride FET (GAAE-GANFET) based biosensor. The novelty of this work lies in its utilization of both Gate-All-Around engineering and channel engineering techniques. The Gate-All-Around engineering leverages the benefits of open gate overlap architecture, providing structural stability and facilitating fabrication. In contrast, channel engineering entails a step-graded channel in conjunction with a GaN-based channel, collectively achieving remarkable sensitivity to various biomolecules. Thus, this work addresses the research gap in biosensing by amalgamating multiple innovative engineering techniques in a single device. It notably resolves issues related to structural instability caused by hovering gate electrodes (resolved through the overlap gate-FET configuration), while concurrently improving sensitivity through the utilization of graded channel architecture and GaN as the channel material. This configuration renders the device highly suitable for biosensing applications. A compact analytical model (based on the centre-channel potential method) of GAAE-GANFET has been proposed in this work which shows remarkable agreement with the TCAD simulations performed on SILVACO TCAD simulator. This work involves simulation, which has undergone validation against results derived from analytical modeling.

5.2.2 Device and Simulator Specifications

The physical structure of Gate-All-Around Engineered Gallium Nitride Field Effect Transistor (GAAE-GANFET) biosensor is shown in Fig. 5.16 (a) and Fig. 5.16 (b). Validation of the TCAD simulation setup is demonstrated through calibration of the proposed device with the experimental work [152], as depicted in Fig. 5.16 (c).

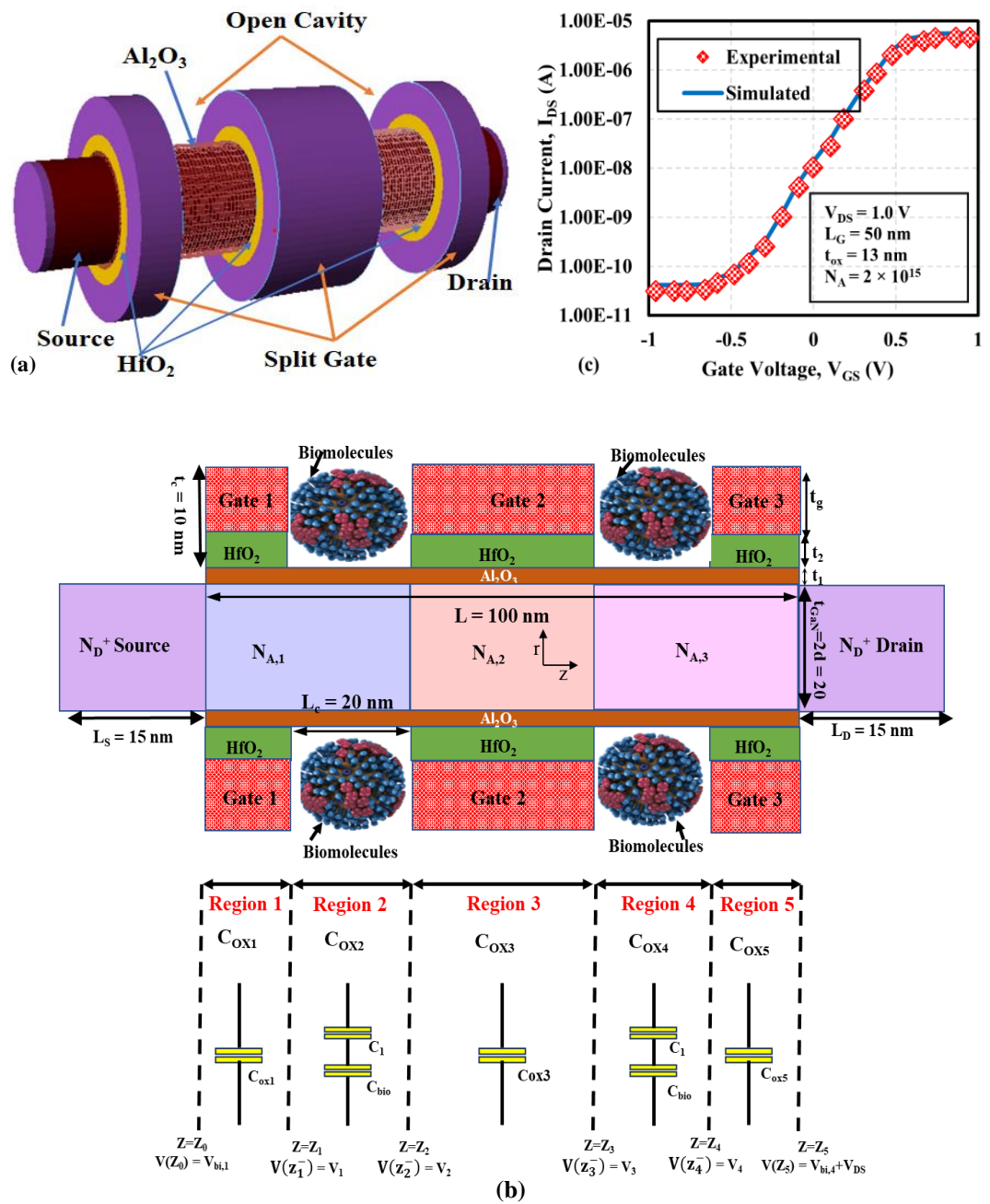


Fig. 5.16 (a) 3-Dimensional View, (b) 2-Dimensional Structure, and (c) Calibration with Experimental Data [152] of GAAE-GANFET Biosensor

The structure features a cylindrical FET with split gate architecture (comprising of three distinct split gates: Gate 1, Gate 2, and Gate 3). As the proposed device adopts a gate-all-around FET structure, it offers robust gate control over the channel to mitigate various short-channel effects, such as off-state leakages, notably Gate Induced Drain Leakage (GIDL) and Drain Induced Barrier Lowering (DIBL) [135], [140], [322]. All the split gates have the same work function (4.9 eV) to reduce fabrication complexity. Later, the effect of work function on the sensitivity has also been taken into account. The biosensor's channel is composed of gallium nitride and is segmented into three separate regions, each characterized by distinct doping concentrations — N_{A1} , N_{A2} , and N_{A3} , respectively. The source and drain materials employed in the device are also composed of gallium nitride (GaN). Doping concentrations in the channel is considered to be a step-graded profile, with N_{A1} being the highest (10^{16} cm^{-3}) and N_{A3} (10^{14} cm^{-3}) the lowest. This graded doping profile in the channel enhances carrier depletion within the channel, leading to reduced OFF-current and improved sensor performance [248], [323]. Additionally, the GaN nanowire FET incorporates the promising dielectric material Al_2O_3 to enhance the obtained sensitivity [258]. Consequently, the proposed device features an Al_2O_3 layer covering the entire channel region. In order to minimize the effective thickness of the gate oxide, a composite layer has been formed by stacking a high-K HfO_2 layer atop of an Al_2O_3 layer [124], a configuration known to improve short-channel effects [303], [311], [324]. This stacking is also capable of enhancing the sensitivity of the proposed biosensor by a significant amount.

The primary biomolecules in this analysis are avian influenza antibody (AI-ab) and DNA. Employing appropriate bio-receptors for DNA and AI-ab can significantly improve the selectivity and specificity of the analytical device. Bioreceptors refer to molecules, enzymes, or biochemical species designed to specifically bind to their target analytes, facilitating their detection and quantification. The specific proteins or molecular components found on the surface of the avian influenza virus are known as avian influenza antigens (AIa).

The host immune system recognizes these antigens, triggering the production of antibodies. Silica-binding proteins (SBP), which establish a strong bond with the oxide surface at one end and combine with the avian influenza antigen (AIa) at the other end, play a crucial role. This enables successful immobilization of AIa on the oxide surface without requiring additional surface modifications [226], [325]. The utilization of SBP-AIa improves the device's selectivity and ensures a secure attachment of the virus marker to the device. The proposed biosensor uses the principle of dielectric modulation to detect the label-free detection of different biomolecules [83]. During the simulations, the absence of biomolecules or the presence of air has been represented with a dielectric constant of $K=1$. Conversely, the presence of biomolecules inside the cavity has been modeled using a dielectric constant $K>1$ along with specific charge density values.

The SILVACO ATLAS-3D tool has been used for device simulations [151]. Table 5.6 presents the structural parameters of GC-SGAA-GaN-FET and the conventional surrounding Gate-All-Around FET with silicon body (SGAA-Si FET), along with the models utilized during the simulation.

Table 5.6 Device Structural Parameters

Physical Device Parameter		GAAE-GANFET	SGAA-Si FET
GaN channel thickness (t_{GaN})		20 nm	20 nm
GaN Channel length (L)		100 nm	100 nm
Source and drain lengths ($L_S = L_D$)		15 nm	15 nm
Gate Metal and its work-function		Molybdenum (4.9 eV)	Molybdenum (4.9 eV)
Oxide thickness (nm)		Al ₂ O ₃ : $t_{\text{ox}} = 1.0$	SiO ₂ : $t_{\text{ox}} = 1.0$
		HfO ₂ : $t_{\text{ox1}} = 3.0$	HfO ₂ : $t_{\text{ox1}} = 3.0$
Source and drain region Doping ($N_S = N_D$)		10^{19} cm^{-3}	10^{19} cm^{-3}
Doping of the channel region	N_{A1}	10^{16} cm^{-3}	10^{16} cm^{-3}
	N_{A2}	10^{15} cm^{-3}	10^{15} cm^{-3}
	N_{A3}	10^{14} cm^{-3}	10^{14} cm^{-3}
Thickness of Cavity (t_C)		10 nm	10 nm
Thickness of Gate		7 nm	7 nm
Length of cavity (L_C)		20 nm	20 nm
Dielectric constants		Al ₂ O ₃ : 9.8	SiO ₂ : 3.9
		HfO ₂ : 22.0	HfO ₂ : 22.0
Physical models [141]		CONMOB : Concentration dependent mobility model.	
		FLDMOB : To model velocity saturation	
		BOLTZMANN : To model the carrier statistics.	
		AUGER : Recombination model which includes the effects at higher doping densities.	
		CVT : It's a Mobility model including doping, temperature and field dependency.	
		SRH : Doping dependent generation-recombination model.	
		BGN : Models the Bandgap narrowing due to high doping.	

5.2.3 Analytical Model

In order to examine the various electrical properties of the GC-SGAA-GaN-FET analytically, it is necessary to solve the 2-D Poisson's equation. The analytical model for channel potential, threshold voltage, and subthreshold slope is built upon the center-channel potential method. Fig. 5.17 illustrates the step-by-step procedure used to develop the analytical model.

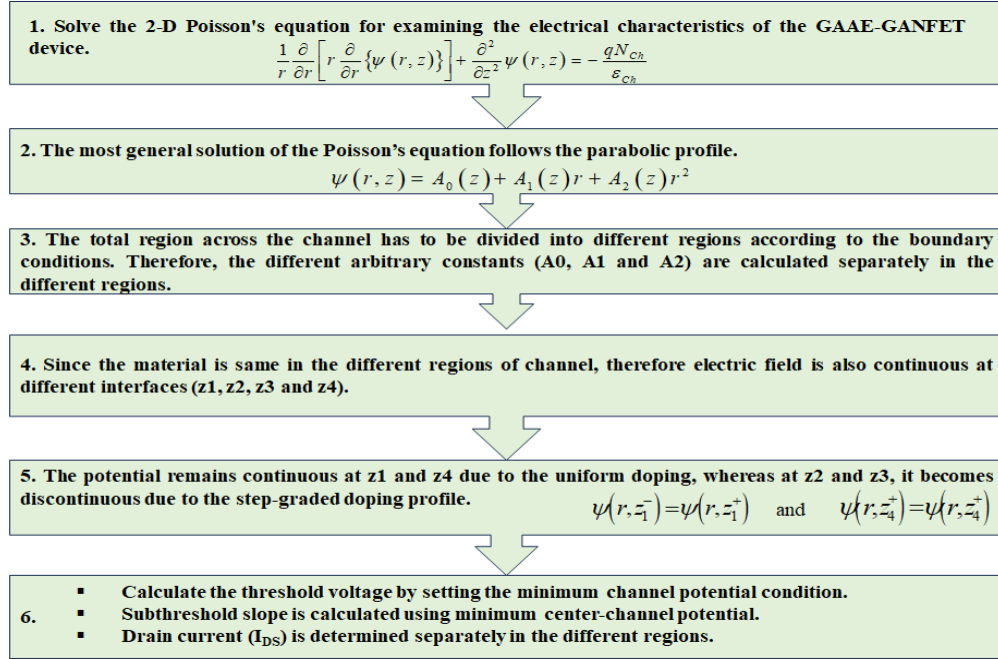


Fig. 5.17 Flowchart demonstrating the Process of Analytical Modeling

5.2.3.1 Surface Potential

The two-dimensional Poisson's equation is

$$\frac{1}{r} \frac{\partial}{\partial r} \left[r \frac{\partial}{\partial r} \{ \psi(r, z) \} \right] + \frac{\partial^2}{\partial z^2} \psi(r, z) = - \frac{qN_{Ch}}{\epsilon_{Ch}} \quad (5.6)$$

The channel potential $\psi(r, z)$, doping concentration N_{Ch} , and dielectric constant ϵ_{Ch} are defined in a cylindrical coordinate system. The channel has a radius r of 'd'. $r = 0$ corresponds to center of channel and the center potential is denoted as $\psi_C(z)$. $r = d$ corresponds to surface interface of the channel and oxide layer. The surface interface potential is expressed as $\psi_I(z)$.

The channel potential's general solution is represented by a parabolic profile, which is written as:

$$\psi(r, z) = A_0(z) + A_1(z)r + A_2(z)r^2 \quad (5.7)$$

Here, A_0 , A_1 and A_2 are the constants. This parabolic profile is commonly used to approximate the potential distribution in FET devices. The solution of equation (5.7) involves applying specific boundary conditions based on the device's structure and characteristics. Different boundary conditions are [25], [248]:

ix. Potential is expressed as follows at the source-channel boundary at ($z = z_0$):

$$\psi(r, z_0) = V_{bi,1} = \frac{k_B T}{q} \left\{ \ln \left(\frac{N_S N_{C1}}{n_i^2} \right) \right\} \quad (5.8)$$

x. At $z = z_5$, the potential is obtained as,

$$\psi(r, z_5) = V_{bi,4} + V_{DS} = \frac{k_B T}{q} \left\{ \ln \left(\frac{N_{C3} N_{Drain}}{n_i^2} \right) \right\} \quad (5.9)$$

xi. Let the potentials at other intermediate boundary positions z_i (z_1, z_2, z_3, z_4) are expressed as:

$$\psi(r, z_1^-) = V_1 \quad (5.10a)$$

$$\psi(r, z_2^-) = V_2 \quad (5.10b)$$

$$\psi(r, z_3^-) = V_3 \quad (5.10c)$$

$$\psi(r, z_4^-) = V_4 \quad (5.10d)$$

- xii. The continuity of the electric field is maintained at $z=z_1, z=z_2, z=z_3, z=z_4$. This continuity ensures a smooth transition and consistency in the electric field profile within the device.

$$\left. \frac{\partial\{\psi(r,z)\}}{\partial z} \right|_{z=z_1^-} = \left. \frac{\partial\{\psi(r,z)\}}{\partial z} \right|_{z=z_1^+} \quad (5.11a)$$

$$\left. \frac{\partial\{\psi(r,z)\}}{\partial z} \right|_{z=z_2^-} = \left. \frac{\partial\{\psi(r,z)\}}{\partial z} \right|_{z=z_2^+} \quad (5.11b)$$

$$\left. \frac{\partial\{\psi(r,z)\}}{\partial z} \right|_{z=z_3^-} = \left. \frac{\partial\{\psi(r,z)\}}{\partial z} \right|_{z=z_3^+} \quad (5.11c)$$

$$\left. \frac{\partial\{\psi(r,z)\}}{\partial z} \right|_{z=z_4^-} = \left. \frac{\partial\{\psi(r,z)\}}{\partial z} \right|_{z=z_4^+} \quad (5.11d)$$

- xiii. At $r=0$, the equation for electric field is written as:

$$\left. \frac{\partial\psi(r,z)}{\partial r} \right|_{r=0} = 0 \quad (5.12)$$

- xiv. At z_1 and z_4 , there is continuous potential. Thus, the two equivalent equations can be expressed as:

$$\psi(r, z_1^-) = \psi(r, z_1^+) \quad (5.13a)$$

$$\psi(r, z_4^-) = \psi(r, z_4^+) \quad (5.13b)$$

- xv. Potential discontinuity at z_2 and z_3 is a result of the step-doping profile. Thus,

$$\psi(r, z_2^+) = V_2 + V_{bi,2} \quad (5.14a)$$

$$\psi(r, z_3^+) = V_3 + V_{bi,3} \quad (5.14b)$$

- xvi. At the channel-oxide interface, the electric field is constant.

$$\epsilon_{ch} \left. \frac{\partial\{\psi(r,z)\}}{\partial r} \right|_{r=d} = C_{ox} [V_{GS} - V_{FB} - \psi(r, z)]|_{r=d} \quad (5.15a)$$

$$\left. \frac{\partial\{\psi(r,z)\}}{\partial r} \right|_{r=d} = \frac{C_{ox}}{\epsilon_{ch}} [V_{GS}^* - \psi_I(z)] \quad (5.15b)$$

The potential function $\psi(r,z)$ can be expressed using $\psi_I(z)$ by applying the previously stated boundary constraints.

$$\psi(r, z) = \frac{1}{2\epsilon_{ch}} [\psi_I(z) \{C_{ox}d + 2\epsilon_{ch}\} - (V_{GS} - V_{fb})C_{ox}d] + \frac{C_{ox}}{2\epsilon_{ch}} [V_{GS} - V_{fb} - \psi_I(z)]r^2 \quad (5.16)$$

A relationship between $\psi_{C,i}(z)$ and $\psi_{I,i}(z)$ by putting $r=0$ in equation 5.14.

$$\psi_I(z) = \frac{[C_{ox}d(V_{GS} - V_{fb}) + 2\psi_C(z)\epsilon_{ch}]}{2\epsilon_{ch} + C_{ox}d} \quad (5.17)$$

Reintroducing equations (5.16) and (5.17) into equation (5.6) allows for the derivation of a differential equation for the center channel potential.

$$\mu^2 \frac{\partial^2 \psi_C(z)}{\partial z^2} + \theta = \psi_C(z) \quad (5.18a)$$

$$\theta = (V_{GS} - V_{fb}) + \frac{qN_{ch}}{2C_{ox}} + \frac{qN_{ch}d^2}{4\epsilon_{ch}} \quad (5.18b)$$

$$\mu = \sqrt{\frac{q\epsilon_{ch}}{2C_{ox}}} \quad (5.18c)$$

The equation (5.16) admits a generalized solution that can be expressed as equation (5.19):

$$\psi_C(z) = pe^{\frac{z}{\mu}} + qe^{-\frac{z}{\mu}} + \theta \quad (5.19)$$

Here, the parameters μ and θ are specific to the material. p and q , however, are just random constant quantities. The effective capacitance in each region (R-I/R-III/R-V) is the series combination of two capacitances ignoring the dielectric leakage current and absorption [249]. In the underlap region, capacitance is modeled by considering the approximate effect of biomolecules occupying the cavity under the fringing fields [250]. Thus, $\psi_C(z)$ is calculated in distinct regions as follows:

Region I: $z_0 \leq z \leq z_1$

$$\psi_{C1}(z) = p_1 e^{\frac{z}{\mu_1}} + q_1 e^{-\frac{z}{\mu_1}} + \theta_1 \quad (5.20a)$$

$$p_1 = \frac{1}{e^{-\frac{(z_0-z_1)}{\mu_1}} - e^{-\frac{(z_0-z_1)}{\mu_1}}} \left[V_1 e^{-\frac{z_0}{\mu_1}} - V_{bi,1} e^{-\frac{z_1}{\mu_1}} - \theta_1 \left(e^{-\frac{z_0}{\mu_1}} - e^{-\frac{z_1}{\mu_1}} \right) \right] \quad (5.20b)$$

$$q_1 = \frac{1}{e^{-\frac{(z_1-z_0)}{\mu_1}} - e^{-\frac{(z_1-z_0)}{\mu_1}}} \left[V_1 e^{\frac{z_0}{\mu_1}} - V_{bi,1} e^{\frac{z_1}{\mu_1}} - \theta_1 \left(e^{\frac{z_0}{\mu_1}} - e^{\frac{z_1}{\mu_1}} \right) \right] \quad (5.20c)$$

$$C_{ox,1} = \frac{\varepsilon_{Al_2O_3}}{d \ln\left(1 + \frac{t_{eff}}{d}\right)}, t_{eff} = t_2 \left(\frac{\varepsilon_{Al_2O_3}}{\varepsilon_{HfO_2}} \right) + t_1 \quad (5.20d)$$

Region II: $z_1 \leq z \leq z_2$

$$\psi_{C2}(z) = p_2 e^{\frac{z}{\mu_2}} + q_2 e^{-\frac{z}{\mu_2}} + \theta_2 \quad (5.21a)$$

$$p_2 = \frac{1}{e^{-\frac{(z_1-z_2)}{\mu_2}} - e^{-\frac{(z_1-z_2)}{\mu_2}}} \left[V_2 e^{-\frac{z_1}{\mu_2}} - V_1 e^{-\frac{z_2}{\mu_2}} - \theta_2 \left(e^{-\frac{z_1}{\mu_2}} - e^{-\frac{z_2}{\mu_2}} \right) \right] \quad (5.21b)$$

$$q_2 = \frac{1}{e^{-\frac{(z_2-z_1)}{\mu_2}} - e^{-\frac{(z_2-z_1)}{\mu_2}}} \left[V_2 e^{\frac{z_1}{\mu_2}} - V_1 e^{\frac{z_2}{\mu_2}} - \theta_2 \left(e^{\frac{z_1}{\mu_2}} - e^{\frac{z_2}{\mu_2}} \right) \right] \quad (5.21c)$$

$$\frac{1}{C_{ox,2}} = \frac{1}{C_1} + \frac{1}{C_{fr}} \quad (5.21d)$$

$$C_1 = \frac{\varepsilon_{SiO_2}}{d \ln\left(1 + \frac{t_{t1}}{d}\right)}, C_{fr} = \frac{2\varepsilon_{bio}}{\pi t_2} \quad (5.21e)$$

Region III: $z_2 \leq z \leq z_3$

$$\psi_{C3}(z) = p_3 e^{\frac{z}{\mu_3}} + q_3 e^{-\frac{z}{\mu_3}} + \theta_3 \quad (5.22a)$$

$$p_3 = \frac{1}{e^{-\frac{(z_2-z_3)}{\mu_3}} - e^{-\frac{(z_2-z_3)}{\mu_3}}} \left[V_3 e^{-\frac{z_2}{\mu_3}} - (V_2 + V_{bi,2}) e^{-\frac{z_3}{\mu_3}} - \theta_3 \left(e^{-\frac{z_2}{\mu_3}} - e^{-\frac{z_3}{\mu_3}} \right) \right] \quad (5.22b)$$

$$q_3 = \frac{1}{e^{-\frac{(z_3-z_2)}{\mu_3}} - e^{-\frac{(z_3-z_2)}{\mu_3}}} \left[V_3 e^{\frac{z_2}{\mu_3}} - (V_2 + V_{bi,2}) e^{\frac{z_3}{\mu_3}} - \theta_3 \left(e^{\frac{z_2}{\mu_3}} - e^{\frac{z_3}{\mu_3}} \right) \right] \quad (5.22c)$$

$$C_{ox,3} = C_{ox,1} \quad (5.22d)$$

Region IV: $z_3 \leq z \leq z_4$

$$\psi_{C4}(z) = p_4 e^{\frac{z}{\mu_4}} + q_4 e^{-\frac{z}{\mu_4}} + \theta_4 \quad (5.23a)$$

$$p_4 = \frac{1}{e^{-\frac{(z_3-z_4)}{\mu_4}} - e^{-\frac{(z_3-z_4)}{\mu_4}}} \left[V_4 e^{-\frac{z_3}{\mu_4}} - (V_3 + V_{bi,3}) e^{-\frac{z_4}{\mu_4}} - \theta_4 \left(e^{-\frac{z_3}{\mu_4}} - e^{-\frac{z_4}{\mu_4}} \right) \right] \quad (5.23b)$$

$$q_4 = \frac{1}{e^{-\frac{(z_4-z_3)}{\mu_4}} - e^{-\frac{(z_4-z_3)}{\mu_4}}} \left[V_4 e^{\frac{z_3}{\mu_4}} - (V_3 + V_{bi,3}) e^{\frac{z_4}{\mu_4}} - \theta_4 \left(e^{\frac{z_3}{\mu_4}} - e^{\frac{z_4}{\mu_4}} \right) \right] \quad (5.23c)$$

$$C_{ox,4} = C_{ox,2} \quad (5.23d)$$

Region V: $z_4 \leq z \leq z_5$

$$\psi_{C5}(z) = p_5 e^{\frac{z}{\mu_5}} + q_5 e^{-\frac{z}{\mu_5}} + \theta_5 \quad (5.24a)$$

$$p_5 = \frac{1}{e^{-\frac{(z_4-z_5)}{\mu_5}} - e^{\frac{(z_4-z_5)}{\mu_5}}} \left[(V_{bi,4} + V_{DS}) e^{\frac{-z_4}{\mu_5}} - V_4 e^{\frac{-z_5}{\mu_5}} - \theta_5 \left(e^{\frac{-z_4}{\mu_5}} - e^{\frac{-z_5}{\mu_5}} \right) \right] \quad (5.24b)$$

$$q_5 = \frac{1}{e^{-\frac{(z_3-z_2)}{\mu_5}} - e^{\frac{(z_3-z_2)}{\mu_5}}} \left[(V_{bi,4} + V_{DS}) e^{\frac{z_4}{\mu_5}} - V_4 e^{\frac{z_5}{\mu_5}} - \theta_5 \left(e^{\frac{z_4}{\mu_5}} - e^{\frac{z_5}{\mu_5}} \right) \right] \quad (5.24c)$$

$$C_{ox,5} = C_{ox,1} \quad (5.24d)$$

Appendix-I consists of the μ_1 - μ_5 and θ_1 - θ_5 values. Equations (5.8) to (5.15) provide boundary conditions that can be used to derive the V_1 , V_2 , V_3 and V_4 .

$$V_1 = \frac{c_6 c_2 - c_3 c_5}{c_2 c_4 - c_1 c_5} \quad (5.25a)$$

$$V_2 = \frac{c_6 c_1 - c_3 c_4}{c_1 c_5 - c_2 c_6} \quad (5.25b)$$

$$V_3 = d_1 + d_2 + d_3 \quad (5.25c)$$

$$V_4 = d_4 V_2 + d_5 V_3 + d_6 \quad (5.25d)$$

Appendix-II contains the values for c_1 - c_6 and d_1 - d_6 .

Each region's electric field can be expressed as,

$$E_{Z_i} = -\frac{1}{\mu_i} \left(p_i e^{\frac{z}{\mu_i}} - q_i e^{-\frac{z}{\mu_i}} \right) \quad (5.26)$$

5.2.3.2 Threshold Voltage

The threshold voltage is obtained by setting the minimum channel-center potential to zero. In this context, the minimum channel-center potential is consistently observed in region-I, attributed to the presence of negative charges deposited by biomolecules in the oxide layer [25]. By equating the derivative of the expression for the channel-center potential in region-I to zero, the precise location of the minimum channel-center potential can be determined.

$$\left. \frac{d\psi_{C_1}(z)}{dz} \right|_{z=z_{Minima}} = 0 \rightarrow z_{Minima} = \mu_1 \ln \left(\sqrt{\frac{q_1}{p_1}} \right) \quad (5.27)$$

By substituting the value of Z_{min} from equation (5.27) into equation (5.20a), the minimum channel potential is denoted as:

$$V_t = \frac{-W_b + \sqrt{W_b^2 - 4W_a W_c}}{2W_a} \quad (5.28)$$

Values of W_a , W_b and W_c are given in Appendix-III.

5.2.3.3 Subthreshold Slope and Drain Current

In the linear region, the drain current (I_{DS}) is determined separately in the five different regions, as outlined in references [99] and [254].

$$I_{DS(Lin,I)} = \frac{2\pi C_{ox1} d \mu_n}{L'_{C1}} \left[(V_{GS} - V_t)(V_1 - V_{bi,1}) - \frac{(V_1 - V_{bi,1})^2}{2} \right] \quad (5.29)$$

$$I_{DS(Lin,II)} = \frac{2\pi C_{ox2} d \mu_n}{L'_{C2}} \left[(V_{GS} - V_t)(V_2 - V_1) - \frac{(V_2 - V_1)^2}{2} \right] \quad (5.30)$$

$$I_{DS(Lin,III)} = \frac{2\pi C_{ox3} d \mu_n}{L'_{C3}} \left[(V_{GS} - V_t)(V_3 - V_x) - \frac{(V_3 - V_x)^2}{2} \right] \quad (5.31)$$

$$I_{DS(Lin,IV)} = \frac{2\pi C_{ox4} d \mu_n}{L'_{C4}} \left[(V_{GS} - V_t)(V_4 - V_y) - \frac{(V_4 - V_y)^2}{2} \right] \quad (5.32)$$

$$I_{DS(Lin,V)} = \frac{2\pi C_{ox5} d \mu_n}{L'_{C5}} \left[(V_{GS} - V_t)(V_5 - V_4) - \frac{(V_5 - V_4)^2}{2} \right] \quad (5.33)$$

By applying suitable boundary conditions, V_x and V_y are computed and presented in mathematical terms, as:

$$V_x = V_{bi,2} + \psi_2(r, z_2) \quad (5.34a)$$

$$V_y = V_{bi,3} + \psi_3(r, z_3) \quad (5.34b)$$

To calculate the drain current in the saturation region, V_{DS} is replaced with $V_{DS,Sat}$ [99], [248]

$$V_{DS,Sat} = \frac{(V_{GS} - V_t)}{1 + \frac{\mu_{efld}(V_{GS} - V_t)}{(L_1 + L_2 + L_3 + L_4 + L_5)v_{Sat}}} \quad (5.35)$$

$$\mu_{efld} = \frac{\mu_n}{\{1 - \zeta(V_{GS} - V_t)\} \left\{ 1 + \Omega \frac{V_{DS}\mu_n}{(L_1 + L_2 + L_3 + L_4 + L_5)v_{Sat}} \right\}} \quad (5.36)$$

$$\Omega = \left[\frac{V_{DS}\mu_n}{(L_1 + L_2 + L_3 + L_4 + L_5)v_{Sat}} \right] \left[1.5 + \left\{ \frac{V_{DS}\mu_n}{(L_1 + L_2 + L_3 + L_4 + L_5)v_{Sat}} \right\} \right]^{-1} \quad (5.37)$$

μ_{efld} stands for the peak low-field mobility of electrons, and μ_n denotes the electron mobility. Electron saturation velocity $v_{Sat} = 1 \times 10^7$ cm/s, and fitting parameter $\eta = 0.43$.

With minimum center-channel potential, the subthreshold slope is computed and is written as,

$$SS = V_T \log(10) \left[\left(\frac{\partial \Psi(d,z)}{\partial V_{GS}} \right)^{-1} \right] \Bigg|_{z=z_{min}} \quad (5.38)$$

5.2.4 Results and Discussion

The investigation includes charged analytes, like ssDNA, dsDNA, avian influenza antigen (AIA), and avian influenza antibody (AI-ab). For DNA detection, the simulation considers single-stranded DNA (ssDNA) with a dielectric constant $K = 2$ and a surface charge density $Q_f = 1 \times 10^{11}$ C/cm² [256]. Conversely, double-stranded DNA (dsDNA) is simulated with a dielectric constant $K = 8$ and a surface charge density $Q_f = 5 \times 10^{11}$ C/cm² [257], [326], [327].

For avian influenza antigen (AIA) detection, Silica binding protein (SBP) and AIA were combined, and the simulation employed a surface charge density of 2×10^{11} C/cm² and a dielectric constant of 2 [255]. Subsequently, the immobilization of avian influenza antibody (AI-ab) within the open cavity was modeled using specific values: a dielectric constant of 3 and a surface charge density of -6×10^{11} C/cm² [255], [327].

When DNA and the Avian Influenza antibody are introduced into the open cavity, the surface potential along the channel varies with the concentration and charge density of biomolecules due to change in effective gate oxide capacitance [25], [328], as depicted in Fig. 5.18 (a). The TCAD simulation's results closely aligns with the analytical data, showcasing a high level of agreement between the two. The channel potential decreases due to the strong coupling between the gate and the channel, and this coupling continues to increase as the dielectric constant of the immobilized biomolecules increases [329]. The presence of negative charges on biomolecules further enhances the coupling between the gate and channel, leading to a further reduction in the channel potential [330]. Among the biomolecules used in this investigation, AI-ab exhibits the lowest surface potential due to highest negative charge density. The reduction in the channel-surface potential implies that a higher gate voltage is required to deplete the channel entirely; consequently, the threshold voltage will increase.

The surface potential variation of the GAAE-GANFET with variations in the open cavity length (L_C) for AI-ab is illustrated in Fig. 5.18 (b). The immobilization of biomolecules increases (more biomolecules can be immobilized) with the increasing cavity length, decreasing energy band bending near the channel's surface. This, in turn, causes a decrease in the surface potential within the channel region beneath the cavity. As a consequence, the threshold voltage gradually increases due to the downward shift in the surface potential profile, which is discussed in reference [89].

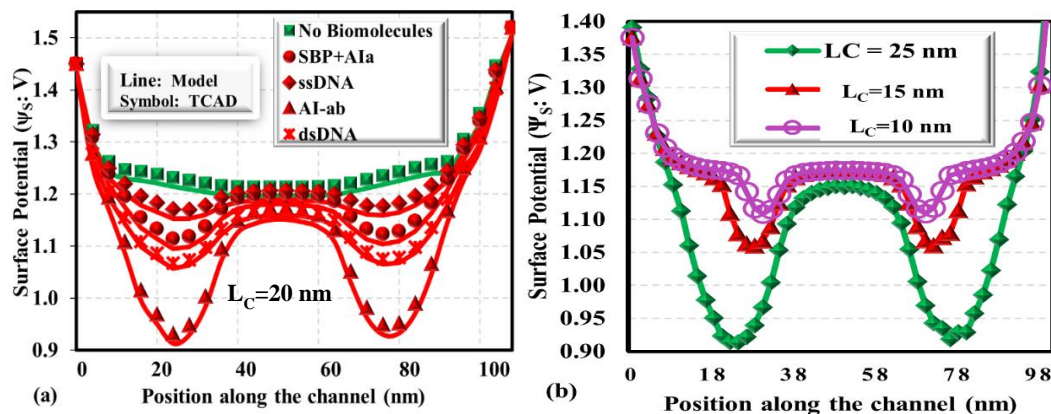


Fig. 5.18 Surface Potential of GAAE-GANFET for Different (a) Biomolecules and (b) Cavity Lengths

Fig. 5.19 depicts the electric field variation in GAAE-GANFET for AI-ab and dsDNA. Notably, the electric field variations are observed under both the gate overlap and underlap regions, indicating the existence of biomolecules. The electric field variations are notably stronger, peaking at 2.08×10^5 V/cm, 1.24×10^5 V/cm beneath the cavity region for AI-ab and dsDNA biomolecules. This variation can be attributed to the substantial negative charge of AI-ab, resulting in a more pronounced modulation (stronger capacitive coupling). Figure 4 distinctly illustrates that the immobilization of the biomolecule inside the cavity doesn't affect the electric field at junction of drain-channel and source-channel. This prevents the device from experiencing velocity saturation due to biomolecules immobilization. Due to effective gate dielectric and charge modulation, this electric field change primarily impacts the threshold voltage sensitivity.

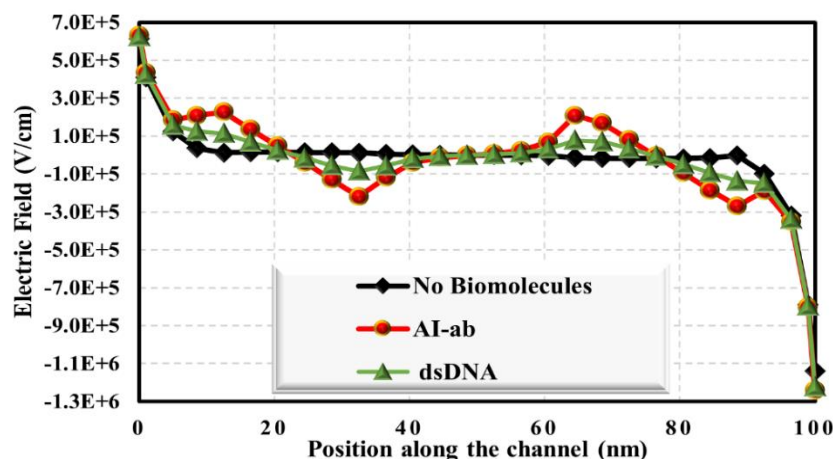


Fig. 5.19 Electric Field Variation along the Channel for AI-ab and DNA Biomolecules

Fig. 5.20 illustrates the contour plots of electron concentration in the channel region of the GAAE-GANFET under different scenarios: when there are no biomolecules in the underlap cavity and when avian influenza antibody and dsDNA biomolecules are immobilized. Referring to the electron concentration profile in figure 5, it's evident that the device's electron concentration diminishes sequentially as the biomolecules starts accumulating inside the cavity. This trend highlights that the electron concentration in the channel decreases as the negative charge concentration of the biomolecules increases. As the electron concentration in the channel reduces due to the presence of immobilized biomolecules, the drain current of the device also decreases [25], [258]. This effect arises because the lower electron concentration leads to a decreased number of charge carriers available in the channel, consequently reducing their contribution to the overall current flow.

In Fig. 5.21, the drain current is shown plotted against the gate-to-source voltage, or V_{GS} . The drain current (I_{DS}) decreases in the following order: ssDNA, SBP+AIa, dsDNA, and AI-ab. Thus, the AI-ab biomolecule exhibit the lowest drain current among the analyzed biomolecules. This reduction can be attributed to the highest negative charge density of the biomolecule, resulting in high coupling between the gate and charge carriers. It is also evident that the subthreshold current (I_{sub}), indicated on the secondary axis, decreases for all the charged biomolecules compared to the I_{sub} value when no biomolecules are immobilized in the cavity. In comparison to the subthreshold current of 7.39×10^{-16} A observed in the absence of biomolecules, the subthreshold current decreases to 1.22×10^{-19} A for AI-ab and 5.81×10^{-19} A for dsDNA, indicating significant reductions for both AI-ab and dsDNA biomolecules. This decrease in subthreshold current is an effective indicator of the enhanced biosensing capability. The remarkably low OFF current (I_{sub}) is credited to the comprehensive regulation of channel by surrounding gate structure, therefore mitigating few short channel effects (SCEs).

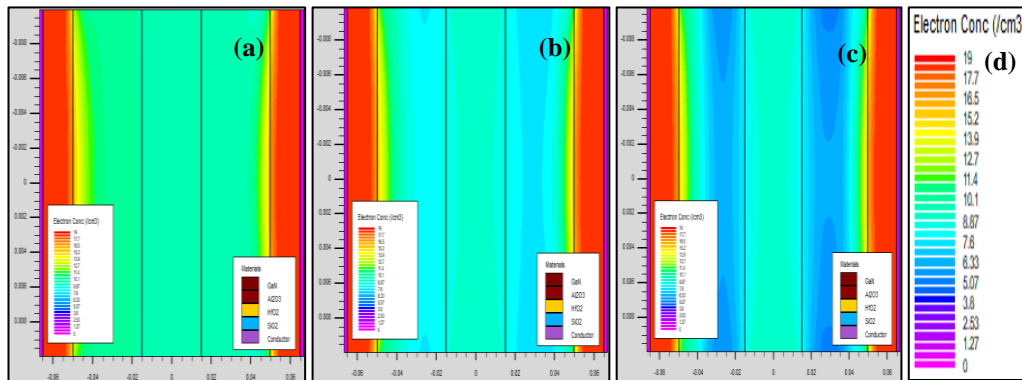


Fig. 5.20 Contour Plots of Electron Concentration Variation along the Channel (a) No Biomolecule (b) dsDNA (c) AI-ab (d) Electron Concentration Profile

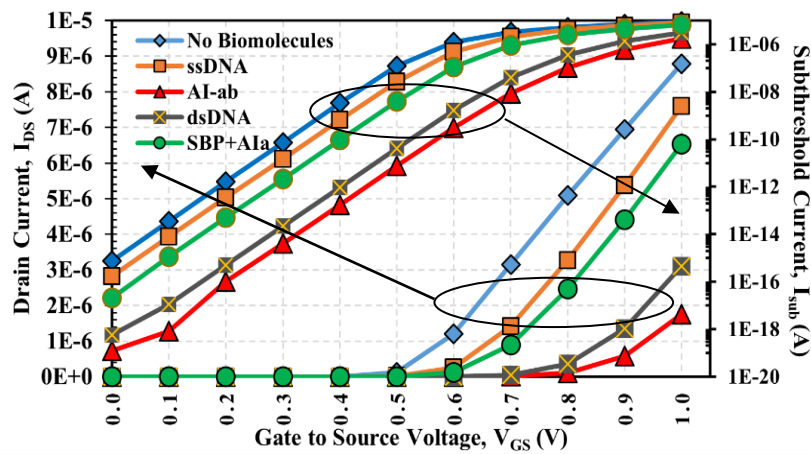


Fig. 5.21 I_D - V_{GS} Characteristics of GAEE-GANFET Biosensor

In the case of biosensors, a shift in the threshold voltage is crucial, as it determines the sensitivity of the device. The threshold voltage sensitivity ($S_{V_{th}}$) is defined as difference in threshold voltage with and without biomolecules into the cavity region. According to equation 34, mathematically $S_{V_{th}}$ is represented as:

$$S_{V_{th}} = |V_{th_{No\ Biomolecule}} - V_{th_{with\ Biomolecules}}| \quad (5.40)$$

Fig. 5.22 illustrates the threshold voltage shift resulting from the introduction of various DNA and avian influenza biomolecules. The analytical and simulated threshold voltage values are in good agreement. When negatively charged biomolecules are present inside the cavity, they introduce additional negative charges near the surface of the device. These charges create an opposing electric field that counteracts the applied positive gate voltage. As a result, a higher gate-to-source voltage is needed to overcome the repulsive force, leading to an increased threshold voltage of the device [25], [229]. Fig. 5.22 also demonstrates the threshold voltage sensitivity of the proposed device for ssDNA, SBP+AIa, dsDNA, and AI-ab biomolecules. The device exhibits remarkably high V_{th} sensitivity, with values of 122.6 mV, 156.6 mV, 286.7 mV, and 318.2 mV for ssDNA, SBP+AIa, dsDNA, and AI-ab biomolecules, respectively.

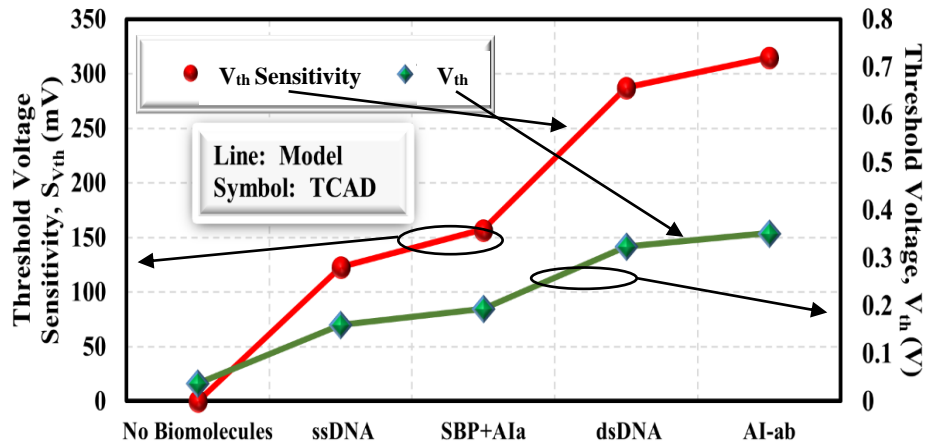


Fig. 5.22 Threshold Voltage (V_{th}) and Threshold Voltage Sensitivity ($S_{V_{th}}$) of GAAE-GANFET Biosensor

In Fig. 5.23 (a), the drain current sensitivity (S_{ID}) is presented for various biomolecules at $V_{GS}=1.0$ V while varying the drain voltage (V_{DS}). S_{ID} represents the change in drain current observed between the presence and absence of immobilized biomolecules within the cavity.

$$S_{ID} = \left| I_{D_{No\ Biomolecule}} - I_{D_{with\ Biomolecules}} \right| \quad (5.41)$$

With an increase in the negative charge on the biomolecules, their binding capacity also rises, consequently exerting greater control over the flow of charge carriers within the channel [248]. This effect causes a shift in the drain current curve towards lower values. Simultaneously, the drain current decreases as the biomolecule's dielectric constant increases, owing to the concurrent rise in the effective gate oxide capacitance. However, the relative change in drain current increases in both scenarios. The combined influence of the increasing dielectric constant and rising negative charge leads to a continual elevation in the drain current sensitivity (measuring the relative change in drain current), as depicted in Fig. 5.23 (a). Among the biomolecules under consideration, the AI-ab variant exhibits the highest current sensitivity owing to the maximum negative charge density. Transconductance (g_m) is the derivative of drain current with respect to V_{GS} . The transconductance curve exhibits a pattern resembling that of the drain current. So, as shown in Fig. 5.23 (b), the largest transconductance sensitivity is also found for the AI-ab biomolecule, which has the highest negative charge density out of the examined biomolecules (ssDNA, SBP-AIa, dsDNA, and AI-ab).

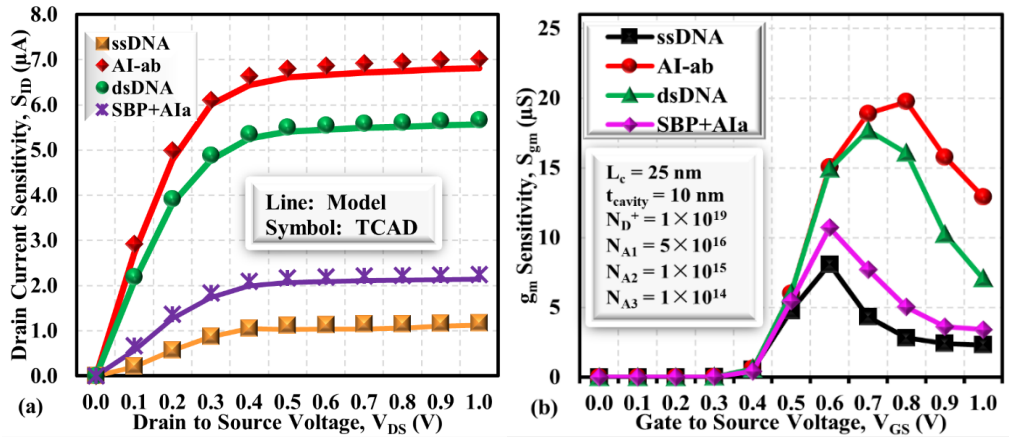


Fig. 5.23 (a) Drain Current Sensitivity (b) Transconductance Sensitivity for Various Biomolecules

Fig. 5.24 (a) illustrates the sensitivity of subthreshold slope on the primary axis and the variation in subthreshold slope on the secondary axis for different biomolecules. The subthreshold slope of a transistor quantifies its effectiveness in controlling the flow of current during turning on and off processes. It holds an inverse relationship with the gate oxide capacitance, implying that a larger gate oxide capacitance corresponds to a smaller subthreshold slope [248]. With increasing dielectric constant (K) of the biomolecule and the presence of negative charge, the gate oxide capacitance increases, resulting in a decrease in subthreshold slope. The subthreshold swing sensitivity (S_{SS}) denotes the absolute variation in subthreshold swing when comparing the conditions with and without immobilized biomolecules in the cavity.

$$S_{SS} = |S_{SS_{No\ Biomolecule}} - S_{SS_{with\ Biomolecules}}| \quad (5.42)$$

Due to increased deviation in the subthreshold slope, the subthreshold slope sensitivity increases for the biomolecules such as ssDNA, SBP+AIa, dsDNA, and AI-ab, respectively according to equation (37) for sensitivity calculation.

Fig. 5.24 (b) illustrates the rising trend of the I_{ON}/I_{OFF} ratio and the corresponding I_{ON}/I_{OFF} sensitivity for ssDNA, SBP+AIa, dsDNA, and AI-ab. The I_{ON}/I_{OFF} sensitivity has been calculated as the relative change in the value of the I_{ON}/I_{OFF} ratio, represented as:

$$I_{ON}/I_{OFF} \text{ Sensitivity} = \frac{I_{ON}/I_{OFF_{No\ Biomolecule}} - I_{ON}/I_{OFF_{with\ Biomolecules}}}{I_{ON}/I_{OFF_{No\ Biomolecule}}} \quad (5.43)$$

The increase in the negative charge density of the biomolecules leads to a decrease in both I_{ON} and I_{OFF} currents, as depicted in Fig. 5.21. However, the reduction in the I_{OFF} current is significantly more prominent compared to the I_{ON} current, resulting in an increased I_{ON}/I_{OFF} ratio. Furthermore, the change in on-current and off-current relative to the 'no-biomolecule' case increases with higher dielectric constants and an augmented negative charge density of the biomolecules.

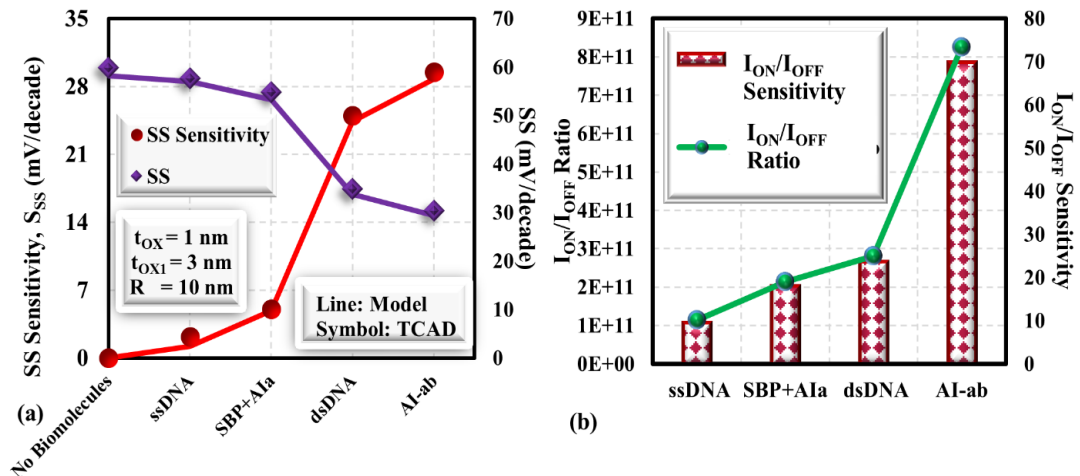


Fig. 5.24 (a) Sensitivity of Subthreshold Voltage Swing and Variation in SS (b) I_{ON}/I_{OFF} Ratio and I_{ON}/I_{OFF} Sensitivity for Different Biomolecules

The influence of an oxide stack consisting of Al_2O_3 and HfO_2 on various biomolecules has also been investigated. This study encompasses two scenarios: the first involves depositing Al_2O_3 as the sole dielectric layer, while the second entails depositing both Al_2O_3 and HfO_2 onto the GaN substrate. The stacking of gate oxides enhances the regulation of charge carrier movement, resulting in a further reduction in drain current as the coupling is intensified [273], [331]–[333]. Consequently, the drain current sensitivity increases when employing a dielectric stack ($Al_2O_3 + HfO_2$) compared to using Al_2O_3 alone, as evidenced in Fig. 5.25.

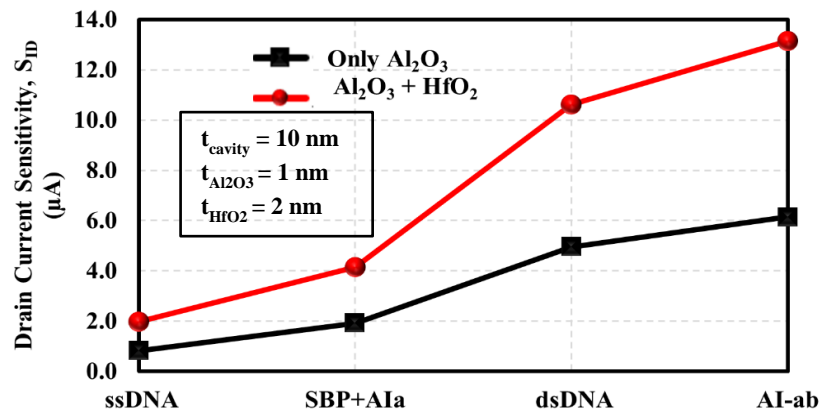


Fig. 5.25 Impact of Stacked Gate Oxide on Sensitivity of Drain Current to Various Biomolecules

Table 5.7 displays the S_{ID} and $S_{V_{th}}$ in the GAAE-GANFET biosensor for variations in the open cavity length. For the two-sided open cavities, three cavity lengths of 10 nm, 15 nm, and 25 nm have been taken into consideration (considering symmetric cavities). As the cavity length increases, the biomolecules' binding area expands, allowing for a greater number of biomolecules to be accommodated [229]. As a result, this causes the drift of the threshold voltage and drain current for various biomolecules to be significantly enhanced.

Table 5.7 Effect of Channel Length Variation on Various Sensitivity Parameters

Biomolecules	L _c = 10 nm		L _c = 15 nm		L _c = 20 nm	
	S _{Vth} (mV)	S _{ID} (μA)	S _{Vth} (mV)	S _{ID} (μA)	S _{Vth} (mV)	S _{ID} (μA)
ssDNA	30.97	0.25	55.29	0.03	122.6	1.16
SBP+AI-ab	36.31	0.54	65.86	0.99	156.6	2.23
dsDNA	72.59	2.59	128.3	3.59	286.7	5.66
AI-ab	82.06	4.03	146.6	5.19	314.2	7.01

Table 5.8 presents different sensitivities for Avian Influenza biomolecules when several graded doping profiles are employed in the channel region of the GAAE-GANFET biosensor. Uniform increasing step-graded doping and uniform decreasing step-graded doping in channels are examples of the various cases considered. Utilizing a horizontal tri-step doping profile in the channel of a device offers multiple benefits beyond just sensitivity enhancement. The incorporation of a tri-step doping profile enables precise channel engineering, resulting in the enhancement in device performance by increasing the driving current, and mitigating Short Channel Effects as well as body effect [334], [335]. It is important to note that graded doping profile-1 ($N_{A1}=1\times 10^{16}/\text{cm}^3$, $N_{A2}=1\times 10^{15}/\text{cm}^3$, $N_{A3}=1\times 10^{14}/\text{cm}^3$) results in the maximum V_{th} sensitivity and drain current sensitivity. While the I_{ON}/I_{OFF} ratio drifts more in favor of the doping profiles 2 and 4 than the doping profile 1.

Table 5.8 Effect of Graded Doping Variation on Various Sensitivity Parameters of GAAE-GANFET Biosensor

Parameters	Doping Profile 1 $N_{A1}=1\times 10^{16}$ $N_{A2}=1\times 10^{15}$ $N_{A3}=1\times 10^{14}$	Doping Profile 2 $N_{A1}=1\times 10^{18}$ $N_{A2}=1\times 10^{17}$ $N_{A3}=1\times 10^{16}$	Doping Profile 3 $N_{A1}=1\times 10^{14}$ $N_{A2}=1\times 10^{15}$ $N_{A3}=1\times 10^{16}$	Doping Profile 4 $N_{A1}=1\times 10^{16}$ $N_{A2}=1\times 10^{17}$ $N_{A3}=1\times 10^{18}$	Doping Profile 5 $N_{A1}=1\times 10^{14}$ $N_{A2}=1\times 10^{13}$ $N_{A3}=1\times 10^{12}$
S _{Vth} (mV)	314.20	110.49	313.96	134.99	312.98
S _{ID} (μA)	7.01	3.23	6.89	3.20	6.86
S _{SS} (mV/decade)	24.98	5.29	26.44	23.41	25.04
I _{ON} /I _{OFF} Sensitivity	8.14×10^{11}	3.62×10^{12}	7.45×10^{11}	6.75×10^{12}	8.04×10^{11}

Table 5.9 presents the threshold voltage sensitivity (S_{Vth}) and current sensitivity (S_{ID}) values for various biomolecules as the temperature is varied from $T = 200$ kelvin to $T = 400$ kelvin. High temperatures result in the formation of a larger number of charge carriers, so the same drain current can now be attained at a lower V_{GS} , leading to a decrease in threshold voltage [336]. While the drain current ($V_{GS}=V_{DS}=1$) increases with rising temperature, this is a result of multiple contributing factors, including enhanced carrier mobility, increased thermally generated charge carriers, and a reduced

bandgap. However, intriguingly, $S_{V_{th}}$ and $S_{I_{D}}$ decrease as temperature rises, owing to the reduction in the relative variation of threshold voltage and ON-current.

Table 5.9 Effect of Temperature Variation on Various Sensitivity Parameters

	T=200K		T=300K		T=400K	
	$S_{V_{th}}$ (mV)	$S_{I_{D}}$ (μ A)	$S_{V_{th}}$ (mV)	$S_{I_{D}}$ (μ A)	$S_{V_{th}}$ (mV)	$S_{I_{D}}$ (μ A)
SBP+AI-ab	166.14	2.57	155.52	2.23	110.38	0.87
ssDNA	127.93	1.28	122.61	1.17	133.72	1.58
AI-ab	325.99	7.98	314.20	7.01	237.98	3.97
dsDNA	303.34	6.57	286.67	5.66	265.24	5.01

In this work, an exhaustive exploration of device sensitivity is undertaken, encompassing various neutral biomolecules, including Streptavidin ($K=2.1$), APTES ($K=3.57$), Hydroprotein ($K=5$), Keratin ($K=8$), and Gelatin ($K=12$). Furthermore, the proposed GAEE-GANFET biosensor is juxtaposed with a silicon (Si) channel FET biosensor, namely the SGAA-Si FET biosensor, to facilitate a comprehensive comparison. This comparison is centered on their drain current characteristics and diverse sensitivities, with particular emphasis on their capability to detect neutral biomolecules.

The SGAA-Si FET biosensor adheres to the same device specifications as the proposed biosensor but features a silicon channel in its design. Fig. 5.26 (a) portrays the graph of drain current with respect to V_{GS} for various biomolecules. Fig. 5.26 (a) makes it abundantly clear that the proposed GaN channel device exhibits a superior current drive capacity in comparison to the SGAA-Si FET biosensor, a distinction attributed to the GaN channel. GaN-offers superior electron mobility and better electron saturation velocity compared to Si, making it more efficient in transporting charge carriers (electrons) through the channel. As depicted in Fig. 5.26 (b), the current sensitivity of the proposed GaN channel biosensor surpasses that of the Si channel FET based biosensor by 93.83%, 97.33%, 98.34%, 100.80%, and 104.11% for streptavidin, APTES, Hydroprotein, Keratin, and Gelatin, respectively. Fig. 5.26 (c) depicts the V_{th} sensitivity variation for neutral biomolecules. The proposed GAEE-GANFET exhibits higher V_{th} sensitivity compared to the SGAA-Si FET biosensor. For instance, when detecting Gelatin biomolecules, the V_{th} sensitivity is 76.9 mV for the SGAA-Si FET biosensor, whereas it increases to 115.51 mV for the GAEE-GANFET, representing a remarkable 50.02% improvement. This enhanced sensitivity is attributed to the GAEE-GANFET's exceptional biocompatibility and chemical stability [337].

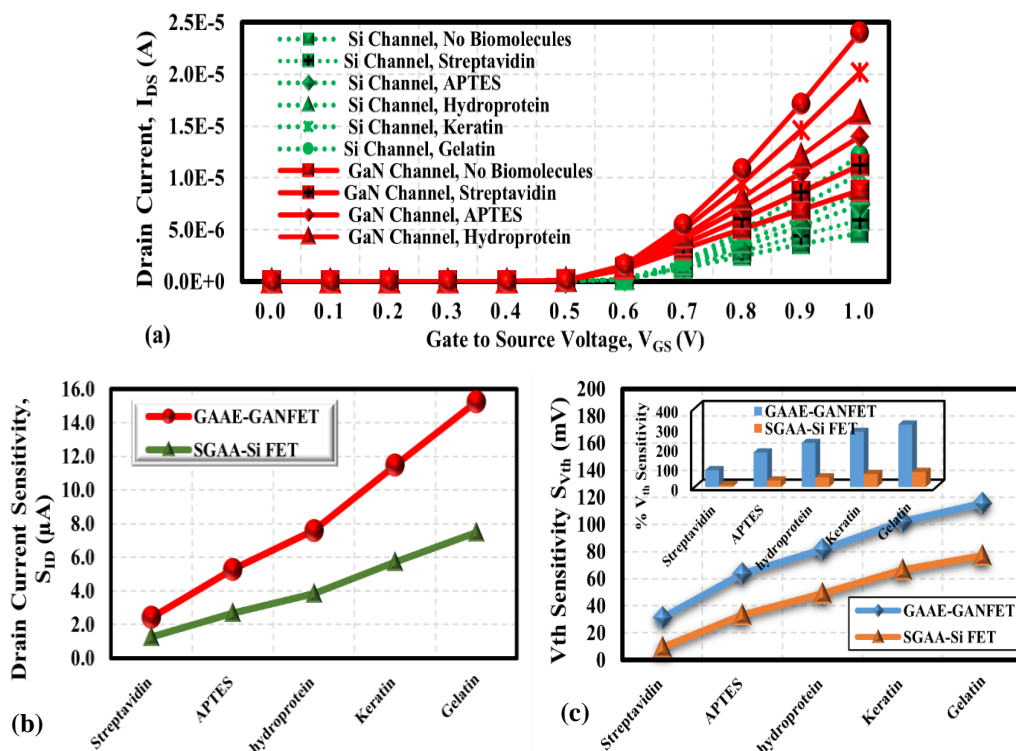


Fig. 5.26 Effect of Neutral Biomolecules (a) Drain Current with respect to Gate to Source Voltage for both Proposed GAAE-GANFET Biosensor and SGAA-Si FET Biosensor (b) Drain Current Sensitivity (c) Threshold Voltage Sensitivity

A comparative sensitivity performance study has been conducted to assess the proposed GAAE-GANFET biosensor against other FET biosensors with similar structural and material specifications, including GaN-GME-DE-SNW-FET [258], GC-GAA-NWFET [259], DETMS/DPDN FET [260], and DM DPDG-TFET [261] biosensor. The findings presented in Figure 12 distinctly show that the GAAE-GANFET biosensor exhibits higher $S_{V_{th}}$ values at both low and high biomolecule charge (Q_f) values. Also, for neutral biomolecules Table VI compares the threshold voltage sensitivity of GAAE-GANFET with several FET biosensors. This implies that compared to other biosensors in contemporary research, the proposed device shows enhanced sensing capabilities.

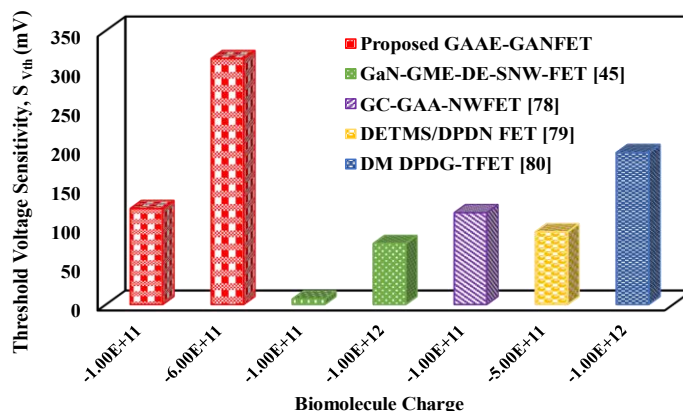


Fig. 5.27 Threshold Voltage Sensitivity ($S_{V_{th}}$) Comparison for Different Charged Biomolecules

Table 5.10 $S_{V_{th}}$ Comparison of GAAE-GANFET with Several FET Biosensors in the Contemporary Literature for Neutral Biomolecules

Structural Parameters	Reference [335]	Reference [338]	Reference [92]	Reference [295]	Our Work	
Cavity length (nm)	20	15	10	8	25	
Cavity thickness (nm)	-	19	1	2	10	
Channel length (nm)	100	45	20	20	100	
(K_{BIO})	12	8	2.1	5	8	12
$S_{V_{th}}$ in terms of ΔV_{th} (mV)	43.2	83.3	17	87	102	115.5

5.2.5 Summary

This work comprehensively investigates the label-free biosensing capability of Gate-All-Around Engineered Gallium Nitride Field Effect Transistor in detecting the avian influenza and DNA biomolecules. A compact analytical model of GAAE-GANFET has been proposed, which has shown excellent agreement with the TCAD simulations. The manuscript highlights the significant influence of the open cavities, graded channel doping and utilizing GaN as the channel material. The influence of these engineering techniques has been studied in terms of current sensitivity, threshold voltage sensitivity, and subthreshold slope sensitivity. The results reveal that the transition from a silicon channel to a gallium nitride channel substantially enhances sensitivity. Remarkably, the achieved threshold voltage sensitivity surpasses 50.02% for gelatin and reaches an impressive 91.69% for APTES biomolecules. This enhancement underscores the robust biosensing capabilities of the GAAE-GANFET. Consequently, the exceptional sensitivity and structural robustness of the GAAE-GANFET biosensor, particularly its open cavity design, make it a promising choice for biosensing applications.

Appendix-I

$$V_{fb,i} = \phi_G - \phi_{GaN}, \theta_1 = (V_{GS} - V_{fb,1}) + \frac{qN_{Ch,1}}{2C_{ox,1}} + \frac{qN_{Ch,1}d^2}{4\epsilon_{Ch,1}}, \theta_2 = (V_{GS} - V_{fb,2}) + \frac{qN_{Ch,1}}{2C_{ox,1}} + \frac{qN_{Ch,1}d^2}{4\epsilon_{Ch,1}}, \mu_2 = \sqrt{\frac{d\epsilon_{Ch,2}}{2C_{ox,2}}}$$

$$\theta_3 = (V_{GS} - V_{fb,3}) + \frac{qN_{Ch,3}}{2C_{ox,3}} + \frac{qN_{Ch,3}d^2}{4\epsilon_{Ch,3}}, \mu_1 = \sqrt{\frac{d\epsilon_{Ch,1}}{2C_{ox,1}}}$$

$$, \mu_3 = \sqrt{\frac{d\epsilon_{Ch,3}}{2C_{ox,3}}}, \mu_5 = \sqrt{\frac{d\epsilon_{Ch,5}}{2C_{ox,5}}}, \theta_5 = (V_{GS} - V_{fb,5}) + \frac{qN_{Ch,5}}{2C_{ox,5}} + \frac{qN_{Ch,5}d^2}{4\epsilon_{Ch,5}}$$

Appendix-II

$$\begin{aligned}
a_1 &= \frac{e^{-\frac{z_0}{\mu_1}}}{e^{\frac{z_0}{\mu_1} - e^{\frac{z_0}{\mu_1}}}}, a_3 = \frac{e^{\frac{z_0}{\mu_1}}}{e^{\frac{z_0}{\mu_1} - e^{\frac{z_0}{\mu_1}}}}, \\
a_2 &= \frac{-1}{e^{\frac{z_0}{\mu_1} - e^{\frac{z_0}{\mu_1}}}} \left[V_{bi,1} e^{\frac{z_1}{\mu_1}} + \theta_1 \left(e^{\frac{z_0}{\mu_1}} - e^{\frac{z_1}{\mu_1}} \right) \right], \\
a_4 &= \frac{-1}{e^{\frac{z_1}{\mu_1} - e^{\frac{z_1}{\mu_1}}}} \left[V_{bi,1} e^{\frac{z_1}{\mu_1}} + \theta_1 \left(e^{\frac{z_0}{\mu_1}} - e^{\frac{z_1}{\mu_1}} \right) \right], a_5 = \frac{e^{-\frac{z_2}{\mu_2}}}{e^{\frac{z_2}{\mu_2} - e^{\frac{z_2}{\mu_2}}}}, a_6 = \\
&\frac{e^{-\frac{z_1}{\mu_2}}}{e^{\frac{z_1}{\mu_2} - e^{\frac{z_1}{\mu_2}}}}, a_7 = \frac{-1}{e^{\frac{z_1}{\mu_2} - e^{\frac{z_1}{\mu_2}}}} \left[\theta_2 \left(e^{\frac{z_1}{\mu_2}} - e^{\frac{z_2}{\mu_2}} \right) \right], \\
a_8 &= \frac{e^{-\frac{z_2}{\mu_2}}}{e^{\frac{z_2}{\mu_2} - e^{\frac{z_2}{\mu_2}}}}, a_9 = \frac{e^{\frac{z_1}{\mu_2}}}{e^{\frac{z_2}{\mu_2} - e^{\frac{z_2}{\mu_2}}}}, a_{10} = \frac{-1}{e^{\frac{z_2}{\mu_2} - e^{\frac{z_2}{\mu_2}}}} \left[\theta_2 \left(e^{\frac{z_1}{\mu_2}} - \right. \right. \\
&\left. \left. e^{\frac{z_2}{\mu_2}} \right) \right], c_1 = a_1 e^{\frac{z_1}{\mu_1}} + a_3 e^{\frac{z_1}{\mu_1}} - a_5 e^{\frac{z_2}{\mu_2}} - a_8 e^{\frac{z_2}{\mu_2}}, a_{12} = \frac{e^{-\frac{z_2}{\mu_3}}}{e^{\frac{z_2}{\mu_3} - e^{\frac{z_2}{\mu_3}}}}, c_4 = \frac{a_1}{\mu_1} e^{\frac{z_1}{\mu_1}} - \\
&\frac{a_3}{\mu_1} e^{\frac{z_1}{\mu_1}} + \frac{a_7}{\mu_2} e^{\frac{z_1}{\mu_2}} + \frac{a_8}{\mu_2} e^{\frac{z_1}{\mu_2}}, c_6 = \frac{-a_2}{\mu_1} e^{\frac{z_1}{\mu_1}} + \frac{a_4}{\mu_1} e^{\frac{z_1}{\mu_1}} + \frac{a_7}{\mu_2} e^{\frac{z_1}{\mu_2}} - \frac{a_{10}}{\mu_2} e^{\frac{z_1}{\mu_2}}, a_{13} = \\
&-(V_{bi,2}) e^{\frac{z_3}{\mu_3}} - \theta_3 \left(e^{\frac{z_2}{\mu_3}} - e^{\frac{z_3}{\mu_3}} \right), a_{14} = \frac{e^{\frac{z_3}{\mu_3}}}{e^{\frac{z_3}{\mu_3} - e^{\frac{z_3}{\mu_3}}}}, a_{15} = \frac{e^{\frac{z_2}{\mu_3}}}{e^{\frac{z_3}{\mu_3} - e^{\frac{z_3}{\mu_3}}}}, \\
a_{16} &= \frac{e^{-\frac{z_4}{\mu_4}}}{e^{\frac{z_3}{\mu_4} - e^{\frac{z_3}{\mu_4}}}}, a_{17} = \frac{e^{-\frac{z_4}{\mu_4}}}{e^{\frac{z_3}{\mu_4} - e^{\frac{z_3}{\mu_4}}}}, q_3 = \frac{-(V_{bi,2}) e^{\frac{z_3}{\mu_3}} - \theta_3 \left(e^{\frac{z_2}{\mu_3}} - e^{\frac{z_3}{\mu_3}} \right)}{e^{\frac{z_3}{\mu_3} - e^{\frac{z_3}{\mu_3}}}}, \\
a_{19} &= \frac{-(V_{bi,3}) e^{\frac{z_4}{\mu_4}} - \theta_4 \left(e^{\frac{z_3}{\mu_4}} - e^{\frac{z_4}{\mu_4}} \right)}{e^{\frac{z_3}{\mu_4} - e^{\frac{z_3}{\mu_4}}}}, a_{20} = \frac{e^{\frac{z_4}{\mu_4}}}{e^{\frac{z_4}{\mu_4} - e^{\frac{z_4}{\mu_4}}}}, a_{21} = \frac{e^{\frac{z_3}{\mu_4}}}{e^{\frac{z_4}{\mu_4} - e^{\frac{z_4}{\mu_4}}}}, \\
a_{22} &= \frac{-(V_{bi,3}) e^{\frac{z_4}{\mu_4}} - \theta_4 \left(e^{\frac{z_3}{\mu_4}} - e^{\frac{z_4}{\mu_4}} \right)}{e^{\frac{z_4}{\mu_4} - e^{\frac{z_4}{\mu_4}}}}, d_1 = \left[\frac{(c_6 c_2 - c_3 c_5)}{(c_2 c_4 - c_3 c_5)} \left(a_5 e^{\frac{z_2}{\mu_2}} + a_8 e^{\frac{z_2}{\mu_2}} \right) \right] \\
d_2 &= \frac{1}{a_{12} e^{\frac{z_2}{\mu_2}} + a_{15} e^{\frac{z_2}{\mu_2}}} \left[\frac{(c_6 c_1 - c_3 c_4)}{(c_1 c_5 - c_2 c_4)} \left(a_6 e^{\frac{z_2}{\mu_2}} + a_9 e^{\frac{z_2}{\mu_2}} - a_{11} e^{\frac{z_2}{\mu_2}} - a_{14} e^{\frac{z_2}{\mu_2}} \right) \right], \\
d_2 &= \frac{1}{a_{12} e^{\frac{z_2}{\mu_2}} + a_{15} e^{\frac{z_2}{\mu_2}}} \left[\frac{(c_6 c_1 - c_3 c_4)}{(c_1 c_5 - c_2 c_4)} \left(a_6 e^{\frac{z_2}{\mu_2}} + a_9 e^{\frac{z_2}{\mu_2}} - a_{11} e^{\frac{z_2}{\mu_2}} - a_{14} e^{\frac{z_2}{\mu_2}} \right) \right] c_2 = -a_6 e^{\frac{z_1}{\mu_2}} - a_9 e^{\frac{z_1}{\mu_2}}, c_3 = \\
a_7 e^{\frac{z_1}{\mu_1}} - a_4 e^{\frac{z_1}{\mu_1}} + a_{10} e^{\frac{z_1}{\mu_2}} + \theta_2 - a_8 e^{\frac{z_1}{\mu_1}} - \theta_1, c_5 &= \frac{-a_6}{\mu_2} e^{\frac{z_1}{\mu_2}} + \frac{a_9}{\mu_2} e^{\frac{z_1}{\mu_2}}, \\
a_{11} &= \frac{e^{-\frac{z_3}{\mu_3}}}{e^{\frac{z_2}{\mu_3} - e^{\frac{z_2}{\mu_3}}}}, d_3 = \frac{1}{a_{12} e^{\frac{z_2}{\mu_2}} + a_{15} e^{\frac{z_2}{\mu_2}}} \left[e^{\frac{z_2}{\mu_2}} (a_7 - a_{13}) + e^{\frac{z_2}{\mu_2}} (a_{10} - a_{16}) + \theta_2 - \right. \\
\theta_3 \left. \right], d_4 &= \frac{1}{\frac{a_{12}}{\mu_4} e^{\frac{z_3}{\mu_4}} + \frac{a_{21}}{\mu_4} e^{\frac{z_3}{\mu_4}}} \left[\left(\frac{a_{11}}{\mu_3} e^{\frac{z_3}{\mu_3}} + \frac{a_{14}}{\mu_3} e^{\frac{z_3}{\mu_3}} \right) \right], a_{18} = \frac{e^{-\frac{z_3}{\mu_4}}}{e^{\frac{z_3}{\mu_4} - e^{\frac{z_3}{\mu_4}}}}, \\
d_5 &= \frac{1}{\frac{a_{18}}{\mu_4} e^{\frac{z_3}{\mu_4}} - \frac{a_{21}}{\mu_4} e^{\frac{z_3}{\mu_4}}} \left[\frac{a_{12}}{\mu_3} e^{\frac{z_3}{\mu_3}} - \frac{a_{15}}{\mu_3} e^{\frac{z_3}{\mu_3}} - \frac{a_{17}}{\mu_4} e^{\frac{z_3}{\mu_4}} - \frac{a_{20}}{\mu_4} e^{\frac{z_3}{\mu_4}} \right],
\end{aligned}$$

$$d_6 = \frac{1}{\frac{a_{18}}{\mu_4} e^{\frac{z_3}{\mu_4}} - \frac{a_{21}}{\mu_4} e^{-\frac{z_3}{\mu_4}}} \left[\frac{a_{22}}{\mu_4} e^{-\frac{z_3}{\mu_4}} + \frac{a_{13}}{\mu_3} e^{\frac{z_3}{\mu_3}} - \frac{a_{19}}{\mu_4} e^{\frac{z_3}{\mu_4}} - \frac{a_{16}}{\mu_3} e^{-\frac{z_3}{\mu_3}} \right]$$

Appendix-III

$$O_1 = \frac{1}{e^{-\frac{(z_1-z_2)}{\mu_2}} - e^{\frac{(z_1-z_2)}{\mu_2}}} \left[\frac{c_1 c_{61} e^{-\frac{z_1}{\mu_2}}}{c_1 c_5 - c_2 c_4} - \frac{c_2 c_{61} e^{-\frac{z_2}{\mu_2}}}{c_2 c_4 - c_1 c_5} + \frac{c_5 c_{31} e^{-\frac{z_2}{\mu_2}}}{c_2 c_4 - c_1 c_5} - \frac{c_4 c_{31} e^{-\frac{z_1}{\mu_2}}}{c_1 c_5 - c_2 c_4} \right], O_2 =$$

$$\frac{1}{e^{-\frac{(z_1-z_2)}{\mu_2}} - e^{\frac{(z_1-z_2)}{\mu_2}}} \left[\frac{(c_1 c_{62} - c_4 c_{32}) e^{-\frac{z_1}{\mu_2}}}{c_1 c_5 - c_2 c_4} - \frac{(c_2 c_{62} - c_5 c_{32}) e^{-\frac{z_2}{\mu_2}}}{c_2 c_4 - c_1 c_5} + n_2 (e^{\frac{z_1}{\mu_2}} - e^{-\frac{z_2}{\mu_2}}) \right] O_3 =$$

$$\frac{1}{e^{-\frac{(z_2-z_1)}{\mu_2}} - e^{\frac{(z_2-z_1)}{\mu_2}}} \left[\frac{(c_1 c_{61} - c_5 c_{31}) e^{\frac{z_1}{\mu_2}}}{c_1 c_5 - c_2 c_4} - \frac{(c_2 c_{61} - c_5 c_{31}) e^{\frac{z_2}{\mu_2}}}{c_2 c_4 - c_1 c_5} \right], O_4 =$$

$$\frac{1}{e^{-\frac{(z_2-z_1)}{\mu_2}} - e^{\frac{(z_2-z_1)}{\mu_2}}} \left[\frac{(c_1 c_{62} - c_4 c_{32}) e^{\frac{z_1}{\mu_2}}}{c_1 c_5 - c_2 c_4} - \frac{(c_2 c_{62} - c_5 c_{32}) e^{\frac{z_2}{\mu_2}}}{c_2 c_4 - c_1 c_5} + n_2 (e^{\frac{z_1}{\mu_2}} - e^{\frac{z_2}{\mu_2}}) \right]$$

$$W_a = O_1 O_3, W_b = O_1 O_4 + O_3 O_4, W_c = -\left(\frac{2\phi_F + n_2}{2}\right)^2, c_{31} = a_7 e^{\frac{z_1}{\mu_1}} - a_{10} e^{-\frac{z_1}{\mu_2}} - n_2 -$$

$$a_2 e^{\frac{z_1}{\mu_1}} - a_4 e^{-\frac{z_1}{\mu_1}} + n_1$$

$$c_{32} = a_7 e^{\frac{z_1}{\mu_1}} - a_{10} e^{-\frac{z_1}{\mu_2}} - n_2 - a_{21} e^{\frac{z_1}{\mu_1}} - a_4 e^{-\frac{z_1}{\mu_1}} + n_1, c_{61} = \frac{a_{22} e^{\frac{z_1}{\mu_1}}}{\mu_1} - \frac{a_{42} e^{-\frac{z_1}{\mu_1}}}{\mu_1}, c_{62} =$$

$$\frac{-a_{21} e^{\frac{z_1}{\mu_1}}}{\mu_1} + \frac{a_{41} e^{-\frac{z_1}{\mu_1}}}{\mu_1} + \frac{a_7 e^{\frac{z_1}{\mu_2}}}{\mu_2} - \frac{a_{10} e^{-\frac{z_1}{\mu_2}}}{\mu_2}$$

$$a_{21} = \frac{-V_{bi} e^{-\frac{z_1}{\mu_1}}}{e^{\frac{(z_0-z_1)}{\mu_1}} - e^{-\frac{(z_0-z_1)}{\mu_1}}} + n_1 a_{22}, a_{22} = \frac{e^{-\frac{z_1}{\mu_1}} - e^{-\frac{z_0}{\mu_1}}}{e^{\frac{(z_0-z_1)}{\mu_1}} - e^{-\frac{(z_0-z_1)}{\mu_1}}}, a_{42} = \frac{e^{\frac{z_0}{\mu_1}} - e^{\frac{z_1}{\mu_1}}}{e^{\frac{(z_1-z_0)}{\mu_1}} - e^{-\frac{(z_1-z_0)}{\mu_1}}},$$

$$a_{41} = \frac{-V_{bi} e^{\frac{z_1}{\mu_1}}}{e^{-\frac{(z_1-z_0)}{\mu_1}} - e^{\frac{(z_1-z_0)}{\mu_1}}} + n_1 a_{42}$$

CHAPTER 6

HIGH SENSITIVITY BIOSENSORS UTILIZING WIDE BANDGAP SEMICONDUCTORS

To further enhance the performance parameters of Gate-All-Around FET biosensors, the integration of wide bandgap semiconductors offers significant potential. This chapter focuses on advancing the design of novel FET biosensors by leveraging wide bandgap materials to achieve superior sensitivity and performance. Wide bandgap semiconductors such as Silicon Carbide (SiC) and Gallium Arsenide (GaAs) are particularly advantageous due to their inherent properties, including higher breakdown voltage, thermal stability, and increased carrier mobility, making them ideal for applications requiring heightened diagnostic sensitivity. It presents two innovative designs: the Dielectric Modulated 4H-SiC Source Triple Metal Gate-All-Around SiC FET (DM-TMGAA-SiCFET) and the Gallium-Arsenide Gate-All-Around Engineered FET (GaAs-GAAE-FET). The DM-TMGAA-SiCFET features a 6H-SiC channel with dual-sided cavities and a triple metal gate, improving sensitivity for gelatin and DNA biomarkers. While, The GaAs-GAAE-FET, with its gallium arsenide channel and dual nanocavities, significantly boosts sensitivity for breast cancer biomarkers.

Section 6.1 discusses the Dielectric Modulated 4H-SiC Source Triple Metal Gate-All-Around Silicon Carbide FET (DM-TMGAA-SiCFET). This section provides a detailed analysis of the DM-TMGAA-SiCFET biosensor, featuring a 6H-Silicon Carbide channel with Junction Accumulation Mode, dual-sided cavities, and a triple metal gate structure. The addition of Al_2O_3 and HfO_2 layers enhances the biosensor's performance. Evaluations show notable improvements in sensitivity, with increased threshold voltage sensitivity for gelatin and DNA, and a significant boost in $I_{\text{ON}}/I_{\text{OFF}}$ sensitivity for gelatin compared to traditional silicon-based biosensors.

Section 6.2 introduces the Gallium-Arsenide Gate-All-Around Engineered Field-Effect Transistor (GaAs-GAAE-FET). This section highlights the design of the GaAs-GAAE-FET biosensor, which includes a gallium arsenide channel in Junction Accumulation Mode, a triple metal gate, and an $\text{Al}_2\text{O}_3+\text{HfO}_2$ oxide stack. The design features two nanocavities that enhance detection sensitivity, particularly for breast cancer biomarkers, by leveraging the unique dielectric properties of MDA-MB-231 and MCF-10A cells. The biosensor demonstrates a significant increase in threshold voltage sensitivity for the MDA-MB-231 biomarker compared to conventional silicon-based Gate-All-Around FET sensors.

Problem Statement

Traditional biosensors frequently encounter challenges with sensitivity and overall performance. This chapter addresses these issues by examining the potential of wide bandgap semiconductors—Silicon Carbide (SiC) and Gallium Arsenide (GaAs). It

evaluates two advanced biosensor designs: the Dielectric Modulated 4H-SiC Source Triple Metal Gate-All-Around SiC FET (DM-TMGAA-SiCFET) and the Gallium-Arsenide Gate-All-Around Engineered FET (GaAs-GAAE-FET). The chapter aims to illustrate how these materials can significantly improve biosensor capabilities, offering enhanced sensitivity for detecting biomarkers like gelatin, DNA, and breast cancer indicators.

6.1 4H-SiC source Triple Metal Gate-All-Around Silicon Carbide FET (DM-TMGAA-SiCFET) biosensor

6.1.1 Background and Overview

In the realm of point-of-care diagnostics (POC), the rapid and direct detection of the biomolecules has emerged as a pivotal frontier, revolutionizing early medical diagnoses for critical diseases [339], [340]. The development of portable, user-friendly, economical, and miniature biosensors is proposed through the incorporation of nanomaterial-based field effect transistor technology in point of care testing and biomolecule detection [341]. Such biosensors allow rapid disease diagnosis at the moment and place of patient care. These devices can detect a wide range of diseases including diabetes, cardiovascular disease, cancer, and various infectious ailments [195], [341]–[343]. The global impact of the COVID-19 pandemic [344], affecting millions of individuals worldwide, underscores the crucial importance of promptly identifying specific biomolecules for global healthcare monitoring systems and for mitigating the risk of its continued spread [345], [346]. Thus, the significance of biosensors has soared exponentially in the wake of global outbreaks such as COVID-19, Ebola, and H1N1 influenza, underlining the urgency for accurate and efficient diagnostic tools to combat such pandemics effectively.

Beyond healthcare, this biosensing technology has found applications in the food industry for detecting pathogenic viruses and genetically modified organisms (GMOs) [347], [348], in environmental protection for monitoring pollutants [349]. Within the landscape of biosensors proposed in the scientific literature, field-effect transistor (FET) based biosensors have attracted a lot of attention [131]. Their label-free detection methodology, coupled with attributes such as high sensitivity, rapid response times, low energy consumption, scalability, affordability, and compatibility with complementary metal-oxide-semiconductor (CMOS) technology, positions them as exemplary candidates for further integration with signal processing tools like system-on-chip (SoC) solutions [131], [350], [351].

Semiconducting nanowires (NWs) as one-dimensional nanostructures, offer a remarkable advantage in biosensor applications due to their exceptionally high surface-to-volume ratio [352]. This characteristic enhances sensitivity, making them ideal candidates for the rapid and precise detection of biological analytes [353]. In particular, nanowire-based Gate-All-Around FETs (GAAFETs) have emerged as a focal point of research in the past decade owing to their advanced gate control abilities over the channel. This heightened level of control leads to enhanced resistance against

short-channel effects (SCEs), more effective field confinement, and greater packing density [83], [217].

When exposed to physiological environment for an extended period of time, silicon (Si) nanowires FETs suffer with limited chemical stability [354]. In this regard, Silicon Carbide (SiC) catches attention as a material of preference. SiC is a material of choice for extremely sensitive devices due to its chemical inertness in various environmental conditions and its compatibility with biological systems [355], [356]. SiC has properties like high electron mobility, breakdown voltage, and thermal conductivity. It also has excellent physical stability. SiC is a wide-bandgap semiconductor material that comes in more than 200 polytypes, the most common of which are 3C, 4H, and 6H [357]. 6H-SiC is a wide bandgap material with a band gap of 3.0 eV [358] while 4H-SiC polytype has a slightly high bandgap of 3.2 eV and electron mobility ($1000\text{--}1140\text{ cm}^2\text{ V}^{-1}\text{ s}^{-1}$) as compared to 6H-SiC [359]. SiC offers a higher critical electric field and a larger energy band gap compared to silicon, which helps minimize leakage current and improve device performance [360], [361].

FET having SiC channel provides the implementation of high-frequency switching applications because of the robust electric field and broad energy bandgap offered by SiC in comparison to silicon. SiC channel FET also leads to decreased leakage currents and improved overall device performance [308], [359].

Mousa et.al [362] fabricated a Silicon Carbide NW-FET with heightened sensitivity, remarkable stability, and minimal sample volume demands presenting a hopeful avenue for the development of biosensors suitable for challenging environmental conditions.

6.1.1.1 Silicon Carbide (SiC) Semiconductor

SiC is a wide-bandgap semiconductor material that comes in more than 200 polytypes, the most common of which are 3C, 4H, and 6H. 6H-SiC is a wide bandgap material with a band gap of 3.0 eV while 4H-SiC polytype has a slightly high bandgap of 3.2 eV [358]. Wide bandgap (WBG) materials like SiC offer significant advantages over traditional silicon, making them excellent choices for advanced bioelectronic devices. Examples include field effect transistors (FETs) based on WBG materials [363], [364]. SiC has gained attention for its following multifunctional properties, including:

1. **Biocompatibility and Stability:** One of the main concerns in materials research for biomedical applications is the search for materials that produce low or no adverse reaction when implanted in the body, and that can be implanted for the long term. In the field of semiconductors, silicon (Si) has always been the preferred substrate material for micro-devices due to its low cost and ready availability. However, it presents several drawbacks that limit its use in biomedical applications. Several researchers maintain that its cytotoxicity is cell-dependent, and Kubo et al. [365] demonstrated the formation of nodules on periodontal fibroblasts as a release from the Si-bearing bioglass. Moreover, the crystal orientation and bond strength of Si make it relatively brittle [4] and hence prone to breakage upon insertion into living

tissues, thus posing problems of retrieval and/or requiring complex packaging techniques. SiC, in contrast, offers superior biocompatibility and long-term stability in harsh environments, including body fluids [366].

2. **Superior Properties:** SiC has excellent electrical, mechanical, and thermal properties which make it suitable as a biosensing substrate. It has high thermal conductivity on par with copper at room temperature [367], a high breakdown field ($\sim 2 \text{ MVcm}^{-1}$; double than that of Si) [368], and chemical inertness, making it suitable for high-temperature and hostile environments. Its high Young's modulus and low friction coefficient [369] make it ideal for smart implants and in-vivo biosensors [370]. SiC's wide band-gap increases its sensing capabilities. For instance, 4H-SiC presents a bandgap of 3.23 eV thus greatly reducing the number of electron-hole pairs formed from the thermal activation across the band-gap, which allows high temperature operation of SiC sensors (indeed the intrinsic carrier concentration of SiC is $\sim 10^{16}$ – 10^{18} cm^{-3} while for Si is $\sim 10^{10} \text{ cm}^{-3}$, more than 6 orders of magnitude lower than SiC [371]).
3. **Surface Functionalization:** SiC is promising for surface functionalization, which is crucial for covalent biomolecule immobilization. Unlike silicon dioxide (SiO₂), which is unstable in electrolytic solutions and high noise levels in Si-based electrolyte SiO₂ FETs have been documented because of trapping and de-trapping carriers at the SiO₂-Si gate interface [372], SiC's surface can form high-quality monolayers, enhancing device performance [373].

6.1.1.2 JAM FET

The concept of Junction Accumulation Mode (JAM) Field Effect Transistor (FET) has been previously discussed in earlier chapters.

6.1.1.3 Oxide Stacking

For SiC substrate material or channel in the FET structure, the dielectric layer of Al₂O₃ is the most suitable as compared to SiO₂. Al₂O₃ has a strong lattice match with Silicon Carbide, excellent thermal stability, and compatibility with 4H-SiC and 6H-SiC [374]. Additionally, SiC and Al₂O₃ have a significant conduction band offset [375], [376]. The thickness of the Al₂O₃ gate dielectric in the DM-TMGAA-SiCFET biosensor affects performance significantly. For decreased thickness of dielectric layers, the gate capacitance increases, which enhances the electrostatic control of the gate over the channel, hence increased sensitivity to biomolecule immobilization. Thinner dielectrics decrease the threshold voltage, enhancing responsiveness, but the drawback is a higher leakage current. Thicker dielectrics raise the threshold voltage and reduce leakage currents but compromise sensitivity.

In the proposed biosensor device, thickness of Al₂O₃ is kept less for improved sensitivity. To supplement the thickness of the oxide layer, a high-K material, hafnium dioxide (HfO₂), has been stacked on Al₂O₃ layer. This stacking also has the potential to boost the sensitivity of the biosensor, as indicated in reference [160]. The materials with

higher dielectric permittivity enable the attainment of a large physical thickness while maintaining a small Effective Oxide Thickness (EOT). High-k dielectrics improve gate control over the channel.

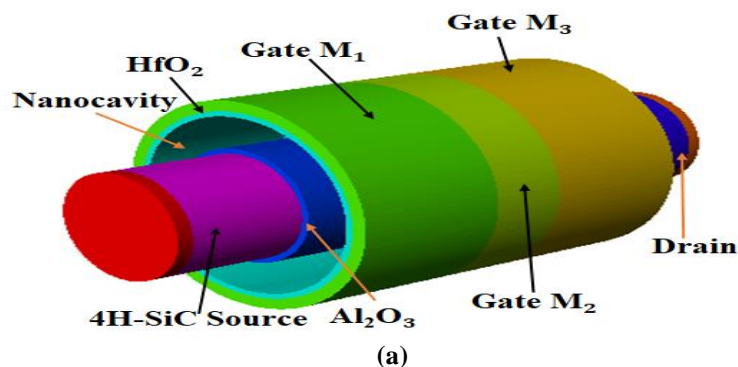
6.1.1.4 Gate Material Engineering

Performance of GAAFETs can be improved via Gate Work Function Engineering. Higher work function (WF) gate metal is utilized on the source side, whereas lower WF gate metal is used closest to the drain. Hot-carrier effects are significantly improved by this configuration because it increases transport effectiveness and decreases the electric field at the drain [228], [229]. The previous chapters have covered the topic of gate material engineering, which involves the usage of gate metals with varying work functions. This chapter presents a design proposal that utilizes gate material engineering with three distinct work function gates.

6.1.2 Device Structure, Specification and Fabrication

Fig. 6.1 (a) depicts the three-dimensional view of the structure of Gate-All-Around Junction Accumulation Mode (JAM) Silicon Carbide FET (DM-TMGAA-SiCFET) biosensor device. This SiCFET device has a cylindrical Gate (all around the channel) with Gate Metal Engineering (GME), which consists of the gates M_1 , M_2 , and M_3 , each of which has a unique work function. Table 1 includes the values for the gate work functions. The inherent capability of gate work function engineering allows for the reduction of various SCEs while enhancing threshold voltage and drain current properties [230]. To immobilize different biomolecules in the device, two-sided nano cavity has been formed by etching the Hafnium oxide (HfO_2) dielectric layer. Fig. 6.1 (b) illustrates the two-dimensional view of the DM-TMGAA-SiCFET biosensor. In this proposed Silicon Carbide FET design, the channel comprises 6H-SiC semiconductor, while the source of the device is constructed using a different polytype of Silicon Carbide, specifically 4H-SiC.

A layer of aluminium oxide (Al_2O_3) of the dimension 1 nm has been deposited on the SiC channel of the proposed FET device. For SiC substrate material or channel in the FET structure, the dielectric layer of Al_2O_3 is the most suitable as compared to SiO_2 . Al_2O_3 has a strong lattice match with Silicon Carbide, excellent thermal stability, and compatibility with 4H-SiC and 6H-SiC [374]. Additionally, SiC and Al_2O_3 have a significant conduction band offset [375], [376].



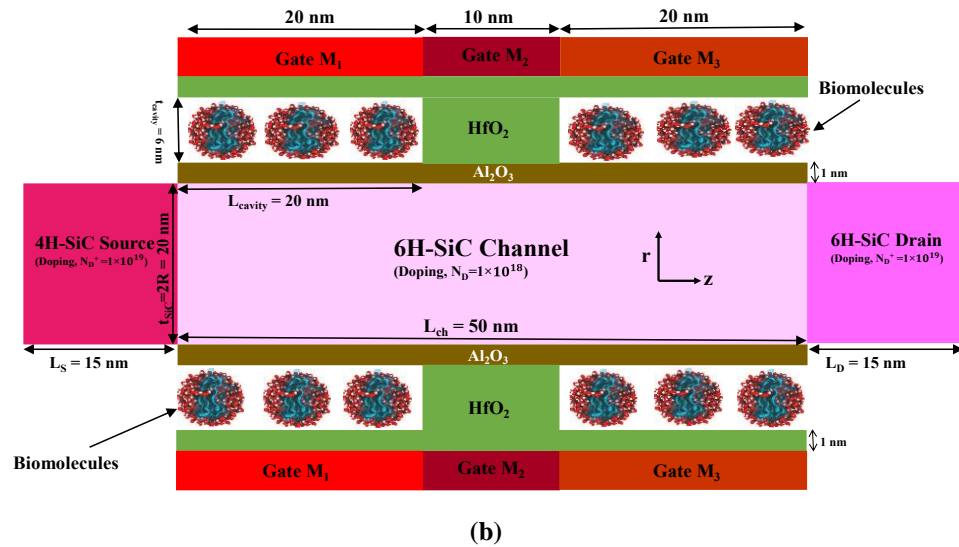


Fig. 6.1 (a) 3-Dimensional View of DM-TMGAA-SiCFET biosensor (b) 2- Dimensional Structure of DM-TMGAA-SiCFET biosensor

The thickness of the Al_2O_3 gate dielectric in the DM-TMGAA-SiCFET biosensor affects performance significantly. For decreased thickness of dielectric layers, the gate capacitance increases, which enhances the electrostatic control of the gate over the channel, hence increased sensitivity to biomolecule immobilization. Thinner dielectrics decrease the threshold voltage, enhancing responsiveness, but the drawback is a higher leakage current. Thicker dielectrics raise the threshold voltage and reduce leakage currents but compromise sensitivity. In the proposed biosensor device, thickness of Al_2O_3 is kept less for improved sensitivity. To supplement the thickness of the oxide layer, a high-K material, hafnium dioxide (HfO_2), has been stacked on Al_2O_3 layer. This stacking also has the potential to boost the sensitivity of the biosensor, as indicated in reference [160].

The sensing mechanism of proposed biosensor for label-free biomolecule detection relies on the principle of dielectric modulation. In the structure of proposed biosensor, there are two nanocavities which works as sensing sites. When target biomolecules are immobilized into the functionalized sensing sites of the biosensor, they alter the local dielectric environment due to their distinct dielectric constants. This change in the dielectric properties affects the gate capacitance, which is a crucial factor in determining the channel conductivity of the FET.

For charged biomolecules, the biomolecules adsorption induces a local electric field that can attract or repel charge carriers in the channel, leading to a measurable change in the drain current. The magnitude and polarity of this change depend on the charge of the biomolecules. For neutral biomolecules, the binding event still alters the dielectric properties at the gate interface, modifying the electrostatic environment and overall capacitance, thus causing detectable variations in the FET's electrical characteristics.

The DM-TMGAA-SiCFET operates in the Junction Accumulation Mode (JAM), which is characterized by the absence of junctions, but the channel's doping level is slightly

lower than that of the source and drain regions. In the proposed device, the channel is doped at $1 \times 10^{18} \text{ cm}^{-2}$, while the source and drain regions are doped at a higher level of $1 \times 10^{19} \text{ cm}^{-2}$. By having a lower doping level in the channel, the device achieves improved gate control and reduced off-state leakage current, which are critical factors in improving the overall performance of FETs and ensuring their efficient operation.

To compare the SiC channel FET with a silicon (Si) channel FET, an analogous device has been designed with identical dimensions to those of the proposed DM-TMGAA-SiCFET biosensor. The device specifications, including device dimensions, material type, and nanocavity dimensions, for both the DM-TMGAA-SiCFET biosensor and the SiFET biosensor, are detailed in Table 6.1.

Table 6.1 Device Design Parameters

Physical Device Parameter	DM-TMGAA-SiCFET Biosensor	Si FET Biosensor
Channel Length, L (nm)	50	50
Radius of silicon film (nm)	10	10
Length of source and drain (nm)	$L_S = L_D = 15$	$L_S = L_D = 15$
Gate Metal work-function (eV)	M ₁ : 4.4	5.04
	M ₂ : 4.1	
	M ₂ : 4.0	
Oxide Thickness (nm)	Al ₂ O ₃ : $t_{ox} = 1.0$	SiO ₂ : $t_{ox} = 1.0$
	HfO ₂ : $t_{ox1} = 6.0 + 1.0$	HfO ₂ : $t_{ox1} = 6.0 + 1.0$
Doping of Channel Region, N _D (/cm ³)	1×10^{18}	1×10^{18}
Doping of Source and Drain Region, N _D ⁺ (/cm ³)	1×10^{19}	1×10^{19}
Thickness of Cavity, t _{cavity} (nm)	6	6
Length of Cavity, L _{cavity} (nm)	20	20
dielectric constants of oxides	Al ₂ O ₃ : 9.8	SiO ₂ : 3.9
	HfO ₂ : 22.0	HfO ₂ : 22.0

The goal of this work is to characterize the behaviour of a range of biomolecules in a biosensing environment by immobilizing them within the nanocavity. These biomolecules are distinguished by their dielectric constant values, which include Streptavidin (K=2.1) [134], Hydroprotein (K=5) [89], Keratin (K=8) [335], Gelatin (K=12) [96], and DNA (characterized by both dielectric constant value K=8 and charge density values ($N_f = -1 \times 10^{10} / \text{cm}^2$, $N_f = -1 \times 10^{10} / \text{cm}^2$, $N_f = -1 \times 10^{11} / \text{cm}^2$, $N_f = -5 \times 10^{11} / \text{cm}^2$, $N_f = -1 \times 10^{12} / \text{cm}^2$) [96], [160].

In this work, two-sided cavities of dimension $20\text{ nm} \times 6\text{ nm}$ each have been considered. There are many biomolecules with sizes typically less than 5 nm , such as folded protein (size $\sim 2.5\text{ nm}$) and streptavidin (size $\sim 5\text{ nm}$). The trapping of streptavidin inside a cavity has been practically proved by Kim et al. [377]. In the past, a lot of publications have even discussed cavities smaller than 10 nm [185], [231], [258], [378]–[381].

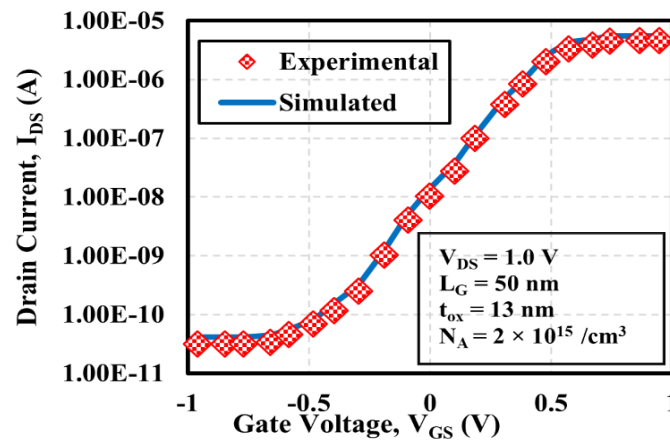
6.1.3 Device Calibration and Fabrication Feasibility

The proposed device has been simulated using the Silvaco ATLAS-3D tool for comprehensive device analysis (ATLAS User's Manual 2018). Fig. 6.2 (a) provides a graphical representation of the simulations for the proposed device calibrated with the experimental data [152], showcasing a high degree of agreement in the drain current versus gate voltage characteristics. This validation process serves as a means to confirm the accuracy of the simulations and models in use. The minority carrier's recombination in semiconductor materials has been employed using the models AUGER and SRH. Additionally, mobility, contingent on carrier concentration, has been characterized using the FLDMOB and CONMOB models. The BGN model has been employed for carrier statistics. In order to aid in the construction of non-planar devices, the Lombardi model (CVT) has also been utilized (ATLAS User's Manual 2018). The viability of fabricating the DM-TMGAA-SiCFET biosensor has been assessed by examining the proposed fabrication procedure outlined in flowchart of Fig. 6. 2 (b).

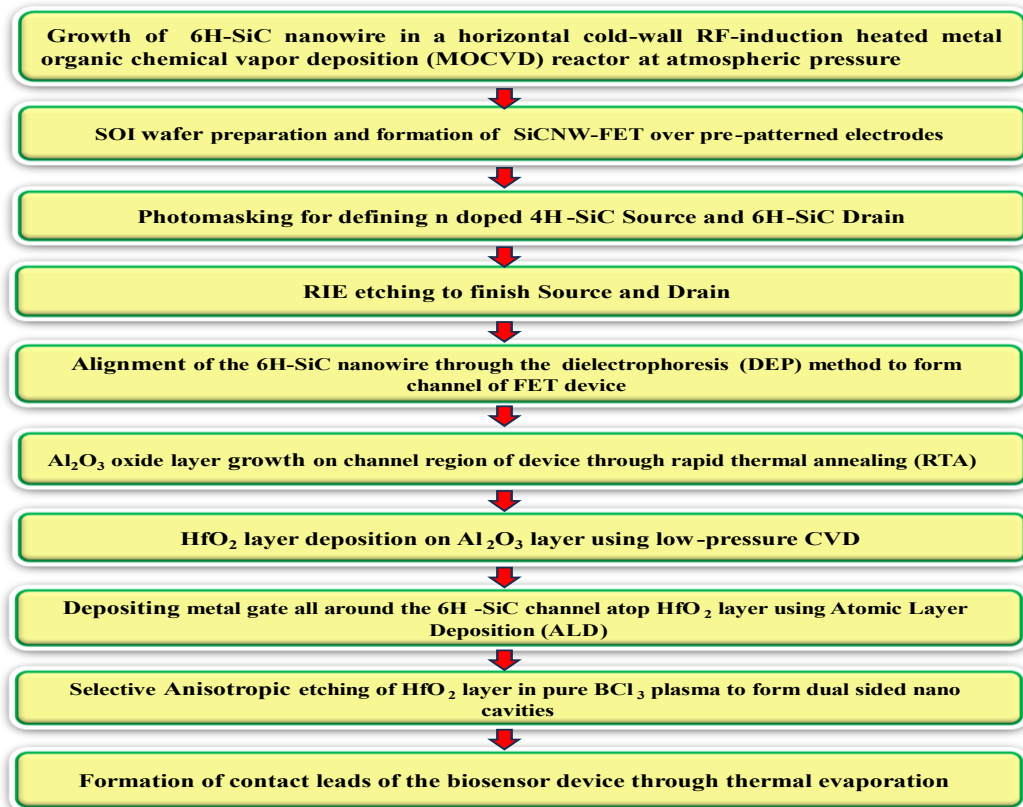
To fabricate silicon carbide nanowire FET biosensors, highly doped n-type SiC nanowires are initially grown using the vapor–liquid–solid (VLS) method [382]. These nanowires are then dispersed onto a substrate and patterned using e-beam lithography to create micro-contacts. Metal is deposited to form these micro-contacts, which are lifted off to establish the source and drain connections, thereby completing the basic FET structure [383]. Subsequently, the steps for constructing a dielectrically modulated FET biosensor are followed. In particular, the fabrication of the DM-TMGAA-SiCFET biosensor starts with growing 6H-SiC nanowires [382] in a horizontal cold-wall RF-induction heated MOCVD reactor at atmospheric pressure [383]. Next, an SOI wafer is prepared to form the SiCNW-FET over pre-patterned electrodes. Photomasking and doping define the 4H-SiC source and 6H-SiC drain regions, with reactive ion etching (RIE) finishing these regions. The 6H-SiC nanowire is aligned using the dielectrophoresis (DEP) method to form the FET channel [362]. An Al_2O_3 layer is grown via rapid thermal annealing (RTA), followed by HfO_2 deposition using low-pressure CVD. A metal gate is deposited around the 6H-SiC channel using atomic layer deposition (ALD) [162]. Selective anisotropic etching of the HfO_2 layer in pure BCl_3 plasma creates sidewall nano-cavities, and contact leads are formed through thermal evaporation [384].

6.1.4 Results and discussion

The immobilization of different biomolecules in FET-based biosensors alters the electric properties of the FET device, including the gate oxide capacitance, potential profile, electric field distribution, and electron concentration along the channel. Variations in these electrical characteristics are often used for the detection and identification of specific biomolecules.



(a)



(b)

Fig. 6.2 (a) Calibration of Simulation Setup with Experimental Data [152] (b) Proposed Fabrication Flowchart of DM-TMGAA-SiCFET Biosensor

The immobilization of various neutral biomolecules as well as DNA biomolecules with varying negative charges into the nanocavity is shown in Fig. 6.3 as a shift in surface potential. As shown in Fig. 6.3 (a), the surface potential decreases from streptavidin to gelatin. When the nanogap is filled with air ($K=1$), the channel surface potential minimum (Ψ_s, min) is at its highest value because the source-channel barrier height is at its lowest compared to all other situations where $K>1$. When biomolecules with increasing dielectric constants, from streptavidin ($K=2.1$) to gelatin ($K=12$), are

immobilized, the channel surface potential minimum (Ψ_s, min) decreases. This occurs because the gate capacitance increases as the dielectric constant in the cavity region rises [106], enhancing the vertical electric field. Consequently, carriers are depleted in the channel, resulting in a lower potential across the channel [84], [385]. This indicates an enhanced coupling between the gate and the channel, leading to an increase in the gate voltage, which further depletes the channel and requires a higher threshold voltage.

The change in surface potential for different biomolecules relative to the case of no biomolecule, is highest for region 1 in channel below the source side nano cavity. This is due to the fact that drain voltage monotonically decreases while moving toward source. As illustrated in Fig. 6.3 (b), among the analyzed charged DNA biomolecules, those with a charge density of $N_f = -1 \times 10^{12}/\text{cm}^2$ exhibit the lowest surface potential. Thus, out of all DNA biomolecules immobilized in the nanocavity region, we obtain the highest variations in surface potential and, consequently, maximum sensitivity for $N_f = -1 \times 10^{12}/\text{cm}^2$. This occurs due to the increase in flat band voltage caused by qN_f/C_{eff} , leading to a reduction in potential. Consequently, it signifies greater depletion within the channel area, thereby amplifying gate control [89].

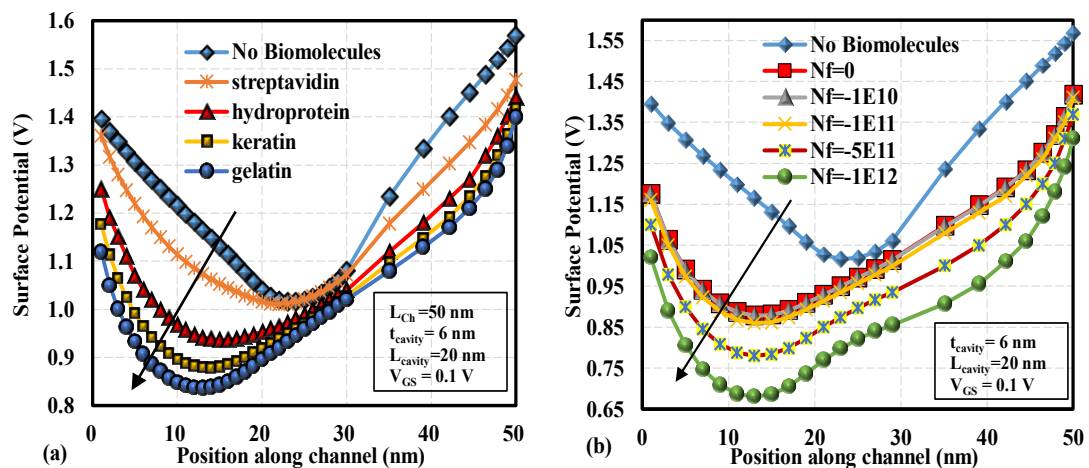


Fig. 6.3 Surface Potential Along the Channel of DM-TMGAA-SiCFET Biosensor for (a) Various Neutral Biomolecules (b) DNA Biomolecules at $K=8$ and Varying Charge

Fig. 6.4 demonstrates the variation in electric field of the DM-TMGAA-SiCFET biosensor for neutral and charged biomolecules. Fig. 6.4 (a) shows the electric field along the channel length for biomolecules with various dielectric constant values, ranging from streptavidin to gelatin. The reduced work function gate close to the drain is the cause of the device's drain side's decreased electric field value. Additionally, it is noticeable that when the dielectric constant increases, the electric field at the source side rises. The highest value of source side electric field for gelatin biomolecules is $6.54 \times 10^5 \text{ V/cm}$.

Fig. 6.4 (b) displays an electric field plot comparing negatively charged DNA biomolecules to neutral biomolecules, both at a dielectric constant K of 8, as well as a case with no biomolecules. The graph clearly shows that the presence of DNA

biomolecules causes noticeable variations in the electric field. Near the source region, the electric field strength increases as the negative charge on the DNA biomolecules becomes more pronounced. But the electric field steadily drops in the channel as it moves towards drain, particularly when dealing with strongly negatively charged DNA biomolecules. Furthermore, Fig. 6.4 (b) reveals that the electric field is at its lowest at the channel-drain junction, and this reduction becomes even more pronounced as the negative charge of the DNA increases. As the electric field progresses along the channel towards the drain, it steadily drops because the gate work function decreases from source to drain. This decrease in work function results in a lower electric field. Additionally, the negatively charged DNA biomolecules create a screening effect that further reduces the electric field as it moves towards the drain. Consequently, the electric field is at its lowest at the channel-drain junction, particularly when dealing with strongly negatively charged DNA biomolecules. This behavior is attributed to the varying gate work function and the interaction with the negatively charged DNA biomolecules.

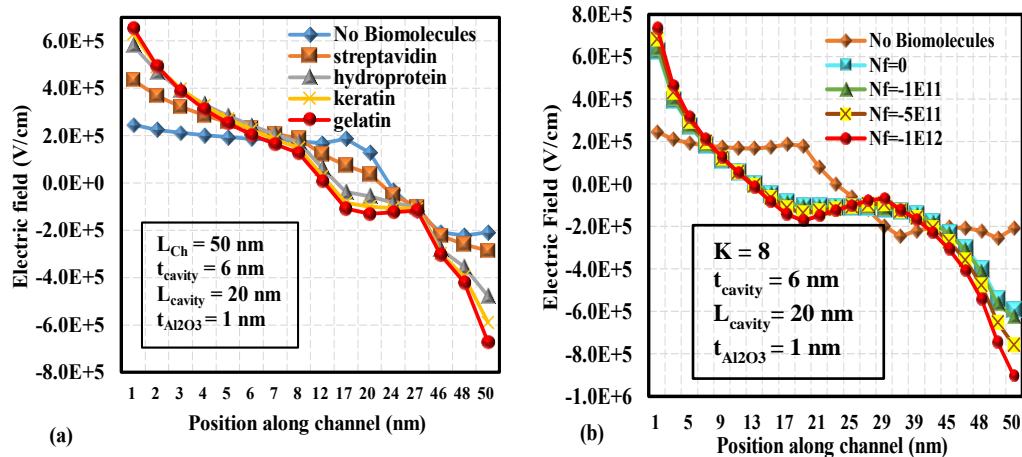


Fig. 6.4 Electric Field of DM-TMGAA-SiCFET Biosensor for (a) Various Neutral Biomolecules (b) DNA Biomolecules at $K=8$ and Varying Charge

In Fig. 6.5, we observe contour plots illustrating the electron concentration within the channel region of the proposed device when both V_{GS} and V_{DS} are set to 0.1V. Notably, the introduction of biomolecules induces significant alterations in these electron concentration contours, highlighting the impact of immobilizing biomolecules on device behaviour. When considering neutral gelatin biomolecules, we observe a discernible decrease in electron concentration compared to the scenario with no biomolecules as indicated by the electron concentration profile. This decrease is clearly delineated in the concentration profile of Fig. 6.5. Furthermore, the introduction of biomolecules possessing negative charges, alongside a dielectric constant (K) of 8, results in a further reduction in electron concentration within the nanocavity compared to the case with biomolecules having only dielectric constant $K=8$ and $N_f=0$. This decline in electron concentration has a consequential effect on the current values within the subthreshold region (referred to as OFF current). As the dielectric constant and negative charge concentration rises, there is a corresponding reduction in the concentration of electrons, leading to drop in the value of OFF current.

This behavior can be attributed to the influence of these factors on the device's electrical characteristics.

The drain current characteristics for immobilizing different biomolecules, such as streptavidin, hydroprotein, keratin, and gelatin, are presented in Fig. 6.6 (a). With rising K values of different biomolecules, both the ON current and OFF current change. This shift in current is a crucial biosensor sensing parameter for identifying specific biomolecules. The graph in Fig. 6.6 (a) shows the drain current with respect to gate to source voltage (V_{GS}) in logarithmic scale showing clearly the subthreshold (leakage) current for $V_{GS} \leq V_{th}$. The leakage current decreases from streptavidin to gelatin in the subthreshold region. The higher dielectric constant of gelatin compared to streptavidin and other biomolecules leads to better gate control, and due to the higher dielectric constant, the threshold voltage shifts upwards, making it harder for the channel to turn on, hence reducing the subthreshold leakage current as observed in graph 6.6 (a).

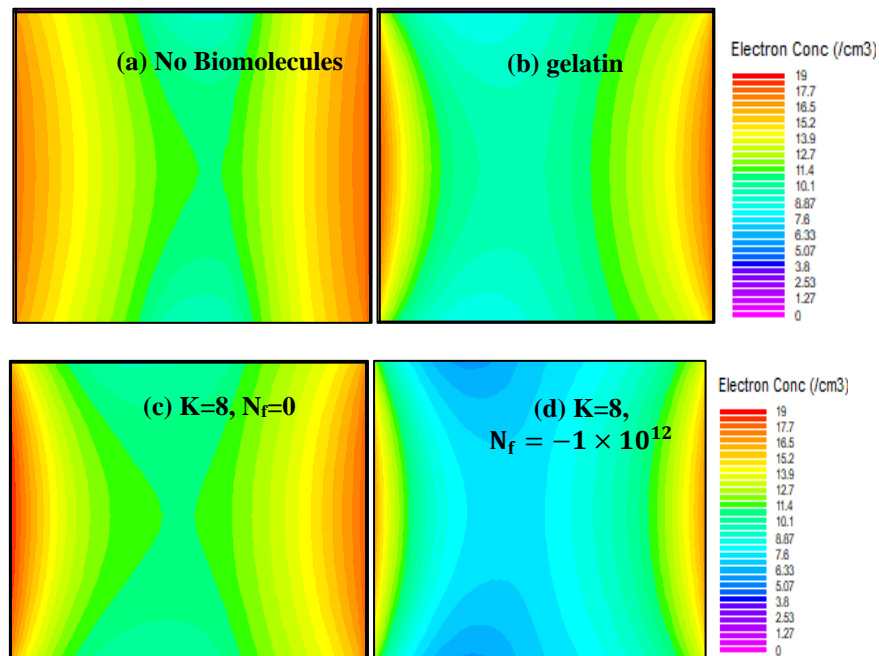


Fig. 6.5 Variation in Electron Concentration in the Silicon Carbide Channel of DM-TMGAA-SiCFET Biosensor

Fig. 6.6 (b) depicts the transconductance (g_m) of the proposed device when different neutral biomolecules are introduced into the nanocavity region. Transconductance (g_m) is the first-order derivative of drain current with respect to gate voltage (V_{GS}). The change in transconductance (g_m) experiences a progressive increase when considering various biomolecules, starting from streptavidin to gelatin as illustrated in Fig. 6.6 (b). The gelatin biomolecule exhibits a highest peak value for transconductance (g_m), reaching $4.15 \times 10^{-5} \text{ A/V}$ at a Gate to Source voltage (V_{GS}) of 1.0 V. This finding highlights the device's ability to convert small input voltage changes into corresponding current variations is maximized with increasing dielectric constant value of the biomolecules.

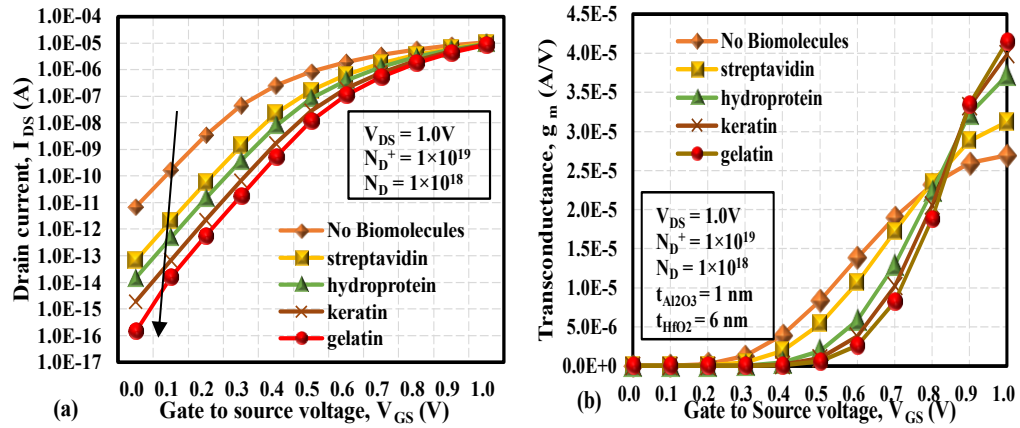


Fig. 6.6 (a) I_D - V_{GS} Characteristics with Different Biomolecules of DM-TMGAA-SiCFET Biosensor (b) Transconductance for Different Biomolecules

Fig. 6.7 (a) shows the drain current characteristics in logarithmic scale indicating the variation in drain OFF current for charged DNA biomolecules. The value of OFF current decreases for negatively charged biomolecules [96]. There is a noticeable drop in the OFF current in the DM-TMGAA-SiCFET. For instance, the OFF current for $K=8$ and ($N_f = -1 \times 10^{12}/\text{cm}^2$) is 1.20×10^{-18} A as compare to No biomolecule case ($K = 1$) is 6.82×10^{-12} A. As the biomolecules with increased negative charges are introduced, the gate's influence becomes more pronounced, leading to a greater degree of carrier depletion and consequently lower OFF current levels.

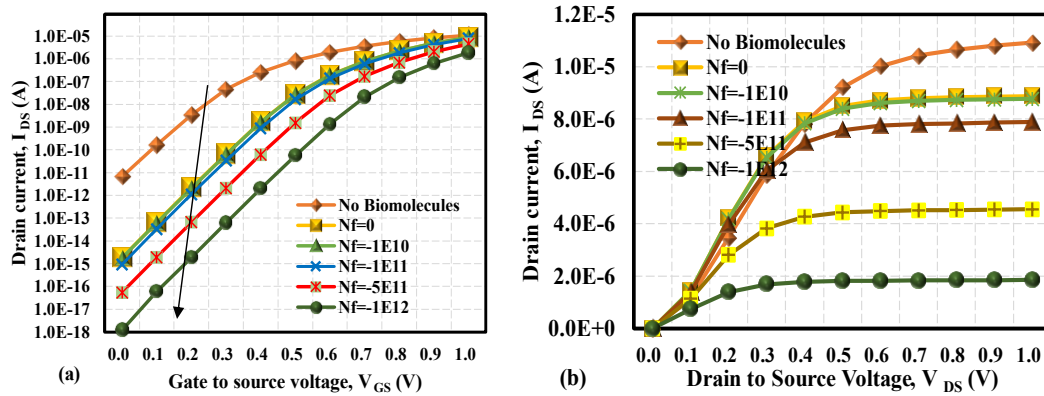


Fig. 6.7 (a) I_D - V_{GS} Characteristics of DM-TMGAA-SiCFET Biosensor for Charged DNA Biomolecules (b) I_D - V_{DS} Characteristics of DM-TMGAA-SiCFET Biosensor for Charged DNA Biomolecules

The drain current vs drain to source voltage (V_{DS}) is depicted in Fig. 6.7 (b), which also shows that the drain ON current, $I_{DS}(\text{ON})$, varies with the change in the DNA biomolecules' negative charge. The drain ON current exhibits a decreasing trend as the negative charge of DNA increases while keeping the dielectric constant fixed at $K=8$. This is related to the fact that when negative biomolecules are immobilized, the drain current reduces due to a downward shift in the surface potential [89]. This noticeable downward shift in surface potential profile can also be observed in Fig. 6.3 (b).

In Fig. 6.8 (a), we observe the impact of immobilizing neutral biomolecules on the output conductance (g_d) of the DM-TMGAA-SiCFET biosensor. The evaluation of g_d is carried out under a constant gate to source voltage (V_{GS}) of 1.0 V, and it is determined by calculating the drain current's derivative relative to the drain voltage (V_{DS}). The output conductance follows a specific trend: it initially increases up to $V_{DS}=0.2$ V and then starts to decrease as biomolecules with higher dielectric constants are introduced into the nanocavity, in comparison to the scenario where no biomolecule is present. Initially, up to $V_{DS} = 0.2$ V, the presence of neutral biomolecules enhances local electric field screening, improving the gate's ability to modulate the channel and increasing conductivity. This results in a higher drain current (I_{DS}) for a given V_{GS} , leading to increased output conductance. However, beyond $V_{DS} = 0.2$ V, the biomolecules do not significantly alter the electric field, and potential barriers within the channel due to biomolecules increase scattering or recombination effects, reducing carrier mobility. This reduction in mobility decreases the drain current for higher V_{DS} , causing a decline in output conductance [386].

In Fig. 6.8 (b), we observe changes in the output conductance concerning varying negative charges on DNA biomolecules. Notably, for all gate-to-source voltage values, when negatively charged biomolecules are present, the output conductance is lower compared to the scenario where the nanocavity is empty (no biomolecules). This is primarily due to the interaction between the negative charges of the biomolecules and the electrons in the channel. The negative charges repel the electrons, reducing the electron density in the channel and thereby decreasing its conductivity. Additionally, the negatively charged biomolecules create potential barriers within the channel, which impede the flow of electrons and increase scattering, further reducing carrier mobility. The presence of these charges can also shift the threshold voltage of the FET, requiring a higher gate to source voltage (V_{GS}) to achieve the same level of conductivity. This shift effectively lowers the current for a given V_{DS} , resulting in lower output conductance [386]. Furthermore, we notice that the increase in negative charge value corresponds to a gradual rise in the output conductance drift.

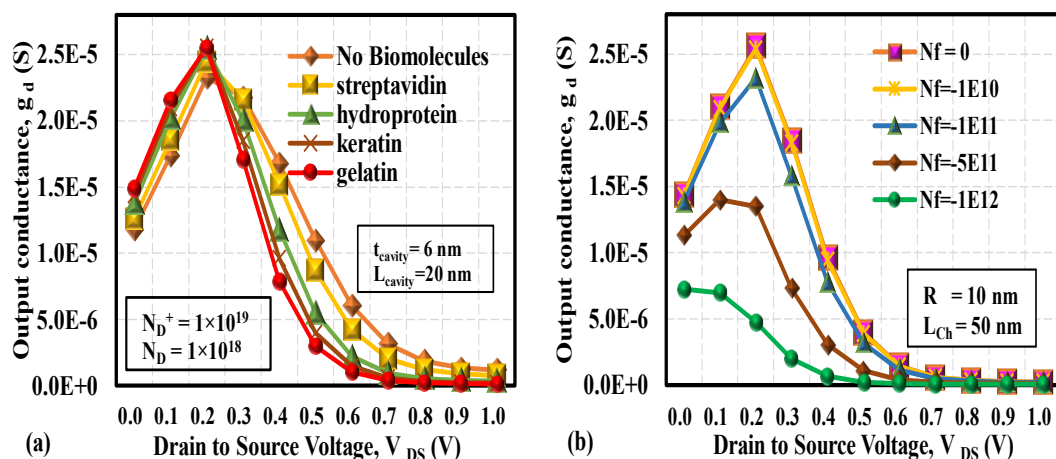


Fig. 6.8 (a) Variation in Output Conductance for Different Neutral Biomolecules (b) Variation in Output Conductance for Charged DNA Biomolecules

The most crucial factor in sensor design is sensitivity. The typical approach for determining the sensitivity of a FET biosensor involves assessing the proportional alteration in a measurable electrical parameter that reflects the existence of biomolecules. This electrical parameter can encompass various factors such as V_{th} , I_{ON} current, and subthreshold slope. In mathematical terms, sensitivity (S) can be formally defined as:

$$S_M = |M_{No\ Biomolecule} - M_{Biomolecules}| \quad (6.1)$$

Where, $M_{No\ Biomolecule}$ is the electrical parameter value before exposure to the biomolecules and $M_{Biomolecules}$ is biosensor's electrical parameter value after immobilization of the biomolecules.

To assess a FET-based biosensor's performance, several device parameters other than sensitivity are also crucial [387]. Sensitivity indicates how the sensor's output changes with analyte variations, influenced by pH, dielectric constant, and biomolecule charge density. Selectivity measures the sensor's ability to differentiate target biomolecules from other substances, essential for specific detections like cancer markers. The detection limit is the smallest analyte concentration the sensor can reliably detect, expressed in units such as concentration, pH, or dielectric constant. Accumulation position refers to where analytes accumulate within the sensor, impacting measurement accuracy and effectiveness [387].

Fig. 6.9 (a) depicts the drain current sensitivity of the DM-TMGAA-SiCFET for neutral biomolecules. According to the results obtained from equation (1), it's evident in Fig. 6.9 (a) that the introduction of biomolecules, ranging from streptavidin to gelatin, consistently enhances drain current sensitivity across all gate voltage values. This trend highlights that biomolecule possessing a higher dielectric constant exhibit greater sensitivity. At $V_{DS}=1.0$ V, Fig. 6.9 (b) depicts the drain current sensitivity (S_{ID}) with respect to gate to source voltage (V_{GS}) for DNA biomolecules with different charge concentrations. The drain current diminishes as the dielectric constant of the biomolecule rises because of the augmented effective gate oxide capacitance. Negatively charged biomolecules possess a greater binding capacity compared to neutral biomolecules. Consequently, the presence of negatively charged biomolecules imposes more control over the flow of charge carriers across the channel, resulting in a further reduction in the drain current. However, it's important to note that as the negative charge on DNA biomolecules increases, the relative change in the drain current continues to rise. At $V_{GS} = V_{DS} = 1.0$ V, DNA biomolecules with $N_f = -1 \times 10^{12}$ exhibit the maximum sensitivity of drain current of $9.06 \mu A$.

The use of three distinct metal work functions in a DM-GAA-SiCFET biosensor enhances its performance by creating pronounced electric field variations, which significantly increase sensitivity to biomolecules. Triple metal gate structure allows fine-tuning of the threshold voltage for precise biosensing and improves selectivity due to varied chemical interactions with target analytes, enhancing accuracy and reliability. The triple-gate architecture, superior to single or double-gate designs, leverages impact ionization to reduce short-channel effects and increase electron velocity, thus boosting biosensing capabilities [160]. The larger work function

differences between gates improve transport efficiency and potential profiles, enabling controlled charge carrier flow and significant changes in sensing parameters in the presence of biomolecules [141].

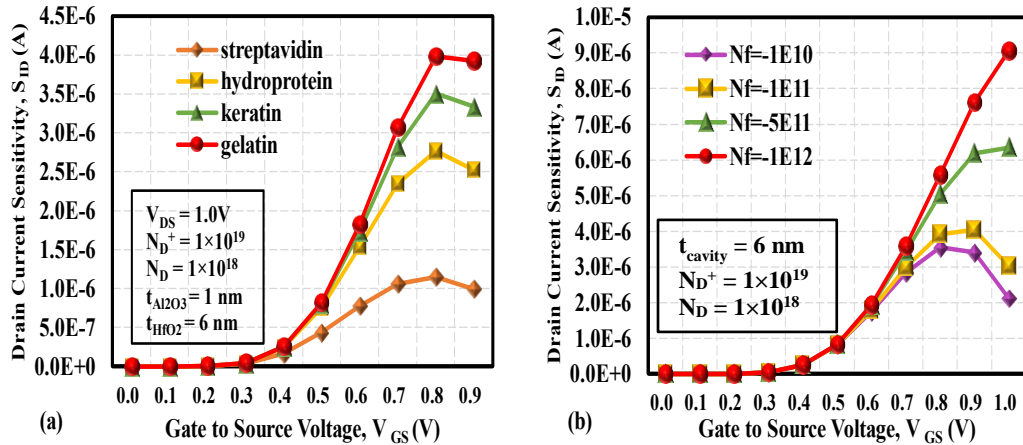
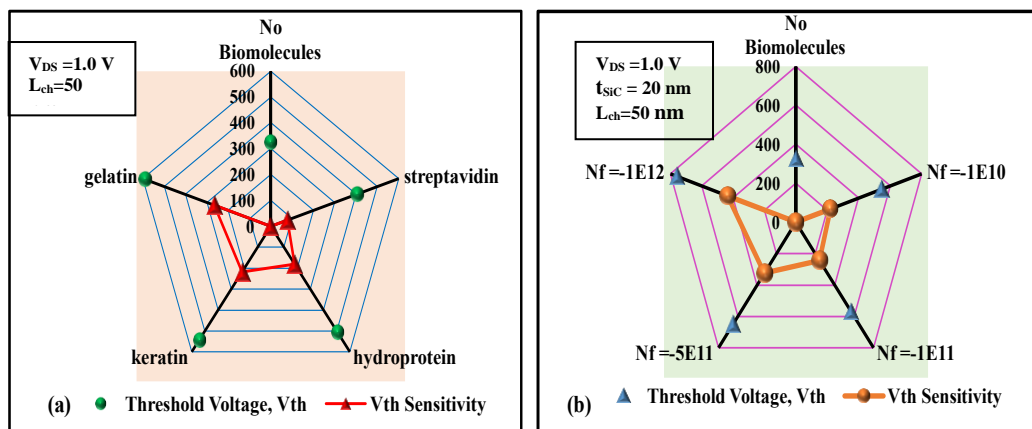


Fig. 6.9 (a) Drain Current Sensitivity for Different Biomolecules (b) Drain Current Sensitivity for DNA Biomolecules with increased Negative Charge

In FET based biosensors, the change in the threshold voltage holds significance as it aids in evaluating the sensitivity of the device. Rising biomolecule permittivity related to different neutral and rising negative charge on DNA biomolecules at $K=8$ increases the threshold voltage as shown in Fig. 6.10 (a) and 10 (b). This is because greater gate voltage is needed to completely deplete the channel when the channel surface potential drops from no biomolecule to neutral and negatively charged DNA biomolecules, as seen in Fig. 6.3, which raises the threshold voltage. The Fig. 6.10 also depicts the increases in threshold voltage sensitivity for increasing K and N_f . The gate oxide capacitance increases with the increasing dielectric constant of biomolecules [25], which is the primary reason for a significant increase in the relative change in threshold voltage and hence the sensitivity. For gelatin biomolecules the V_{th} sensitivity is 202.34 mV. As shown in Fig. 6.10 (b), the V_{th} sensitivity for DNA biomolecule with $N_f = -1 \times 10^{12}$ is 254.46 mV.



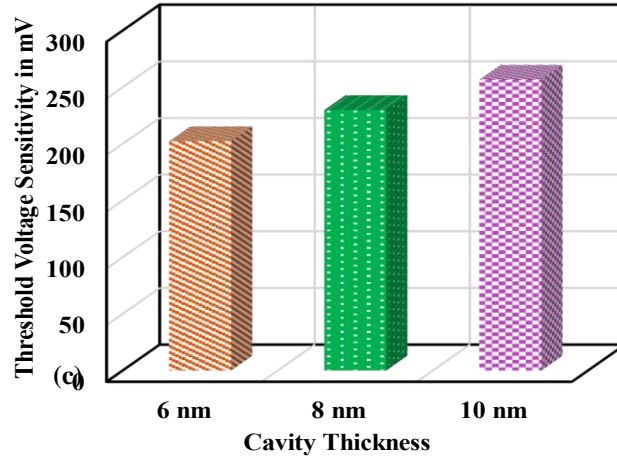


Fig. 6.10 Threshold Voltage and Threshold Voltage Sensitivity for Various (a) Neutral Biomolecules (b) DNA Charged Biomolecules (c) Threshold Voltage Sensitivity with Varying Cavity Thickness

The I_{ON}/I_{OFF} ratio sensitivity for various biomolecules streptavidin, hydroprotein, keratin, and gelatin is shown in Fig. 6.11. The inset in Fig. 6.11 depicts the ratio of I_{ON} to I_{OFF} for different types of biomolecules. The I_{ON}/I_{OFF} ratio is expressed mathematically as:

$$\frac{I_{ON}}{I_{OFF}} = \frac{I_{DS(ON)} \text{ at } V_{GS}=1.0V}{I_{DS(OFF)} \text{ at } V_{GS}=0.0V} \quad (6.2)$$

As the biomolecule's dielectric constant rises, the gate oxide capacitance becomes stronger, giving the gate greater control over charge carriers and reducing the ON-current. Even before reaching the threshold voltage (V_{th}), there is some current known as subthreshold current. The increased oxide capacitance weakly inverts the channel early, reducing the drain OFF-current [181]. This enhances the I_{ON}/I_{OFF} ratio with increased K of the biomolecules due to the dominance of reduction in OFF-current, which drives an increase in the I_{ON}/I_{OFF} ratio. It is rather important to point out that the I_{ON}/I_{OFF} ratio can also be utilized as a metric to examine the sensitivity of the biosensor due to higher shifts in its value for small changes in the dielectric constant. For instance, the I_{ON}/I_{OFF} ratio sensitivity for gelatin is 1.30×10^4 while for some biomolecule the I_{ON} sensitivity is 1.29. Here, the I_{ON}/I_{OFF} ratio sensitivity has been calculated with the equation below [358]:

$$I_{ON}/I_{OFF} \text{ sensitivity, } S_{I_{ON}/I_{OFF}} = \frac{I_{ON}/I_{OFF}(\text{with biomolecules})}{I_{ON}/I_{OFF}(\text{No biomolecules})} \quad (6.3)$$

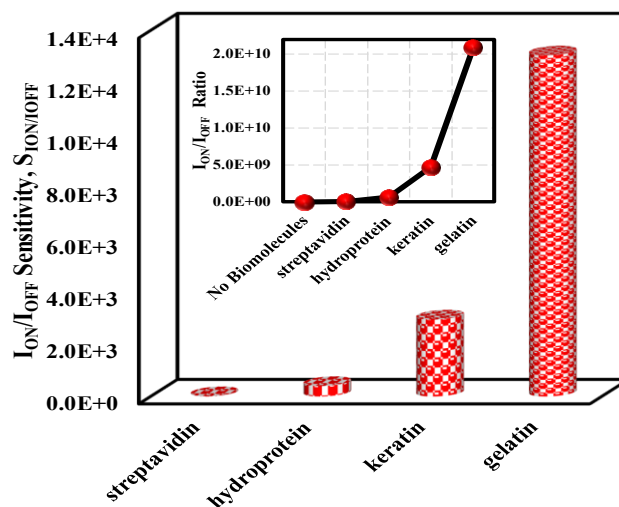


Fig. 6.11 I_{ON}/I_{OFF} Ratio and I_{ON}/I_{OFF} Sensitivity of DM-TMGAA-SiCFET Biosensor

The Subthreshold slope (SS), which measures a FET's responsiveness to gate voltage changes, plays a crucial role in determining device reliability. FETs typically exhibit a minimum SS value of approximately 60 mV/decade at room temperature [96]. As observed in Fig. 6.12, the subthreshold slope diminishes when biomolecules with a higher dielectric constant are immobilized, primarily due to the escalation in gate oxide capacitance. The secondary axis in Fig. 6.12 represents the SS sensitivity based on equation (1). Among all the biomolecules studied, gelatin exhibits the highest SS sensitivity at 9.0 mV/decade.

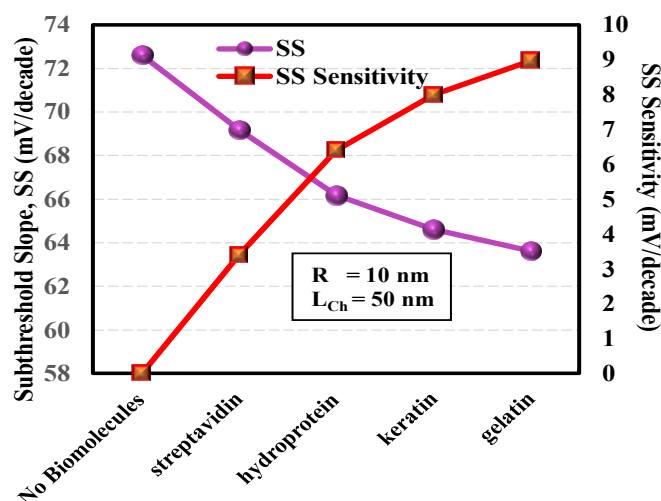


Fig. 6.12 Subthreshold Slope (SS) and SS Sensitivity of DM-TMGAA-SiCFET Biosensor for Various Biomolecules

Gelatin, with the highest dielectric constant ($K = 12$) among biomolecules like streptavidin, hydroprotein, and keratin, significantly impacts the effective gate oxide capacitance and gate control over the channel. And hence all the considered electrical parameters variation according to equation (1) with respect to no biomolecules where $K=1$, is more for gelatin as compare to other biomolecules. In the conduction mode ($V_{GS} > V_{th}$), this high dielectric constant increases the sensitivity of the biosensor to

gelatin by causing larger shifts in the drain current (I_{ON}). In the subthreshold region ($V_{GS} \leq V_{th}$), gelatin's high dielectric constant improves gate control, resulting in a greater upward shift in the threshold voltage (V_{th}) and reduced subthreshold leakage current. These effects collectively enhance the sensor's sensitivity to gelatin, improving parameters such as V_{th} , subthreshold slope (SS), and the I_{ON}/I_{OFF} ratio.

To prove the importance of having different polytype of the silicon carbide as the source of the FET biosensor, different sensitivities have been calculated. The sensitivity contrast between the proposed device using 6H-SiC as the source material and using 4H-SiC as the source material is illustrated in Table 6.2. It is clear that using 4H-SiC channel there is 3.13% and 1.52% increase in V_{th} sensitivity, 57.55% and 58.84% increase in I_{ON} current sensitivity and 5.76 times and 196.1 times increase in I_{ON}/I_{OFF} ratio sensitivity for hydroprotein and gelatin biomolecules respectively. For charged DNA biomolecules ($K=8$, $N_f = -1 \times 10^{12}$) the increase in $S_{V_{th}}$, $S_{I_{ON}}$ and $S_{I_{ON}/I_{OFF}}$ is 3.1%, 12.06% and 39.02 times respectively. A 4H-SiC source outperforms a 6H-SiC source by offering higher electron mobility [359]. This enhancement in electron mobility plays a pivotal role in enhancing the subthreshold properties of DM-TMGAA-SiCFET biosensor. Consequently, a biosensor based on a 4H-SiC source will exhibit a more substantial change in current for the identical gate voltage range when compared to a biosensor based on 6H-SiC. This implies that the proposed biosensor with a 4H-SiC source will also demonstrate more significant variations in various sensing metrics, including threshold voltage, I_{ON}/I_{OFF} ratio, and drain I_{ON} current sensitivity.

Various sensitivities of proposed DM-TMGAA-SiCFET biosensor ($S_{I_{ON}}$, $S_{I_{ON}/I_{OFF}}$, and $S_{V_{th}}$) have been compared to those of SiliconFET biosensors in order to examine the devices' sensing capacity. The device dimensions of the SiliconFET biosensor are the same as those of the DM-TMGAA-SiCFET biosensor.

Table 6.2 Sensitivity Comparison of DM-TMGAA-SiCFET Biosensor with Different Source Materials

Biomolecules	Source Material: 4H-SiC			Source Material: 6H-SiC		
	V_{th} Sensitivity	I_{ON} Sensitivity (μA)	I_{ON}/I_{OFF} sensitivity	V_{th} Sensitivity	I_{ON} Sensitivity (μA)	I_{ON}/I_{OFF} sensitivity
Hydroprotein	198.421	1.50603	4.00E+03	192.382	0.95589	6.94E+02
Gelatin	264.866	2.478	1.30E+04	260.922	1.56	6.63E+02
DNA Biomolecules $K=8$, $N_f = -1E11$	243.603	3.042	5.31E+03	235.006	2.5	2.82E+02
DNA Biomolecules $K=8$, $N_f = -1E12$	434.673	9.077	9.60E+05	421.575	8.1	2.46E+04

Similar device dimensions apply to the SiliconFET biosensor and the DM-TMGAA-SiCFET biosensor. In addition, it has JAM gates all around, and above the silicon channel region, a dielectric stack made of SiO₂ and HfO₂ has been employed. The threshold voltage for both devices has been set to be the same when there are no biomolecules in order to fairly compare the various sensitivity parameters.

The proposed DM-TMGAA-SiCFET and the SiliconFET biosensor's I_{ON} current sensitivities are shown in Fig. 6.13. The current sensitivity, $S_{I_{ON}}$ of DM-TMGAA-SiCFET is substantially higher than that of the SiliconFET. The DM-TMGAA-SiCFET benefits from the intrinsic property of silicon carbide, characterized by a wider bandgap. This characteristic allows the device to generate a higher drive current. This elevated drive current plays a crucial role in enhancing the sensor's responsiveness to changes in the dielectric constants of various biomolecules, consequently boosting its I_{ON} current sensitivity. Furthermore, the DM-TMGAA-SiCFET leverages gate metal work function engineering and incorporates Al₂O₃+HfO₂ stacking in its design. These engineering techniques contribute further to increased drain current sensitivity.

As illustrated in Fig. 6.14, the DM-TMGAA-SiCFET biosensor demonstrates a higher sensitivity in terms of the I_{ON}/I_{OFF} ratio compared to the SiliconFET biosensor. This enhanced sensitivity is attributed to several key factors, including the silicon carbide channel in the device, the use of a distinct material source with superior mobility, gate work function engineering, and the incorporation of a double-sided open cavity. For gelatin biomolecules, the I_{ON}/I_{OFF} ratio sensitivity of the DM-TMGAA-SiCFET Biosensor stands impressively at 1.3×10^4 , surpassing the SiliconFET biosensor, which records a notably lower sensitivity of 2.6×10^3 .

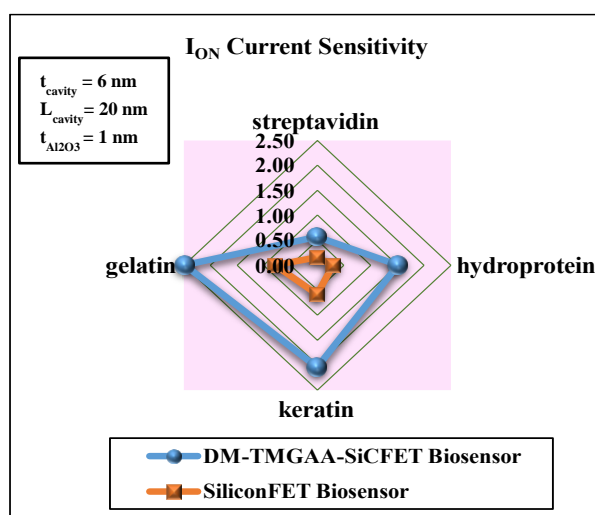


Fig. 6.13 I_{ON} Current Sensitivity Comparison of DM-TMGAA-SiCFET and SiliconFET Biosensor

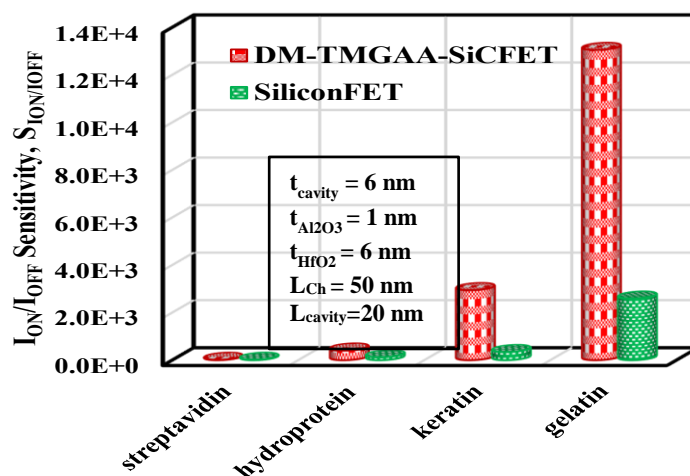


Fig. 6.14 $I_{\text{ON}}/I_{\text{OFF}}$ ratio Sensitivity Comparison of DM-TMGAA-SiCFET and SiliconFET Biosensor

The comparison of the threshold voltage sensitivity for SiliconFET and DM-TMGAA-SiCFET biosensors is shown in Fig. 6.15. The presence of biomolecules within the biosensor's nanocavity poses a challenge for the formation of a conducting layer at the channel surface. Consequently, in order to initiate current conduction, a greater gate voltage is needed. This increase in the device's threshold voltage becomes evident as various biomolecules are introduced into the cavity region, as depicted in Fig. 6.10. The sensitivity of the threshold voltage ($S_{V_{\text{th}}}$) is directly related to the extent of variation in threshold voltage values across different biomolecules, as indicated by equation (6.1). The DM-TMGAA-SiCFET biosensor consistently exhibits a greater $S_{V_{\text{th}}}$ in comparison to $S_{V_{\text{th}}}$ of SiliconFET, whether dealing with neutral or charged DNA biomolecules. This heightened $S_{V_{\text{th}}}$ is attributed to the presence of a 6H-SiC material channel, the incorporation of a GAA gate structure, and the implementation of gate work function engineering, as depicted in Fig. 6.15.

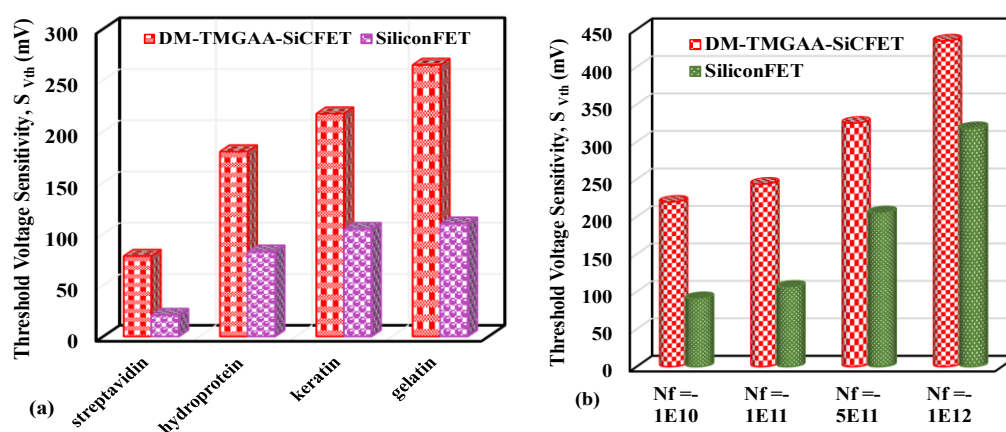


Fig. 6.15 Threshold Voltage Sensitivity ($S_{V_{\text{th}}}$) Comparison of DM-TMGAA-SiCFET and SiliconFET Biosensor for (a) Various Neutral Biomolecules (b) Various Negative Charge on DNA Biomolecules

A comprehensive sensitivity analysis was conducted to evaluate the performance of the DM-TMGAA-SiCFET biosensor in comparison to other FET biosensors with similar structural characteristics. Table 6.3 provides a comparison of threshold voltage sensitivity ($S_{V_{th}}$) for various neutral biomolecules, characterized solely by their dielectric constants. In Fig. 6.16, it is evident that the proposed biosensor exhibits notably higher $S_{V_{th}}$ when compared to several recent biosensors, including the GaN-GME-DE-SNW-FET [258], GC-GAA-NWFET [259], DG-6H-SiC SB-FET [358], and DM DPDG-TFET [261] biosensors, across two different values of charged biomolecules. This comparative analysis unequivocally highlights the superior sensing capabilities of the proposed DM-TMGAA-SiCFET biosensor.

Table 6.3 Comparison of the DM-TMGAA-SiCFET's Threshold Voltage Sensitivity ($S_{V_{th}}$) for Several Biomolecules

Device Specifications	Ref. (Kumari et al. 2022)	Ref. (Sharma et al. 2022)	Ref. (Maiti et al. 2022)	Ref. (Getnet and Chaujar 2022)	Ref. (Singh and Dutta 2020)	Ref. (Kumar et al. 2020)	Our Work
Cavity length (nm)	25	15	20	10	20	8	20
Cavity thickness	9	4	9	1	10	2	6
Channel length	100	50	40	20	40	20	50
Dielectric Constant of biomolecules	5	8	12	2.1	5	5	8
$S_{V_{th}}$ (mV)	130	105	161	17	137	87	183

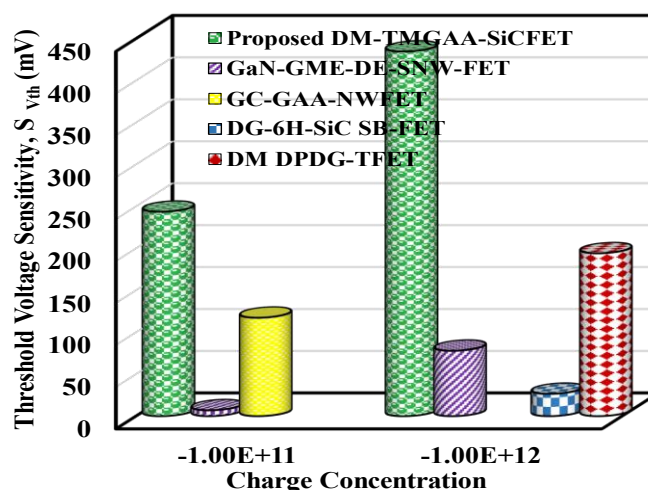


Fig. 6.16 $S_{V_{th}}$ Comparison of DM-TMGAA-SiCFET Biosensor with Recent Published FET Biosensors for Different Charge of the Biomolecules

6.1.5 Summary

In this work, we have introduced an innovative Gate-All-Around Field Effect Transistor (FET) made from silicon carbide, specifically designed for efficient label-free detection of biomolecules. The choice of silicon carbide as the channel material offers distinct

advantages for biosensor design, primarily attributed to its wide band gap. The manuscript demonstrates that the utilization of two distinct silicon carbide polytypes, specifically 4H-SiC as the source material and 6H-SiC as the channel material, significantly impacts the sensing performance of the proposed biosensor. This influence is particularly evident in terms of threshold voltage sensitivity, I_{ON} current sensitivity, and I_{ON}/I_{OFF} sensitivity. Additionally, enhanced control of the channel through the gate and improved device performance are achieved through gate triple metal work function engineering and oxide engineering, which involves the stacking of Al_2O_3 and HfO_2 layers. Various parameters including surface potential, threshold voltage, electric field, drain current, transconductance, output conductance, and subthreshold slope, have all been used to evaluate the sensitivity of the DM-TMGAA-SiCFET biosensor. To underscore the significance of proposed structure in silicon carbide FET, we conducted a comparative sensitivity analysis between the DM-TMGAA-SiCFET biosensor and the SiliconFET biosensor. The DM-TMGAA-SiCFET stands out for its attributes of high sensitivity, robust performance in challenging environmental conditions, and compatibility with biological systems, positioning it as a highly promising candidate for biosensing applications.

6.2 Gallium-arsenide Gate-All-Around engineered Field Effect Transistor (GaAs-GAAE-FET)

6.2.1 Background and Overview

Cancer is a serious global health concern, considering its widespread impact on human health and well-being. One of the main features of cancer is that abnormal cells multiply more quickly than usual, piercing adjacent tissues in the process. Uncontrolled growth can result in metastasis, which is the spread of malignant cells to other organs and ultimately the main cause of cancer-related deaths. In 2020, cancer emerged as a predominant cause of global mortality, claiming nearly 10 million lives [388]. With 2.26 million fresh cases recorded in 2020, breast cancer topped the list of the most common cancer kinds; closely followed by lung cancer with 2.21 million cases [389]. The development of malignant tumors within the female breast leads to breast cancer. The lifetime risk of experiencing breast cancer stands at 12%, while early detection contributes to an overall survival rate of over 70% among documented cases [390].

Current diagnostic methods for cancer, including clinical exams, mammography, ultrasonography, and biopsies, sometimes require advanced tools like MRI and PET scans [391]. Extensive use of these diagnostic methods for early cancer diagnosis is, however, constrained by their dependence on complex machinery and professional interpretation. The identification of novel molecular markers, genetic patterns, and aberrant molecular alterations, such as miRNA and protein expression, for early breast cancer diagnosis is becoming increasingly crucial in an effort to address this [392]. In order to identify particular cancer biomarkers at clinically meaningful levels, it is imperative that novel biosensing technologies be developed.

The identification and management of diseases like cancer depend heavily on biomarkers. Cells present in breast cancer can be classified as T-47D, MDA-MB-231, HS578t, and MCF-7, on the other hand, MCF-10A is a known benign cell line. MDA-MB-231 and HS578t are the most invasive breast cancer cells. Early diagnosis of these invasive cells is crucial due to their potential harm and rapid dissemination [393].

Field-effect transistor (FET) biosensor applications have increased substantially in the last several years. These biosensors are becoming more and more popular because of their rapid and label-free biomolecule identification capabilities, low power consumption, affordability, and possibility for on-chip integration [135]. Researchers have examined strategies to improve the sensitivity of biomolecule detection in biosensors by utilizing a range of nanomaterials, including silicon, gallium nitride, and gallium arsenide, as well as other nanostructures, such as nanowires and nanotubes. Over the past ten years, nanowire-based Gate-All-Around FETs (GAAFETs) have been increasingly popular due to their improved gate control capabilities [159]. GAAFETs are the major focus for research because of this increased gate control, which also improves packing density, minimizes short-channel effects, and maximizes field confinement.

GaAs is recognized for having better electrical characteristics than silicon because it has a larger energy band gap and higher electron mobility. Field effect transistors can be made with semiconductors made of gallium arsenide (GaAs) [121]. The lack of reliable insulators like SiO₂ is one of the issues facing GaAs-based devices. Advances in MBE and ALD have made it feasible to use aluminum oxide (Al₂O₃) as a preferred gate dielectric. Its superb GaAs interface and non-crystalline structure make it an excellent choice. Further, to enhance the performance of GAAFETs, Gate metal Engineering and the dielectric layer stack [321] can be opted. Additionally, the gate-stack (GS) design resolves mobility degradation, V_{th} instability, and leakage current, which are frequently encountered issues when applying high-k dielectrics directly [153] [394].

6.2.2 Device structure

The gallium-arsenide Gate-All-Around engineered FET (GaAs-GAAE-FET) biosensor device's three-dimensional structure is depicted in Fig. 6.17 (a). This device incorporates gate oxide stack engineering (GOSE) and gate metal engineering (GME) with a cylindrical gate encircling the channel. Using three gate metals with different work functions, (5.0 for Gate M1, 4.7 for Gate M2, and 4.5 for Gate M3) the GME have been implemented. Device operates in Junction Accumulation Mode. The two-dimensional perspective of the GaAs-GAAE-FET is shown in Fig. 6.17 (b). It also showcases the visual depiction of the process involving biomarker extraction and the immobilization of biomarkers within the nanocavity of the proposed FET biosensor. Gallium arsenide (GaAs) serves as the semiconductor material for the channel of FET. It is classified as III-V semiconductor, known for its direct band gap characteristic.

GaAs-based devices face a challenge due to the lack of stable insulators like SiO₂. Advances in MBE and ALD have enabled the use of aluminium oxide (Al₂O₃) as a preferred gate dielectric. Its noncrystalline nature, excellent interface with GaAs, a 9eV

energy band gap, and high thermal stability make it a top choice. Consequently, a 1 nm layer of Al_2O_3 has been deposited on the GaAs channel in the proposed FET device. To leverage the benefits of oxide stacking, a 7 nm layer of HfO_2 has been added on top of the Al_2O_3 layer. A dual-sided cavity measuring 6 nm in thickness and 20 nm in length has been etched into the HfO_2 oxide layer to facilitate the immobilization of cancer biomarkers.

The specifics of the GaAs-GAAE-FET biosensor, encompassing device dimensions, material type, and nanocavity dimensions, are outlined in Table 6.4. The Silvaco ATLAS-3D tool has been used to simulate the proposed device for a thorough analysis. Furthermore, an extensive list of the models used to simulate the biosensor device is given in Table 6.4.

Table 6.4 Biosensor Specifications and Parameters

Physical Device Parameter	GaAs-GAAE-FET	Si-GAA-FET
Channel thickness (t_{ch})	20 nm	20 nm
Channel length (L)	50 nm	50 nm
Source and drain lengths ($L_S = L_D$)	15 nm	15 nm
Gate Metal work-function (eV)	$M_1: 5.0, M_2: 4.7, M_3: 4.5$	5.0
Oxide thickness (nm)	$\text{Al}_2\text{O}_3: t_{ox} = 1.0$	$\text{SiO}_2: t_{ox} = 1.0$
	$\text{HfO}_2: t_{ox1} = 6.0 + 1.0$	$\text{HfO}_2: t_{ox1} = 6.0 + 1.0$
Source/drain doping (N_{D^+})	10^{19} cm^{-3}	10^{19} cm^{-3}
channel doping (N_D)	10^{18} cm^{-3}	10^{18} cm^{-3}
Thickness of Cavity (t_C)	6 nm	6 nm
Length of cavity (L_C)	20 nm	20 nm
Physical models [21]	CONMOB: Concentration dependent mobility model.	
	FLDMOB: To model velocity saturation	
	BOLTZMANN: To model the carrier statistics.	
	AUGER: Recombination model which includes the effects at higher doping densities.	
	CVT: It's a Mobility model including doping, temperature and field dependency.	
	SRH: Doping dependent generation-recombination model.	
	BGN: Models the Bandgap narrowing due to high doping.	

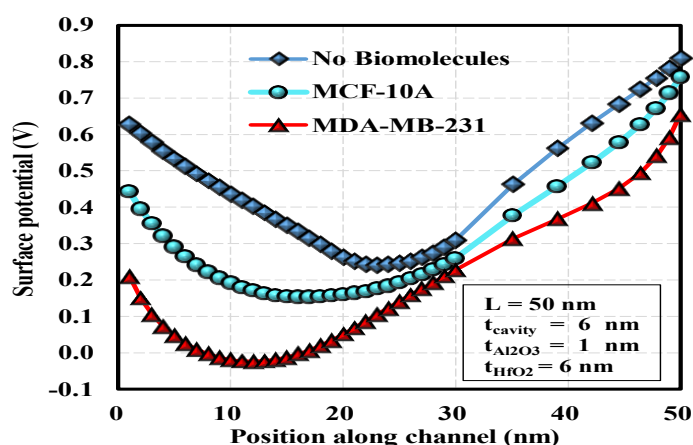


Fig. 6.18 Surface Potential Variation of GaAs-GAAE-FET Biosensor

In Fig. 6. 19, the plot illustrates the drain current (I_{DS}) against the V_{GS} . A discernible trend emerges where the I_{DS} progressively decreases from the case where biomolecules are absent to the existence of MCF-10A and subsequently to MDA-MB-231 biomarkers. MDA-MB-231 is notable for having the lowest drain current of all the biomolecules examined. Additionally, it's observable that the subthreshold current, represented by the drain current at $V_{GS} = 0V$ (indicated on the secondary axis), decreases for all breast cancer biomarkers compared to the I_{Sub} value in nonexistence of immobilized biomarkers within the cavity.

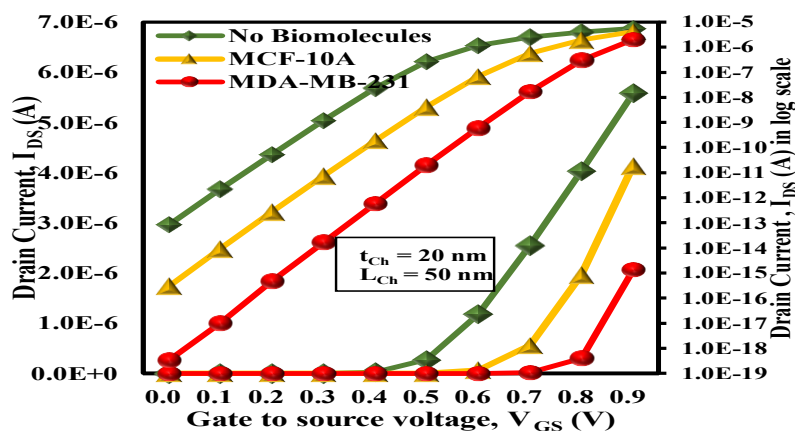


Fig. 6.19 I_{DS} - V_{GS} Characteristics of GaAs-GAAE-FET with Different Biomarkers

The contour plots in Fig. 6.20 show the concentration of electrons in the channel area. Specifically, referring to electron concentration profile in Fig. 6.20 (d), it is notable that in case of air or no biomolecules in the nanocavities, the electron concentration profile in middle of channel is green signifying maximum concentration and as the biomolecules accumulate within the cavity, there's a subsequent reduction in the device's electron concentration. The minimum electron concentration is for MDA-MB-231 as depicted in Fig. 6. 20 (c) which displays blue colored profile in channel region because of the highest dielectric constant of the aforementioned biomarkers.

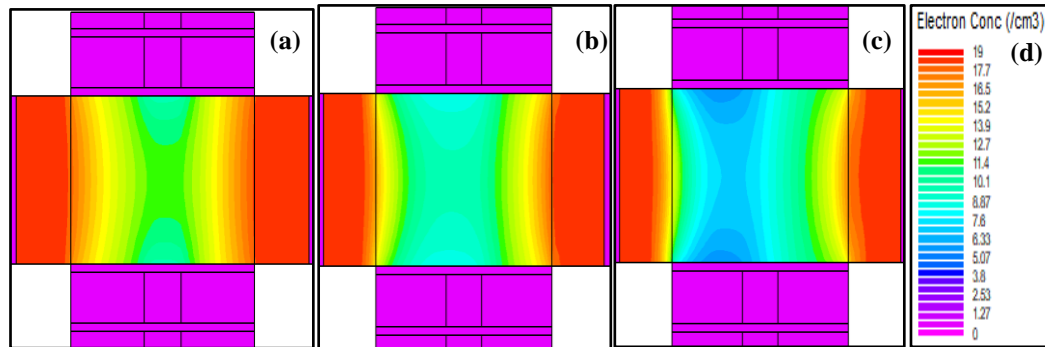


Fig. 6.20 Electron Concentration along the Channel of GaAs-GAAE-FET (a) No Biomolecule (b) MCF-10A (c) MDA-MB-231 (d) Electron Concentration Profile

6.2.3.2 Sensitivity Analysis of Proposed Biosensor

The measurement of a biosensor's sensitivity typically involves assessing the proportional alteration in a sensing parameter. This parameter could encompass different electrical metrics like threshold voltage, current, or any quantifiable attribute indicative of biomolecule presence or absence. In mathematical terms, sensitivity (S_P) is calculated as the absolute difference between the parameter's value in the absence of biomolecules ($P_{No\ Biomolecule}$) and when biomolecules are immobilized inside the cavity ($P_{With\ biomolecules}$), expressed as:

$$S_P = |P_{No\ Biomolecule} - P_{with\ Biomolecules}| \quad (6.4)$$

For field effect transistors, drain current is a crucial characteristic. At $V_{GS} = 1.0\text{ V}$, the drain current value is known as the drain ON current. According to equation (6.4), the drain ON current sensitivity S_{ID} , in milliamperere is calculated as:

$$S_{ID} = I_{D[With\ biomolecules]} - I_{D[Without\ biomolecules]} \quad (6.5)$$

Fig. 6.21 clearly demonstrates that at $V_{DS}=1.0\text{ V}$, MDA-MB-231 exhibits a higher S_{ID} (883 nA) in comparison to the S_{ID} for MCF-10A (332 nA). This difference arises due to the significantly higher dielectric constant of MDA-MB-231, consequently leading to a more substantial variation in gate oxide capacitance associated with the device.

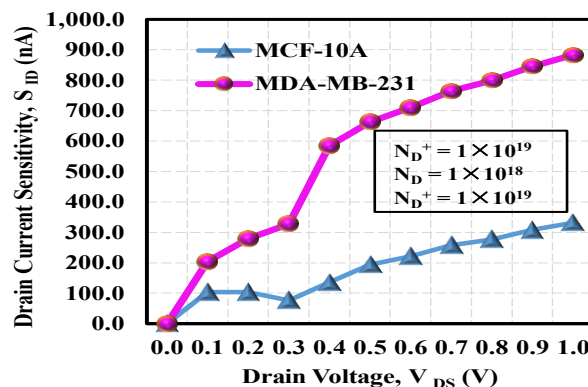


Fig. 6.21 Drain Current Sensitivity (S_{ID}) of GaAs-GAAE-FET with Variation to the Drain Voltage (V_{DS})

The transconductance (g_m) represents the rate of change of I_{DS} in respect to V_{GS} . The trend of the g_m curve in Fig. 6.22 is comparable to that of the drain current in Fig. 6.19, indicating higher g_m values corresponding to increasing dielectric constants of cancer biomarkers. Consequently, as in Fig. 6.22, the most significant transconductance sensitivity is identified in MDA-MB-231.

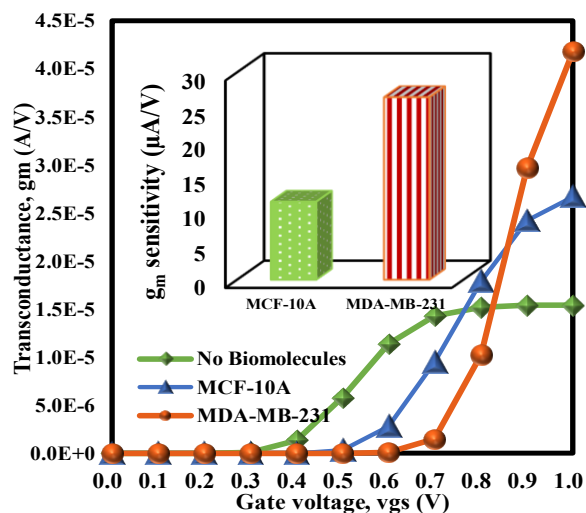


Fig. 6.22 Transconductance (g_m) and Transconductance Sensitivity for Various Biomarkers

Fig. 6.23 displays the influence of different biomolecules, namely MCF-10A and MDA-MB-231, upon the threshold voltage sensitivity ($S_{V_{th}}$) for both the GaAs-GAAE-FET and the silicon-Gate-All-Around FET (Si-GAA-FET). The Si-GAA-FET mirrors the dimensions and specifications of the proposed GaAs-GAAE-FET, except for utilizing a silicon channel instead of gallium arsenide in the proposed device. From Fig. 6.23, it can be observed that the GaAs-GAAE-FET exhibits higher threshold voltage sensitivity compared to that of the Si-GAA-FET for all biomolecules. This advantage is attributed to the utilization of GaAs in channel, source, and drain region in the GaAs-GAAE-FET device.

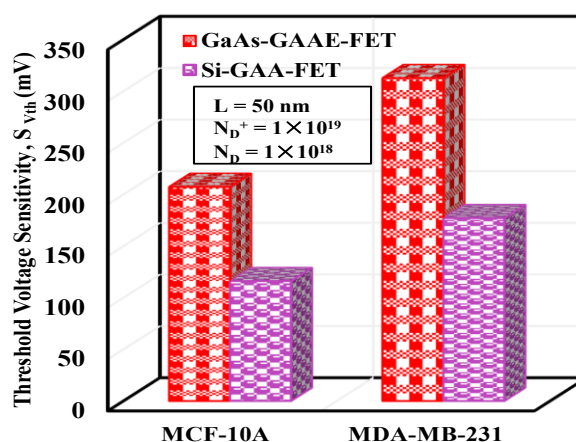


Fig. 6.23 Threshold Voltage Sensitivity Comparison of GaAs-GAAE-FET and Si-GAA-FET

6.2.4 Summary

The potential of the GaAs-GAAE-FET biosensor for the identification of malignant MDA-MB-231 cells is thoroughly examined in this work. In comparison to the Gate-All-Around FET with a silicon channel, the cylindrical Gate-All-Around FET with a GaAs channel performs better in the identification of breast cancerous cells. The sensor demonstrates a drain ON current sensitivity (S_{ID}) of 332 nA and a threshold voltage sensitivity of 207.31 mV for healthy MCF-10A cells. In contrast, for malignant MDA-MB-231 breast cells, it exhibits a higher drain ON current sensitivity of 883 nA and a corresponding threshold voltage sensitivity of 312.78 mV. The biosensor has also been evaluated for changes in transconductance, drain ON and OFF current, electron concentration, and channel surface potential. Sensitivity is improved by innovative device engineering methods such as Junction Accumulation Mode gallium arsenide channel, customized triple metal gate, and dual sided nanocavity integration. The exceptional sensitivity and structural resilience of the GaAs-GAAE-FET biosensor establish it as a viable option for the rapid identification of breast cancer.

CHAPTER 7

CONCLUSION, FUTURE SCOPE AND SOCIAL IMPACT

Here, in this chapter, the summarized conclusions have been discussed from all the previous chapters. This chapter sums up that the biosensing applications of the conventional Gate-All-Around FET can be improvised by formulating novel device architectures. The research presented in this thesis addresses significant advancements in the field of biosensors, particularly through the design, analysis, and implementation of novel Gate-All-Around Field Effect Transistors (GAAFETs) for sensing applications.

The objectives are accomplished through analytical formulations and extensive simulations; however, certain aspects still remain unrevealed. It also talks about the future scope of the work that has been addressed in this dissertation.

7.1 Summary of the Work Done in the Thesis

The primary objective of this thesis has been to showcase the suitability of GAA-MOSFET for biosensing applications, accomplished through the implementation of different structural and material engineering approaches. This thesis contributes to the overarching goal of developing high-performance biosensors with enhanced sensitivity.

Chapter 2 focused on low-leakage, high-frequency sensors using the HDTG-JAM-GAAFET structure. The effect of biomolecules on HDTG-JAM-GAAFET biosensor's output properties, including surface potential, electron concentration, threshold voltage drift (ΔV_{TH}), subthreshold leakage current (I_{OFF}), subthreshold slope (SS), switching ratio (I_{ON}/I_{OFF}), I_{ON} current sensitivity, transconductance (g_m), output conductance (g_d), channel resistance (R_{ch}) and intrinsic gain ($A_{V_{int}}$) investigated. The HDTG-JAM-GAAFET biosensor device exhibits exceptional performance characteristics and it can effectively identify specific biomolecules to diagnose many diseases, such as breast cancer, lung cancer, and numerous viral infections, using their respective biomarkers.

Chapter 3 explored the impact of trench gate engineering on device sensitivity. The detailed investigation into Trench Gate Engineered Junction Accumulation Mode GAAFETs (TGE-JAM-GAAFET) demonstrated the effectiveness of its design in improving sensitivity. The numerical simulations showed that by carefully engineering the gate structures and utilizing dielectric modulation, the performance of these biosensors could be optimized for label-free detection of a wide range of biomolecules. The comparative performance analysis in terms of channel center potential, electron concentration, drain current characteristics, and various sensitivities exhibit that the TGE-JAM-GAA BioFET significantly outperforms the TMNG-JAM-GAAFET and

SMNG-JAM-GAAFET. For neutral APTES biomolecules, the TGE-JAM-GAA BioFET demonstrates 46.45% and 143.58% greater I_{ON} current sensitivity and six times and 14 times higher V_{TH} sensitivity than that of the TMNG-JAM-GAAFET and SMNG-JAM-GAAFET.

Chapter 4 provided a detailed analytical model for the GJAM-SGAA Bio-FET, offering a deeper understanding of device physics. presented a comprehensive analytical model for the Graded JAM Split GAAFET (GJAM-SGAA) Bio-FET, specifically designed for the detection of Avian Influenza antibodies and DNA. The analytical results, corroborated by numerical simulations, provided insights into the critical parameters influencing device performance, thereby validating the proposed models and designs. The relevance of the proposed structural modification in the GAA-NWFET is shown by a comparison of the sensitivity analysis of the proposed GJAM-SGAA Bio-FET with Junction Accumulation Mode Split Gate-All-Around FET (SGAA-FET) biosensor. Surface potential, electric field, drain ON current, drain OFF current, I_{ON}/I_{OFF} ratio, g_m , subthreshold slope and threshold voltage have all been used to assess the proposed device's sensitivity to the avian influenza virus and DNA analytes. The proposed BioFET has 430.32% higher threshold voltage sensitivity for the case of avian influenza antibody (AI-ab) biomolecule immobilization in the cavity region, while for dsDNA biomolecules it has 402.22% increase in threshold voltage sensitivity.

Chapter 5 expanded the application of GAAFETs to the detection of specific viruses, such as SARS-CoV-2 and Avian Influenza, using novel nanowire FET designs. This chapter demonstrates that the Dual Metal and Dual Layered Gate-All-Around structure has a persuasive effect on the sensing ability of the proposed biosensor. The combination of layered structure and dual metal work function engineering allows greater Gate control over the channel and improved analog performance. The DMDL-GAA-NW-FET achieves a V_{TH} shift of 225.74 mV as compare to conventional GAA-NW-FET biosensor which produces a V_{TH} shift of 93.56 mV while varying the dielectric constant (K) from 1 to 4. The simulation findings show that DMDL-GAA-NW-FET is 7 times more sensitive to threshold voltage and 2.4 times more sensitive to I_{ON} current than GAA-NW-FET when it comes to immobilizing biomolecules with $K=4$ inside the cavity. This chapter also investigates the label-free biosensing capability of Gate-All-Around Engineered Gallium Nitride Field Effect Transistor (GAAE-GANFET) in detecting the avian influenza and DNA biomolecules. A compact analytical model of GAAE-GANFET has been proposed, which has shown excellent agreement with the TCAD simulations. The manuscript highlights the significant influence of the open cavities, graded channel doping and utilizing GaN as the channel material. The results reveal that the transition from a silicon channel to a gallium nitride channel substantially enhances sensitivity. Remarkably, the achieved threshold voltage sensitivity surpasses 50.02% for gelatin and reaches an impressive 91.69% for APTES biomolecules.

Chapter 6 introduced the use of wide bandgap semiconductors, like SiC and GaAs, to further enhance the sensitivity and robustness of biosensors. In a novel DM-TMGAA-SiCFET biosensor design, the choice of silicon carbide as the channel material offers distinct advantages for biosensor design, primarily attributed to its wide band gap. The

utilization of two distinct silicon carbide polytypes, specifically 4H-SiC as the source material and 6H-SiC as the channel material, significantly impacts the sensing performance of the proposed biosensor. Additionally, enhanced control of the channel through the gate and improved device performance are achieved through gate triple metal work function engineering and oxide engineering, which involves the stacking of Al_2O_3 and HfO_2 layers. This chapter also examines the potential of the GaAs-GAAE-FET biosensor for the identification of malignant MDA-MB-231 breast cancer cells. In comparison to the Gate-All-Around FET with a silicon channel, the cylindrical Gate-All-Around FET with a GaAs channel performs better in the identification of breast cancerous cells. For MDA-MB-231, the GaAs-GAAE-FET biosensor demonstrates, a higher drain ON current sensitivity of 883 nA and a threshold voltage sensitivity of 312.78 mV.

In conclusion, the findings of this research demonstrate the potential of GAAFET-based biosensors in advancing the field of diagnostics, particularly in the detection of viral and cancer biomarkers. The innovative designs and analytical models developed in this thesis lay the groundwork for future exploration and optimization of biosensors, potentially leading to more sensitive, specific, and reliable diagnostic tools in medical and environmental applications.

7.2 Future Scope and Social Impact

Some important directions for further research in the following areas can be:

1. Advanced Material Integration

- Exploration of other wide bandgap for enhanced sensitivity and stability in extreme environments.
- Investigation of 2D materials like Graphene and MoS_2 in GAAFET structures to improve surface-to-volume ratios and biofunctionalization efficiency.

2. Miniaturization and Fabrication

- Development of scalable fabrication techniques for GAAFET biosensors to enable mass production and commercialization.
- Exploration of nanofabrication techniques to further miniaturize GAAFET structures, enhancing sensitivity and reducing power consumption.

3. Multi-Target Detection

- Design and implementation of multi-channel GAAFET sensors for simultaneous detection of multiple biomarkers, improving diagnostic efficiency.
- Integration of multiplexing techniques to allow real-time, parallel detection of various diseases.

4. Integration with IoT and Wearable Technology:

- Development of GAAFET-based biosensors integrated with Internet of Things (IoT) platforms for real-time health monitoring and data analysis.
- Exploration of wearable biosensors using GAAFET technology for continuous monitoring of health parameters and early disease detection.

5. Artificial Intelligence and Data Analysis:

- Incorporation of machine learning algorithms to analyze biosensor data, enhancing the accuracy and reliability of disease detection.
- Development of AI-driven models to predict sensor responses to various biomolecules, optimizing sensor design and functionality.

6. Clinical and Environmental Applications:

- Validation of GAAFET biosensors in clinical settings for early diagnosis of diseases such as cancer, viral infections, and neurodegenerative disorders.
- Application of GAAFET-based sensors in environmental monitoring, such as detecting pollutants and pathogens in water and air.

Bibliography

- [1] M. Mitchell Waldrop, "The chips are down for Moore's law," *Nature*, vol. 530, pp. 144–147, 2016, [Online]. Available: <https://www.nature.com/news/the-chips-are-down-for-moore-s-law-1.19338>
- [2] "[https://www.kla.com/advance/innovation/kla-celebrates-the-75th-anniversary-of-the-transistor.](https://www.kla.com/advance/innovation/kla-celebrates-the-75th-anniversary-of-the-transistor)"
- [3] I. Corp, "MOORE'S LAW : past , present ,and future," *IEEE Spectr.*, vol. 34, no. 6, pp. 52–59, 1997.
- [4] H. Radamson and L. Thylén, "Monolithic Nanoscale Photonics-Electronics Integration in Silicon and Other Group IV Elements," *Monolith. Nanoscale Photonics-Electronics Integr. Silicon Other Gr. IV Elem.*, pp. 1–168, 2014, doi: 10.1016/C2013-0-08324-7.
- [5] D. K. Ferry and L. A. Akers, *Scaling theory in modern VLSI*, vol. 13, no. 5. 1997. doi: 10.1109/101.621606.
- [6] V. K. Khanna, "Short-Channel Effects in MOSFETs," *Nanosci. Technol.*, pp. 73–93, 2016, doi: 10.1007/978-81-322-3625-2_5.
- [7] A. Singh, S. Chaudhury, C. K. Sarkar, I. Hussain, and A. Ganguly, "A Multi Vt Approach for Silicon Nanotube FET with Halo Implantation for Improved DIBL," *Proc. Int. Conf. 2018 IEEE Electron Device Kolkata Conf. EDKCON 2018*, pp. 328–331, 2018, doi: 10.1109/EDKCON.2018.8770441.
- [8] A. Chaudhry and M. J. Kumar, "Controlling Short-Channel Effects in Deep-Submicron SOI MOSFETs for Improved Reliability: A Review," *IEEE Trans. Device Mater. Reliab.*, vol. 4, no. 1, pp. 99–109, 2004, doi: 10.1109/TDMR.2004.824359.
- [9] Y. Liu, P. Wang, Y. Wang, Y. Huang, and X. Duan, "Suppressed threshold voltage roll-off and ambipolar transport in multilayer transition metal dichalcogenide feed-back gate transistors," *Nano Res.*, vol. 13, no. 7, pp. 1943–1947, 2020, doi: 10.1007/s12274-020-2760-6.
- [10] S. Jaiswal and S. K. Gupta, "Quantum Mechanical Study of Double Gate MOSFET with Core Insulator in Channel for Immune Short Channel Effects," *Silicon*, vol. 15, no. 8, pp. 3419–3430, 2023, doi: 10.1007/s12633-022-02269-3.
- [11] J. Saint Martin, A. Bournel, and P. Dollfus, "On the ballistic transport in nanometer-scaled DG MOSFETs," *IEEE Trans. Electron Devices*, vol. 51, no. 7, pp. 1148–1155, 2004, doi: 10.1109/TED.2004.829904.
- [12] A. Sarkar, A. Kumar Das, S. De, and C. Kumar Sarkar, "Effect of gate engineering in double-gate MOSFETs for analog/RF applications," *Microelectronics J.*, vol. 43, no. 11, pp. 873–882, 2012, doi: 10.1016/j.mejo.2012.06.002.
- [13] H. S. P. Wong, D. J. Frank, P. M. Solomon, C. H. J. Wann, and J. J. Welser, "Nanoscale CMOS," *Proc. IEEE*, vol. 87, no. 4, pp. 537–570, 1999, doi: 10.1109/5.752515.
- [14] T. Sekigawa and Y. Hayashi, "Calculated threshold-voltage characteristics of an XMOS transistor having an additional bottom gate," *Solid State Electron.*, vol. 27, no. 8–9, pp. 827–828, 1984, doi: 10.1016/0038-1101(84)90036-4.

- [15] X. Huang *et al.*, “Sub 50-nm FinFET: PMOS,” *Tech. Dig. - Int. Electron Devices Meet.*, pp. 67–70, 1999, doi: 10.1109/iedm.1999.823848.
- [16] C. P. Auth and J. D. Plummer, “Scaling theory for cylindrical, fully-depleted, surrounding-gate MOSFET’s,” *IEEE Electron Device Lett.*, vol. 18, no. 2, pp. 74–76, 1997, doi: 10.1109/55.553049.
- [17] Y. Pratap, P. Ghosh, S. Haldar, R. S. Gupta, and M. Gupta, “An analytical subthreshold current modeling of cylindrical gate all around (CGAA) MOSFET incorporating the influence of device design engineering,” *Microelectronics J.*, vol. 45, no. 4, pp. 408–415, 2014, doi: 10.1016/j.mejo.2014.01.015.
- [18] H. Takato, K. Sunouchi, N. Okabe, A. Nitayama, K. Hieda, and F. Masuoka, “Impact of Surrounding Gate Transistor (SGT) for Ultra-High-Density LSI’s,” *IEEE Trans. Electron Devices*, vol. 38, no. 3, pp. 573–578, 1991, doi: 10.1109/16.75168.
- [19] A. Motamedi, A. A. Orouji, and D. Madadi, “Physical analysis of β -Ga2O3 gate-all-around nanowire junctionless transistors: short-channel effects and temperature dependence,” *J. Comput. Electron.*, vol. 21, no. 1, pp. 197–205, 2022, doi: 10.1007/s10825-021-01837-x.
- [20] K. E. Moselund, D. Bouvet, L. Tschuor, V. Pott, P. Dainesi, and A. M. Ionescu, “Local volume inversion and corner effects in triangular gate-all-around MOSFETs,” *ESSDERC 2006 - Proc. 36th Eur. Solid-State Device Res. Conf.*, vol. 2006-Janua, pp. 359–362, 2006, doi: 10.1109/essder.2006.307712.
- [21] L. Zhang, C. Ma, J. He, X. Lin, and M. Chan, “Analytical solution of subthreshold channel potential of gate underlap cylindrical gate-all-around MOSFET,” *J. End-to-End-testing*, 2010, doi: 10.1016/j.endend.2010.06.030.
- [22] A. Kranti, S. Haldar, and R. S. Gupta, “Analytical model for threshold voltage and I-V characteristics of fully depleted short channel cylindrical/surrounding gate MOSFET,” *Microelectron. Eng.*, vol. 56, no. 3–4, pp. 241–259, 2001, doi: 10.1016/S0167-9317(00)00419-6.
- [23] A. Pal and A. Sarkar, “Analytical study of Dual Material Surrounding Gate MOSFET to suppress short-channel effects (SCEs),” *Eng. Sci. Technol. an Int. J.*, vol. 17, no. 4, pp. 205–212, 2014, doi: 10.1016/j.jestch.2014.06.002.
- [24] E. Goel, S. Kumar, K. Singh, B. Singh, M. Kumar, and S. Jit, “2-D Analytical Modeling of Threshold Voltage for Graded-Channel Dual-Material Double-Gate MOSFETs,” *IEEE Trans. Electron Devices*, vol. 63, no. 3, pp. 966–973, 2016, doi: 10.1109/TED.2016.2520096.
- [25] A. Chakraborty and A. Sarkar, “Analytical modeling and sensitivity analysis of dielectric-modulated junctionless gate stack surrounding gate MOSFET (JLGSSRG) for application as biosensor,” *J. Comput. Electron.*, vol. 16, no. 3, pp. 556–567, 2017, doi: 10.1007/s10825-017-0999-2.
- [26] R. Ramesh, “Influence of gate and channel engineering on multigate MOSFETs-A review,” *Microelectronics J.*, vol. 66, pp. 136–154, 2017, doi: 10.1016/j.mejo.2017.06.009.
- [27] K. Natori, “New solution to high-field transport in semiconductors: Ii. velocity saturation and ballistic transmission,” *Jpn. J. Appl. Phys.*, vol. 48, no. 3, p. 034504, 2009, doi: 10.1143/JJAP.48.034504.
- [28] J. P. Colinge *et al.*, “Nanowire transistors without junctions,” *Nat. Nanotechnol.*, vol. 5, no. 3, pp. 225–229, 2010, doi: 10.1038/nnano.2010.15.

- [29] J. E. Lilienfeld, "Method and apparatus for controlling electric currents," *US Pat. 1,745,175*, pp. 1–4, 1930, [Online]. Available: <http://www.google.com/patents?hl=en&lr=&vid=USPAT1745175&id=uBFMAAAAEBAJ&oi=fnd&dq=Method+and+apparatus+for+controlling+electric+currents&printsec=abstract>
- [30] "TCAD Manual, 'SILVACO ATLAS device simulation software.' p. 318, 2018."
- [31] J. Yoon, M. Shin, T. Lee, and J. W. Choi, "Highly sensitive biosensors based on biomolecules and functional nanomaterials depending on the types of nanomaterials: A perspective review," *Materials (Basel)*, vol. 13, no. 2, 2020, doi: 10.3390/ma13020299.
- [32] S. Dwivedi *et al.*, "Diseases and Molecular Diagnostics: A Step Closer to Precision Medicine," *Indian J. Clin. Biochem.*, vol. 32, no. 4, pp. 374–398, 2017, doi: 10.1007/s12291-017-0688-8.
- [33] V. Naresh and N. Lee, "A review on biosensors and recent development of nanostructured materials-enabled biosensors," *Sensors (Switzerland)*, vol. 21, no. 4, pp. 1–35, 2021, doi: 10.3390/s21041109.
- [34] S. Yadav, A. Saini, R. Devi, and S. Lata, "Transducers in Biosensors," *Biomater. Sensors Recent Adv. Appl.*, pp. 101–125, 2023, doi: 10.1007/978-981-19-8501-0_4.
- [35] N. Shafi, A. M. Bhat, J. S. Parmar, C. Sahu, and C. Periasamy, "Biologically Sensitive FETs: Holistic Design Considerations from Simulation, Modeling and Fabrication Perspectives," *Silicon*, vol. 14, no. 15, pp. 9237–9261, 2022, doi: 10.1007/s12633-022-01709-4.
- [36] N. K. Rajan, X. Duan, A. Vacic, D. A. Routenberg, and M. A. Reed, "Limits of detection for silicon nanowire BioFETs," *Device Res. Conf. - Conf. Dig. DRC*, pp. 91–92, 2012, doi: 10.1109/DRC.2012.6256954.
- [37] P. Bergveld, "Thirty years of ISFETOLOGY," *Sensors Actuators B Chem.*, vol. 88, no. 1, pp. 1–20, 2003, doi: 10.1016/s0925-4005(02)00301-5.
- [38] M. Mahdavi, A. Samaeian, M. Hajmirzaheydarali, M. Shahmohammadi, S. Mohajerzadeh, and M. A. Malboobi, "Label-free detection of DNA hybridization using a porous poly-Si ion-sensitive field effect transistor," *RSC Adv.*, vol. 4, no. 69, pp. 36854–36863, 2014, doi: 10.1039/c4ra07433e.
- [39] K. Y. Park, S. B. Choi, M. Lee, B. K. Sohn, and S. Y. Choi, "ISFET glucose sensor system with fast recovery characteristics by employing electrolysis," *Sensors Actuators, B Chem.*, vol. 83, no. 1–3, pp. 90–97, 2002, doi: 10.1016/S0925-4005(01)01049-8.
- [40] S. Caras and J. Janata, "Field effect transistor sensitive to penicillin," *Anal. Chem.*, vol. 52, no. 12, pp. 1935–1937, 1980, doi: 10.1021/ac50062a035.
- [41] A. P. Soldatkin, J. Montoriol, W. Sant, C. Martelet, and N. Jaffrezic-Renault, "A novel urea sensitive biosensor with extended dynamic range based on recombinant urease and ISFETs," *Biosens. Bioelectron.*, vol. 19, no. 2, pp. 131–135, 2003, doi: 10.1016/S0956-5663(03)00175-1.
- [42] A. Gao, N. Lu, Y. Wang, and T. Li, "Robust ultrasensitive tunneling-FET biosensor for point-of-care diagnostics," *Sci. Rep.*, vol. 6, 2016, doi: 10.1038/srep22554.
- [43] Y. Cui, Q. Wei, H. Park, and C. M. Lieber, "Nanowire nanosensors for highly

- sensitive and selective detection of biological and chemical species,” *Science* (80-.), vol. 293, no. 5533, pp. 1289–1292, 2001, doi: 10.1126/science.1062711.
- [44] E. Buitrago, G. Fagas, M. F. B. Badia, Y. M. Georgiev, M. Berthomé, and A. M. Ionescu, “Junctionless silicon nanowire transistors for the tunable operation of a highly sensitive, low power sensor,” *Sensors Actuators, B Chem.*, vol. 183, pp. 1–10, 2013, doi: 10.1016/j.snb.2013.03.028.
- [45] S. M. Biswal, B. Baral, D. De, and A. Sarkar, “Study of effect of gate-length downscaling on the analog/RF performance and linearity investigation of InAs-based nanowire Tunnel FET,” *Superlattices Microstruct.*, vol. 91, pp. 319–330, 2016, doi: 10.1016/j.spmi.2016.01.021.
- [46] B. Baral, S. M. Biswal, D. De, and A. Sarkar, “Effect of gate-length downscaling on the analog/RF and linearity performance of InAs-based nanowire tunnel FET,” *Int. J. Numer. Model. Electron. Networks, Devices Fields*, vol. 30, no. 3–4, 2017, doi: 10.1002/jnm.2186.
- [47] S. Tayal and A. Nandi, “Analog/RF performance analysis of inner gate engineered junctionless Si nanotube,” *Superlattices Microstruct.*, vol. 111, pp. 862–871, 2017, doi: 10.1016/j.spmi.2017.07.045.
- [48] S. Misra, S. M. Biswal, B. Bara, S. K. Swain, and S. K. Pati, “Study of Effect of downscaling on the Analog/RF Performance of Gate all around JLMOSFET,” *Proc. Int. Conf. 2018 IEEE Electron Device Kolkata Conf. EDKCON 2018*, pp. 234–241, 2018, doi: 10.1109/EDKCON.2018.8770424.
- [49] M. Asad *et al.*, “The Dependence of the High-Frequency Performance of Graphene Field-Effect Transistors on Channel Transport Properties,” *IEEE J. Electron Devices Soc.*, vol. 8, pp. 457–464, 2020, doi: 10.1109/JEDS.2020.2988630.
- [50] D. Krasnozhan, D. Lembke, C. Nyffeler, Y. Leblebici, and A. Kis, “MoS2 transistors operating at gigahertz frequencies,” *Nano Lett.*, vol. 14, no. 10, pp. 5905–5911, 2014, doi: 10.1021/nl5028638.
- [51] E. Kasper, “Strained silicon germanium heterostructures for device applications,” *Int. J. Mod. Phys. B*, vol. 16, no. 28–29, pp. 4189–4194, 2002, doi: 10.1142/s0217979202015054.
- [52] T. Vogelsang and K. R. Hofmann, “IIA-8 Electron Mobilities and High-Field Drift Velocities in Strained Silicon on Silicon-Germanium Substrates,” *IEEE Trans. Electron Devices*, vol. 39, no. 11, pp. 2641–2642, 1992, doi: 10.1109/16.163490.
- [53] P. Hannah Blessy, A. Shenbagavalli, and T. S. Arun Samuel, “A Comprehensive Review on the Single Gate, Double Gate, Tri-Gate, and Heterojunction Tunnel FET for Future Generation Devices,” *Silicon*, vol. 15, no. 5, pp. 2385–2405, 2023, doi: 10.1007/s12633-022-02189-2.
- [54] V. B. Sreenivasulu and V. Narendar, “Circuit Analysis and Optimization of GAA Nanowire FET Towards Low Power and High Switching,” *Silicon*, vol. 14, no. 16, pp. 10401–10411, 2022, doi: 10.1007/s12633-022-01777-6.
- [55] R. D. Kumar, M. R. Prabhu, K. L. Priya, M. Renuga, K. S. S. Kumar, and V. Vennisa, “An investigation of low power VLSI design techniques,” *J. Sci. Comput. Eng. Res.*, vol. 6, no. 4, 2023.
- [56] J. A. Del Alamo, “Nanometre-scale electronics with III-V compound

- semiconductors,” *Nature*, vol. 479, no. 7373, pp. 317–323, 2011, doi: 10.1038/nature10677.
- [57] S. Furber, “Microprocessors: The engines of the digital age,” *Proc. R. Soc. A Math. Phys. Eng. Sci.*, vol. 473, no. 2199, 2017, doi: 10.1098/rspa.2016.0893.
- [58] A. Basak, W. Banerjee, A. Singh, A. Chakraborty, and M. Chanda, “Emerging non-CMOS devices and technologies,” *Nanoelectron. Physics, Mater. Devices*, pp. 263–303, 2023, doi: 10.1016/B978-0-323-91832-9.00014-2.
- [59] U. E. Avci, R. Rios, K. J. Kuhn, and I. A. Young, “Comparison of power and performance for the TFET and MOSFET and considerations for P-TFET,” *Proc. IEEE Conf. Nanotechnol.*, pp. 869–872, 2011, doi: 10.1109/NANO.2011.6144631.
- [60] A. Sirohi, C. Sahu, and J. Singh, “Analog/RF Performance Investigation of Dopingless FET for Ultra-Low Power Applications,” *IEEE Access*, vol. 7, pp. 141810–141816, 2019, doi: 10.1109/ACCESS.2019.2937444.
- [61] S. Sharma, A. Goel, S. Rewari, V. Nath, and R. S. Gupta, “Enhanced Analog Performance and High-Frequency Applications of Dielectric Engineered High-K Schottky Nanowire FET,” *Silicon*, vol. 14, no. 15, pp. 9733–9749, 2022, doi: 10.1007/s12633-022-01663-1.
- [62] P. Goyal, G. Srivastava, J. Madan, R. Pandey, and R. S. Gupta, “Source material valuation of charge plasma based DG-TFET for RFIC applications,” *Semicond. Sci. Technol.*, vol. 37, no. 9, 2022, doi: 10.1088/1361-6641/ac7ede.
- [63] P. Ghosh, S. Haldar, R. S. Gupta, and M. Gupta, “An analytical drain current model for dual material engineered cylindrical/surrounded gate MOSFET,” *Microelectronics J.*, vol. 43, no. 1, pp. 17–24, 2012, doi: 10.1016/j.mejo.2011.10.001.
- [64] S. Rewari, V. Nath, S. Haldar, S. S. Deswal, and R. S. Gupta, “Gate-induced drain leakage reduction in cylindrical dual-metal hetero-dielectric gate all around MOSFET,” *IEEE Trans. Electron Devices*, vol. 65, no. 1, pp. 3–10, 2018, doi: 10.1109/TED.2017.2771814.
- [65] S. Rewari, S. Haldar, V. Nath, S. S. Deswal, and R. S. Gupta, “Numerical modeling of Subthreshold region of junctionless double surrounding gate MOSFET (JLDSG),” *Superlattices Microstruct.*, vol. 90, pp. 8–19, 2016, doi: 10.1016/j.spmi.2015.11.026.
- [66] J. T. Park and J. P. Colinge, “Multiple-gate SOI MOSFETs: Device design guidelines,” *IEEE Trans. Electron Devices*, vol. 49, no. 12, pp. 2222–2229, 2002, doi: 10.1109/TED.2002.805634.
- [67] J. P. Colinge, M. H. Gao, A. Romano-Rodriguez, H. Maes, and C. Claeys, “Silicon-on-insulator ‘gate-all-around device,’” *Tech. Dig. - Int. Electron Devices Meet.*, pp. 595–598, 1990, doi: 10.1109/iedm.1990.237128.
- [68] P. Kerber, Q. Zhang, S. Koswatta, and A. Bryant, “GIDL in doped and undoped FinFET devices for low-leakage applications,” *IEEE Electron Device Lett.*, vol. 34, no. 1, pp. 6–8, 2013, doi: 10.1109/LED.2012.2224089.
- [69] J. Fan, M. Li, X. Xu, Y. Yang, H. Xuan, and R. Huang, “Insight into gate-induced drain leakage in silicon nanowire transistors,” *IEEE Trans. Electron Devices*, vol. 62, no. 1, pp. 213–219, 2015, doi: 10.1109/TED.2014.2371916.
- [70] B. E. Rapp, F. J. Gruhl, and K. Länge, “Biosensors with label-free detection designed for diagnostic applications,” *Anal. Bioanal. Chem.*, vol. 398, no. 6, pp.

- 2403–2412, 2010, doi: 10.1007/s00216-010-3906-2.
- [71] N. J. Ronkainen, H. B. Halsall, and W. R. Heineman, “Electrochemical biosensors,” *Chem. Soc. Rev.*, vol. 39, no. 5, pp. 1747–1763, 2010, doi: 10.1039/b714449k.
- [72] P. Dwivedi and A. Kranti, “Overcoming Biomolecule Location-Dependent Sensitivity Degradation Through Point and Line Tunneling in Dielectric Modulated Biosensors,” *IEEE Sens. J.*, vol. 18, no. 23, pp. 9604–9611, 2018, doi: 10.1109/JSEN.2018.2872016.
- [73] M. J. Schöning and A. Poghossian, “Recent advances in biologically sensitive field-effect transistors (BioFETs),” *Analyst*, vol. 127, no. 9, pp. 1137–1151, 2002, doi: 10.1039/b204444g.
- [74] K. I. Chen, B. R. Li, and Y. T. Chen, “Silicon nanowire field-effect transistor-based biosensors for biomedical diagnosis and cellular recording investigation,” *Nano Today*, vol. 6, no. 2, pp. 131–154, 2011, doi: 10.1016/j.nantod.2011.02.001.
- [75] S. Kyu Kim, H. Cho, H. J. Park, D. Kwon, J. Min Lee, and B. Hyun Chung, “Nanogap biosensors for electrical and label-free detection of biomolecular interactions,” *Nanotechnology*, vol. 20, no. 45, 2009, doi: 10.1088/0957-4484/20/45/455502.
- [76] A. Aggarwal, S. Sharma, V. K. Chaubey, and S. Sinha, “Design and Simulation of Dielectric-Modulated Field-Effect Transistor for Biosensing Applications,” *Proc. 2019 3rd IEEE Int. Conf. Electr. Comput. Commun. Technol. ICECCT 2019*, 2019, doi: 10.1109/ICECCT.2019.8869543.
- [77] J. P. Colinge *et al.*, “Junctionless Nanowire Transistor (JNT): Properties and design guidelines,” *Solid. State. Electron.*, vol. 65–66, no. 1, pp. 33–37, 2011, doi: 10.1016/j.sse.2011.06.004.
- [78] J. H. Choi *et al.*, “Origin of device performance enhancement of junctionless accumulation-mode (JAM) bulk FinFETs with high- κ gate spacers,” *IEEE Electron Device Lett.*, vol. 35, no. 12, pp. 1182–1184, 2014, doi: 10.1109/LED.2014.2364093.
- [79] S. Rewari, V. Nath, S. Haldar, S. S. Deswal, and R. S. Gupta, “Improved analog and AC performance with increased noise immunity using nanotube junctionless field effect transistor (NJLFET),” *Appl. Phys. A Mater. Sci. Process.*, vol. 122, no. 12, 2016, doi: 10.1007/s00339-016-0583-9.
- [80] H. Yang, “Threshold Voltage Characteristics for Silicon Nanowire Field-Effect Transistor with a Double-Layer Gate Structure,” *IEEE Trans. Electron Devices*, vol. 66, no. 1, pp. 771–776, 2019, doi: 10.1109/TED.2018.2879868.
- [81] S. Kumar, Y. Singh, B. Singh, and P. K. Tiwari, “Simulation study of dielectric modulated dual channel trench gate TFET-Based biosensor,” *IEEE Sens. J.*, vol. 20, no. 21, pp. 12565–12573, 2020, doi: 10.1109/JSEN.2020.3001300.
- [82] C. W. Chen, R. Z. Lin, L. C. Chiang, F. M. Pan, and J. T. Sheu, “Junctionless gate-all-around nanowire field-effect transistors with an extended gate in biomolecule detection,” *Jpn. J. Appl. Phys.*, vol. 58, no. 2, 2019, doi: 10.7567/1347-4065/aaf46b.
- [83] A. Das, S. Rewari, B. K. Kanaujia, and R. S. Gupta, “Recent Technological Advancement in Surrounding Gate MOSFET for Biosensing Applications - a Synoptic Study,” *Silicon*, vol. 14, no. 10, pp. 5133–5143, 2022, doi:

- 10.1007/s12633-021-01288-w.
- [84] P. Kaur, A. S. Buttar, and B. Raj, "Design and Performance Analysis of Proposed Biosensor based on Double Gate Junctionless Transistor," *Silicon*, vol. 14, no. 10, pp. 5577–5584, 2022, doi: 10.1007/s12633-021-01335-6.
- [85] J. Gao *et al.*, "Poly-L-Lysine-Modified Graphene Field-Effect Transistor Biosensors for Ultrasensitive Breast Cancer miRNAs and SARS-CoV-2 RNA Detection," *Anal. Chem.*, vol. 94, no. 3, pp. 1626–1636, 2022, doi: 10.1021/acs.analchem.1c03786.
- [86] S. Yadav, A. Gedam, and S. Tirkey, "A Dielectric Modulated Biosensor for SARS-CoV-2," *IEEE Sens. J.*, vol. 21, no. 13, pp. 14483–14490, 2021, doi: 10.1109/JSEN.2020.3019036.
- [87] V. D. Wangkheirakpam, B. Bhowmick, and P. D. Pukhrambam, "Detection of SARS-CoV-2 using dielectric modulated TFET-based biosensor," *J. Mater. Sci. Mater. Electron.*, vol. 33, no. 13, pp. 10323–10334, 2022, doi: 10.1007/s10854-022-08020-3.
- [88] K. N. Priyadarshani, S. Singh, and M. K. A. Mohammed, "Gate-all-around junctionless FET based label-free dielectric/charge modulation detection of SARS-CoV-2 virus," *RSC Adv.*, vol. 12, no. 15, pp. 9202–9209, 2022, doi: 10.1039/d1ra08587e.
- [89] A. Goel, S. Rewari, S. Verma, S. S. Deswal, and R. S. Gupta, "Dielectric Modulated Junctionless Biotube FET (DM-JL-BT-FET) Bio-Sensor," *IEEE Sens. J.*, vol. 21, no. 15, pp. 16731–16743, 2021, doi: 10.1109/JSEN.2021.3077540.
- [90] P. Banerjee and J. Das, "Analytical Exploration and Simulation of Dual-Material Gate Macaroni Channel MOSFET biosensor using dielectric-modulation technique," *Micro and Nanostructures*, vol. 165, 2022, doi: 10.1016/j.micrna.2022.207196.
- [91] S. Kanungo, S. Chattopadhyay, P. S. Gupta, K. Sinha, and H. Rahaman, "Study and Analysis of the Effects of SiGe Source and Pocket-Doped Channel on Sensing Performance of Dielectrically Modulated Tunnel FET-Based Biosensors," *IEEE Trans. Electron Devices*, vol. 63, no. 6, pp. 2589–2596, 2016, doi: 10.1109/TED.2016.2556081.
- [92] M. Getnet and R. Chaujar, "Sensitivity Analysis of Biomolecule Nanocavity Immobilization in a Dielectric Modulated Triple-Hybrid Metal Gate-All-Around Junctionless NWFET Biosensor for Detecting Various Diseases," *J. Electron. Mater.*, vol. 51, no. 5, pp. 2236–2247, 2022, doi: 10.1007/s11664-022-09466-1.
- [93] L. Capua *et al.*, "Label-Free C-Reactive Protein Si Nanowire FET Sensor Arrays with Super-Nernstian Back-Gate Operation," *IEEE Trans. Electron Devices*, vol. 69, no. 4, pp. 2159–2165, 2022, doi: 10.1109/TED.2022.3144108.
- [94] "T. Holtij, M. Graef, F. Marie Hain, A. Kloes, B. Iniguez 'Compact model for short channel junctionless accumulation mode double gate MOSFETs', IEEE Trans Electron Devices 2014; 61(2):288–299".
- [95] S. Rewari, V. Nath, S. Haldar, S. S. Deswal, and R. S. Gupta, "Hafnium oxide based cylindrical junctionless double surrounding gate (CJLDSG) MOSFET for high speed, high frequency digital and analog applications," *Microsyst. Technol.*, vol. 25, no. 5, pp. 1527–1536, 2019, doi: 10.1007/s00542-017-3436-

- 3.
- [96] S. Kumar, B. Singh, and Y. Singh, "Analytical Model of Dielectric Modulated Trench Double Gate Junctionless FET for Biosensing Applications," *IEEE Sens. J.*, vol. 21, no. 7, pp. 8896–8902, 2021, doi: 10.1109/JSEN.2021.3056385.
- [97] R. Das, A. Chattopadhyay, M. Chanda, C. K. Sarkar, and C. Bose, "Analytical Modeling of Sensitivity Parameters Influenced by Practically Feasible Arrangement of Bio-Molecules in Dielectric Modulated FET Biosensor," *Silicon*, vol. 14, no. 15, pp. 9417–9430, 2022, doi: 10.1007/s12633-021-01617-z.
- [98] D. Kumar and S. Singh, "Analytical Model of Triple Metal Stack Engineered Pocket Dielectric Gate All Around (TMSEPDGAA) MOSFET for Improved Analog Applications," *Silicon*, vol. 14, no. 9, pp. 4575–4588, 2022, doi: 10.1007/s12633-021-01213-1.
- [99] Ajay, R. Narang, M. Saxena, and M. Gupta, "Modeling and simulation investigation of sensitivity of symmetric split gate junctionless fet for biosensing application," *IEEE Sens. J.*, vol. 17, no. 15, pp. 4853–4861, 2017, doi: 10.1109/JSEN.2017.2716102.
- [100] M. Chen *et al.*, "Highly sensitive, scalable, and rapid SARS-CoV-2 biosensor based on In₂O₃ nanoribbon transistors and phosphatase," *Nano Res.*, vol. 15, no. 6, pp. 5510–5516, 2022, doi: 10.1007/s12274-022-4190-0.
- [101] G. Seo *et al.*, "Rapid Detection of COVID-19 Causative Virus (SARS-CoV-2) in Human Nasopharyngeal Swab Specimens Using Field-Effect Transistor-Based Biosensor," *ACS Nano*, vol. 14, no. 4, pp. 5135–5142, 2020.
- [102] G. Thriveni and K. Ghosh, "Advancement and Challenges of Biosensing Using Field Effect Transistors," *Biosensors*, vol. 12, no. 8, 2022, doi: 10.3390/bios12080647.
- [103] A. Dixit, D. P. Samajdar, and N. Bagga, "Dielectric modulated GaAs_{1-x}Sb_x FinFET as a label-free biosensor: Device proposal and investigation," *Semicond. Sci. Technol.*, vol. 36, no. 9, 2021, doi: 10.1088/1361-6641/ac0d97.
- [104] R. Saha, Y. Hirpara, and S. Hoque, "Sensitivity Analysis on Dielectric Modulated Ge-Source DMDG TFET Based Label-Free Biosensor," *IEEE Trans. Nanotechnol.*, vol. 20, pp. 552–560, 2021, doi: 10.1109/TNANO.2021.3093927.
- [105] A. P. Michael J. Schöning, "Label-Free Biosensing, Advanced Materials, Devices and Applications," pp. 133–178, 2017.
- [106] J. M. Choi, J. W. Han, S. J. Choi, and Y. K. Choi, "Analytical modeling of a nanogap-embedded FET for application as a biosensor," *IEEE Trans. Electron Devices*, vol. 57, no. 12, pp. 3477–3484, 2010, doi: 10.1109/TED.2010.2076152.
- [107] C. H. Kim, J. H. Ahn, K. B. Lee, C. Jung, H. G. Park, and Y. K. Choi, "A new sensing metric to reduce data fluctuations in a nanogap-embedded field-effect transistor biosensor," *IEEE Trans. Electron Devices*, vol. 59, no. 10, pp. 2825–2831, 2012, doi: 10.1109/TED.2012.2209650.
- [108] A. Das, S. Rewari, B. K. Kanaujia, S. S. Deswal, and R. S. Gupta, "Physics Based Numerical Model of a Nanoscale Dielectric Modulated Step Graded Germanium Source Biotube FET Sensor: Modelling and Simulation," *Phys. Scr.*, 2023, doi: 10.1088/1402-4896/acf4c9.

- [109] K. Björkqvist and T. Arnborg, "Short Channel Effects in MOS-Transistors," *Phys. Scr.*, vol. 24, no. 2, pp. 418–421, 1981, doi: 10.1088/0031-8949/24/2/016.
- [110] Ashita, S. A. Loan, A. G. Alharbi, and M. Rafat, "Ambipolar leakage suppression in electron–hole bilayer TFET: investigation and analysis," *J. Comput. Electron.*, vol. 17, no. 3, pp. 977–985, 2018, doi: 10.1007/s10825-018-1184-y.
- [111] S. A. Loan, M. Rafat, and others, "A high-performance inverted-C tunnel junction FET with source–channel overlap pockets," *IEEE Trans. Electron Devices*, vol. 65, no. 2, pp. 763–768, 2018.
- [112] M. R. Uddin Shaikh and S. A. Loan, "Drain-Engineered TFET With Fully Suppressed Ambipolarity for High-Frequency Application," *IEEE Trans. Electron Devices*, vol. 66, no. 4, pp. 1628–1634, 2019, doi: 10.1109/TED.2019.2896674.
- [113] M. Ehteshamuddin, S. A. Loan, A. G. Alharbi, A. M. Alamoud, and M. Rafat, "Investigating a Dual MOSCAP Variant of Line-TFET with Improved Vertical Tunneling Incorporating FIQC Effect," *IEEE Trans. Electron Devices*, vol. 66, no. 11, pp. 4638–4645, 2019, doi: 10.1109/TED.2019.2942423.
- [114] M. Haris, S. A. Loan, and Mainuddin, "Si/GaAs Hetero Junction Tunnel FET: Design and Investigation," *J. Nanoelectron. Optoelectron.*, vol. 14, no. 10, pp. 1434–1444, 2019, doi: 10.1166/jno.2019.2575.
- [115] M. Ehteshamuddin, A. G. Alharbi, and S. A. Loan, "Electrostatically-Doped Hetero-Barrier Tunnel Field Effect Transistor: Design and Investigation," *IEEE Access*, vol. 6, pp. 65376–65383, 2018, doi: 10.1109/ACCESS.2018.2876771.
- [116] "Nanowires - Recent Progress," in *Nanowires - Recent Progress*, 2020. doi: 10.5772/intechopen.87902.
- [117] S. Tayal, A. K. Upadhyay, D. Kumar, and S. B. Rahi, *Emerging Low-Power Semiconductor Devices: Applications for Future Technology Nodes*. 2022. doi: 10.1201/9781003240778.
- [118] S. Nandy, S. Srivastava, S. Rewari, V. Nath, and R. S. Gupta, "Dual metal Schottky barrier asymmetric gate stack cylindrical gate all around (DM-SB-ASMGS-CGAA) MOSFET for improved analog performance for high frequency application," *Microsyst. Technol.*, vol. 28, no. 3, pp. 761–770, 2022, doi: 10.1007/s00542-019-04577-y.
- [119] "A. Das, B. K. Kanaujia, S. S. Deswal, S. Rewari and R. S. Gupta, 'Doping induced threshold voltage and ION/IOFF ratio modulation in surrounding gate MOSFET for analog applications,' 2022 IEEE International Conference of Electron Devices Society Kolkata Ch."
- [120] A. Das, S. Rewari, B. K. Kanaujia, S. S. Deswal, and R. S. Gupta, "Ge/Si interfaced label free nanowire BIOFET for biomolecules detection - analytical analysis," *Microelectronics J.*, vol. 138, 2023, doi: 10.1016/j.mejo.2023.105832.
- [121] A. Das, S. Rewari, B. K. Kanaujia, S. S. Deswal, and R. S. Gupta, "Analytical modeling and doping optimization for enhanced analog performance in a Ge/Si interfaced nanowire MOSFET," *Phys. Scr.*, vol. 98, no. 7, 2023, doi: 10.1088/1402-4896/acde16.
- [122] G. Dhiman, "Investigation of Junction - less Double Gate MOSFET With High - k Gate - oxide and Metal Gate Layers," *Int. J. Innov. Res. Sci. Eng. Technol.*,

- vol. 8, no. 6S3, pp. 289–292, 2019.
- [123] C. S. H. Rani, R. S. Roach, T. S. A. Samuel, and S. E. Lawrence, “Performance Analysis of Heterojunction and Hetero Dielectric Triple Material Double Gate TFET,” *Silicon*, vol. 14, no. 11, pp. 5827–5834, 2022, doi: 10.1007/s12633-021-01355-2.
- [124] A. Das, B. K. Kanaujia, V. Nath, S. Rewari, and R. S. Gupta, “Impact of Reverse Gate Oxide Stacking on Gate All around Tunnel FET for High Frequency Analog and RF Applications,” *2020 IEEE 17th India Counc. Int. Conf. INDICON 2020*, 2020, doi: 10.1109/INDICON49873.2020.9342175.
- [125] C. A. Vu and W. Y. Chen, “Field-effect transistor biosensors for biomedical applications: Recent advances and future prospects,” *Sensors (Switzerland)*, vol. 19, no. 19, 2019, doi: 10.3390/s19194214.
- [126] Y. Pratap, M. Kumar, S. Kabra, S. Haldar, R. S. Gupta, and M. Gupta, “Analytical modeling of gate-all-around junctionless transistor based biosensors for detection of neutral biomolecule species,” *J. Comput. Electron.*, vol. 17, no. 1, pp. 288–296, 2018, doi: 10.1007/s10825-017-1041-4.
- [127] N. Bagga, S. Sarkhel, and S. K. Sarkar, “Recent research trends in gate engineered tunnel FET for improved current behavior by subduing the ambipolar effects: A review,” *Int. Conf. Comput. Commun. Autom. ICCCA 2015*, pp. 1264–1267, 2015, doi: 10.1109/CCAA.2015.7148569.
- [128] R. Ghosh, A. Karmakar, and P. Saha, “Investigation of gate-engineered heterostructure tunnel field effect transistor as a label-free biosensor: a compact study,” *Appl. Phys. A Mater. Sci. Process.*, vol. 129, no. 2, 2023, doi: 10.1007/s00339-023-06393-8.
- [129] Ashima, D. Vaithyanathan, and B. Raj, “Performance Analysis of Channel and Inner Gate Engineered GAA Nanowire FET,” *Silicon*, vol. 13, no. 6, pp. 1863–1869, 2021, doi: 10.1007/s12633-020-00575-2.
- [130] T. Joshi, Y. Singh, and B. Singh, “Dual-channel trench-gate tunnel FET for improved ON-current and subthreshold swing,” *Electron. Lett.*, vol. 55, no. 21, pp. 1152–1155, 2019, doi: 10.1049/el.2019.2219.
- [131] H. Im, X. J. Huang, B. Gu, and Y. K. Choi, “A dielectric-modulated field-effect transistor for biosensing,” *Nat. Nanotechnol.*, vol. 2, no. 7, pp. 430–434, 2007, doi: 10.1038/nnano.2007.180.
- [132] B. Gu, T. J. Park, J. H. Ahn, X. J. Huang, S. Y. Lee, and Y. K. Choi, “Nanogap field-effect transistor biosensors for electrical detection of avian influenza,” *Small*, vol. 5, no. 21, pp. 2407–2412, 2009, doi: 10.1002/sml.200900450.
- [133] S. Kanungo, S. Chattopadhyay, K. Sinha, P. S. Gupta, and H. Rahaman, “A Device Simulation-Based Investigation on Dielectrically Modulated Fringing Field-Effect Transistor for Biosensing Applications,” *IEEE Sens. J.*, vol. 17, no. 5, pp. 1399–1406, 2017, doi: 10.1109/JSEN.2016.2633621.
- [134] A. Goel, S. Rewari, S. Verma, and R. S. Gupta, “Dielectric Modulated Triple Metal Gate All around MOSFET (TMGAA) for DNA Bio-Molecule Detection,” *Proc. Int. Conf. 2018 IEEE Electron Device Kolkata Conf. EDKCON 2018*, pp. 337–340, 2018, doi: 10.1109/EDKCON.2018.8770406.
- [135] A. Goel, S. Rewari, S. Verma, and R. S. Gupta, “Modeling of shallow extension engineered dual metal surrounding gate (SEE-DM-SG) MOSFET gate-induced drain leakage (GIDL),” *Indian J. Phys.*, vol. 95, no. 2, pp. 299–308, 2021, doi:

- 10.1007/s12648-020-01704-8.
- [136] A. Gnudi, S. Reggiani, E. Gnani, and G. Baccarani, “Analysis of threshold voltage variability due to random dopant fluctuations in junctionless FETs,” *IEEE Electron Device Lett.*, vol. 33, no. 3, pp. 336–338, 2012, doi: 10.1109/LED.2011.2181153.
- [137] S. Gupta, N. Pandey, and R. S. Gupta, “Investigation of Dual-Material Double Gate Junctionless Accumulation-Mode Cylindrical Gate All around (DMDG-JLAM-CGAA) MOSFET with High-k Gate Stack for low Power Digital Applications,” *2020 IEEE 17th India Counc. Int. Conf. INDICON 2020*, 2020, doi: 10.1109/INDICON49873.2020.9342380.
- [138] B. J. Baliga *et al.*, “First Demonstration of Junctionless Accumulation-Mode Bulk FinFETs With Robust Junction Isolation,” *IEEE Trans. Electr. Dev.*, vol. 13, no. 8, pp. 1479–1481, 1992.
- [139] B. Kumar and R. Chaujar, “Analog and RF Performance Evaluation of Junctionless Accumulation Mode (JAM) Gate Stack Gate All Around (GS-GAA) FinFET,” *Silicon*, vol. 13, no. 3, pp. 919–927, 2021, doi: 10.1007/s12633-020-00910-7.
- [140] A. Goel, S. Rewari, S. Verma, and R. S. Gupta, “Physics-based analytic modeling and simulation of gate-induced drain leakage and linearity assessment in dual-metal junctionless accumulation nano-tube FET (DM-JAM-TFET),” *Appl. Phys. A Mater. Sci. Process.*, vol. 126, no. 5, 2020, doi: 10.1007/s00339-020-03520-7.
- [141] S. Yadav and S. Rewari, “Analytical modeling and numerical simulation of graded JAM Split Gate-All-Around (GJAM-SGAA) Bio-FET for label free Avian Influenza antibody and DNA detection,” *Microelectronics J.*, vol. 142, p. 106011, 2023, doi: 10.1016/j.mejo.2023.106011.
- [142] A. Kaur, R. Mehra, and A. Saini, “Hetero-Dielectric oxide engineering on dopingless gate all around nanowire MOSFET with Schottky contact source/drain,” *AEU - Int. J. Electron. Commun.*, vol. 111, 2019, doi: 10.1016/j.aeue.2019.152888.
- [143] A. Gupta *et al.*, “A Novel Approach to Investigate the Impact of Hetero-High-K Gate Stack on SiGe Junctionless Gate-All-Around (JL-GAA) MOSFET,” *Silicon*, vol. 14, no. 3, pp. 1005–1012, 2022, doi: 10.1007/s12633-020-00860-0.
- [144] M. S. Narula and A. Pandey, “Performance Evaluation of Stacked Gate Oxide/High K Spacers Based Gate All Around Device Architectures at 10 nm Technology Node,” *Silicon*, vol. 14, no. 5, pp. 2397–2407, 2022, doi: 10.1007/s12633-022-01685-9.
- [145] Donggun Park *et al.*, “SiON/Ta/sub 2/O/sub 5//TiN gate-stack transistor with 1.8 nm equivalent SiO/sub 2/ thickness,” 2002, pp. 381–384. doi: 10.1109/iedm.1998.746379.
- [146] S. Yadav and S. Rewari, “Trench Gate JAM Dielectric Modulated Nanowire FET (TG-JAM-DM-NWFET) Biosensor,” *Proc. 2022 IEEE Int. Conf. Electron Devices Soc. Kolkata Chapter, EDKCON 2022*, pp. 23–28, 2022, doi: 10.1109/EDKCON56221.2022.10032912.
- [147] J. Korec and C. Bull, “History of FET Technology and the Move to NexFET TM,” *Mosfet*, no. May, pp. 44–6, 2009, [Online]. Available:

- www.Bodospower.com
- [148] J. Na, J. Cheon, and K. Kim, “4H-Sic Double Trench Mosfet With Split Heterojunction Gate for Improving Switching Characteristics,” *Materials (Basel)*, vol. 14, no. 13, 2021, doi: 10.3390/ma14133554.
- [149] C. Chong, H. Liu, S. Du, S. Wang, and H. Zhang, “Study on the Simulation of Biosensors Based on Stacked Source Trench Gate TFET,” *Nanomaterials*, vol. 13, no. 3, 2023, doi: 10.3390/nano13030531.
- [150] E. Leobandung, J. Gu, L. Guo, and S. Y. Chou, “Wire-channel and wrap-around-gate metal–oxide–semiconductor field-effect transistors with a significant reduction of short channel effects,” *J. Vac. Sci. Technol. B Microelectron. Nanom. Struct. Process. Meas. Phenom.*, vol. 15, no. 6, pp. 2791–2794, 1997, doi: 10.1116/1.589729.
- [151] “ATLAS User’s Manual: 3-D Device Simulator, SILVACO International, Version5.14.0.R, 2018.”
- [152] S. J. Choi, D. Il Moon, S. Kim, J. P. Duarte, and Y. K. Choi, “Sensitivity of threshold voltage to nanowire width variation in junctionless transistors,” *IEEE Electron Device Lett.*, vol. 32, no. 2, pp. 125–127, 2011, doi: 10.1109/LED.2010.2093506.
- [153] S. Yadav and S. Rewari, “Numerical Simulation of Hetero Dielectric Trench Gate JAM Gate-All-Around FET (HDTG-JAM-GAAFET) for Label Free Biosensing Applications,” *ECS J. Solid State Sci. Technol.*, vol. 12, no. 12, p. 127008, 2023, doi: 10.1149/2162-8777/ad161f.
- [154] A. S. Hoffman and J. A. Hubbell, “Surface-Immobilized Biomolecules,” *Biomater. Sci. An Introd. to Mater. Third Ed.*, pp. 339–349, 2013, doi: 10.1016/B978-0-08-087780-8.00032-2.
- [155] M. Asal, Ö. Özen, M. Şahinler, H. T. Baysal, and İ. Polatoğlu, “An overview of biomolecules, immobilization methods and support materials of biosensors,” *Sens. Rev.*, vol. 39, no. 3, pp. 377–386, 2019, doi: 10.1108/SR-04-2018-0084.
- [156] B. Prieto-Simon, M. Campas, and J.-L. Marty, “Biomolecule Immobilization in Biosensor Development: Tailored Strategies Based on Affinity Interactions,” *Protein Pept. Lett.*, vol. 15, no. 8, pp. 757–763, 2008, doi: 10.2174/092986608785203791.
- [157] S. Rashid, F. Bashir, F. A. Khanday, and M. R. Beigh, “Dielectrically Modulated III-V Compound Semiconductor based Pocket doped Tunnel FET for Label Free Biosensing Applications,” *IEEE Trans. Nanobioscience*, 2022, doi: 10.1109/TNB.2022.3178763.
- [158] C. Li, F. Liu, R. Han, and Y. Zhuang, “A Vertically Stacked Nanosheet Gate-All-Around FET for Biosensing Application,” *IEEE Access*, vol. 9, pp. 63602–63610, 2021, doi: 10.1109/ACCESS.2021.3074906.
- [159] S. Yadav and S. Rewari, “Dual metal dual layer GAA NW–FET (DMDL–GAA–NW–FET) biosensor for label free SARS-CoV-2 detection,” *Microsyst. Technol.*, 2023, doi: 10.1007/s00542-023-05560-4.
- [160] A. Das, S. Rewari, B. K. Kanaujia, S. S. Deswal, and R. S. Gupta, “Analytical investigation of a triple surrounding gate germanium source metal–oxide–semiconductor field-effect transistor with step graded channel for biosensing applications,” *Int. J. Numer. Model. Electron. Networks, Devices Fields*, 2023, doi: 10.1002/jnm.3106.

- [161] K. Han, Y. Zhang, and Z. Deng, "A simulation study of gate-all-around nanowire transistor with a core-substrate," *IEEE Access*, vol. 8, pp. 62181–62190, 2020, doi: 10.1109/ACCESS.2020.2983724.
- [162] S. Ye, K. Yamabe, and T. Endoh, "Ultimate vertical gate-all-around metal–oxide–semiconductor field-effect transistor and its three-dimensional integrated circuits," *Mater. Sci. Semicond. Process.*, vol. 134, 2021, doi: 10.1016/j.mssp.2021.106046.
- [163] F. Bibi, M. Villain, C. Guillaume, B. Sorli, and N. Gontard, "A review: Origins of the dielectric properties of proteins and potential development as biosensors," *Sensors (Switzerland)*, vol. 16, no. 8, 2016, doi: 10.3390/s16081232.
- [164] V. B. Sreenivasulu and V. Narendar, "Junctionless Gate-all-around Nanowire FET with Asymmetric Spacer for Continued Scaling," *Silicon*, vol. 14, no. 13, pp. 7461–7471, 2022, doi: 10.1007/s12633-021-01471-z.
- [165] Ashima, V. Dhandapani, and B. Raj, "Design and Performance Assessment of Graded Channel Gate-All-Around Silicon Nanowire FET for Biosensing Applications," *Silicon*, 2023, doi: 10.1007/s12633-022-02272-8.
- [166] A. Bafekry, B. Akgenc, M. Ghergherehchi, and F. M. Peeters, "Strain and electric field tuning of semi-metallic character WCrCO₂MXenes with dual narrow band gap," *J. Phys. Condens. Matter*, vol. 32, no. 35, 2020, doi: 10.1088/1361-648X/ab8e88.
- [167] R. Gautam, M. Saxena, R. S. Gupta, and M. Gupta, "Numerical model of gate-all-around MOSFET with vacuum gate dielectric for biomolecule detection," *IEEE Electron Device Lett.*, vol. 33, no. 12, pp. 1756–1758, 2012, doi: 10.1109/LED.2012.2216247.
- [168] R. Das, M. Chanda, and C. K. Sarkar, "Analytical Modeling of Charge Plasma-Based Optimized Nanogap Embedded Surrounding Gate MOSFET for Label-Free Biosensing," *IEEE Trans. Electron Devices*, vol. 65, no. 12, pp. 5487–5493, 2018, doi: 10.1109/TED.2018.2872466.
- [169] A. Ortiz-Conde, F. J. García-Sánchez, J. Muci, A. Terán Barrios, J. J. Liou, and C. S. Ho, "Revisiting MOSFET threshold voltage extraction methods," *Microelectron. Reliab.*, vol. 53, no. 1, pp. 90–104, 2013, doi: 10.1016/j.microrel.2012.09.015.
- [170] Ajay, R. Narang, M. Saxena, and M. Gupta, "Investigation of dielectric modulated (DM) double gate (DG) junctionless MOSFETs for application as a biosensors," *Superlattices Microstruct.*, vol. 85, pp. 557–572, 2015, doi: 10.1016/j.spmi.2015.04.040.
- [171] P. Dwivedi and A. Kranti, "Applicability of Transconductance-to-Current Ratio (gm/Ids) as a Sensing Metric for Tunnel FET Biosensors," *IEEE Sens. J.*, vol. 17, no. 4, pp. 1030–1036, 2017, doi: 10.1109/JSEN.2016.2640192.
- [172] N. Thapa and L. Maurya, "Performance advancement of High-K dielectric MOSFET," *Int. J. Innov. Adv. Comput. Sci.*, vol. 3, no. 3, pp. 98–103, 2014.
- [173] R. Singh, S. Kaim, R. MedhaShree, A. Kumar, and S. Kale, "Dielectric Engineered Schottky Barrier MOSFET for Biosensor Applications: Proposal and Investigation," *Silicon*, vol. 14, no. 8, pp. 4053–4062, 2022, doi: 10.1007/s12633-021-01191-4.
- [174] S. Kanungo, S. Chattopadhyay, P. S. Gupta, and H. Rahaman, "Comparative performance analysis of the dielectrically modulated full- gate and short-gate

- tunnel FET-based biosensors,” *IEEE Trans. Electron Devices*, vol. 62, no. 3, pp. 994–1001, 2015, doi: 10.1109/TED.2015.2390774.
- [175] G. Wadhwa and B. Raj, “Design, Simulation and Performance Analysis of JLTFET Biosensor for High Sensitivity,” *IEEE Trans. Nanotechnol.*, vol. 18, pp. 567–574, 2019, doi: 10.1109/TNANO.2019.2918192.
- [176] B. Buvaneshwari and N. B. Balamurugan, “2D analytical modeling and simulation of dual material DG MOSFET for biosensing application,” *AEU - Int. J. Electron. Commun.*, vol. 99, pp. 193–200, 2019, doi: 10.1016/j.aeue.2018.11.039.
- [177] A. Gedam, B. Acharya, and G. P. Mishra, “Design and Performance Assessment of Dielectrically Modulated Nanotube TFET Biosensor,” *IEEE Sens. J.*, vol. 21, no. 15, pp. 16761–16769, 2021, doi: 10.1109/JSEN.2021.3080922.
- [178] D. Sharma, D. Singh, S. Pandey, S. Yadav, and P. N. Kondekar, “Comparative analysis of full-gate and short-gate dielectric modulated electrically doped Tunnel-FET based biosensors,” *Superlattices Microstruct.*, vol. 111, pp. 767–775, 2017, doi: 10.1016/j.spmi.2017.07.035.
- [179] A. Chakraborty, D. Singha, and A. Sarkar, “Staggered heterojunctions-based tunnel-FET for application as a label-free biosensor,” *Int. J. Nanoparticles*, vol. 10, no. 1–2, pp. 107–116, 2018, doi: 10.1504/IJNP.2018.092681.
- [180] P. Venkatesh, K. Nigam, S. Pandey, D. Sharma, and P. N. Kondekar, “A dielectrically modulated electrically doped tunnel FET for application of label free biosensor,” *Superlattices Microstruct.*, vol. 109, pp. 470–479, 2017, doi: 10.1016/j.spmi.2017.05.035.
- [181] A. Das, S. Rewari, B. K. Kanaujia, S. S. Deswal, and R. S. Gupta, “Numerical modeling of a dielectric modulated surrounding-triple-gate germanium-source MOSFET (DM-STGGS-MOSFET)-based biosensor,” *J. Comput. Electron.*, vol. 22, no. 2, pp. 742–759, 2023, doi: 10.1007/s10825-023-02008-w.
- [182] S. A. Hafiz, I. Ishaq, M. Ehteshamuddin, and S. A. Loan, “Dielectrically Modulated Source-Engineered Charge-Plasma-Based Schottky-FET as a Label-Free Biosensor,” *IEEE Trans. Electron Devices*, vol. 66, no. 4, pp. 1905–1910, 2019, doi: 10.1109/TED.2019.2896695.
- [183] S. Rashid, F. Bashir, F. A. Khanday, and M. R. Beigh, “L-Shaped High Performance Schottky Barrier FET as Dielectrically Modulated Label Free Biosensor,” *IEEE Trans. Nanobioscience*, vol. 21, no. 4, pp. 542–548, 2022, doi: 10.1109/TNB.2021.3131372.
- [184] P. Dwivedi, R. Singh, B. S. Sengar, A. Kumar, and V. Garg, “A New Simulation Approach of Transient Response to Enhance the Selectivity and Sensitivity in Tunneling Field Effect Transistor-Based Biosensor,” *IEEE Sens. J.*, vol. 21, no. 3, pp. 3201–3209, 2021, doi: 10.1109/JSEN.2020.3028153.
- [185] A. Kumar and S. Kale, “A Comparative Analysis of Cavity Positions in Charge Plasma based Tunnel FET for Biosensor Application,” *IETE J. Res.*, 2023, doi: 10.1080/03772063.2023.2189631.
- [186] M. M. N. Nuzaihan *et al.*, “Electrical detection of dengue virus (DENV) DNA oligomer using silicon nanowire biosensor with novel molecular gate control,” *Biosens. Bioelectron.*, vol. 83, pp. 106–114, 2016, doi: 10.1016/j.bios.2016.04.033.
- [187] M. F. M. Fathil *et al.*, “The impact of different channel doping concentrations

- on the performance of polycrystalline silicon nanowire field-effect transistor biosensor,” *AIP Conf. Proc.*, vol. 2045, 2018, doi: 10.1063/1.5080819.
- [188] B. E.B. and S. M.K., “Applications of commercial biosensors in clinical, food, environmental, and biothreat/biowarfare analyses,” *Anal. Biochem.*, vol. 478, pp. 107–120, 2015, [Online]. Available: <http://www.embase.com/search/results?subaction=viewrecord&from=export&id=L603629295%5Cnhttp://dx.doi.org/10.1016/j.ab.2015.03.011%5Cnhttp://sfx.library.uu.nl/utrecht?sid=EMBASE&issn=10960309&id=doi:10.1016%2Fj.ab.2015.03.011&atitle=Applications+of+commerc>
- [189] M. N. Velasco-Garcia and T. Mottram, “Biosensor technology addressing agricultural problems,” *Biosyst. Eng.*, vol. 84, no. 1, pp. 1–12, 2003, doi: 10.1016/S1537-5110(02)00236-2.
- [190] S. Neethirajan, V. Ragavan, X. Weng, and R. Chand, “Biosensors for sustainable food engineering: Challenges and perspectives,” *Biosensors*, vol. 8, no. 1, 2018, doi: 10.3390/bios8010023.
- [191] G. J. Zhang and Y. Ning, “Silicon nanowire biosensor and its applications in disease diagnostics: A review,” *Anal. Chim. Acta*, vol. 749, pp. 1–15, 2012, doi: 10.1016/j.aca.2012.08.035.
- [192] A. Gao *et al.*, “Multiplexed detection of lung cancer biomarkers in patients serum with CMOS-compatible silicon nanowire arrays,” *Biosens. Bioelectron.*, vol. 91, pp. 482–488, 2017, doi: 10.1016/j.bios.2016.12.072.
- [193] N. Lu *et al.*, “Ultrasensitive Detection of Dual Cancer Biomarkers with Integrated CMOS-Compatible Nanowire Arrays,” *Anal. Chem.*, vol. 87, no. 22, pp. 11203–11208, 2015, doi: 10.1021/acs.analchem.5b01729.
- [194] H. C. Lau, T. E. Bae, H. J. Jang, J. Y. Kwon, W. J. Cho, and J. O. Lim, “Saliva-based screening approach for Alzheimer’s disease via the cell-oriented ion-sensitive field-effect transistor,” *Sens. Lett.*, vol. 12, no. 6–7, pp. 1096–1101, 2014, doi: 10.1166/sl.2014.3200.
- [195] V. M. Generalov *et al.*, “Detection of Ebola Virus VP40 Protein using a Nanowire SOI Biosensor,” *Optoelectron. Instrum. Data Process.*, vol. 55, no. 6, pp. 618–622, 2019, doi: 10.3103/S875669901906013X.
- [196] I. Fahmi, “World Health Organization Coronavirus Disease 2019 (Covid-19) Situation Report,” *DroneEmprit*, vol. 2019, no. March, pp. 1–19, 2020, [Online]. Available: <https://pers.droneemprit.id/covid19/>
- [197] P. Fathi-Hafshejani *et al.*, “Two-Dimensional-Material-Based Field-Effect Transistor Biosensor for Detecting COVID-19 Virus (SARS-CoV-2),” *ACS Nano*, vol. 15, no. 7, pp. 11461–11469, 2021, doi: 10.1021/acsnano.1c01188.
- [198] M. Barbaro, A. Bonfiglio, and L. Raffo, “A charge-modulated FET for detection of biomolecular processes: Conception, modeling, and simulation,” *IEEE Trans. Electron Devices*, vol. 53, no. 1, pp. 158–166, 2006, doi: 10.1109/TED.2005.860659.
- [199] I. Sarangadharan *et al.*, “Review—High Field Modulated FET Biosensors for Biomedical Applications,” *ECS J. Solid State Sci. Technol.*, vol. 7, no. 7, pp. Q3032–Q3042, 2018, doi: 10.1149/2.0061807jss.
- [200] Z. Li, Z. Li, Y. Chen, Y. Chen, X. Li, and X. Li, “Sequence-specific label-free DNA sensors based on silicon nanowires,” *Nano Lett.*, vol. 4, no. 2, pp. 245–247, 2004.

- [201] D. Nagy, G. Espineira, G. Indalecio, A. J. Garcia-Loureiro, K. Kalna, and N. Seoane, "Benchmarking of FinFET, Nanosheet, and Nanowire FET Architectures for Future Technology Nodes," *IEEE Access*, vol. 8, pp. 53196–53202, 2020, doi: 10.1109/ACCESS.2020.2980925.
- [202] D. Nagy, G. Indalecio, A. J. Garcia-Loureiro, M. A. Elmessary, K. Kalna, and N. Seoane, "FinFET versus gate-all-around nanowire FET: Performance, scaling, and variability," *IEEE J. Electron Devices Soc.*, vol. 6, no. 1, pp. 332–340, 2018, doi: 10.1109/JEDS.2018.2804383.
- [203] T. K. Kim *et al.*, "First demonstration of junctionless accumulation-mode bulk FinFETs with robust junction isolation," *IEEE Electron Device Lett.*, vol. 34, no. 12, pp. 1479–1481, 2013, doi: 10.1109/LED.2013.2283291.
- [204] K. Long, W. Ou, H. Kuo, JM & Chin, "Dual-Material Gate (DMG) Field Effect Transistor," *IEEE Trans. Electron Devices*, vol. 46, no. 5, pp. 865–870, 1999.
- [205] E. G. Marin, F. G. Ruiz, A. Godoy, I. M. Tienda-Luna, C. Martinez-Blanque, and F. Gamiz, "Impact of the back-gate biasing on trigate MOSFET electron mobility," *IEEE Trans. Electron Devices*, vol. 62, no. 1, pp. 224–227, 2015, doi: 10.1109/TED.2014.2367574.
- [206] M. Najmzadeh, D. Bouvet, W. Grabinski, J. M. Sallese, and A. M. Ionescu, "Accumulation-mode gate-all-around si nanowire nMOSFETs with sub-5 nm cross-section and high uniaxial tensile strain," *Solid. State. Electron.*, vol. 74, pp. 114–120, 2012, doi: 10.1016/j.sse.2012.04.021.
- [207] N. Trivedi, M. Kumar, S. Haldar, S. S. Deswal, M. Gupta, and R. S. Gupta, "Analytical modeling of Junctionless Accumulation Mode Cylindrical Surrounding Gate MOSFET (JAM-CSG)," *Int. J. Numer. Model. Electron. Networks, Devices Fields*, vol. 29, no. 6, pp. 1036–1043, 2016, doi: 10.1002/jnm.2162.
- [208] B. Singh, D. Gola, K. Singh, E. Goel, S. Kumar, and S. Jit, "2-D analytical threshold voltage model for dielectric pocket double-gate junctionless FETs by considering source/drain depletion effect," *IEEE Trans. Electron Devices*, vol. 64, no. 3, pp. 901–908, 2017, doi: 10.1109/TED.2016.2646460.
- [209] P. Ambhorkar *et al.*, "Nanowire-based biosensors: From growth to applications," *Micromachines*, vol. 9, no. 12, 2018, doi: 10.3390/mi9120679.
- [210] X. T. Vu, J. F. Eschermann, R. Stockmann, R. Ghoshmoulick, A. Offenhäusser, and S. Ingebrandt, "Top-down processed silicon nanowire transistor arrays for biosensing," *Phys. Status Solidi Appl. Mater. Sci.*, vol. 206, no. 3, pp. 426–434, 2009, doi: 10.1002/pssa.200880475.
- [211] N. Gupta and R. Chaujar, "Optimization of high-k and gate metal workfunction for improved analog and intermodulation performance of Gate Stack (GS)-GEWE-SiNW MOSFET," *Superlattices Microstruct.*, vol. 97, pp. 630–641, 2016, doi: 10.1016/j.spmi.2016.07.021.
- [212] A. Kumar, D. Kaur, M. M. Tripathi, and R. Chaujar, "Reliability of high-k gate stack on transparent gate recessed channel (TGRC) MOSFET," *2017 Int. Conf. Microelectron. Devices, Circuits Syst. ICMDCS 2017*, vol. 2017-Janua, pp. 1–4, 2017, doi: 10.1109/ICMDCS.2017.8211533.
- [213] W. V. Devi, B. Bhowmick, and P. D. Pukhrambam, "N+ pocket-doped vertical TFET for enhanced sensitivity in biosensing applications: Modeling and simulation," *IEEE Trans. Electron Devices*, vol. 67, no. 5, pp. 2133–2139,

- 2020, doi: 10.1109/TED.2020.2981303.
- [214] D. E. Stallknecht, E. Nagy, D. B. Hunter, and R. D. Slemons, *Avian Influenza*. 2008. doi: 10.1002/9780470344668.ch5.
- [215] A. Poghosian, A. Cherstvy, S. Ingebrandt, A. Offenhäusser, and M. J. Schöning, “Possibilities and limitations of label-free detection of DNA hybridization with field-effect-based devices,” *Sensors Actuators, B Chem.*, vol. 111–112, no. SUPPL., pp. 470–480, 2005, doi: 10.1016/j.snb.2005.03.083.
- [216] C. H. Kim, C. Jung, K. B. Lee, H. G. Park, and Y. K. Choi, “Label-free DNA detection with a nanogap embedded complementary metal oxide semiconductor,” *Nanotechnology*, vol. 22, no. 13, 2011, doi: 10.1088/0957-4484/22/13/135502.
- [217] M. A. Abdi, F. Djeflal, Z. Dibi, and D. Arar, “A two-dimensional analytical subthreshold behavior analysis including hot-carrier effect for nanoscale gate stack gate all around (GASGAA) MOSFETs,” *J. Comput. Electron.*, vol. 10, no. 1–2, pp. 179–185, 2011, doi: 10.1007/s10825-010-0329-4.
- [218] A. S. Verhulst, B. Sorée, D. Leonelli, W. G. Vandenberghe, and G. Groeseneken, “Modeling the single-gate, double-gate, and gate-all-around tunnel field-effect transistor,” *J. Appl. Phys.*, vol. 107, no. 2, 2010, doi: 10.1063/1.3277044.
- [219] N. Kannan and M. J. Kumar, “Charge-Modulated Underlap I-MOS Transistor as a Label-Free Biosensor: A Simulation Study,” *IEEE Trans. Electron Devices*, vol. 62, no. 8, pp. 2645–2651, 2015, doi: 10.1109/TED.2015.2446612.
- [220] M. Chanda, R. Das, A. Kundu, and C. K. Sarkar, “Analytical modeling of label free biosensor using charge plasma based gate underlap dielectric modulated MOSFET,” *Superlattices Microstruct.*, vol. 104, pp. 451–460, 2017, doi: 10.1016/j.spmi.2017.03.010.
- [221] P. Kumar and B. Raj, “Design and simulation of junctionless nanowire tunnel field effect transistor for highly sensitive biosensor,” *Microelectronics J.*, vol. 137, 2023, doi: 10.1016/j.mejo.2023.105826.
- [222] K. Baruah and S. Baishya, “Numerical assessment of dielectrically-modulated short- double-gate PNP TFET-based label-free biosensor,” *Microelectronics J.*, vol. 133, p. 105717, 2023, doi: 10.1016/j.mejo.2023.105717.
- [223] D. Luo, C. Li, Y. qi Wang, O. wen Li, F. yu Kuang, and H. long You, “A novel inverted T-shaped negative capacitance TFET for label-free biosensing application,” *Microelectronics J.*, vol. 139, 2023, doi: 10.1016/j.mejo.2023.105886.
- [224] A. Mangla, R. Saha, and R. Goswami, “Impact on performance of dual stack hetero- gated dielectric modulated TFET biosensor due to Si_{1-x}G_x pocket variation,” *Microelectronics J.*, vol. 129, 2022, doi: 10.1016/j.mejo.2022.105603.
- [225] S. K. Swain, S. Singh, and S. K. Sharma, “Performance analysis of dielectrically modulated InSb/Si TFET based label free biosensor,” *Microelectronics J.*, vol. 129, 2022, doi: 10.1016/j.mejo.2022.105607.
- [226] K. W. Lee *et al.*, “An underlap field-effect transistor for electrical detection of influenza,” *Appl. Phys. Lett.*, vol. 96, no. 3, 2010, doi: 10.1063/1.3291617.
- [227] K. N. Singh and P. K. Dutta, “Analytical modeling of a high-K underlap dielectric- and charge-modulated silicon-on-nothing FET-based biosensor,” *J.*

- Comput. Electron.*, vol. 19, no. 3, pp. 1126–1135, 2020, doi: 10.1007/s10825-020-01511-8.
- [228] Y. Pratap, S. Haldar, R. S. Gupta, and M. Gupta, “Localized Charge-Dependent Threshold Voltage Analysis of Gate-Material-Engineered Junctionless Nanowire Transistor,” *IEEE Trans. Electron Devices*, vol. 62, no. 8, pp. 2598–2605, 2015, doi: 10.1109/TED.2015.2441777.
- [229] A. Das, S. Rewari, B. K. Kanaujia, S. S. Deswal, and R. S. Gupta, “Numerical modeling of a dielectric modulated surrounding-triple-gate germanium-source MOSFET (DM-STGGS-MOSFET)-based biosensor,” *J. Comput. Electron.*, 2023, doi: 10.1007/s10825-023-02008-w.
- [230] G. M. Paolucci, A. S. Spinelli, C. Monzio Compagnoni, and P. Tessariol, “A Semi-Analytical Model for Macaroni MOSFETs With Application to Vertical Flash Memories,” *IEEE Trans. Electron Devices*, vol. 63, no. 5, pp. 1871–1876, 2016, doi: 10.1109/TED.2016.2543605.
- [231] A. Das, S. Rewari, B. K. Kanaujia, S. S. Deswal, and R. S. Gupta, “Analytical investigation of a triple surrounding gate germanium source metal–oxide–semiconductor field-effect transistor with step graded channel for biosensing applications,” *Int. J. Numer. Model. Electron. Networks, Devices Fields*, 2023, doi: 10.1002/jnm.3106.
- [232] V. Narendar and K. A. Girdhardas, “Surface Potential Modeling of Graded-Channel Gate-Stack (GCGS) High-K Dielectric Dual-Material Double-Gate (DMDG) MOSFET and Analog/RF Performance Study,” *Silicon*, vol. 10, no. 6, pp. 2865–2875, 2018, doi: 10.1007/s12633-018-9826-z.
- [233] D. Chowdhury, B. P. De, S. K. Maity, N. K. Singh, R. Kar, and D. Mandal, “Performance Assessment of Graded Channel Gate-Stack based Double Gate MOSFET for Bio-sensing Applications,” *Silicon*, vol. 15, no. 4, pp. 1679–1689, 2023, doi: 10.1007/s12633-022-02136-1.
- [234] A. Das, S. Rewari, B. K. Kanaujia, S. S. Deswal, and R. S. Gupta, “Analytical investigation of a triple surrounding gate germanium source metal–oxide–semiconductor field-effect transistor with step graded channel for biosensing applications,” *Int. J. Numer. Model. Electron. Networks, Devices Fields*, vol. 36, no. 6, 2023, doi: 10.1002/jnm.3106.
- [235] A. Chattopadhyay, S. Tewari, and P. S. Gupta, “Dual-Metal Double-Gate with Low-k/High-k Oxide Stack Junctionless MOSFET for a Wide Range of Protein Detection: a Fully Electrostatic Based Numerical Approach,” *Silicon*, vol. 13, no. 2, pp. 441–450, 2021, doi: 10.1007/s12633-020-00430-4.
- [236] H. Jung, “Analysis of subthreshold swing in symmetric junctionless double gate MOSFET using high-k gate oxides,” *Int. J. Electr. Electron. Eng. Telecommun.*, vol. 8, no. 6, pp. 334–339, 2019.
- [237] S. S. Mohanty, S. Mishra, M. Mohapatra, and G. P. Mishra, “Impact of biomolecules position and filling area on the sensitivity of hetero stack gate MOSFET,” *Microelectronics J.*, vol. 126, 2022, doi: 10.1016/j.mejo.2022.105504.
- [238] M. Kumari, N. K. Singh, M. Sahoo, and H. Rahaman, “2-D Analytical Modeling and Simulation of Dual Material, Double Gate, Gate Stack Engineered, Junctionless MOSFET based Biosensor with Enhanced Sensitivity,” *Silicon*, vol. 14, no. 9, pp. 4473–4484, 2022, doi: 10.1007/s12633-

- 021-01223-z.
- [239] P. Udar, A. Goel, and R. S. Gupta, “Quantum Effect Dependent Modelling of Short Channel Junctionless Double Gate Stack(SC-JL-DG) MOSFET for High Frequency Analog Applications,” *Microelectronics J.*, vol. 134, 2023, doi: 10.1016/j.mejo.2023.105726.
- [240] W. SHOCKLEY and W. T. READ, “Statistics of the Recombinations of Holes and Electrons,” *Semicond. Devices Pioneer. Pap.*, pp. 62–69, 1991, doi: 10.1142/9789814503464_0002.
- [241] C. D. Vedel, T. Gunst, S. Smidstrup, and V. P. Georgiev, “Shockley-Read-Hall recombination and trap levels in In_{0.53}Ga_{0.47}As point defects from first principles,” *Phys. Rev. B*, vol. 108, no. 9, 2023, doi: 10.1103/PhysRevB.108.094113.
- [242] D. Sharma and S. K. Vishvakarma, “Precise analytical model for short channel Cylindrical Gate (CylG) Gate-All-Around (GAA) MOSFET,” *Solid. State. Electron.*, vol. 86, pp. 68–74, 2013, doi: 10.1016/j.sse.2012.08.006.
- [243] A. Tsormpatzoglou, D. H. Tassis, C. A. Dimitriadis, G. Ghibaud, G. Pananakakis, and R. Clerc, “A compact drain current model of short-channel cylindrical gate-all-around MOSFETs,” *Semicond. Sci. Technol.*, vol. 24, no. 7, 2009, doi: 10.1088/0268-1242/24/7/075017.
- [244] H. Cheng, S. Uno, and K. Nakazato, “Analytic compact model of ballistic and quasi-ballistic transport for cylindrical gate-all-around MOSFET including drain-induced barrier lowering effect,” *J. Comput. Electron.*, vol. 14, no. 1, pp. 321–328, 2015, doi: 10.1007/s10825-014-0659-8.
- [245] A. Ortiz-Conde, F. J. García-Sánchez, and S. Malobabic, “Analytic solution of the channel potential in undoped symmetric dual-gate MOSFETs,” *IEEE Trans. Electron Devices*, vol. 52, no. 7, pp. 1669–1672, 2005, doi: 10.1109/TED.2005.850629.
- [246] M. Shin, *Shin, M. (2009). Quantum Simulations of Ballistic Nanowire Field Effect Transistors. In: Meyers, R. (eds) Encyclopedia of Complexity and Systems Science. Springer, New York, NY. https://doi.org/10.1007/978-0-387-30440-3_441. 2009.*
- [247] V. Gupta, H. Awasthi, N. Kumar, A. K. Pandey, and A. Gupta, “A Novel Approach to Model Threshold Voltage and Subthreshold Current of Graded-Doped Junctionless-Gate-All-Around (GD-JL-GAA) MOSFETs,” *Silicon*, vol. 14, no. 6, pp. 2989–2997, 2022, doi: 10.1007/s12633-021-01084-6.
- [248] A. Das, S. Rewari, B. K. Kanaujia, S. S. Deswal, and R. S. Gupta, “Analytical investigation of a triple surrounding gate germanium source metal – oxide – semiconductor field-effect transistor with step graded channel for biosensing applications,” *Int. J. Numer. Model. Electron. Networks, Devices Fields*, no. February, pp. 1–25, 2023, doi: 10.1002/jnm.3106.
- [249] A. Das, S. Rewari, B. K. Kanaujia, S. S. Deswal, and R. S. Gupta, “Ge/Si interfaced label free nanowire BIOFET for biomolecules detection-analytical analysis,” *Microelectronics J.*, vol. 138, no. August, p. 105832, 2023, doi: https://doi.org/10.1016/j.mejo.2023.105832.
- [250] M. Sharma, R. Narang, M. Saxena, and M. Gupta, “Modeling and Simulation-Based Investigation of 2-D Symmetric Double Gate Dopingless-TFET and Its Circuit Performance for Low-Power Applications,” *IETE Tech. Rev. (Institution*

- Electron. Telecommun. Eng. India*), vol. 39, no. 4, pp. 838–849, 2022.
- [251] P. Saha, D. Kumar Dash, and S. Kumar Sarkar, “Nanowire reconfigurable FET as biosensor: Based on dielectric modulation approach,” *Solid. State. Electron.*, vol. 161, 2019, doi: 10.1016/j.sse.2019.107637.
- [252] S. Singh, B. Raj, and S. K. Vishvakarma, “Analytical modeling of split-gate junction-less transistor for a biosensor application,” *Sens. Bio-Sensing Res.*, vol. 18, pp. 31–36, 2018, doi: 10.1016/j.sbsr.2018.02.001.
- [253] A. Gnudi, S. Reggiani, E. Gnani, and G. Baccarani, “Semianalytical model of the subthreshold current in short-channel junctionless symmetric double-gate field-effect transistors,” *IEEE Trans. Electron Devices*, vol. 60, no. 4, pp. 1342–1348, 2013, doi: 10.1109/TED.2013.2247765.
- [254] Ajay, R. Narang, M. Saxena, and M. Gupta, “Modeling of gate underlap junctionless double gate MOSFET as bio-sensor,” *Mater. Sci. Semicond. Process.*, vol. 71, no. 15, pp. 240–251, 2017.
- [255] J. H. Ahn *et al.*, “Charge and dielectric effects of biomolecules on electrical characteristics of nanowire FET biosensors,” *Appl. Phys. Lett.*, vol. 111, no. 11, 2017, doi: 10.1063/1.5003106.
- [256] K. Tamersit and F. Djeflal, “Double-Gate Graphene Nanoribbon Field-Effect Transistor for DNA and Gas Sensing Applications: Simulation Study and Sensitivity Analysis,” *IEEE Sens. J.*, vol. 16, no. 11, pp. 4180–4191, 2016, doi: 10.1109/JSEN.2016.2550492.
- [257] A. Cuervo, P. D. Dans, J. L. Carrascosa, M. Orozco, G. Gomila, and L. Fumagalli, “Direct measurement of the dielectric polarization properties of DNA,” *Proc. Natl. Acad. Sci. U. S. A.*, vol. 111, no. 35, 2014, doi: 10.1073/pnas.1405702111.
- [258] S. Sharma, V. Nath, S. S. Deswal, and R. S. Gupta, “Analytical modelling and sensitivity analysis of Gallium Nitride-Gate Material and, dielectric engineered-Schottky nano-wire fet(GaN-GME-DE-SNW-fet) based label-free biosensor,” *Microelectronics J.*, vol. 129, 2022, doi: 10.1016/j.mejo.2022.105599.
- [259] Ashima, V. Dhandapani, and B. Raj, “Design and Performance Assessment of Graded Channel Gate-All-Around Silicon Nanowire FET for Biosensing Applications,” *Silicon*, vol. 15, no. 8, pp. 3535–3542, 2023, doi: 10.1007/s12633-022-02272-8.
- [260] K. Sirohi and S. Singh, “Numerical Model of Dielectric Engineered Triple Metal Source/Drain Pocket Doped Nanowire (DETMS/DPDN) FET Based Biosensor,” *Silicon*, vol. 14, no. 17, pp. 11647–11658, 2022, doi: 10.1007/s12633-022-01857-7.
- [261] N. Shaw and B. Mukhopadhyay, “Modeling and Performance Analysis of a Split-Gate T-Shape Channel DM DPDG-TFET Label-Free Biosensor,” *IEEE Sens. J.*, vol. 23, no. 2, pp. 1206–1213, 2023, doi: 10.1109/JSEN.2022.3224036.
- [262] S. Kalra, M. J. Kumar, and A. Dhawan, “Reconfigurable FET Biosensor for a Wide Detection Range and Electrostatically Tunable Sensing Response,” *IEEE Sens. J.*, vol. 20, no. 5, pp. 2261–2269, 2020, doi: 10.1109/JSEN.2019.2952333.
- [263] D. Cucinotta and M. Vanelli, “WHO declares COVID-19 a pandemic,” *Acta Biomed.*, vol. 91, no. 1, pp. 157–160, 2020, doi: 10.23750/abm.v91i1.9397.
- [264] Gorbalenya *et al.*, “Coronaviridae Study Group of the International Committee on Taxonomy of Viruses. The species Severe acute respiratory syndromerelated

- coronavirus,” 2020.
- [265] W. Shao, M. R. Shurin, S. E. Wheeler, X. He, and A. Star, “Rapid Detection of SARS-CoV-2 Antigens Using High-Purity Semiconducting Single-Walled Carbon Nanotube-Based Field-Effect Transistors,” *ACS Appl. Mater. Interfaces*, vol. 13, no. 8, pp. 10321–10327, 2021, doi: 10.1021/acscami.0c22589.
- [266] Y. Chen *et al.*, “Field-Effect Transistor Biosensor for Rapid Detection of Ebola Antigen,” *Sci. Rep.*, vol. 7, no. 1, 2017, doi: 10.1038/s41598-017-11387-7.
- [267] F. N. Ishikawa *et al.*, “Label-free, electrical detection of the SARS virus n-protein with nanowire biosensors utilizing antibody mimics as capture probes,” *ACS Nano*, vol. 3, no. 5, pp. 1219–1224, 2009, doi: 10.1021/nn900086c.
- [268] J. M. Kinsella and A. Ivanisevic, “Biosensing: Taking charge of biomolecules,” *Nat. Nanotechnol.*, vol. 2, no. 10, pp. 596–597, 2007, doi: 10.1038/nnano.2007.313.
- [269] A. Das, B. K. Kanaujia, S. S. Deswal, S. Rewari, and R. S. Gupta, “Doping induced threshold voltage and ION/IOFF ratio modulation in surrounding gate MOSFET for analog applications,” in *2022 IEEE International Conference of Electron Devices Society Kolkata Chapter (EDKCON), Kolkata, India, 2022*, pp. 1–6. doi: 10.1109/EDKCON56221.2022.10032940.
- [270] H. Lou *et al.*, “A Junctionless Nanowire Transistor With a Dual-Material Gate,” *IEEE Trans. Electron Devices*, vol. 59, no. 7, pp. 1829–1836, 2012.
- [271] S. Singh and A. Raman, “Gate-All-Around Charge Plasma-Based Dual Material Gate-Stack Nanowire FET for Enhanced Analog Performance,” *IEEE Trans. Electron Devices*, vol. 65, no. 7, pp. 3026–3032, 2018, doi: 10.1109/TED.2018.2816898.
- [272] A. Kaul, S. Rewari, and D. Nand, “Macaroni Channel-Nanowire-Field Effect Transistor (MC-NW-FET) for Gate Induced Drain Leakage (GIDL) Reduction Application,” in *Proceedings of 2022 IEEE International Conference of Electron Devices Society Kolkata Chapter, EDKCON 2022, 2022*, pp. 35–38. doi: 10.1109/EDKCON56221.2022.10032964.
- [273] A. Goel, S. Rewari, S. Verma, and R. S. Gupta, “High-K Spacer Dual-Metal Gate Stack Underlap Junctionless Gate All Around (HK-DMGS-JGAA) MOSFET for high frequency applications,” *Microsyst. Technol.*, vol. 26, no. 5, pp. 1697–1705, 2020, doi: 10.1007/s00542-019-04715-6.
- [274] Quest Diagnostics, “SARS-CoV-2 RNA, Qualitative Real-Time RT-PCR,” pp. 1–27, 2020, [Online]. Available: <https://www.fda.gov/media/136231/download>
- [275] R. Weissleder, H. Lee, J. Ko, and M. J. Pittet, “COVID-19 diagnostics in context,” *Sci. Transl. Med.*, vol. 12, no. 546, 2020, doi: 10.1126/scitranslmed.abc1931.
- [276] G. Liu and J. F. Rusling, “COVID-19 Antibody Tests and Their Limitations,” *ACS Sensors*, vol. 6, no. 3, pp. 593–612, 2021, doi: 10.1021/acssensors.0c02621.
- [277] N. J. Hardenbrook and P. Zhang, “A structural view of the SARS-CoV-2 virus and its assembly,” *Curr. Opin. Virol.*, vol. 52, pp. 123–134, 2022, doi: 10.1016/j.coviro.2021.11.011.
- [278] A. N. Pelletier, R. P. Sekaly, and J. A. Tomalka, “Translating known drivers of COVID-19 disease severity to design better SARS-CoV-2 vaccines,” *Curr.*

- Opin. Virol.*, vol. 52, pp. 89–101, 2022, doi: 10.1016/j.coviro.2021.11.012.
- [279] H. Yang and Z. Rao, “Structural biology of SARS-CoV-2 and implications for therapeutic development,” *Nat. Rev. Microbiol.*, vol. 19, no. 11, pp. 685–700, 2021, doi: 10.1038/s41579-021-00630-8.
- [280] C. rong Wu, W. chao Yin, Y. Jiang, and H. E. Xu, “Structure genomics of SARS-CoV-2 and its Omicron variant: drug design templates for COVID-19,” *Acta Pharmacol. Sin.*, vol. 43, no. 12, pp. 3021–3033, 2022, doi: 10.1038/s41401-021-00851-w.
- [281] P. Nag *et al.*, “Diagnosing COVID-19: The Disease and Tools for Detection,” *ACS Nano*, vol. 14, no. 4, pp. 5135–5142, 2020, [Online]. Available: <https://doi.org/10.1016/j.dsx.2020.05.008><https://doi.org/10.1016/j.nantod.2020.100883><https://doi.org/10.1007/s41403-020-00128-4>
- [282] S. Dastjerdi, M. Malikan, B. Akgöz, Ö. Civalek, T. Wiczenbach, and V. A. Eremeyev, “On the deformation and frequency analyses of SARS-CoV-2 at nanoscale,” *Int. J. Eng. Sci.*, vol. 170, 2022, doi: 10.1016/j.ijengsci.2021.103604.
- [283] C. Warsame, D. Valerini, I. Llavori, A. H. Barber, and S. Goel, “Modal analysis of novel coronavirus (SARS COV-2) using finite element methodology,” *J. Mech. Behav. Biomed. Mater.*, vol. 135, 2022, doi: 10.1016/j.jmbbm.2022.105406.
- [284] T. Wierzbicki, W. Li, Y. Liu, and J. Zhu, “Effect of receptors on the resonant and transient harmonic vibrations of Coronavirus,” *J. Mech. Phys. Solids*, vol. 150, 2021, doi: 10.1016/j.jmps.2021.104369.
- [285] M. Prof Nanshan Chen *et al.*, “Epidemiological and clinical characteristics of 99 cases of 2019 novel coronavirus pneumonia in Wuhan, China: a descriptive study,” *Lancet*, vol. 395, no. 10223, pp. 507–513, 2020.
- [286] N. Zhu *et al.*, “A Novel Coronavirus from Patients with Pneumonia in China, 2019,” *N. Engl. J. Med.*, vol. 382, no. 8, pp. 727–733, 2020, doi: 10.1056/nejmoa2001017.
- [287] R. Lu, Z. X. L. J, N. P, Y. B, and et al Wu H, “Genomic characterisation and epidemiology of 2019 novel coronavirus: implications for virus origins and receptor binding,” *Lancet*, vol. <https://www.lancet.com>, no. January, pp. 1–3, 2020.
- [288] Y. Xie *et al.*, “Revealing the Mechanism of SARS-CoV-2 Spike Protein Binding with ACE2,” *Comput. Sci. Eng.*, vol. 22, no. 6, pp. 21–29, 2020, doi: 10.1109/MCSE.2020.3015511.
- [289] P. Kasturi, M. Saxena, and R. S. Gupta, “Modeling and simulation of STacked Gate Oxide (STGO) architecture in Silicon-On-Nothing (SON) MOSFET,” *Solid. State. Electron.*, vol. 49, no. 10, pp. 1639–1648, 2005, doi: 10.1016/j.sse.2005.07.004.
- [290] A. Das, B. K. Kanaujia, V. Nath, and S. Rewari, “Impact of Reverse Gate Oxide Stacking on Gate All Around Tunnel FET for High Frequency Analog and RF Applications,” no. December, 2020, doi: 10.1109/INDICON49873.2020.9342175.
- [291] C. K. Sarkar, *Technology computer aided design: Simulation for VLSI MOSFET*. 2016.
- [292] M. K. Gilson and B. H. Honig, “The dielectric constant of a folded protein,” *Biopolymers*, vol. 25, no. 11, pp. 2097–2119, 1986, doi:

- 10.1002/bip.360251106.
- [293] K. Talley, C. Ng, M. Shoppell, P. Kundrotas, and E. Alexov, "On the electrostatic component of protein-protein binding free energy," *PMC Biophys.*, vol. 1, no. 1, 2008, doi: 10.1186/1757-5036-1-2.
- [294] S. Maiti, A. De, and S. K. Sarkar, "Analytical Modelling of Symmetric Gate Underlap Quadruple Gate Multichannel Junctionless MOSFET Biosensor," *Silicon*, vol. 14, no. 12, pp. 6921–6932, 2022, doi: 10.1007/s12633-021-01415-7.
- [295] A. Kumar, N. Gupta, M. M. Tripathi, and R. Chaujar, "Analysis of structural parameters on sensitivity of black phosphorus junctionless recessed channel MOSFET for biosensing application," *Microsyst. Technol.*, vol. 26, no. 7, pp. 2227–2233, 2020, doi: 10.1007/s00542-019-04545-6.
- [296] S. Tayal, B. Majumdar, S. Bhattacharya, and S. Kanungo, "Performance Analysis of the Dielectrically Modulated Junction-Less Nanotube Field Effect Transistor for Biomolecule Detection," *IEEE Trans. Nanobioscience*, 2022, doi: 10.1109/TNB.2022.3172702.
- [297] C. Dincer *et al.*, "Disposable Sensors in Diagnostics, Food, and Environmental Monitoring," *Adv. Mater.*, vol. 31, no. 30, 2019, doi: 10.1002/adma.201806739.
- [298] D. Kell, *Biosensors. Fundamentals and Applications*, vol. 19, no. 3. 1988. doi: 10.1016/0302-4598(88)80042-4.
- [299] A. Theja and M. Panchore, "Performance Investigation of GaSb/Si Heterojunction based Gate Underlap and Overlap Vertical TFET Biosensor," *IEEE Trans. Nanobioscience*, 2022, doi: 10.1109/TNB.2022.3183934.
- [300] R. Ranjan Thakur and P. Singh, "Investigations of Interface Trap Densities (Dit) and Interface Charges (Qit) for Steep Retrograded Al₂O₃ and HfO₂ based Nano Regime GAA FinFETs," *Mater. Today Proc.*, vol. 24, pp. 2011–2018, 2019, doi: 10.1016/j.matpr.2020.03.630.
- [301] P. Goyal, G. Srivastava, S. Rewari, and R. S. Gupta, "Controlling Ambipolarity and Rising Ion in TFETs for Enhanced Reliability: A Review," *2020 5th IEEE Int. Conf. Recent Adv. Innov. Eng. ICRAIE 2020 - Proceeding*, 2020, doi: 10.1109/ICRAIE51050.2020.9358322.
- [302] T. S. Arun Samuel, N. B. Balamurugan, T. Niranjana, and B. Samyuktha, "Analytical surface potential model with TCAD simulation verification for evaluation of surrounding gate TFET," *J. Electr. Eng. Technol.*, vol. 9, no. 2, pp. 655–661, 2014, doi: 10.5370/JEET.2014.9.2.655.
- [303] P. Kumar, M. Vashisht, N. Gupta, and R. Gupta, "Subthreshold Current Modeling of Stacked Dielectric Triple Material Cylindrical Gate All Around (SD-TM-CGAA) Junctionless MOSFET for Low Power Applications," *Silicon*, vol. 14, no. 11, pp. 6261–6269, 2022, doi: 10.1007/s12633-021-01399-4.
- [304] S. Sharma, A. Goel, S. Rewari, V. Nath, and R. S. Gupta, "Characterisation and Analysis of Schottky-Tube FET exhibiting Superior Characteristic Parameters," *Arab. J. Sci. Eng.*, vol. 48, no. 1, pp. 907–917, 2023, doi: 10.1007/s13369-022-07200-x.
- [305] P. Goyal, G. Srivastava, J. Madan, R. Pandey, and R. S. Gupta, "Source Material-Engineered Charge Plasma based Double Gate TFET for Analog/RF Applications," *ICIARA 2021 - 1st Int. Conf. Ind. Electron. Res. Appl. Proc.*, 2021, doi: 10.1109/ICIARA53202.2021.9726718.

- [306] IEEE, “International Roadmap for Devices and Systems 2017 Edition : More Moore,” 2017.
- [307] R. R. Thakur and N. Chaturvedi, “Design, optimization, and analysis of Si and GaN nanowire FETs for 3 nm technology,” *Semicond. Sci. Technol.*, vol. 36, no. 7, 2021, doi: 10.1088/1361-6641/abfee2.
- [308] Neeraj, A. Goel, S. Sharma, S. Rewari, and R. S. Gupta, “SiC-based analytical model for gate-stack dual metal nanowire FET with enhanced analog performance,” *Int. J. Numer. Model. Electron. Networks, Devices Fields*, vol. 35, no. 4, 2022, doi: 10.1002/jnm.2986.
- [309] P. Goyal, G. Srivastava, J. Madan, R. Pandey, and R. S. Gupta, “Design and Investigation of Mg₂Si Source Charge Plasma Based DGTFFET for Biomolecule Detection,” in *Proceedings of 2022 IEEE International Conference of Electron Devices Society Kolkata Chapter, EDKCON 2022*, 2022, pp. 474–478. doi: 10.1109/EDKCON56221.2022.10032967.
- [310] A. Dixit, D. P. Samajdar, R. P. Shukla, N. Bagga, and M. K. Hossain, “Biomolecule Detection using GaAs_{1-x}Sb_x FET based Dielectric Modulated Label-Free Biosensor,” *Phys. Scr.*, 2023, doi: 10.1088/1402-4896/ad1964.
- [311] S. Mishra, S. S. Mohanty, and G. P. Mishra, “Gate electrode stacked source/drain SON trench MOSFET for biosensing application,” *Phys. Scr.*, vol. 98, no. 12, 2023, doi: 10.1088/1402-4896/ad0d69.
- [312] G. P. Dash, Sidhartha; Mishra, “Ambipolarity Sensitivity Investigation using a Charge-Plasma TFET with Graphene Channel for Biomolecule Detection,” *ECS J. Solid State Sci. Technol.*, vol. 13, p. 011005, 2024.
- [313] M. Rahmani, “Performance Analysis of Electrochemical Detection Platform for DNA Hybridization Using TGN-Based Nanobiosensor,” *ECS J. Solid State Sci. Technol.*, vol. 12, no. 12, p. 127001, 2023, doi: 10.1149/2162-8777/ad1206.
- [314] Y. J. Yoon, J. S. Lee, D. S. Kim, J. H. Lee, and I. M. Kang, “Gallium nitride normally off mosfet using dual-metal-gate structure for the improvement in current drivability,” *Electron.*, vol. 9, no. 9, pp. 1–10, 2020, doi: 10.3390/electronics9091402.
- [315] S. Sugiura *et al.*, “Fabrication of normally-off mode GaN and AlGa_N/GaN MOSFETs with HfO₂ gate insulator,” *Solid. State. Electron.*, vol. 54, no. 1, pp. 79–83, 2010, doi: 10.1016/j.sse.2009.10.007.
- [316] J. Millan, P. Godignon, X. Perpina, A. Perez-Tomas, and J. Rebollo, “A survey of wide bandgap power semiconductor devices,” *IEEE Trans. Power Electron.*, vol. 29, no. 5, pp. 2155–2163, 2014, doi: 10.1109/TPEL.2013.2268900.
- [317] Y. Chu *et al.*, “Superior Performance of 5-nm Gate Length GaN Nanowire nFET for Digital Logic Applications,” *IEEE Electron Device Lett.*, vol. 40, no. 6, pp. 874–877, 2019, doi: 10.1109/LED.2019.2894416.
- [318] M. Ruzzarin *et al.*, “Exploration of gate trench module for vertical GaN devices,” *Microelectron. Reliab.*, vol. 114, 2020, doi: 10.1016/j.microrel.2020.113828.
- [319] F. Djeflal, M. Meguellati, and A. Benhaya, “A two-dimensional analytical analysis of subthreshold behavior to study the scaling capability of nanoscale graded channel gate stack DG MOSFETs,” *Phys. E Low-Dimensional Syst. Nanostructures*, vol. 41, no. 10, pp. 1872–1877, 2009, doi: 10.1016/j.physe.2009.08.002.

- [320] M. Emam, P. Sakalas, D. Vanhoenacker-Janvier, J. P. Raskin, T. C. Lim, and F. Danneville, "Experimental investigation of RF noise performance improvement in graded-channel MOSFETs," *IEEE Trans. Electron Devices*, vol. 56, no. 7, pp. 1516–1522, 2009, doi: 10.1109/TED.2009.2021361.
- [321] A. Das, S. Rewari, B. K. Kanaujia, S. S. Deswal, and R. S. Gupta, "Physics based numerical model of a nanoscale dielectric modulated step graded germanium source biotube FET sensor: modelling and simulation," *Phys. Scr.*, vol. 98, no. 11, 2023, doi: 10.1088/1402-4896/acf4c9.
- [322] A. Goel, S. Rewari, S. Verma, and R. S. Gupta, "Shallow Extension Engineered Dual Material Surrounding Gate (SEE-DM-SG) MOSFET for improved gate leakages, analysis of circuit and noise performance," *AEU - Int. J. Electron. Commun.*, vol. 111, 2019, doi: 10.1016/j.aeue.2019.152924.
- [323] V. Pathak and G. Saini, "A Graded Channel Dual-Material Gate Junctionless MOSFET for Analog Applications," *Procedia Comput. Sci.*, vol. 125, pp. 825–831, 2018.
- [324] M. S. Equbal and S. Sahay, "Scaling the MOSFET: detrimental short channel effects and mitigation techniques," in *Nanoelectronics: Physics, Materials and Devices*, 2023, pp. 11–37. doi: 10.1016/B978-0-323-91832-9.00003-8.
- [325] J. Y. Kim *et al.*, "A Dual-Gate Field-Effect Transistor for Label-Free Electrical Detection of Avian Influenza," *Bionanoscience*, vol. 2, no. 1, pp. 35–41, 2012, doi: 10.1007/s12668-011-0035-0.
- [326] R. Narang, M. Saxena, R. S. Gupta, and M. Gupta, "Dielectric modulated tunnel field-effect transistor-a biomolecule sensor," *IEEE Electron Device Lett.*, vol. 33, no. 2, pp. 266–268, 2012, doi: 10.1109/LED.2011.2174024.
- [327] K. N. Singh and P. K. Dutta, "Analytical Investigation of a Split Double Gate Graded Channel Field Effect Transistor for Biosensing Applications," *Silicon*, vol. 14, no. 17, pp. 11303–11313, 2022, doi: 10.1007/s12633-022-01774-9.
- [328] A. Das, S. Rewari, B. K. Kanaujia, S. S. Deswal, and R. S. Gupta, "Analytical modeling and doping optimization for enhanced analog performance in a Ge / Si interfaced nanowire MOSFET," *Phys. Scr.*, vol. 98, no. 7, p. 74005, 2023, doi: 10.1088/1402-4896/acde16.
- [329] J. Wei, J. Lei, X. Tang, B. Li, S. Liu, and K. J. Chen, "Channel-to-Channel Coupling in Normally-Off GaN Double-Channel MOS-HEMT," *IEEE Electron Device Lett.*, vol. 39, no. 1, pp. 59–62, 2018, doi: 10.1109/LED.2017.2771354.
- [330] L. Abarca-Cabrera, P. Fraga-García, and S. Berensmeier, "Bio-nano interactions: binding proteins, polysaccharides, lipids and nucleic acids onto magnetic nanoparticles," *Biomater. Res.*, vol. 25, no. 1, 2021, doi: 10.1186/s40824-021-00212-y.
- [331] H. Jung, "Analysis of subthreshold swing in junctionless double gate MOSFET using stacked high-k gate oxide," *Int. J. Electr. Comput. Eng.*, vol. 11, no. 1, pp. 240–248, 2021, doi: 10.11591/ijece.v11i1.pp240-248.
- [332] P. Goyal, G. Srivastava, J. Madan, and R. S. Gupta, "Performance investigation of hetero gate dielectric DGTFET with drain pocket for analog/RF applications," *Mater. Today Proc.*, vol. 71, pp. 145–149, 2022, doi: 10.1016/j.matpr.2022.08.195.
- [333] P. Goyal, J. Madan, G. Srivastava, R. Pandey, and R. S. Gupta, "Performance Analysis of Drain Pocket Hetero Gate Dielectric DG-TFET: Solution for

- Ambipolar Conduction and Enhanced Drive Current,” *Silicon*, 2022, doi: 10.1007/s12633-021-01564-9.
- [334] J. Ma *et al.*, “Graded-channel MOSFET (GCMOSFET) for high performance, low voltage DSP applications,” *IEEE Trans. Very Large Scale Integr. Syst.*, vol. 5, no. 4, pp. 352–359, 1997, doi: 10.1109/92.645061.
- [335] K. N. Singh and P. K. Dutta, “Analytical modeling of underlap graded channel field effect transistor as a label-free biosensor,” *Superlattices Microstruct.*, vol. 155, 2021, doi: 10.1016/j.spmi.2021.106897.
- [336] A. Goel, S. Rewari, S. Verma, and R. S. Gupta, “Temperature-Dependent Gate-Induced Drain Leakages Assessment of Dual-Metal Nanowire Field-Effect Transistor - Analytical Model,” *IEEE Trans. Electron Devices*, vol. 66, no. 5, pp. 2437–2445, 2019, doi: 10.1109/TED.2019.2898444.
- [337] A. M. Bhat, A. Varghese, N. Shafi, and C. Periasamy, “A Dielectrically Modulated GaN/AlN/AlGaIn MOSHEMT with a Nanogap Embedded Cavity for Biosensing Applications,” *IETE J. Res.*, 2021, doi: 10.1080/03772063.2020.1869593.
- [338] M. Maji and G. Saini, “Modeling of dual material surrounding split gate junctionless transistor as biosensor,” *Superlattices Microstruct.*, vol. 135, 2019, doi: 10.1016/j.spmi.2019.106290.
- [339] S. K. Vashist, “Point-of-care diagnostics: Recent advances and trends,” *Biosensors*, vol. 7, no. 4, 2017, doi: 10.3390/bios7040062.
- [340] A. N. Konwar and V. Borse, “Current status of point-of-care diagnostic devices in the Indian healthcare system with an update on COVID-19 pandemic,” *Sensors Int.*, vol. 1, 2020, doi: 10.1016/j.sintl.2020.100015.
- [341] L. Syedmoradi, A. Ahmadi, M. L. Norton, and K. Omidfar, “A review on nanomaterial-based field effect transistor technology for biomarker detection,” *Microchim. Acta*, vol. 186, no. 11, 2019, doi: 10.1007/s00604-019-3850-6.
- [342] B. D. Malhotra, S. Kumar, and C. M. Pandey, “Nanomaterials based biosensors for cancer biomarker detection,” *J. Phys. Conf. Ser.*, vol. 704, no. 1, 2016, doi: 10.1088/1742-6596/704/1/012011.
- [343] Y.-C. Syu, W.-E. Hsu, and C.-T. Lin, “Review—Field-Effect Transistor Biosensing: Devices and Clinical Applications,” *ECS J. Solid State Sci. Technol.*, vol. 7, no. 7, pp. Q3196–Q3207, 2018, doi: 10.1149/2.0291807jss.
- [344] Gorbalenya *et al.*, “Coronaviridae Study Group of the International Committee on Taxonomy of Viruses. The species Severe acute respiratory syndrome-related coronavirus,” *Nat. Microbiol.*, vol. 5, no. 4, pp. 536–544, 2020.
- [345] L. J. Carter *et al.*, “Assay Techniques and Test Development for COVID-19 Diagnosis,” *ACS Cent. Sci.*, vol. 6, no. 5, pp. 591–605, 2020, doi: 10.1021/acscentsci.0c00501.
- [346] P. Fathi-Hafshejani *et al.*, “Two-Dimensional-Material-Based Field-Effect Transistor Biosensor for Detecting COVID-19 Virus (SARS-CoV-2),” *ACS Nano*, vol. 15, no. 7, pp. 11461–11469, 2021, doi: 10.1021/acsnano.1c01188.
- [347] X. Feng *et al.*, “Recent advances in the detection of pathogenic microorganisms and toxins based on field-effect transistor biosensors,” *Crit. Rev. Food Sci. Nutr.*, 2023, doi: 10.1080/10408398.2023.2208677.
- [348] Z. Kotsiri, J. Vidic, and A. Vantarakis, “Applications of biosensors for bacteria and virus detection in food and water—A systematic review,” *J. Environ. Sci.*

- (China), vol. 111, pp. 367–379, 2022, doi: 10.1016/j.jes.2021.04.009.
- [349] R. C. Nnachi *et al.*, “Biosensors for rapid detection of bacterial pathogens in water, food and environment,” *Environ. Int.*, vol. 166, 2022, doi: 10.1016/j.envint.2022.107357.
- [350] E. Stern *et al.*, “Label-free immunodetection with CMOS-compatible semiconducting nanowires,” *Nature*, vol. 445, no. 7127, pp. 519–522, 2007, doi: 10.1038/nature05498.
- [351] X. P. A. Gao, G. Zheng, and C. M. Lieber, “Subthreshold regime has the optimal sensitivity for nanowire FET biosensors,” *Nano Lett.*, vol. 10, no. 2, pp. 547–552, 2010, doi: 10.1021/nl9034219.
- [352] G. Wenga, E. Jacques, A. C. Salaün, R. Rogel, L. Pichon, and F. Geneste, “Step-gate polysilicon nanowires field effect transistor compatible with CMOS technology for label-free DNA biosensor,” *Biosens. Bioelectron.*, vol. 40, no. 1, pp. 141–146, 2013, doi: 10.1016/j.bios.2012.07.001.
- [353] V. P. Georgiev *et al.*, “Experimental and Simulation Study of Silicon Nanowire Transistors Using Heavily Doped Channels,” *IEEE Trans. Nanotechnol.*, vol. 16, no. 5, pp. 727–735, 2017, doi: 10.1109/TNANO.2017.2665691.
- [354] A. Peled, A. Pevzner, H. Peretz Soroka, and F. Patolsky, “Morphological and chemical stability of silicon nanostructures and their molecular overlayers under physiological conditions: Towards long-term implantable nanoelectronic biosensors,” *J. Nanobiotechnology*, vol. 12, no. 1, 2014, doi: 10.1186/1477-3155-12-7.
- [355] R. Bange *et al.*, “Chemical stability of Si-SiC nanostructures under physiological conditions,” *Mater. Sci. Forum*, vol. 897 MSF, pp. 638–641, 2017, doi: 10.4028/www.scientific.net/MSF.897.638.
- [356] Sadow SE, “Silicon carbide biotechnology: a biocompatible semiconductor for advanced biomedical devices and applications.,” *Elsevier Ltd*, 2001.
- [357] B. Ptb Shaffer, “A Review of the Structure of Silicon Carbide,” *Acta Crystallogr. Sect. B Struct. Crystallogr. Cryst. Chem.*, vol. B25, p. 477, 1969, [Online]. Available: <http://journals.iucr.org/b/issues/1969/03/00/a06657/a06657.pdf>
- [358] S. Rashid, F. Bashir, F. A. Khanday, and M. R. Beigh, “Double Gate 6H-Silicon Carbide Schottky Barrier FET as Dielectrically Modulated Label Free Biosensor,” *Silicon*, vol. 15, no. 8, pp. 3387–3398, 2023, doi: 10.1007/s12633-022-02273-7.
- [359] N. Neeraj, S. Sharma, A. Goel, S. Rewari, and R. S. Gupta, “Improved analog and AC performance for high frequency linearity based applications using gate-stack dual metal (DM) nanowire (NW) FET (4H-SiC),” *Microsyst. Technol.*, 2023, doi: 10.1007/s00542-023-05480-3.
- [360] W. S. Lee, C. W. Lin, M. H. Yang, C. F. Huang, J. Gong, and Z. Feng, “Demonstration of 3500-V 4H-SiC lateral MOSFETs,” *IEEE Electron Device Lett.*, vol. 32, no. 3, pp. 360–362, 2011, doi: 10.1109/LED.2010.2101041.
- [361] T. Kimoto and J. A. Cooper, “Fundamentals of Silicon Carbide Technology: Growth, Characterization, Devices and Applications,” *Fundam. Silicon Carbide Technol. Growth, Charact. Devices Appl.*, vol. 9781118313, pp. 1–538, 2014, doi: 10.1002/9781118313534.
- [362] H. Mousa, M. Awais, and K. Teker, “Investigation of pH Effect on the

- Performance of Undoped Silicon Carbide Nanowire Field-Effect Transistors for the Development of Chemical Sensors and Biosensors,” *J. Electron. Mater.*, vol. 51, no. 5, pp. 2062–2069, 2022, doi: 10.1007/s11664-022-09468-z.
- [363] R. A. Andrievski, “Nanostructured superhard films as typical nanomaterials,” *Surf. Coatings Technol.*, vol. 201, no. 13, pp. 6112–6116, 2007, doi: 10.1016/j.surfcoat.2006.08.119.
- [364] A. L. Spetz *et al.*, “New materials for chemical and biosensors,” *Mater. Manuf. Process.*, vol. 21, no. 3, pp. 253–256, 2006, doi: 10.1080/10426910500464495.
- [365] K. Kubo *et al.*, “Calcium and silicon from bioactive glass concerned with formation of nodules in periodontal-ligament fibroblasts in vitro,” *J. Oral Rehabil.*, vol. 24, no. 1, pp. 70–75, 1997, doi: 10.1111/j.1365-2842.1997.tb00263.x.
- [366] G. Gabriel *et al.*, “Manufacturing and full characterization of silicon carbide-based multi-sensor micro-probes for biomedical applications,” *Microelectronics J.*, vol. 38, no. 3, pp. 406–415, 2007, doi: 10.1016/j.mejo.2006.11.008.
- [367] N. G. Wright and A. B. Horsfall, “SiC sensors: A review,” *J. Phys. D. Appl. Phys.*, vol. 40, no. 20, pp. 6345–6354, 2007, doi: 10.1088/0022-3727/40/20/S17.
- [368] G. L. Harris, *Properties of Silicon Carbide*. 1995.
- [369] V. Bougrov, M. E. Levinshtein, S. L. Rumyantsev, and A. Zubrilov, “Properties of Advanced Semiconductor Materials: GaN, AlN, InN, BN, SiC, SiGe,” p. 194, 2001, [Online]. Available: http://books.google.com/books?id=u26CpULkD_wC&pgis=1
- [370] X. Li, X. Wang, R. Bondokov, J. Morris, Y. H. An, and T. S. Sudarshan, “Micro/nanoscale mechanical and tribological characterization of SiC for orthopedic applications,” *J. Biomed. Mater. Res. - Part B Appl. Biomater.*, vol. 72, no. 2, pp. 353–361, 2005, doi: 10.1002/jbm.b.30168.
- [371] Y. Goldberg, M. Levinshtein, and S. Rumyantsev, “Silicon carbide (SiC) Properties of Advanced Semiconductor Materials: GaN, AlN, InN, BN, SiC, SiGe,” p. 216, 2001, [Online]. Available: <https://www.wiley.com/en-us/Properties+of+Advanced+Semiconductor+Materials%3A+GaN%2C+AlN%2C+InN%2C+BN%2C+SiC%2C+SiGe-p-9780471358275>
- [372] C. Jakobson, I. Bloom, and Y. Nemirovsky, “1/F noise in CMOS transistors for analog applications from subthreshold to saturation,” *Solid. State. Electron.*, vol. 42, no. 10, pp. 1807–1817, 1998, doi: 10.1016/S0038-1101(98)00162-2.
- [373] S. Dhar, O. Seitz, M. D. Halls, S. Choi, Y. J. Chabal, and L. C. Feldman, “Chemical properties of oxidized silicon carbide surfaces upon etching in hydrofluoric acid,” *J. Am. Chem. Soc.*, vol. 131, no. 46, pp. 16808–16813, 2009, doi: 10.1021/ja9053465.
- [374] S. Rewari, R. S. Gupta, S. S. Deswal, and V. Nath, “Silicon carbide based DSG MOSFET for high power, high speed and high frequency applications,” *India Int. Conf. Power Electron. IICPE*, vol. 2015-May, 2015, doi: 10.1109/IICPE.2014.7115857.
- [375] E. Schilirò, R. Lo Nigro, P. Fiorenza, and F. Roccaforte, “Negative charge trapping effects in Al₂O₃ films grown by atomic layer deposition onto thermally oxidized 4H-SiC,” *AIP Adv.*, vol. 6, no. 7, 2016, doi:

- 10.1063/1.4960213.
- [376] P. Fiorenza, F. Giannazzo, and F. Roccaforte, "Characterization of SiO₂/4H-SiC interfaces in 4H-SiC MOSFETs: A review," *Energies*, vol. 12, no. 12, 2019, doi: 10.3390/en12122310.
- [377] S. Kim, J. H. Ahn, T. J. Park, S. Y. Lee, and Y. K. Choi, "A biomolecular detection method based on charge pumping in a nanogap embedded field-effect-transistor biosensor," *Appl. Phys. Lett.*, vol. 94, no. 24, 2009, doi: 10.1063/1.3148340.
- [378] S. Kumar, Y. Singh, and B. Singh, "Extended Source Double-Gate Tunnel FET Based Biosensor with Dual Sensing Capabilities," *Silicon*, vol. 13, no. 6, pp. 1805–1812, 2021, doi: 10.1007/s12633-020-00565-4.
- [379] S. K. Vijay Thakur, Anil Kumar, "Numerical Modeling and Performance Analysis of underlap gate cavity integrated reconfigurable silicon nanowire schottky barrier transistor biosensors," *Appl. Phys. A Mater. Sci. Process.*, 2024.
- [380] A. Kumar and S. Kale, "Noise and sensitivity analysis of the dielectric modulated reconfigurable SiNW-SBT for biosensor applications," *Micro and Nanostructures*, vol. 193, 2024, doi: 10.1016/j.micrna.2024.207923.
- [381] D. Singh, B. S. Sengar, P. Dwivedi, and V. Garg, "Comparative analysis of gate structure dependent FET-based biosensor," *Mater. Today Commun.*, vol. 35, 2023, doi: 10.1016/j.mtcomm.2023.106301.
- [382] I. B. Khriplovich and A. A. Pomeransky, "Vapor-Liquid-Solid Mechanism of Single Crystal Growth," *Appl. Phys. Lett.*, vol. 4, no. 5, p. 89, 1998, [Online]. Available: <http://scitation.aip.org/content/aip/journal/apl/4/5/10.1063/1.1753975%5Cnhttp://arxiv.org/abs/gr-qc/9809069%5Cnhttp://dx.doi.org/10.1080/01422419908228843>
- [383] L. Fradetal, E. Bano, G. Attolini, F. Rossi, and V. Stambouli, "A silicon carbide nanowire field effect transistor for DNA detection," *Nanotechnology*, vol. 27, no. 23, 2016, doi: 10.1088/0957-4484/27/23/235501.
- [384] K. Rogdakis, E. Bano, L. Montes, M. Bechelany, D. Cornu, and K. Zekentes, "Rectifying source and drain contacts for effective carrier transport modulation of extremely doped SiC nanowire FETs," *IEEE Trans. Nanotechnol.*, vol. 10, no. 5, pp. 980–984, 2011, doi: 10.1109/TNANO.2010.2091147.
- [385] M. S. Parihar and A. Kranti, "Enhanced sensitivity of double gate junctionless transistor architecture for biosensing applications," *Nanotechnology*, vol. 26, no. 14, 2015, doi: 10.1088/0957-4484/26/14/145201.
- [386] P. Sriramani, N. Mohankumar, and Y. Prasamsa, "Drain current sensitivity analysis using a surface potential-based analytical model for AlGa_N/Ga_N double gate MOS-HEMT," *Micro and Nanostructures*, vol. 185, 2024, doi: 10.1016/j.micrna.2023.207720.
- [387] T. By PRAVEEN DWIVEDI, "Influence of Transistor Architecture on the Performance of Dielectric Modulated Biosensor," 2018.
- [388] E. M. L. F. C. M. Ferlay J, L. Mery, M. Piñeros, A. Znaor, I. Soerjomataram, and F. Bray, "Global Cancer Observatory: Cancer Today," *International Agency for Research on Cancer*. 2020.
- [389] "Cancer. Accessed: Dec. 21, 2021. [Online]. Available: <https://www.who.int/news-room/fact-sheets/detail/cancer>".

- [390] “Effects of chemotherapy and hormonal therapy for early breast cancer on recurrence and 15-year survival: an overview of the randomised trials. *Lancet*. 2005, 365: 1687-1717. 10.1016/S0140-6736(05)66544-0.”
- [391] J. S. Michaelson *et al.*, “Predicting the survival of patients with breast carcinoma using tumor size,” *Cancer*, vol. 95, no. 4, pp. 713–723, 2002, doi: 10.1002/cncr.10742.
- [392] A. A. Blood *et al.*, “An Antibody-based Blood Test Utilizing a Panel of Biomarkers as a New Method for Improved Breast Cancer Diagnosis,” *Biomark. Cancer*, vol. 5, pp. 71–80, 2013.
- [393] H. D. Sehgal, Y. Pratap, and S. Kabra, “Detection of Breast Cancer Cell-MDA-MB-231 by Measuring Conductivity of Schottky Source/Drain GaN FinFET,” *IEEE Sens. J.*, vol. 22, no. 6, pp. 6108–6115, 2022, doi: 10.1109/JSEN.2022.3148117.
- [394] S. Yadav, S. Rewari, and R. Pandey, “Surface potential and mobile charge based drain current modeling of double gate junctionless accumulation mode negative capacitance field effect transistor,” *Int. J. Numer. Model. Electron. Networks, Devices Fields*, 2023, doi: 10.1002/jnm.3172.
- [395] M. Hussein, F. Awwad, D. Jithin, H. El Hasasna, K. Athamneh, and R. Iratni, “Breast cancer cells exhibits specific dielectric signature in vitro using the open-ended coaxial probe technique from 200 MHz to 13.6 GHz,” *Sci. Rep.*, vol. 9, no. 1, 2019, doi: 10.1038/s41598-019-41124-1.

List of Publications Related to the Thesis

Journal Papers

1. **Shivani Yadav** and Sonam Rewari, "Numerical Simulation of Hetero Dielectric Trench Gate JAM Gate-All-Around FET (HDTG-JAM-GAAFET) for Label Free Biosensing Applications," *ECS Journal of Solid State Science and Technology*, vol. 12, no. 12, p. 127008, 2023, doi: 10.1149/2162-8777/ad161f.
2. **Shivani Yadav** and Sonam Rewari, "Analytical modeling and numerical simulation of graded JAM Split Gate-All-Around (GJAM-SGAA) Bio-FET for label free Avian Influenza antibody and DNA detection," *Microelectronics Journal*, vol. 142, p. 106011, 2023, doi: 10.1016/j.mejo.2023.106011.
3. **Shivani Yadav** and Sonam Rewari, "Dual metal dual layer GAA NW-FET (DMDL-GAA-NW-FET) biosensor for label free SARS-CoV-2 detection," *Microsystem Technologies*, 2023, doi: 10.1007/s00542-023-05560-4.
4. **Shivani Yadav**, Amit Das and Sonam Rewari, "Dielectric Modulated GANFET Biosensor for Label-Free Detection of DNA and Avian Influenza Virus: Proposal and Modeling" *ECS Journal of Solid State Science and Technology*, vol. 13, no. 4, p. 047001, 2024, doi: 10.1149/2162-8777/ad3364.
5. **Shivani Yadav** and Sonam Rewari, "Nanoscale Trench Gate Engineered JAM Gate-All-Around (TGE-JAM-GAA) Label-Free BioFET for Charged/Neutral Biomolecules Detection," *IETE Journal of Research*, 70(11), 8263–8277, 2024, <https://doi.org/10.1080/03772063.2024.2368636>
6. **Shivani Yadav** and Sonam Rewari, "Dielectric modulated 4 H-SiC source triple metal gate-all-around silicon carbide FET (DM-TMGAA-SiCFET) biosensor for label-free biomolecule detection," *Microsystem Technologies* (2024). <https://doi.org/10.1007/s00542-024-05796-8>

Conference Papers

1. **Shivani Yadav** and Sonam Rewari, "Dielectric Modulated Gallium-Arsenide Gate-All-Around Engineered Field Effect Transistor (GaAs-GAAE-FET) Biosensor for Breast Cancer Detection," 2024 IEEE International Conference on

Computing, Power and Communication Technologies (IC2PCT), Greater Noida, India, 2024, pp. 1553-1557, doi: 10.1109/IC2PCT60090.2024.10486515.

2. **Shivani Yadav** and Sonam Rewari, “Trench Gate JAM Dielectric Modulated Nanowire FET (TG-JAM-DM-NWFET) Biosensor,” Proc. 2022 IEEE Int. Conf. Electron Devices Soc. Kolkata Chapter, EDKCON 2022, pp. 23–28, 2022, doi: 10.1109/EDKCON56221.2022.10032912.



DELHI TECHNOLOGICAL UNIVERSITY

Formerly Delhi College of Engineering

Shahbad Daulatpur, Main Bawana Road, Delhi –42

PLAGIARISM VERIFICATION

Title of the Thesis: **Analytical Modeling and Numerical Simulation of Gate-All-Around Field Effect Transistor for Sensing Applications**

Total Pages: **234**

Name of the Scholar: **Shivani Yadav**

Supervisor: **Dr. Sonam Rewari**

Department: **Electronics and Communication Engineering**

This is to report that the above thesis was scanned for similarity detection. Process and outcome are given below:

Software used: **Turnitin**

Submission ID: **oid:27535:67099389**

Similarity Index: **31%**

Self-Publication(s) Similarity Index: **25%**

Final Total Similarity Index: **6%**

Total Word Count: **86,546**

Date: **September 18, 2024**

Candidate's Signature

Signature of Supervisor

Curriculum Vitae/ Brief Profile of Ms. Shivani Yadav



SHIVANI YADAV

shivaniyadav.ece@gmail.com

+91 9599903078

[linkedin.com/in/shivani-yad/](https://www.linkedin.com/in/shivani-yad/)

PROFILE SUMMARY

Dedicated and accomplished research associate/scholar with a strong background in semiconductor device modeling, VLSI design, and nanotechnology. Equipped with extensive experience in device simulation, analytical modeling, and numerical simulation, eager to contribute to innovative projects in the VLSI industry.

TECHNICAL PROFICIENCY

Device simulation software:

SILVACO ATLAS TCAD, LTSPICE, PSPICE, HSPICE

EDA Tools: Cadance Virtuoso, Xilinx Vivado design suite

Programming languages: Verilog, MATLAB, C

Other Software: MS Office Suite, Linux

Technical Subjects: Digital Electronics, CMOS Digital VLSI Design, ASIC Design Flow, Integrated circuits, Low Power VLSI Design.

SKILLS

VLSI Design & Semiconductor Device Modelling
Analytical Modeling & Numerical Simulation
Device Simulation and Analysis
Technical Writing & Publication
Team Collaboration & Communication
Research and Development

EDUCATION

PH.D IN ELECTRONICS & COMMUNICATION ENGG.

Delhi Technological University, Delhi

Date of Joining: July 2021

M.TECH. IN VLSI DESIGN (2011)

Malviya National Institute of Technology, (NIT Jaipur)

CGPA: 8.75/10

B.TECH. IN ELECTRONICS & COMMUNICATION ENGG. (2009)

UIET, Chatrapati Shahu Ji Maharaj University Kanpur

CGPA: 9.50/10

EXPERIENCE

1. RESEARCH SCHOLAR

DELHI TECHNOLOGICAL UNIVERSITY, DELHI

AUGUST 2021 – AUGUST 2024

Conducted advanced research in nano semiconductor devices, focusing on Gate-All-Around FETs.

Published multiple papers in high-impact journals and conferences.

Developed and implemented simulation models using SILVACO TCAD and Cadence tools.

2. ASSISTANT PROFESSOR

INDERPRASTHA ENGINEERING COLLEGE
GHAZIABAD **(DECEMBER 2014 TO AUGUST 2021)**

Led the setup and management of the IC lab with new Texas Instruments kits.

Guided multiple B.Tech. projects focused on innovative VLSI design solutions.

Structured and led the upskilling initiative for faculties on trending technologies

Played a key role in the successful NBA accreditation of the ECE department.

3. ASSISTANT PROFESSOR

SHARDA GROUP OF INSTITUTIONS, HCST,
MATHURA **(AUGUST 2011 TO NOVEMBER 2014)**

Guided B.Tech. and M.Tech. projects on advanced topics in electronics.

Worked as Class Teacher and counsellor for the program of B. Tech.

PAPERS PUBLISHED IN JOURNALS

1. **Shivani Yadav** and Sonam Rewari, "Numerical Simulation of Hetero Dielectric Trench Gate JAM Gate-All-Around FET (HDTG-JAM-GAAFET) for Label Free Biosensing Applications," **ECS Journal of Solid State Science and Technology**, vol. 12, no. 12, p. 127008, **2023**, doi: 10.1149/2162-8777/ad161f (**IOP Science, SCIE**).
2. **Shivani Yadav** and Sonam Rewari, "Analytical modeling and numerical simulation of graded

Technology integration

CERTIFICATIONS & ADDITIONAL TRAINING

"Programming for Everybody (Getting Started with Python)" - University of Michigan (Coursera)
"The Data Science Course 2020: Complete Data Science Bootcamp" - Udemy
NPTEL certifications in CMOS Digital VLSI Design and Switching Circuits and Logic Design.
GATE Qualified (2009) in ECE.

THESIS AND PROJECTS

Thesis in Ph.D: Analytical Modeling and Numerical Simulation of Gate-All-Around Field Effect Transistor for Sensing Applications
Major Project in M.Tech: Modeling And Simulation of CMOS Logic Circuits using ANN and ANFIS
Minor Project in M.Tech: Analysis of Leakage Power Reduction Techniques for Flip-Flops
Project in B.Tech: Distributed PID Controller and Kalman Filter for Linear and Non-Linear Systems

LANGUAGES

English
Hindi

- JAM Split Gate-All-Around (GJAM-SGAA) Bio-FET for label free Avian Influenza antibody and DNA detection," **Microelectronics Journal**, vol. 142, p. 106011, **2023**, doi: 10.1016/j.mejo.2023.106011 (**Elsevier, SCIE**).
3. **Shivani Yadav** and Sonam Rewari, "Dual metal dual layer GAA NW-FET (DMDL-GAA-NW-FET) biosensor for label free SARS-CoV-2 detection," **Microsystem Technologies**, **2023**, doi: 10.1007/s00542-023-05560-4 (**Springer, SCIE**).
 4. **Shivani Yadav**, Amit Das and Sonam Rewari, "Dielectric Modulated GANFET Biosensor for Label-Free Detection of DNA and Avian Influenza Virus: Proposal and Modeling" **ECS Journal of Solid State Science and Technology**, vol. 13, no. 4, p. 047001, **2024**, doi: 10.1149/2162-8777/ad3364 (**IOP Science, SCIE**).
 5. Shivani Yadav and Sonam Rewari, "Nanoscale Trench Gate Engineered JAM Gate-All-Around (TGE-JAM-GAA) Label-Free BioFET for Charged/Neutral Biomolecules Detection," **IETE Journal of Research**, 70(11), 8263–8277, **2024**,
<https://doi.org/10.1080/03772063.2024.2368636> (**Taylor & Francis, SCIE**)
 6. **Shivani Yadav** and Sonam Rewari, "Dielectric modulated 4 H-SiC source triple metal gate-all-around silicon carbide FET (DM-TMGAA-SiCFET) biosensor for label-free biomolecule detection," **Microsystem Technologies**, **2024**,
<https://doi.org/10.1007/s00542-024-05796-8> (**Springer, SCIE**).

PAPERS PUBLISHED/ PRESENTED IN INTERNATIONAL CONFERENCES

1. **Shivani Yadav** and Sonam Rewari, "Dielectric Modulated Gallium-Arsenide Gate-All-Around Engineered Field Effect Transistor (GaAs-GAAE-FET) Biosensor for Breast Cancer Detection," 2024 IEEE International Conference on Computing, Power and Communication Technologies (IC2PCT), Greater Noida, India, **2024**, pp. 1553-1557, doi: 10.1109/IC2PCT60090.2024.10486515.
2. **Shivani Yadav** and Sonam Rewari, "Trench Gate JAM Dielectric Modulated Nanowire FET (TG-JAM-DM-NWFET) Biosensor." Proc. 2022 IEEE Int. Conf. Electron Devices Soc. Kolkata Chapter, EDKCON 2022, pp. 23–28, **2022**, doi: 10.1109/EDKCON56221.2022.10032912.
3. **Shivani Yadav**, Shafali Jagga, Shalini Singh, "A Survey on Neuromorphic Computing with

Beyond CMOS Technologies,” “International Conference on Intelligent Systems Electrical and Communication Technology” (ICISECT–21) on 12th & 13th March **2021**.

4. **Shivani Yadav**, Ashish Sharma, Neeraj Yadav, “PID Controller with Distributed P, I, D Actions for Linear and Non-Linear Plants,” International Conference on Adaptive Computer Technologies in Various Engineering Applications, 24th – 26th February **2011**.
5. Neeraj Yadav, Sanjeev Agarwal, **Shivani Yadav**, “Low Voltage CMOS Four Quadrant Analog Multiplier,” International Conference on Adaptive Computer Technologies in Various Engineering Applications, 24th – 26th February **2011**.

PAPERS PUBLISHED/ PRESENTED IN NATIONAL CONFERENCES (6)

1. Shubham Singh, Vikas Yadav, Sunny Kumar, **Shivani Yadav**, “Design and Implementation of Two Stage OPAMP,” National Conference on Recent Trends in Electronics and Electrical Engineering (NCRTEEE-2020), 25th – 26th June **2020**.
2. Sonali, Swati Upadhyay, Nivedita Yadav, Shweta Yadav, **Shivani Yadav**, “Area and Delay Optimization of Digital Circuits,” National Conference on Recent Trends in Electronics and Electrical Engineering (NCRTEEE-2020), 25th – 26th June **2020**.
3. Ayush Sharma, Abhishek Sharma, Akash Shukla, Abhishek Chaudhary, **Shivani Yadav**, “Smart Home and Smart Security System,” National Conference on Recent Trends in Electronics and Electrical Engineering (NCRTEEE-2019), 10th – 11th June **2019**.
4. Ashutosh Yadav, Ankit Maurya, **Shivani Yadav**, “Design and Testing of Analog Circuits Using ANN,” National Conference on Recent Trends in Electronics and Electrical Engineering (NCRTEEE-2017), 16th – 17th February **2017**.
5. **Shivani Yadav**, D. Boolchandani, “A Low Power Flip-Flop Design Using MTCMOS Technique in 65 nm Technology”, National Conference on Innovative Developments in Electronics Arena (IDEA’11)”, 19th – 20th February **2011**.
6. Neeraj Yadav, Sanjeev Agarwal, **Shivani Yadav**, “A Low Voltage Four Quadrant Analog Multiplier Using Different Techniques,” National Conference on Innovative Developments in Electronics Arena (IDEA’11)”, 19th – 20th February **2011**.

Thank you very much for reading.

“Excellence is a continuous process and not an accident.”

--Dr. A.P.J. Abdul Kalam

~ to new beginnings
Shivani Yadav